New Oxides for Oxygen Evolution Catalysis from Hydrothermal Synthesis

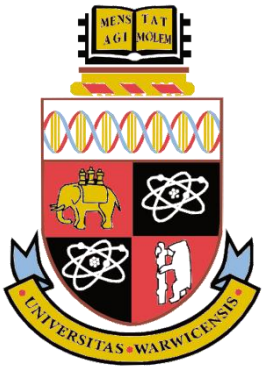

by

David Lawrence Burnett

Thesis submitted for the degree of

Doctor of Philosophy in Chemistry

Department of Chemistry, University of Warwick

September 2016

Contents

Acknowledgements v
Declaration vi
Abstract vii
Chapter 1 – Introduction 1
1.1 Fuel Cells 1
1.2 Polymer Electrolyte Membrane Fuel Cells 4
1.3 Oxygen Evolution Reaction Catalysts 6
1.4 Oxygen Evolution Reaction Mechanism in PEMFCs 8
1.5 Ruthenium and Iridium Oxides 13
1.5 Synthetic Techniques for Production of Oxides 18
1.5 Aims of This Work and Organisation of the Thesis 20
References 20
Chapter 2 – Experimental 25
2.1 Synthesis 25
2.1.1 Hydrothermal Synthesis 25
2.1.2 Ceramic/Molten Salt Synthesis and Annealing 26
2.2 Characterisation 26
2.2.1 Powder X-ray Diffraction 26
2.2.2 Powder Neutron Diffraction 28
2.2.3 Total Scattering 30
2.2.4 Data Fitting 31
2.2.5 Software Used 32
2.2.6 Scanning Electron Microscopy (SEM) 32
2.2.7 Transmission Electron Microscopy (TEM) 33
2.2.8 Raman Spectroscopy 33
2.2.9 Fourier Transform Infra-Red Spectroscopy 34
2.2.10 X-ray Absorption Spectroscopy 34
2.2.11 Thermal Analysis 36
2.2.12 Pycnometry 36
2.2.13 Magnetometry 36
2.2.14 Surface Area Measurement 37

2.2.15 Inductively Coupled Plasma Optical Emission Spectroscopy 37
2.2.16 X-ray Fluorescence 37
References 37
Chapter 3 – Substituted Ruthenium Rutiles 39
3.1 Introduction and Scope of Chapter 39
3.2 Synthesis 39
3.2.1 Peroxide Synthesis 39
3.2.2 Synthesis of Substituted Ruthenate Rutiles 40
3.3 Characterisation of Peroxide Precursors 41
3.4 Powder XRD of Substituted Rutiles 50
3.5 Raman Spectroscopy 53
3.6 Electron Microscopy 54
3.7 X-ray Absorption Spectroscopy 56
3.8 Powder Neutron Diffraction 60
3.9 Pair Distribution Function Analysis 64
3.10 Thermal Stability 67
3.10 Magnetic Susceptibility Studies 78
3.10 Summary 80
References 81
Chapter 4 – Iridate Pyrochlores 83
4.1 Introduction and Scope of Chapter 83
4.2 Materials Synthesis 83
4.3 Pyrochlores with A = Ca, Na and B = Ir 85
4.4 B-site Substitution in A = Ca and Na and B = Ir and M 96
4.4.1 Antimony Substitution 96
4.4.2 Zirconium Substitution 107
4.4.3 Ruthenium Substitution 118
4.4.4 Osmium Substitution 128
4.4.5 Rhodium Substitution 131
4.4.6 Manganese Substitution 141
4.4.7 B-site Substitution Discussion 148
4.5 Calcium Sodium Iridium Oxide Variations 150
4.5.1 Sodium Free Pyrochlore 150
4.5.2 Particle Size Exploration 156

4.5.3 Acid Leaching 158
4.5.4 Discussion 172
References 173
Chapter 5 – Exploratory Synthesis of New Iridium and Ruthenium Oxide Materials 175
5.1 Introduction to and Scope of Chapter 175
5.2 $K_{0.25}IrO_2$ Hollandite 176
5.2.1 Synthesis of IrO_2 Precursor 176
5.2.2 IrO_2 Precursor Characterisation 177
5.2.3 Characterisation of Hollandite Phase 180
5.3$ARuO_3$ A = Sr, Ba 186
5.3.1 Synthesis of $ARuO_3$ A = Sr, Ba 186
5.3.2 Characterisation of $SrRuO_3$ 186
5.3.3 Characterisation of 4H-$BaRuO_3$ 190
5.4 Iridium and Ruthenium Substituted Sodium Tantalates and Niobates 194
5.4.1 Synthesis of Substituted Sodium Tantalates and Niobates 194
5.4.2 Characterisation of Substituted Sodium Tantalates and Niobates 194
5.5 Strontium Iridate 202
5.5.1 Synthesis of Strontium Iridate 202
5.5.2 Characterisation of Strontium Iridate 203
5.6 Barium Iridate 206
5.6.1 Synthesis of Barium Iridate 206
5.6.2 Characterisation of Barium Iridate 207
5.2.2 Attempts at Improving the Crystallinity of the New Barium Iridate 214
References: 220
Chapter 6 – Electrocatalysis Using New Precious Metal Oxides 222
6.1 Introduction to and Scope of Chapter 222
6.2 Experimental 222
6.2.1 Powder Conductivity 222
6.2.2 Gold Rotating Disc Electrode 222
6.2.3 Wet Cell Testing 223
6.2.4 Electrode Fabrication 223
6.2.5 Membrane Electrode Assembly Testing 224
6.2.6 *In situ* XANES and EXAFS 229
6.3 Substituted Rutile OER Catalysis 233

6.4 Pyrochlore OER Catalysis 237
6.4.1 $(Ca,Na)_{2-x}Ir_2O_6O'$ 237
6.4.2 $(Ca,Na)_{2-x}(Ir_{1-y}M_y)_2O_6O'$ (M = Sb, Zr, Ru, Rh and Mn) 239
6.4.3 Summary of Electrocatalysis from B-Site Substituted Iridate Pyrochlores 247
6.4.4 A-Site Variations of $(Ca,Na)_{2-x}Ir_2O_6O'$ 248
6.4.5 Summary of Electrocatalysis from A-Site Substituted Iridate Pyrochlores 254
6.5 Other Iridium Oxides for OER Catalysis 254
6.6 *In situ* XAS 257
6.7 Conclusions 271
References 276
Chapter 7 – Conclusions and Further Work 278
7.1 Substituted Ruthenium Oxides 278
7.2 Iridium Oxide Pyrochlores 279
7.3 Other Ruthenium and Iridium Oxides 280
7.4 Catalytic Studies 281
References 283

Acknowledgements

First I would like to thank Professor Richard Walton. The last five years spent as part of his group have been marvellous. His endless patience and encouragement have made this work possible.

I would like to thank Enrico Petrucco and Jonathon Sharman for their supervision and valuable input. Trips to Johnson Matthey Technology Centre were infinitely more productive than they would have been without Enrico's aid. I am grateful to the rest of the fuel cells group at Johnson Matthey for general help around there labs during these visits and many informative conversations.

I am immensely grateful to Helen Playford whose guidance with all things neutron was unending. I am also thankful for the GEM Xpress data collection service provided by Ron Smith.

Thanks to the entirety of the Walton group past and present, who have been a pleasure to work with. Craig's instruction in the use of GSAS and Luke's general help with everything else was invaluable. Many experiments have been undertaken at either ISIS or diamond, and I am hugely grateful for the company of everyone who apart of these, in particular Dan Cook who undertook one of mine while I was gallivanting around the south of Italy. Thanks to everyone involved with all the various PACs for making the final two years of the PhD particularly memorable.

Lastly I would like to thank my family, and while they still can not describe what I do, they have supported me through this whole process, and for that I am unendingly grateful.

Declaration

All the work presented herein was carried out by the author, except when stated otherwise, at the University of Warwick. This thesis has been composed by myself and has not been submitted at any other academic institution in any application for a higher degree.

Abstract

The hydrothermal synthesis of complex oxides of ruthenium and iridium with potential application as oxygen evolution reaction catalysts in polymer electrolyte membrane fuel cells is reported.

The materials $M_{0.15}Ru_{0.85}O_2$, where M = Zn, Mg, Ni, Co or Cu, have been synthesised from peroxide reagents and potassium perruthenate. Structural refinement against powder neutron diffraction data shows these materials adopt the rutile structure with space group $P4_2/mnm$ with the metals substituting ruthenium and no evidence of oxide vacancies. X-ray absorption near-edge structure spectra recorded at the Ru K-edge show that to compensate for the inclusion of these metals, the ruthenium is oxidised above +4.

New oxides based on $(Ca_{0.59}Na_{0.27})_2Ir_2O_6{\cdot}0.66H_2O$ were produced with substitutions made on both the A and B-site. All materials were shown to adopt the pyrochlore structure with space group $Fd\bar{3}m$. The level of B-site substitution was found to be dependent on the substituent element (Sb, Ru, Rh, Mn or Zr), with maximum substitution levels ranging from 30-100 %. The zirconium substituted material, $(Ca_{0.58}Na_{0.32}Zr_{0.12})_2(Ir_{0.56}Zr_{0.44})_2O_6{\cdot}0.97H_2O$, shows significant deviation from the average structure at the local scale. The synthesis of the pure iridium material was further investigated and it was found both the A-site composition and particle size could be controlled. Treatment in concentrated H_2SO_4 at elevated temperature yielded materials with vacant A-sites.

The hydrothermal synthesis of a number of other mixed metal oxides is reported. These include the perovskites $Na(Ta_{1-x}M_x)O_3$, $Na(Nb_{1-x}Ir_x)O_3$and $SrRuO_3$, where M = Ir or Ru, and $x < 0.15$, the hexagonal perovskite 4H-$BaRuO_3$, $Sr_{2.85}Ir_3O_{11}$ a material with a $KSbO_3$-type structure and a barium iridate with an unknown structure.

In electrochemical tests, performed in membrane electrode assemblies, all materials outperform the benchmark materials, iridium tantalum oxide and ruthenium iridium oxide under acidic conditions. The substituted rutile materials are highly active, but not as durable or selective towards the oxygen evolution reaction as the iridate materials. *In situ* studies of catalyst layers using X-ray absorption fine structure spectroscopy at the Ir L_{III}, Ru K, Rh K and Sb K-edges show that both iridium and ruthenium participate in redox chemistry at oxygen evolution conditions, however antimony and rhodium are redox inactive.

Chapter 1 – Introduction

1.1 Fuel Cells

Energy production from burning fossil fuels has underpinned society since the industrial revolution. The ever increasing demand for energy and depleting oil supply has lead to a need to reduce the dependence on fossil fuels, through diversification of power generation. Energy security and the desire to protect the environment are a couple of the reasons renewable energy sources such as solar, wind and tidal are being increasingly deployed, however none of these can produce power on demand as they are dependent on the weather conditions and time of day.[1] As such fossil fuels are currently required to compensate when renewables are not able to generate required power. This problem can be tackled using the excess energy when demand is low to produce fuel which can later be consumed when demand is high.

Fuel cells are energy converters that convert the chemical energy of fuels directly into electrical energy. While in principle sounding similar to the internal combustion engine, the combustion engine has an intermediate mechanical energy conversion, which drastically reduces their potential efficiency when compared to fuel cells. Fuel cells typically operate with an efficiency between 40 - 60 %, however when using pure hydrogen and oxygen as fuel and oxidiser the theoretical maximum is increased to 83 %, and this can be further increased using a combined heat and power system where the heat generated by the cell can be put to further use, resulting in operating efficiencies as high as 90 %.[2] On the other hand typical internal combustion engines operate at 25 % efficiency, with a theoretical maximum of 58 %, which again can be increased using a combined heat and power system.[3]

There are many varieties of fuel cell, and they are named according to what fuel and electrolyte they utilise.[4] A brief summary of the 6 main types can be found in Table 1.1, highlighting each variant's advantages and disadvantages. Due to the low power density of

direct methanol fuel cells (DMFC) they are typically aimed at portable electronic devices. Phosphoric acid (PAFC), alkaline (AFC) and polymer electrolyte membrane (PEMFC) fuel cells are the next tier up in terms of size and output. These have the greatest potential for use in the automotive industry, but also in aviation and space travel. Due to their very high operating temperatures, molten carbonate (MCFC) and solid oxide (SOFC) fuel cells, have the greatest potential in static power generation, ranging from residential power generation to use in power plants or large naval vessels. Of those suitable for the automotive industry, polymer electrolyte membrane fuel cells have the greatest potential given they vastly outperform the other variants in terms of power density.

Table 1.1: Comparison of six main types of fuel cell. Adapted from Nema *et al.*[4]

	Fuel cell types					
Parameters	PEMFC	AFC	PAFC	MCFC	SOFC	DMFC
Electrolyte	Solid polymer membrane (Nafion™)	Liquid solution of KOH	Phosphoric acid (H_3PO_4)	Lithium and potassium carbonate ($LiAlO_2$)	Stabilized solid oxide electrolyte (Y_2O_3, ZrO_2)	Solid polymer membrane
Operating temperature (°C)	50–100	50–200	~200	~650	800–1000	60–200
Anode reaction	$H_2 \rightarrow 2H^+ + 2e^-$	$H_2 + 2(OH^-) \rightarrow 2H_2O + 2e^-$	$H_2 \rightarrow 2H^+ + 2e^-$	$H_2O + CO_3^{2-} \rightarrow H_2O + CO_2 + 2e^-$	$H_2 + O_2 \rightarrow H_2O + 2e^-$	$CH_3OH + H_2O \rightarrow CO2 + 6H^+ + 6H^-$
Cathode reaction	$½O_2 + 2H^+ + 2e^- \rightarrow H_2O$	$½O_2 + H_2O + 2e^- \rightarrow 2(OH)^-$	$½O_2 + 2H^+ + 2e^- \rightarrow H_2O$	$½O_2 + CO_2 + 2e^- \rightarrow CO_3^{2-}$	$½O_2 + 2e^- \rightarrow O^{2-}$	$3O_2 + 12H^+ + 12H^- \rightarrow 6H_2O$
Charge carrier	H^+	OH^-	H^+	CO_3^{2-}	O^{2-}	H^+
Fuel	Pure H_2	Pure H_2	Pure H_2	H_2, CO, CH_4, other hydrocarbons	H_2, CO, CH_4, other hydrocarbons	CH_3OH
Oxidant	O_2 in air	O_2 in air	O_2 in air	O_2 in air	O_2 in air	O_2 in air
Efficiency	40–50%	~50%	40%	>50%	>50%	40%
Cell Voltage	1.1	1	1.1	0.7–1.0	0.8–1.0	0.2–0.4
Power density (kW/m^3)	3.8–6.5	~1	0.8–1.9	1.5–2.6	0.1–1.5	~0.6
Capacity	30 W- 250 kW	10–100 kW	100 kW - 1.3 MW	155 kW - 2 MW	1 kW - 1.7 MW	1 W - 1 MW
Advantages	High power density; quick start up; solid non-corrosive electrolyte	High power density; quick start up	Produce high grade waste heat; stable electrolyte characteristics	High efficiency; no metal catalysts needed	Solid electrolyte; high efficiency; generate high grade waste heat	Reduced cost due to absence of fuel reformer
Drawbacks	Expensive platinum catalyst; sensitive to fuel impurities (CO, H_2S)	Expensive platinum catalyst; sensitive to fuel impurities (CO, CO_2, CH_4, H_2S)	Corrosive liquid electrolyte; sensitive to fuel impurities (CO, H_2S)	High cost; corrosive liquid electrolyte; slow start up; intolerance to sulfur	High cost; slow start up; intolerance to sulfur	Lower efficiency and power density

1.2 Polymer Electrolyte Membrane Fuel Cells

One of the biggest advantages of PEMFCs is their comparatively low operating temperature of between 50 and 100 °C. PEMFCs are comprised of membrane electrode assemblies, a schematic for which can be found below, Figure 1.1. The defining characteristic of PEMFCs is the polymer electrolyte membrane, most commonly Nafion™, a sulfonated tetrafluoroethylene based fluoropolymer-copolymer. It is critical that the membrane allows the conduction of protons, while blocking the conduction of electrons, since if the membrane was electrically conducting the fuel cell would short circuit. The membrane must also be resistant to the oxidative and reductive atmospheres on the anode and cathode respectively. As well as being chemically resistant it must be impermeable to the gases, as this leads to a problem known as gas crossover.[5]

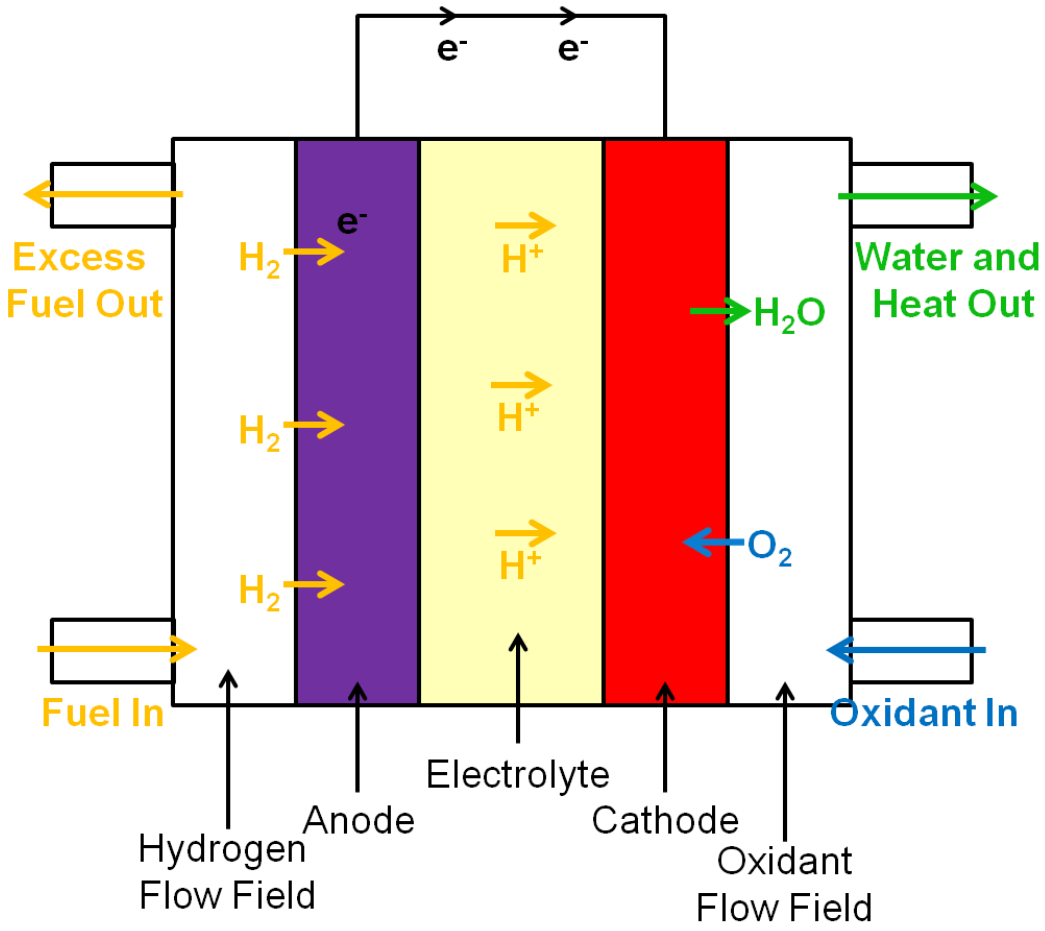

Figure 1.1: Schematic diagram of polymer electrolyte membrane fuel cell.

When operating in an ideal world there would two reactions half-cell reactions taking place. At the anode the hydrogen oxidation reaction (HOR) is taking place. This entails hydrogen being delivered to the anode of the MEA, where it is divided into protons and electrons. The protons are then carried across the polymer membrane to the cathode. At the cathode the oxygen reduction reaction (ORR) takes place. This is where oxygen reacts with the protons drawn across the membrane and the electrons arriving through the external circuit to produce water. The reaction scheme from which can be found below.

Anode : $H_2 \rightarrow 2H^+ + 2e^-$ ($E^{\Theta} = 0\ V_{RHE}$)

Cathode : $½O_2 + 2H^+ + 2e^- \rightarrow H_2O$ ($E^{\Theta} = 1.229\ V_{RHE}$)

Overall: $½O_2 + H_2 \rightarrow H_2O$ ($E^{\Theta} = 1.229\ V_{RHE}$)

These reactions typically occur on a carbon supported platinum catalyst, however due to the cost associated with platinum based catalysts, platinum alloys such as PtCo, PtNi, and PtCr, and non platinum catalysts are increasingly being ultilised.[6]

Unfortunately there is a further reaction that must be contended with in a PEMFC, the carbon oxidation reaction (COR). This is where the carbon support is electrochemically oxidised by water producing either carbon dioxide or monoxide.

$C + 2H_2O \rightarrow CO_2 + 4H^+ + 4e^-$ ($E^{\Theta} = 0.207\ V_{RHE}$)

$C + H_2O \rightarrow CO + 2H^+ + 2e^-$ ($E^{\Theta} = 0.518\ V_{RHE}$)

Figure 1.2 shows a PEMFC divided into two sections by a H_2/O_2 front, one is H_2 rich and generates power like normal, the other region is H_2 free and is load driven by the portion of the cell acting normally. In this situation the ORR takes place at the anode, and to get the required protons this induces carbon oxidation at the cathode. This front arises from two situations, stop-start events, which are common in automotive applications, or a blockage of the flow field, from gas crossover or water droplets, preventing the hydrogen from reaching the electrode.[7] This carbon oxidation is undesirable, as the carbon supports the platinum

which generates the power, and as such losses in carbon can lead to deactivation of portions of the layer.[8] Additionally CO is known to poison platinum. Therefore to avoid the COR reaction, another catalyst is often added to the layer to catalyse the oxygen evolution reaction (OER), which will occur instead of the unwanted COR. The OER is the reverse of the ORR, as such it can supply the required protons in place of those generated from the COR, while not consuming any carbon.

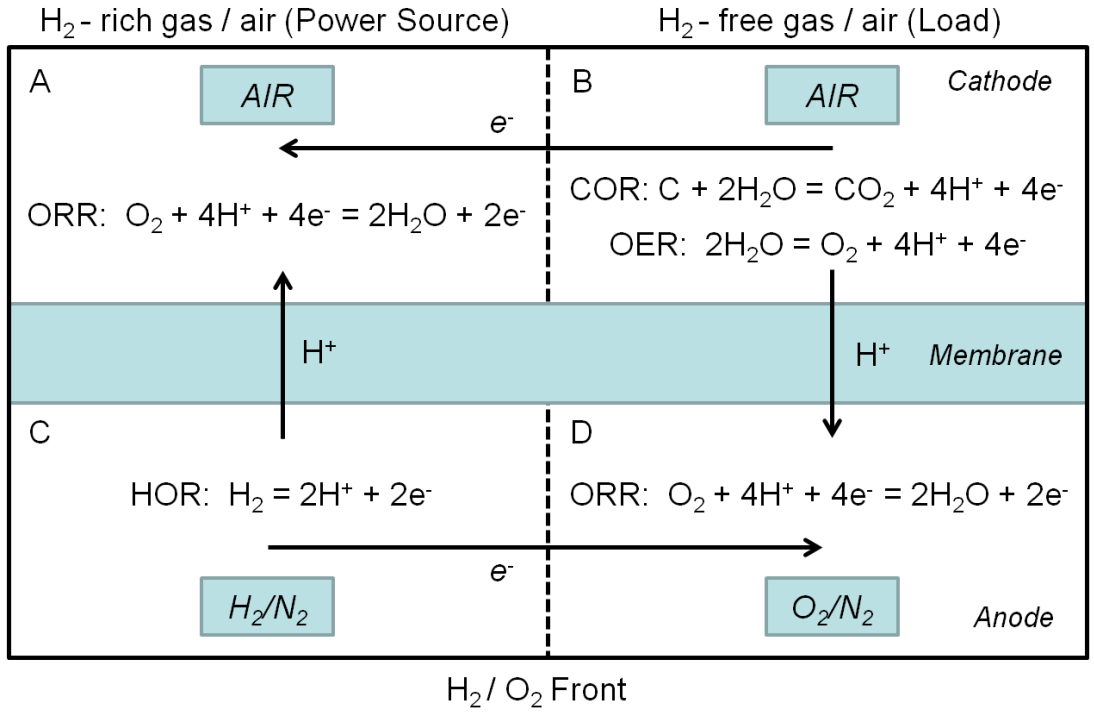

Figure 1.2: Schematic diagram of PEMFC having an H_2/O_2 front. Adapted from Gu *et al.*[7]

1.3 Oxygen Evolution Reaction Catalysts

Conducting precious metal oxides of the elements ruthenium and iridium are widely used as electrocatalysts for the oxygen evolution reaction in both PEMFCs and AFCs, as they display favourable activity and stability, in particular in aqueous acid electrolytes.[9–11] In addition these materials have found use in water electrolysers, which are devices that use energy to split water into oxygen and hydrogen gas for use as fuel.[12]

Studies of thin films of iridium and ruthenium oxides have shown that the activity of the catalyst is dependent on the crystal face exposed, with the (110) facet outperforming the (100) facet for both oxides.[13] There are examples demonstrating that by combining IrO_2 and

RuO_2 with materials such as SnO_2, ZrO_2, TiO_2, Nb_2O_5 and Ta_2O_5, either as a physical mixture or by forming a solid solution, improved stability and performance can be achieved.[14,15] In some cases it has been shown that there can be significant local inhomogeneity within crystallites, and surface segregation of one metal is often observed with use.[10] Even with the improvements observed by mixing these materials the catalysts still are not active or stable enough to make them commercially viable due to the large over potential and corrosion at the anode specifically when high potential is applied.[16,17] The "best" OER catalysts require > 320 mV overpotential to achieve 10 $mAcm^{-2}$. Stability of catalysts is also a problem, with catalyst failure during start up and shut down and when the electrode becomes fuel starved.[18] However it has been shown through the use of surface capping layer of iridium oxide the mixed ruthenium iridium oxides can be made up to four times more stable.[19]

Materials have been produced whose activity in an order of magnitude greater than RuO_2-IrO_2 mixed oxide in AFCs, one of the best catalysts for OER produced to date is $Ba_{0.5}Sr_{0.5}Co_{0.8}Fe_{0.2}O_{3-\delta}$,[20] however this has only been successful in alkaline media as oxides without PGMs tend to dissolve in acidic media. Under the acidic conditions materials containing iridium and ruthenium tend to be much more resilient. It is accepted that ruthenium and iridium are both relatively stable in the +4 and +5 oxidation states but when oxidised further they can solubilise.[21] This is especially true for ruthenium, as the RuO_4^{2-} ion is extremely soluble, which is produced when ruthenium is oxidised during periods of high applied potential. Iridium undergoes similar chemical changes but the iridium ions produced are not as soluble, making the RuO_2-IrO_2 systems much more stable, than RuO_2 alone.

Improvements in the activity and stability of OER catalysts correlate directly with the efficiency and cost effectiveness of the fuel cell. Thus work is being continually carried out trying to improve upon the existing materials. Recent advances in the growth of epitaxial thin films through pulsed laser deposition, have lead to the production of a $IrO_x/SrIrO_3$ catalyst which significantly outperforms IrO_2 in an acidic electolyte,[22] expanding the work

on $SrIrO_3$ thin films.[23] Due to the shortage of metal oxides that are chemically stable under acid conditions, work has been carried out where instead of substituting iridium or ruthenium with another metal the oxide in the rutile structure has been substituted with fluoride.[24] This yielded increases in activity up until 20 wt% fluorine, without changing the onset of oxygen evolution to any appreciable degree. There is limited work exploiting the chemistry of mixed metal iridium and ruthenium oxides adopting structures other than that of rutile. Under alkaline conditions a variety of iridium containing oxide materials have been tested, including pyrochlores, perovskites and fluorite like materials.[25] The pyrochlore ruthenates $Pb_2Ru_{(2-x)}Pb_{(x)}O_{7-y}$ and $Bi_2Ru_{(2-x)}Bi_{(x)}O_{7-y}$ have been shown to be active OER catalysts under acidic conditions,[26] and the pyrochlore iridate $Bi_2Ir_2O_7$ has been shown to be chemically stable and has activity similar to the most active IrO_2/RuO_2 materials.[27] The hollandite $K_{0.25}IrO_2$,[28] and the double perovskites Ba_2MIrO_6(where M = Y, La, Ce, Pr, Nd and Tb),[29] have all been proposed to be more active than IrO_2. Some non-PGM oxide materials have been investigated as suitable OER catalysts for PEMFCs in an effort to reduce costs, these include MnO_x[30] and the composition space $(Co\text{-}Mn\text{-}Ta\text{-}Sb)O_x$.[31] Manganese oxide is active, however dissolution of the oxide is observed during operation, meaning it is unstable OER catalyst. The cobalt and manganese rich portions of $(Co\text{-}Mn\text{-}Ta\text{-}Sb)O_x$ composition space proved active, with the cobalt rich materials proving more active the manganese rich materials, but like manganese oxide all these materials proved unstable. Those materials containing low percentages, typically 5-10 %, of tantalum or antimony displayed small stability gains, like observed with iridium and ruthenium oxides.

1.4 Oxygen Evolution Reaction Mechanism in PEMFCs

Owing to the lack of knowledge of the OER mechanism, it has been hard to rationalise why one material outperforms another; some have suggested that the band structure of the materials could be linked to their activity,[32] others believe the metal oxygen binding energy plays a significant part in how activate a material will be.[33] It is also likely that the ability of

a structure to accommodate oxide ion vacancies will play a role as this would offer binding sites, facilitating water coordination to metal sites.[34,35]

In an attempt to better design OER catalysts, the mechanism by which water is split into oxygen and hydrogen has been investigated using DFT calculations. The two most commonly proposed mechanisms are the electrochemical oxide path and the oxide path,[36] Figure 1.3. In the electrochemical oxide path water binds to a surface site on the catalyst particle, the protons associated with the water molecule are then irreversibly removed. Two surface bound oxygen atoms then combine forming an oxygen molecule, which can then be expelled from the surface. Like in the electrochemical oxide path, the oxide path begins with water binding to a surface site from which a proton is removed to create a hydroxide group. Then however two hydroxide groups react producing a water molecule, which is released into solution, and an oxygen atom, which remains bound to the surface. At this point two oxygen atoms react forming an oxygen molecule, which can then be released from the surface.

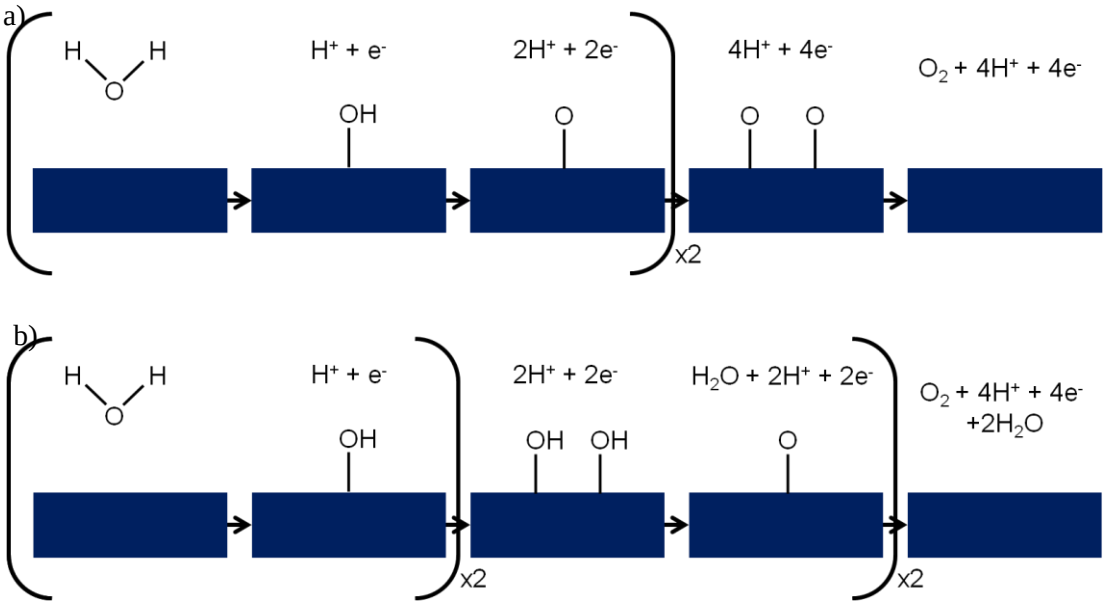

Figure 1.3: a) Electrochemical oxide path and b) oxide path for oxygen evolution reaction under acidic conditions.[36]

There are a further two proposed mechanisms by which the oxygen evolution reaction can take place: the Krasil'shchkov path[37] and the Wade and Hackerman's path.[38] The

Krasil'shchkov path is a variation on the electrochemical oxide path where instead of the proton and electron been extracted simultaneously in the conversion of **S**-OH to **S**-O they are extracted in a two step process going through the intermediate **S**-O^- state, where S is an active surface site. The pathway by which the Wade and Hackerman path proceeds is more complicated than the other proposed mechanisms, the scheme for whish is displayed below. First two water molecules approach surface sites, from there a proton is stripped from each off the water molecules. The OH^- groups then react liberating water and producing a surface oxide species. The surface oxide species then reacts with further two OH^- groups simultaneously expelling water and oxygen.

$$2\mathbf{S} + 2H_2O \rightarrow 2\mathbf{S}\text{-}OH^- + 2H^+$$

$$2\mathbf{S}\text{-}OH^- \rightarrow \mathbf{S}\text{-}O + H_2O + 2e^-$$

$$\mathbf{S}\text{-}O + 2\mathbf{S}\text{-}OH^- \rightarrow 3\mathbf{S} + H_2O + O_2 + 2e^-$$

The overpotential required for oxygen evolution is believed to be connected to the kinetic constraints of the reaction steps in each mechanism.[39] The kinetics of a system are generally governed by the rate determining step, however in these systems, the potential determining step is equally as important, as it governs the overpotential of the oxygen evolution reaction.[40] The reaction step with the largest change in Gibbs free chemisorption energy of two subsequent intermediates is the potential determining step. Using DFT calculations, it has been calculated that for an ideal catalyst all reaction steps would have a barrier of 1.23 eV under acidic conditions.[41] However in real systems normally one step has a much larger energy requirement than the others, typically the step where two oxygen atoms combine prior to the release O_2. This has been plotted against the theoretical overpotential of a large number of binary oxide and perovskite oxide systems, yielding the volcano plots seen in Figure 1.4. IrO_2 and RuO_2 are found very close to the peak of the volcano indicating minimal overpotential is required for oxygen evolution.

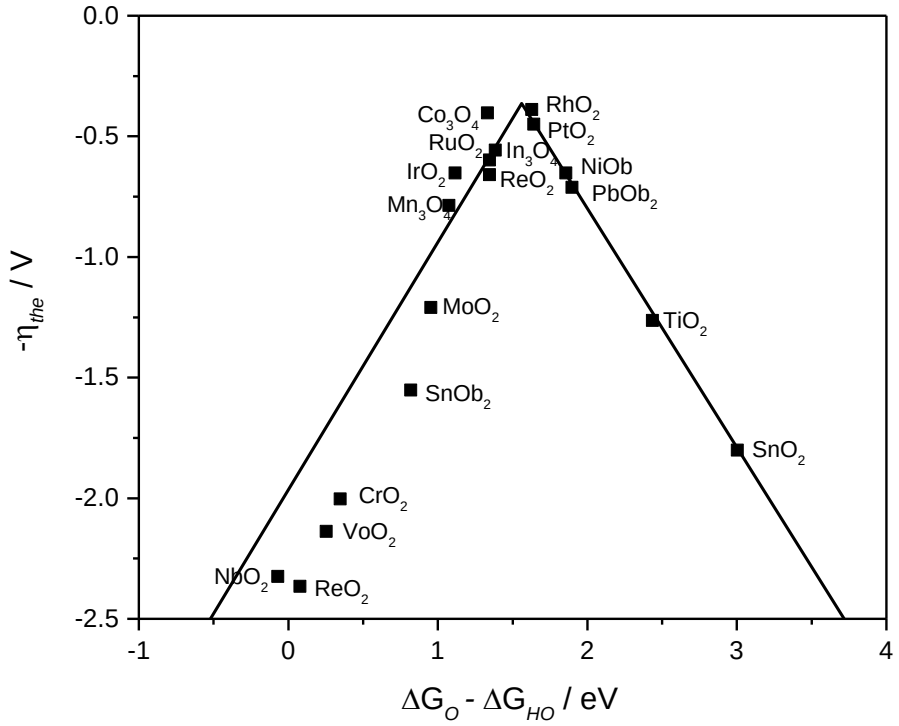

Figure 1.4: Theoretical overpotential for oxygen evolution *vs* the difference in Gibbs free chemisorption energy of two subsequent intermediates for various binary oxides under acidic conditions. Data taken from Man et al.[41]

It has been theorised that the minimum overpotential observed in the volcano plot can be further reduced by replacing a portion of the surface ruthenium sites with either nickel or cobalt.[42] However for this to be realised in practice the surface bound species would have to bridge a ruthenium and a cobalt or nickel atom. Figure 1.5 clearly shows that if this where to be achieved the energy required for each reaction step becomes much more like that of the perfect catalysts when compared with RuO_2.

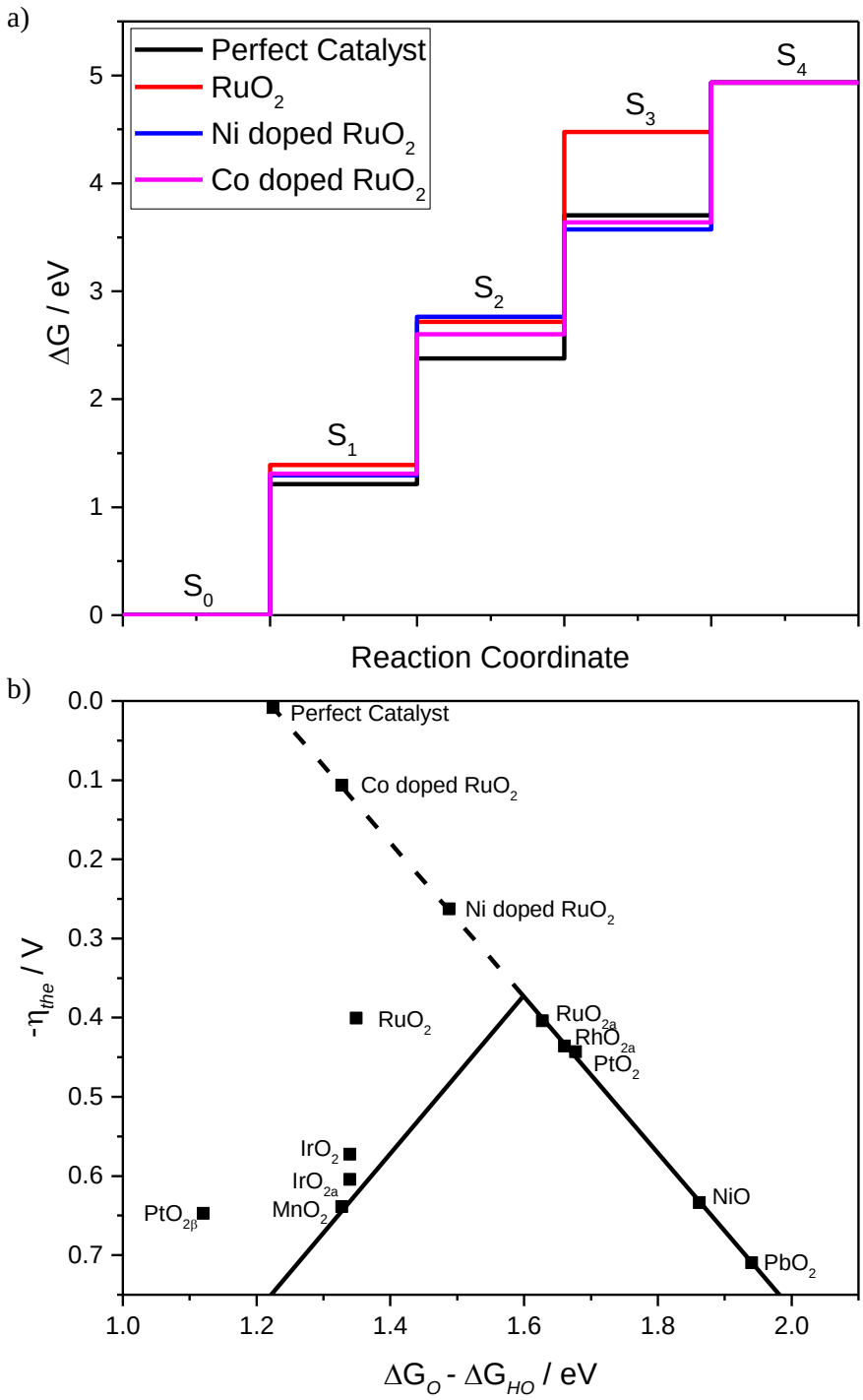

Figure 1.5: a) Energy barriers to oxygen evolution for selected catalysts. b) Theoretical overpotential for oxygen evolution *vs* the difference in Gibbs free chemisorption energy of two subsequent intermediates showing how cobalt and nickel substituted materials do not conform to the volcano. Data taken from Halck et al.[42]

The use of *in situ* XAS experiments to attempt to elucidate a mechanism for the oxygen evolution reaction in acidic, neutral and basic conditions for IrO_2 have become possible with recent advances in light source and detector technologies. Hillman *et al.* proposed two separate scenarios from these experiments. The first assumes all the atoms of a given type

have identical environments, whereas the second allows identical atoms to occupy more than one type of site. There are then two possible modes of operation within each scenario. The Band model stipulates that the chemically active electrons occupy a partially filled band. The Fermi level is within this band and conductivity arises from the motion of free electrons. Alternatively the bond model describes a situation where the electrochemically active charge is situated around specific molecular bonds and that conductivity arises from hopping between specific sites.[43] In aqueous and basic conditions there is strong evidence that the mechanism proceeds via a two site reaction with only the surface layer responding to the applied potential.[43] In acidic conditions no conclusions are drawn as to mechanism by which oxygen evolution occurs however the surface area dependence on the oxidation state shift with regards to applied potential, makes a strong case that once again only the surface layer is responding to the applied potential.

1.5 Ruthenium and Iridium Oxides

Many binary metal oxides of tetravalent metals adopt the rutile structure, Figure 1.6, ruthenium and iridium dioxide are examples of these. The rutile structure is tetragonal and in the case of ruthenium dioxide this can be changed by applying a pressure to the system (5.3 GPa), at which point a phase transition is observed and ruthenium dioxide adopts an orthorhombic structure.[44] This tetragonal symmetry is maintained when substituting ruthenium or iridium with metals of comparable ionic radii.[45–47]

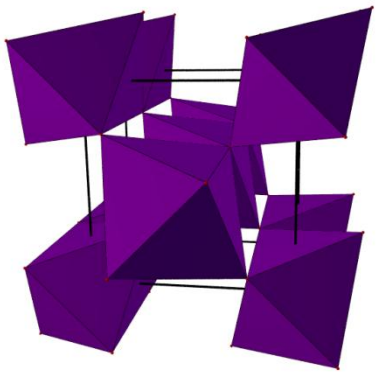

Figure 1.6: Rutile structure with metal atoms in purples and oxygens in red.

In the rutile structure ruthenium and iridium are found in the +4 state, however these metals are not limited to this. Ruthenium is very flexible in terms of oxidation state, with reports of Ru^{2+},[48] Ru^{3+},[49] Ru^{4+},[50] Ru^{5+},[51] Ru^{6+}[52,53], Ru^{7+}[53] and Ru^{8+}[54] oxides. In practical terms iridium is less flexible in terms of oxidation state, with reports of $Ir^{3.75+}$,[28] Ir^{4+},[55] Ir^{5+}[56] and Ir^{6+}.[57,58] Though of little practical use, the cation $[IrO_4]^+$ which contains Ir^{9+} has recently been produced and identified though the use of infrared photodissociation spectroscopy.[59] When larger electropositive elements are combined with ruthenium or iridium, the mixed metal oxides that form adopt a variety of structures, including pyrochlores,[27,60–66] perovskites[67–69] and hexagonal perovskite structures.[52,67,70–72] The perovskite and pyrochlore structures can be seen in Figure 1.7.

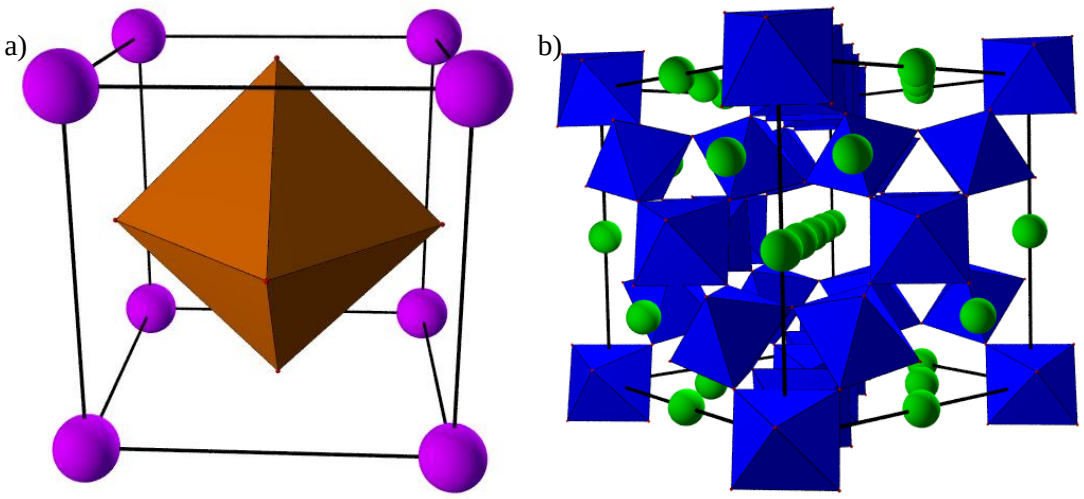

Figure 1.7: a) (A site origin) cubic perovskite structure with A site metals in pink, B site metal in orange and oxygen in red. b) (B site origin) pyrochlore structure with A site metals in green B site metal in blue and oxygen in red.

Pyrochlores are very flexible is terms of composition, adopting the general formula $A_2B_2O_6O'$. The pyrochlore structure is a derivative of the fluorite structure, AO_2, with a systematic oxygen vacancy. This vacant oxygen bridges two adjacent B-site metals as such when it is removed the remaining oxygens contract around the B-site. The remaining oxygen atoms either bridge A and B-site nearest neighbours, occupying the 48*f* site, or two A-site nearest neighbours, occupying the 8*b* site. Thus the A-site cations are larger than the B-site cations, and are typically eight coordinate, whereas the smaller B metal is six coordinate.

Stoichiometric pyrochlores tend to fall into two categories depending how the charge is distributed across the A and B sites. The A metal is normally a +2 or +3 ion and the B metal is then a +5 or +4, respectively. Examples of $A^{3+}{}_2B^{4+}{}_2O_7$ include the cases of A = Bi, Y, In, Tl, La-Lu and B = Ir or Ru.[27,62,63,65,73–79] Examples of $A^{2+}{}_2B^{5+}{}_2O_7$ include the cases of A = Ca, Cd, Hg and B = Ir or Ru.[80–83] While at first glance the pyrochlore appears simple, there is potential for a great deal of disorder within the structure. The majority of disorder relates to the O' site, where there is not only the possibility of oxygen vacancies,[66] but the inclusion of other groups like OH^-,[84] H_2O[35] and halides.[85] Additionally there is the possibility of vacancies on the A site of the pyrochlore, yielding $A_{2-x}B_2O_6O'$ materials like KTa_2O_6[86]. The inclusion of large +4 ions like Ce^{4+} on the A-site is possible, however to maintain charge balance ions of lower valance must also occupy the same site like in $(Ce_{0.67}Na_{0.33})_2M_2O_7$ M = Ir or Ru.[61,87] Much rarer are β-pyrochlores like KOs_2O_6[88] and $RbOs_2O_6$,[89] these adopt the same basic structure as the standard pyrochlore but with the large metal occupying the O' site leaving the A-site completely vacant.

The unit cell of perovskites and related materials can be rationalised using the Goldschmidt tolerance factor, *t*, where *r* is the ionic radius of the constituent ions.[90]

$$t = \frac{r_A + r_X}{\sqrt{2}(r_B + r_X)} \tag{1.1}$$

In its simplest form the perovskite structure is cubic, with the formula ABX_3, where the A metal is significantly larger than the B metal, and the tolerance factor is typically between 0.9 and 1.0. When perovskites adopt cubic space groups the A-site cations have a coordination number of twelve and a B-site coordination of 6. However, as the tolerance factor decreases from 1.0, rhombohedrally distorted structures are more commonly adopted, followed by orthorhombically and tetragonally distorted structures as the tolerance factor further decreases to 0.71. These distortions arise due to the A-site cation being too small to be twelve coordinate. Both the A and B metal oxygen bonds are stressed, as a result the B-site octahedron undergo tilting and the coordination number of the A-site cation decreases

typically to eight or nine, as observed for the orthorhombic perovskites $CaRuO_3$, $SrRuO_3$ and $SrIrO_3$.[67,91] Reductions in the tolerance factor below 0.71 can result in materials that are no longer perovskites, such as ilmenites.[92]

When the A-site is occupied by an extremely large ion like barium it is possible to form hexagonal perovskites, which are common when the tolerance factor exceeds 1.0. These are not strictly perovskites, as they are completely different structurally, but they may share the same ABX_3 chemical formula, for example; 4H,[68] 9R,[93] 10H[94] $BaRuO_3$ and 6M $BaIrO_3$.[95] However there are other examples that have a different stoichiometry, such as the 8H hexagonal perovskites $Sr_4Ru_3O_{12}$[96] and $Ba_5Ru_2O_{10}$,[97] the 6H hexagonal perovskites $Ba_3MRu_2O_9$ where M = Na, Li, Co, Zn, Ce, Pr and Tb[52,98,99]and $Ba_3MIr_2O_9$ where M = Na, Li, Y or any lanthanide.[100,101] The prefixes describe the crystal system as well as the connectivity between B - O octahedral. M denoting a monoclinic form, R a trigonal form and H a hexagonal form. In all of these both hexagonal and cubic stacking of B - O octahedra can occur; this is demonstrated with idealised models which can be found in Figure 1.8.

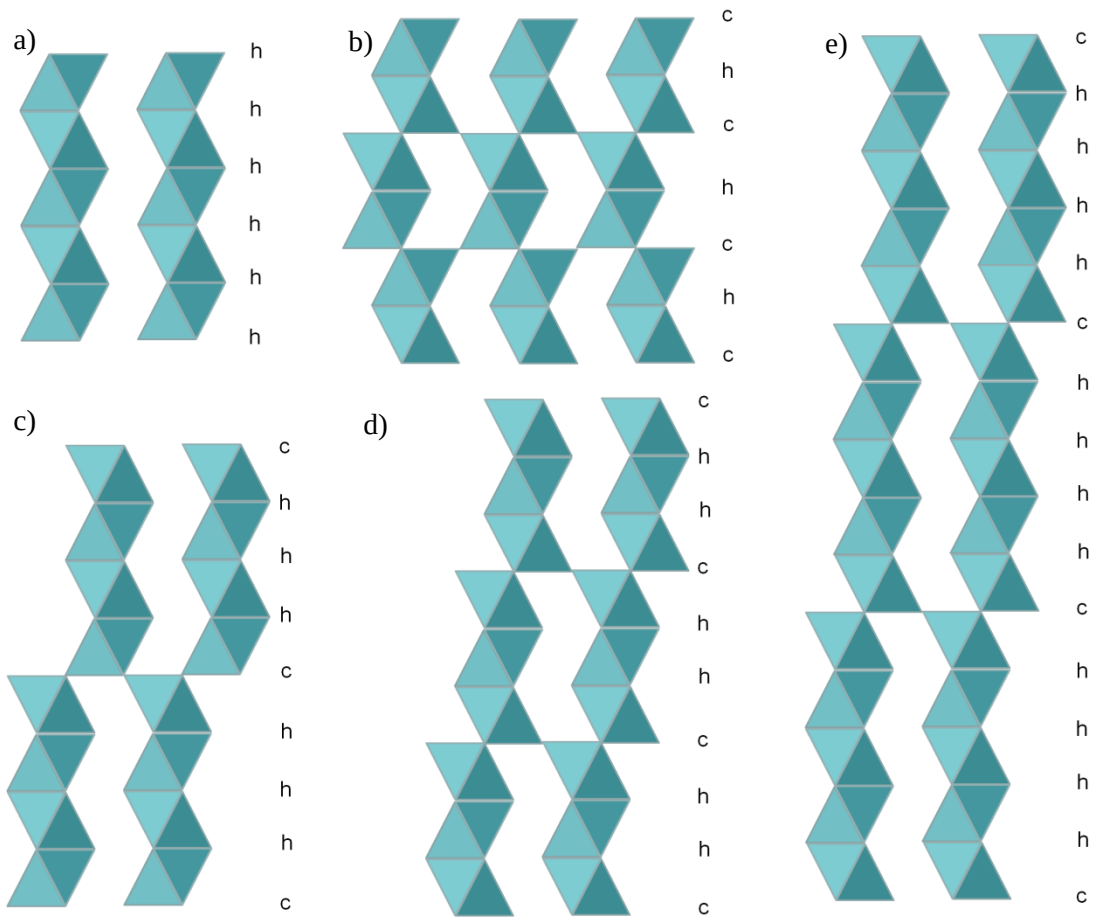

Figure 1.8: Stacking motif of B-metal oxygen octahedral for hexagonal perovskites a) 2H, b) $(ch)_2$ 4H, c) $(chhh)_2$ 8H, d) $(chh)_3$ 9R and e) $(chhhh)_3$ 15R projected down [110].

The other perovskite related phases that both iridium and ruthenium oxides can adopt are the Ruddlesden-Popper phases. These materials attracted interest due to Sr_2RuO_4, which is a copper free superconductor.[102] The phases are comprised of any number displaced slices of perovskite, which are then capped with by a layer of A - O polyhedra yielding materials with the formula $A_{n+1}B_nO_{3n+1}$, like $Sr_3Ir_2O_7$ and Sr_2IrO_4,[103] the structures for which can be seen in Figure 1.9.

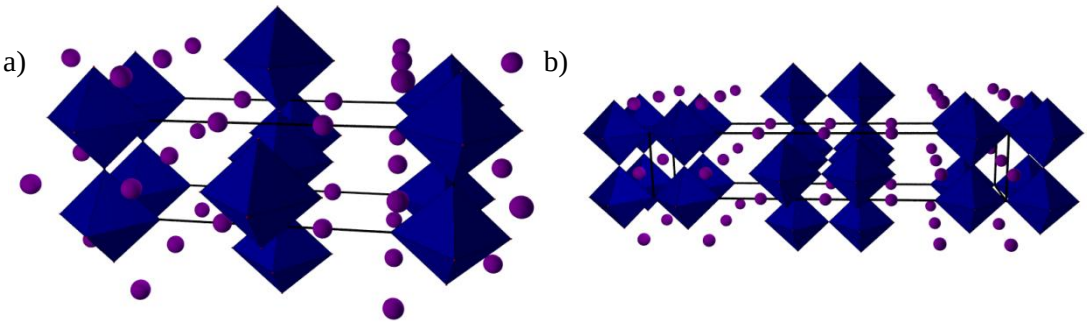

Figure 1.9: Structures of two Ruddlesden-Popper phases with formula $A_{n+1}B_nO_{3n+1}$ where a) n = 1 and b) n = 2 with A metals in purple, B metals in blue and oxygen in red.

Other structure types can be found for ruthenates and iridates depending on the reagents and reaction conditions used for their preparation, including hollandites,[28,104] $KSbO_3$-type structures,[35,105] and extended 2D structures.[56,106] The various structure types described here illustrate the great diversity in oxide chemistry of ruthenium and iridium, which has largely so far gone untapped in the search for potential OER catalysts, with the majority instead studied for their interesting magnetic properties.

1.5 Synthetic Techniques for Production of Oxides

There are many synthetic routes for preparing oxides with the majority of the oxides mentioned in the previous section produced through solid state (ceramic) methods. The ceramic method involves the heating of mixtures of separate precursors, typically carbonates and oxides, to temperatures of 1000 °C or above for extended periods of time, facilitating ion migration. Owing to the large distances the ions must migrate, materials synthesised in this fashion must be ground and fired multiple times.[107] Local inhomogeneity and concentration gradients are common among materials synthesised in this fashion. The synthesis of some phases calls for not only these high temperatures but vast pressures be applied during the synthesis.[95] Additionally some reactions require the use of oxidising or reducing atmospheres in order to control the oxidation state of the metals in the final material.[53,57] Because of the extreme temperatures used, only the most thermodynamically stable phases are formed and these techniques offer very little in terms of control of particle size, generally yielding materials with a high crystallinity and large particle sizes. This makes them poor candidates

for any catalysis applications, where generally small particle sizes are preferred with high surface areas.

The issues arising from the inhomogeneous mixing of precursors and uncontrollable particle size in solid-state synthesis can be overcome through the use of sol-gel or co-precipitation techniques, both examples of soft chemical synthesis. Sol-gel methods involve the hydrolysis of ~~a~~ suitable metal organic precursors, commonly alkoxides, and the solvent is then extracted to produce a gel. This gel is then treated at high temperature (although often lower than ceramic synthesis and with only one heating step), driving off the organics and crystallising the oxide.[108,109] The co-precipitation method begins with the dissolution of reagents, to which a precipitation agent like ammonium hydroxide added. The resulting precipitate is an atomically mixed amorphous material containing the metals, and this can then be collected and fired to form a crystalline oxide.

Hydrothermal synthesis is another example of a soft materials synthesis. A reaction can be described as hydrothermal when it is carried out in aqueous medium at temperatures exceeding 100 °C, generating autogeneous pressure.[110] When the solvent used is no longer aqueous, the reaction can be described as solvothermal, as long as the reaction temperature exceeds that of the solvent's boiling point. Ideally a solvent is chosen that the reagents dissolve in at room temperature to facilitate atomic scale mixing but then crystallise the desired material at reaction temperature.[111] If this is not possible mineralisers or surfactants can be added to the reaction, to induce dissolution of reagents and/or crystallisation of the final material. Utilising these, along with judicious selection of reagents, reaction duration, reaction temperature and solvent control of particle size, morphology and the phase can be achieved.[110,112–116] Generally subcritical hydrothermal reactions are used for the synthesis of inorganic materials, as above the supercritical temperature of water the pressure generated by the system can increase rapidly. This increase is a function of both reaction temperature and vessel fill factor, as the ideal gas law is no longer obeyed due to there being no distinction between the liquid and gas phases. While reactions can be carried out at higher temperatures

and pressures, stronger more specialised vessels are required and the choice of reagents and additives is limited.[117] Unlike many other solution based methods, a great advantage of hydrothermal and solvothermal techniques is that they can yield crystalline materials directly, without the need for post synthesis annealing.

1.5 Aims of This Work and Organisation of the Thesis

The work presented herein is concerned with the synthesis and characterisation of new iridium and ruthenium oxide materials, which the aim of producing active OER catalysts for use in PEMFCs. Hydrothermal synthesis is utilised in an attempt to produce metastable phases that ceramic methods are unlikely to yield, following on from recent advances in the hydrothermal chemistry of mixed metal iridium and ruthenium oxides.[27,35,51,61] The materials presented in each chapter differ in both composition and structure, Chapter 3 contains data on substituted ruthenium oxide rutiles, Chapter 4 deals with substituted calcium iridium oxide pyrochlores and Chapter 5 contains a selection of materials with different structures. The last results chapter, Chapter 6, documents the electrocatalytic performance of all the synthesised materials, as well as *in situ* XAS studies of selected materials in an attempt to better understand the mechanism by which the OER takes place. Chapter 7 includes some general conclusions and suggestions of future work.

References

1 J. P. Painuly, *Renew. Energy*, 2001, **24**, 73–89.
2 J. Larminie, A. Dicks and M. S. McDonald, *Fuel cell systems explained*, J. Wiley, Chichester, UK, 2003.
3 A. Schäfer, J. B. Heywood and M. A. Weiss, *Energy*, 2006, **31**, 2064–2087.
4 A. Kirubakaran, S. Jain and R. K. Nema, *Renew. Sustain. Energy Rev.*, 2009, **13**, 2430–2440.
5 M. Inaba, T. Kinumoto, M. Kiriake, R. Umebayashi, A. Tasaka and Z. Ogumi, *Electrochim. Acta*, 2006, **51**, 5746–5753.
6 H. A. Gasteiger, S. S. Kocha, B. Sompalli and F. T. Wagner, *Appl. Catal. B Environ.*, 2005, **56**, 9–35.
7 W. Gu, P. T. Yu, R. N. Carter, R. Makharia and H. A. Gasteiger, in *Modeling and Diagnostics of Polymer Electrolyte Fuel Cells*, eds. C.-Y. Wang and U. Pasaogullari, Springer New York, New York, NY, 2010, pp. 45–87.
8 S. Maass, F. Finsterwalder, G. Frank, R. Hartmann and C. Merten, *J. Power Sources*, 2008, **176**, 444–451.
9 K. Kinoshita, *Electrochemical Oxygen Technology*, John Wiley & Sons, New York, USA, 1992.
10 L.-E. Owe, M. Tsypkin, K. S. Wallwork, R. G. Haverkamp and S. Sunde,

Electrochim. Acta., 2012, **70**, 158–164.
11 Y. Lee, J. Suntivich, K. J. May, E. E. Perry and Y. Shao-Horn, *J. Phys. Chem. Lett.*, 2012, **3**, 399–404.
12 M. Carmo, D. L. Fritz, J. Mergel and D. Stolten, *Int. J. Hydrogen Energy*, 2013, **38**, 4901–4934.
13 K. A. Stoerzinger, L. Qiao, M. D. Biegalski and Y. Shao-Horn, *J. Phys. Chem. Lett.*, 2014, **5**, 1636–1641.
14 S. Song, H. Zhang, X. Ma, Z. Shao, R. T. Baker and B. Yi, *Int. J. Hydrog. Energy*, 2008, **33**, 4955–4961.
15 X. Zhang, Z. Wu, J. Zang, D. Li and Z. Zhang, *J. Phys. Chem. Solids*, 2007, **68**, 1583–1590.
16 J. Sharman, B. Theoblad and E. Wright, 2012, UK Patent, Catalyst for fuel cells, WO2012107738A1.
17 J. Cheng, H. Zhang, G. Chen and Y. Zhang, *Electrochim. Acta.*, 2009, **54**, 6250–6256.
18 R. Atanasoski, L. Atanasoska, D. Cullen, G. Haugen, K. More and G. Vernstrom, *Electrocatal.*, 2012, **3**, 284–297.
19 N. Danilovic, R. Subbaraman, K. C. Chang, S. H. Chang, Y. Kang, J. Snyder, A. P. Paulikas, D. Strmcnik, Y. T. Kim, D. Myers, V. R. Stamenkovic and N. M. Markovic, *Angew. Chemie Int. Ed.*, 2014, **53**, 14016–14021.
20 J. Suntivich, K. J. May, H. A. Gasteiger, J. B. Goodenough and Y. Shao-Horn, *Science.*, 2011, **334**, 1383–1385.
21 N. Danilovic, R. Subbaraman, K.-C. Chang, S. H. Chang, Y. J. Kang, J. Snyder, A. P. Paulikas, D. Strmcnik, Y.-T. Kim, D. Myers, V. R. Stamenkovic and N. M. Markovic, *J. Phys. Chem. Lett.*, 2014, **5**, 2474–2478.
22 L. C. Seitz, C. F. Dickens, K. Nishio, Y. Hikita, J. Montoya, A. Doyle, C. Kirk, A. Vojvodic, H. Y. Hwang, J. K. Norskov and T. F. Jaramillo, *Science.*, 2016, **353**, 1011–1014.
23 R. Tang, Y. Nie, J. K. Kawasaki, D.-Y. Kuo, G. Petretto, G. Hautier, G.-M. Rignanese, K. M. Shen, D. G. Schlom and J. Suntivich, *J. Mater. Chem. A*, 2016, **4**, 6831–6836.
24 K. Kadakia, M. K. Datta, P. H. Jampani, S. K. Park and P. N. Kumta, *J. Power Sources*, 2013, **222**, 313–317.
25 M. V ten Kortenaar, J. F. Vente, D. J. W. Ijdo, S. Müller and R. Kötz, *J. Power Sources*, 1995, **56**, 51–60.
26 J. M. Zen, R. Manoharan and J. B. Goodenough, *J. Appl. Electrochem.*, 1992, **22**, 140–150.
27 K. Sardar, S. C. Ball, J. D. B. Sharman, D. Thompsett, J. M. Fisher, R. A. P. Smith, P. K. Biswas, M. R. Lees, R. J. Kashtiban, J. Sloan and R. I. Walton, *Chem. Mater.*, 2012, **24**, 4192–4200.
28 A. Talanov, W. A. Phelan, Z. A. Kelly, M. A. Siegler and T. M. McQueen, *Inorg. Chem.*, 2014, **53**, 4500–4507.
29 O. Diaz-Morales, S. Raaijman, R. Kortlever, P. J. Kooyman, T. Wezendonk, J. Gascon, W. T. Fu and M. T. M. Koper, *Nat. Commun*, 2016, **7**, 12363.
30 M. Huynh, D. K. Bediako and D. G. Nocera, *J. Am. Chem. Soc.*, 2014, **136**, 6002–6010.
31 A. Shinde, R. J. R. Jones, D. Guevarra, S. Mitrovic, N. Becerra-Stasiewicz, J. A. Haber, J. Jin and J. M. Gregoire, *Electrocatalysis*, 2015, **6**, 229–236.
32 N. A. Vante, B. Schubert, H. Tributsch and A. Perrin, *J. Catal.*, 1988, **112**, 384–391.
33 S. Trasatti, *Electrochim. Acta.*, 1984, **29**, 1503–1512.
34 J. B. Goodenough, R. Manoharan and M. Paranthaman, *J. Am. Chem. Soc.*, 1990, **112**, 2076–2082.
35 K. Sardar, J. Fisher, D. Thompsett, M. R. Lees, G. J. Clarkson, J. Sloan, R. J. Kashtiban and R. I. Walton, *Chem. Sci.*, 2011, **2**, 1573–1578.
36 J. O. Bockris, *J. Chem. Phys.*, 1956, **24**, 817.

37 A. I. Krasil'shchkov, *Zh. Fiz. Khim*, 1963, **37**, 273.
38 W. H. Wade and N. Hackerman, *Trans. Faraday Soc.*, 1957, **53**, 1636–1647.
39 H. Dau, C. Limberg, T. Reier, M. Risch, S. Roggan and P. Strasser, *ChemCatChem*, 2010, **2**, 724–761.
40 M. T. M. Koper, *J. Solid State Electrochem.*, 2013, **17**, 339–344.
41 I. C. Man, H.-Y. Su, F. Calle-Vallejo, H. A. Hansen, J. I. Martínez, N. G. Inoglu, J. Kitchin, T. F. Jaramillo, J. K. Nørskov and J. Rossmeisl, *ChemCatChem*, 2011, **3**, 1159–1165.
42 N. B. Halck, V. Petrykin, P. Krtil and J. Rossmeisl, *Phys. Chem. Chem. Phys.*, 2014, **16**, 13682–13688.
43 S. Trasatti, *J. Electroanal. Chem.*, 1980, **111**, 125–131.
44 J. Haines, J. M. Léger, O. Schulte and S. Hull, *Acta Crystallogr. Sect. B*, 1997, **53**, 880–884.
45 Y. E. Roginskaya, I. D. Belova, B. S. Galyamov, F. K. Chibirova and R. R. Shiprina, *Mater. Chem. Phys.*, 1989, **22**, 203–229.
46 E. N. Balko and C. R. Davidson, *J. Inorg. Nucl. Chem.*, 1980, **42**, 1778–1781.
47 E. N. Balko and P. H. Nguyen, *J. Appl. Electrochem.*, 1991, **21**, 678–682.
48 F. D. Romero, S. J. Burr, J. E. McGrady, D. Gianolio, G. Cibin and M. A. Hayward, *J. Am. Chem. Soc.*, 2013, **135**, 1838–1844.
49 A. Sinclair, J. A. Rodgers, C. V Topping, M. Míšek, R. D. Stewart, W. Kockelmann, J.-W. G. Bos and J. P. Attfield, *Angew. Chemie Int. Ed.*, 2014, **53**, 8343–8347.
50 H. Müller-Buschbaum, *Z. Anorg. Allg. Chem.*, 2006, **632**, 1625–1659.
51 C. I. Hiley, M. R. Lees, J. M. Fisher, D. Thompsett, S. Agrestini, R. I. Smith and R. I. Walton, *Angew. Chemie Int. Ed.*, 2014, **53**, 4423–4427.
52 Katharine E. Stitzer, Mark D. Smith, William R. Gemmill and and Hans-Conrad zur Loye, *J. Am. Chem. Soc.*, 2002, **124**, 13877–13885.
53 N. Greenwood, *Chemistry of the Elements (2nd ed.).*, New York, Butterworth–Heinemann, 1997.
54 M. Pley and M. S. Wickleder, *J. Solid State Chem.*, 2005, **178**, 3206–3209.
55 H. Müller-Buschbaum, *Z. Anorg. Allg. Chem.*, 2005, **631**, 1005–1028.
56 D. C. Wallace and T. M. McQueen, *Dalt. Trans.*, 2015, **44**, 20344–20351.
57 D.-Y. Jung, G. Demazeau, J. Etourneau and M. A. Subramanian, *Mater. Res. Bull.*, 1995, **30**, 113–123.
58 G. Demazeau, D.-Y. Jung, J.-P. Sanchez, E. Colineau, A. Blaise and L. Fournes, *Solid State Commun.*, 1993, **85**, 479–484.
59 G. Wang, M. Zhou, J. T. Goettel, G. J. Schrobilgen, J. Su, J. Li, T. Schloder and S. Riedel, *Nature*, 2014, **514**, 475–477.
60 C. Cosio-Castaneda, P. de la Mora and G. Tavizon, *J. Solid State Chem.*, 2011, **184**, 1251–1256.
61 K. Sardar, E. Petrucco, C. I. Hiley, J. D. B. Sharman, P. P. Wells, A. E. Russell, R. J. Kashtiban, J. Sloan and R. I. Walton, *Angew. Chem. Int. Ed. Engl.*, 2014, **53**, 10960–4.
62 C. Abate, K. Duncan, V. Esposito, E. Traversa and E. D. Wachsman, *ECS Trans.* , 2006, **1**, 255–261.
63 G. Goekagac and B. J. Kennedy, *ChemInform*, 1994, **25**, no--no.
64 J. M. Zen, A. S. Kumar and J. C. Chen, *J. Mol. Catal. A Chem.*, 2001, **165**, 177–188.
65 Y. Linran, W. Dong, P. Wen, H. Weiwei, Y. Hongming and F. Shouhua, *Sci. China-Chemistry*, 2011, **54**, 941–946.
66 R. A. Beyerlein, H. S. Horowitz, J. M. Longo, M. E. Leonowicz, J. D. Jorgensen and F. J. Rotella, *J. Solid State Chem.*, 1984, **51**, 253–265.
67 N. F. Atta, A. Galal and S. M. Ali, *Int. J. Electrochem. Sci.*, 2012, **7**, 725–746.
68 S.-T. Hong and A. W. Sleight, *J. Solid State Chem.*, 1997, **128**, 251–255.
69 R. F. Sarkozy, C. W. Moeller and B. L. Chamberland, *J. Solid State Chem.*, 1974, **9**, 242–246.
70 C. I. Hiley, M. R. Lees, D. L. Hammond, R. J. Kashtiban, J. Sloan, R. I. Smith and R.

I. Walton, *Chem. Commun.*, 2016, **52**, 6375–6378.
71 M. W. Lufaso and and Hans-Conrad zur Loye, *Inorg. Chem.*, 2005, **44**, 9143–9153.
72 T. Götzfried, A. Reller and S. G. Ebbinghaus, *Inorg. Chem.*, 2005, **44**, 6550–6557.
73 J. N. Millican, R. T. Macaluso, S. Nakatsuji, Y. Machida, Y. Maeno and J. Y. Chan, *Mater. Res. Bull.*, 2007, **42**, 928–934.
74 S. M. Disseler, C. Dhital, A. Amato, S. R. Giblin, C. de la Cruz, S. D. Wilson and M. J. Graf, *Phys. Rev. B*, 2012, **86**, 14428.
75 K. Matsuhira, M. Wakeshima, R. Nakanishi, T. Yamada, A. Nakamura, W. Kawano, S. Takagi and Y. Hinatsu, *J. Phys. Soc. Japan*, 2007, **76**, 43706.
76 W. D. Komer and D. J. Machin, *J. Less Common Met.*, 1978, **61**, 91–105.
77 B. J. Kennedy and T. Vogt, *J. Solid State Chem.*, 1996, **126**, 261–270.
78 N. Taira, M. Wakeshima and Y. Hinatsu, *J. Mater. Chem.*, 2002, **12**, 1475–1479.
79 N. Taira, M. Wakeshima and Y. Hinatsu, *J. Solid State Chem.*, 1999, **144**, 216–219.
80 T. Munenaka and H. Sato, *J. Phys. Soc. Japan*, 2006, **75**, 103801.
81 A. W. Sleight, *Mater. Res. Bull.*, 1974, **9**, 1177–1184.
82 W. Klein, R. K. Kremer and M. Jansen, *J. Mater. Chem.*, 2007, **17**, 1356–1360.
83 R. Wang and A. W. Sleight, *Mater. Res. Bull.*, 1998, **33**, 1005–1007.
84 Q. Dong, H. Jiang, N. Kumada, Y. Yonesaki, T. Takei and N. Kinomura, *J. Solid State Chem.*, 2011, **184**, 1899–1902.
85 M. A. Aia, R. W. Mooney and C. W. W. Hoffman, *J. Electrochem. Soc.* , 1963, **110**, 1048–1054.
86 G. Goh, S. Haile, C. Levi and F. Lange, *J. Mater. Res.*, 2002, **17**, 3168–3176.
87 R. J. Darton, S. S. Turner, J. Sloan, M. R. Lees and R. I. Walton, *Cryst. Growth Des.*, 2010, **10**, 3819–3823.
88 S. Yonezawa, Y. Muraoka, Y. Matsushita and Z. Hiroi, *J. Phys. Condens. Matter*, 2004, **16**, L9.
89 S. M. Kazakov, N. D. Zhigadlo, M. Brühwiler, B. Batlogg and J. Karpinski, *Supercond. Sci. Technol.*, 2004, **17**, 1169.
90 V. M. Goldschmidt, *Naturwissenschaften*, 1926, **14**, 477–485.
91 I. Qasim, B. J. Kennedy and M. Avdeev, *J. Mater. Chem. A*, 2013, **1**, 13357–13362.
92 X. Liu, R. Hong and C. Tian, *J. Mater. Sci. Mater. Electron.*, 2008, **20**, 323–327.
93 P. C. Donohue, L. Katz and R. Ward, *Inorg. Chem.*, 1965, **4**, 306–310.
94 T. Ogawa and H. Sato, *J. Alloys Compd.*, 2004, **383**, 313–318.
95 J. Zhao, L. Yang, Y. Yu, F. Li, R. Yu and C. Jin, *Inorg. Chem.*, 2009, **48**, 4290–4294.
96 C. Renard, S. Daviero-Minaud, M. Huvé and F. Abraham, *J. Solid State Chem.*, 1999, **144**, 125–135.
97 F. Grasset, C. Dussarrat and J. Darriet, *J. Mater. Chem.*, 1997, **7**, 1911–1915.
98 P. Lightfoot and P. D. Battle, *J. Solid State Chem.*, 1990, **89**, 174–183.
99 Y. Doi, M. Wakeshima, Y. Hinatsu, A. Tobo, K. Ohoyama and Y. Yamaguchi, *J. Mater. Chem.*, 2001, **11**, 3135–3140.
100 S.-J. Kim, M. D. Smith, J. Darriet and H.-C. zur Loye, *J. Solid State Chem.*, 2004, **177**, 1493–1500.
101 Y. Doi and Y. Hinatsu, *J. Phys. Condens. Matter*, 2004, **16**, 2849.
102 C. Kallin and A. J. Berlinsky, *J. Phys. Condens. Matter*, 2009, **21**, 164210.
103 A. Yamasaki, H. Fujiwara, S. Tachibana, D. Iwasaki, Y. Higashino, C. Yoshimi, K. Nakagawa, Y. Nakatani, K. Yamagami, H. Aratani, O. Kirilmaz, M. Sing, R. Claessen, H. Watanabe, T. Shirakawa, S. Yunoki, A. Naitoh, K. Takase, J. Matsuno, H. Takagi, A. Sekiyama and Y. Saitoh, *Phys. Rev. B*, 2016, **94**, 115103.
104 F. Djafri, J. Canonne, F. Abraham and D. Thomas, *J. Less Common Met.*, 1985, **109**, 323–329.
105 P. Khalifah and R. J. Cava, *Phys. Rev. B*, 2001, **64**, 85111.
106 B. E. Prasad, P. Kazin, A. C. Komarek, C. Felser and M. Jansen, *Angew. Chemie Int. Ed.*, 2016, **55**, 4467–4471.
107 C. N. R. Rao and J. Gopalakrishnan, *Acc. Chem. Res.*, 1987, **20**, 228–235.
108 J. Málek, A. Watanabe and T. Mitsuhashi, *J. Therm. Anal. Calorim.*, 2000, **60**, 699–

705.
109 Y. Tong, Y. Wang, Z. Yu, X. Wang, X. Yang and L. Lu, *Mater. Lett.*, 2008, **62**, 889–891.
110 A. Rabenau, *Angew. Chem. Int. Ed.*, 1985, **24**, 1026–1040.
111 D. L. Burnett, M. H. Harunsani, R. J. Kashtiban, H. Y. Playford, J. Sloan, A. C. Hannon and R. I. Walton, *J. Solid State Chem.*, 2014, **214**, 30–37.
112 Y. Mathieu, B. Lebeau and V. Valtchev, *Langmuir*, 2007, **23**, 9435–9442.
113 I. S. Neira, Y. V Kolen'ko, O. I. Lebedev, G. Van Tendeloo, H. S. Gupta, F. Guitián and M. Yoshimura, .
114 G. Demazeau, *Res. Chem. Intermed.*, 2011, **37**, 107–123.
115 K. Chen and D. Xue, *CrystEngComm*, 2012, **14**, 8068–8075.
116 K. Huang, W. Feng, L. Yuan, J. Zhang, X. Chu, C. Hou, X. Wu and S. Feng, *CrystEngComm*, 2014, **16**, 9842–9846.
117 L. M. Daniels, M. C. Weber, M. R. Lees, M. Guennou, R. J. Kashtiban, J. Sloan, J. Kreisel and R. I. Walton, *Inorg. Chem.*, 2013, **52**, 12161–12169.

Chapter 2 – Experimental

2.1 Synthesis

2.1.1 Hydrothermal Synthesis

All hydrothermal synthesis war carried out using Teflon®-lined stainless-steel autoclaves, with an internal volume of 20-25 ml, a schematic diagram of which can be seen in Figure 2.1.

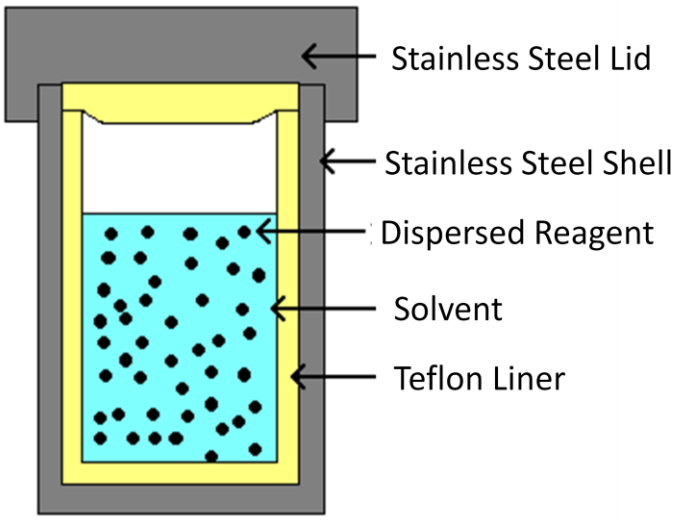

Figure 2.1: Schematic diagram of the Teflon®-lined stainless-steel autoclave.

To prevent the liners bursting due to over pressurisation the fill was limited to 50 % of the internal volume. The synthesis sections of Chapters 3, 4 and 5 contain specifics of the reagents used. Many of the syntheses required the addition of peroxide or superoxide to the vessels. In the presence of sodium and potassium hydroxide, peroxides rapidly decompose, generating heat and releasing oxygen gas. As such when adding aqueous peroxide to solid hydroxide, or vice versa, this was done drop wise. Hydrogen peroxide also decomposes rapidly in the presence of the ruthenium salts used, so similar precautions were taken.

The vessels where then sealed and subsequently agitated, to ensure the reagents were homogeneously dispersed. The autoclaves were placed in a preheated fan oven (Genlab

MINO/40) at the desired reaction temperature and kept there for an allotted time period. Once the reaction had run to completion the autoclave was allowed to cool to room temperature. When cool, products were collected via vacuum filtration. Normally the synthesised materials were then washed with 3 M nitric acid, as explained in the synthesis sections in Chapters 3,4 and 5. Materials were then dried in air at 70 °C before characterisation.

2.1.2 Ceramic/Molten Salt Synthesis and Annealing

Ceramic synthesis and annealing experiments were carried out in two types of crucible. Experiments performed at up to 900 °C were carried out using alumina crucibles. If the reaction exceeded this temperature a platinum crucible was used. The majority of this type of work was carried out in box furnaces but those carried under oxygen atmospheres were done in a tube furnace.

Molten salt syntheses were performed in a silver crucible, up to 600 °C. These reactions took place in box furnaces.

2.2 Characterisation

2.2.1 Powder X-ray Diffraction

X-ray diffraction is an extremely powerful technique as electromagnetic waves of an appropriate wave length can be diffracted by a crystal lattice. X-rays are scattered by the electron cloud around atoms, and the observed diffraction patterns are the result of constructive interference of X-rays of wavelength λ, at angles of incidence θ, which satisfy the Bragg equation.[1]

$$n\lambda = 2d \sin\theta \qquad (2.1)$$

In powder diffraction measurements there are an extremely large number of small crystallites, and ideally this means every crystallographic orientation is represented equally. By varying the angle of incidence and the detector angle, a one-dimensional diffraction

pattern can be collected, with the detected X-rays plotted against 2θ. Combining the Bragg equation with knowledge of interplanar spacing it is possible to index the unit cell to a specific lattice and crystal symmetry. The equation for cubic lattice spacing is given below, where *d* is the spacing between adjacent planes, *a* is the length of the unit cell and *hkl* are the Miller indices of the plane in question.[2]

$$\frac{1}{d^2} = \frac{h^2 + k^2 + l^2}{a^2} \tag{2.2}$$

Information regarding crystallite size can be obtained using the Scherrer equation. Where, τ is the crystallite size, κ the shape factor (typically 0.9, but varies with crystallite shape), θ is the Bragg angle and β the Bragg broadening, which is the FWHM of the peak corrected for instrumental broadening. This equation only applies to crystallites with a size < 1μm.[3]

$$\tau = \frac{\kappa\lambda}{\beta \cos\theta} \tag{2.3}$$

Three diffractometers where used to gather powder X-ray diffraction data. Preliminary phase identification was carried out on a Siemens D5000 using unmonochromated copper K_α radiation, ($K_\alpha 1$ λ = 1.54056 Å, $K_\alpha 2$ λ = 1.54443 Å). For these measurements the samples were pressed into a aluminium sample holder using a glass slide. On occasion X-rays are diffracted from the holder and peaks in the diffraction pattern that can be attributed to aluminium occur at 2θ = 38.5, 44.8 and 65.2 °. Typical scans involved data collection over a 2θ range of 10 to 60 or 70 °, with a step size of 0.025 or 0.01 ° and a collection time of either 1.4 or 14 seconds per step, depending on the quality of data required.

High resolution data were collected using a Panalytical X'pert Pro MPD, using monochromatic copper $K_{\alpha 1}$ radiation and a PIXcel solid state detector. In an attempt to reduce the effects of preferred orientation, the sample was spun at a rate of 4 revolutions per second. Data were collected over a 2θ range of 10 to 70 °, with a step size of 0.0131° and a collection time of 13 seconds per step.

A Bruker D8 Advance using copper K_α radiation, ($K_\alpha 1$ λ = 1.54056 Å, $K_\alpha 1$ λ = 1.54443 Å) and a VÅNTEC-1 high-speed detector was employed to collect *in situ* thermodiffractometry under flowing N_2, in order to mimic the conditions used in thermogravimetric analysis. Samples were heated at 0.2 °C per minute inside an Anton Paar XRK 900 reaction chamber controlled with a TCU 750 temperature unit. Generally diffraction patterns were collected every 25 °C, and materials where held at temperature for 10 minutes in order to thermally equilibrate prior to data collection, unless otherwise stated.

2.2.2 Powder Neutron Diffraction

Like X-rays, neutrons are scattered by a repeating periodic lattice. There are several differences between the techniques however, first the form factor of X-rays originates from the size of the electron cloud around the nucleus, however as the nucleus is a similar size to the neutron wavelength there is no dependence on scattering angle, this means the low d-spacing peaks, those measured at high angles, do not see the same drop off in intensity observed in X-ray diffraction. The second major difference is that neutron scattering cross sections have no relationship to atomic number so unlike X-rays it is much easier to refine the positions and occupancies of light elements like oxygen and hydrogen, in the presence of heavier ones.

Neutron diffraction data presented herein were collected on the GEM instrument, Figure 2.2,[4,5] at ISIS (U.K), a pulsed neutron spallation source, making it ideal for Time-of-Flight diffraction.

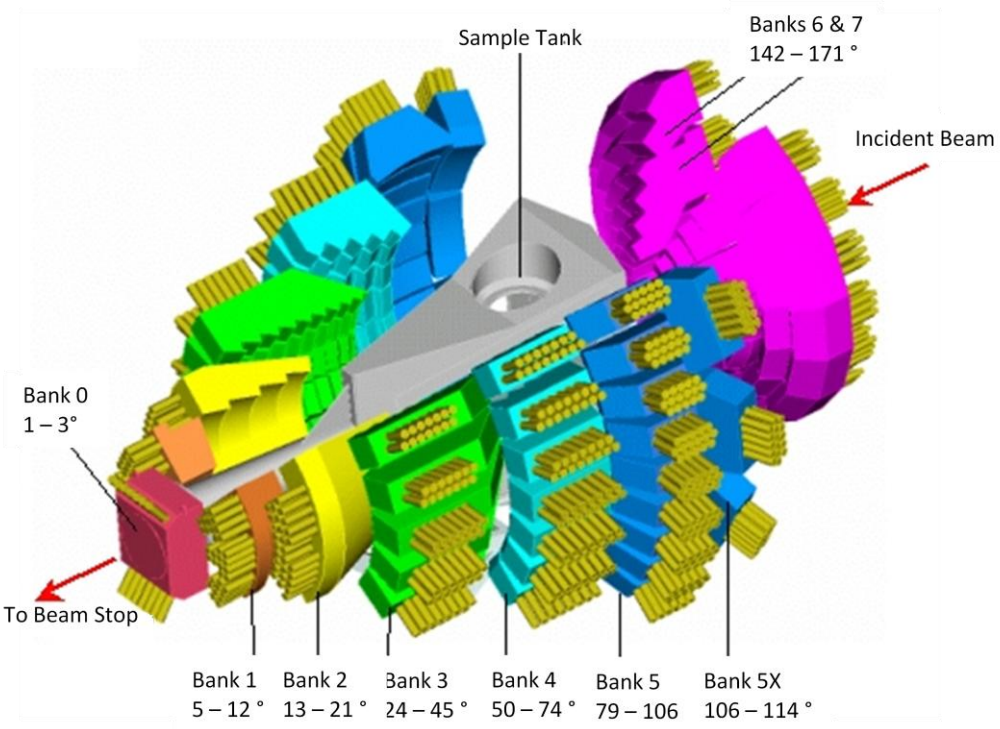

Figure 2.2: The GEM time-of-flight diffractometer, showing all detector banks.[5]

Time-of-Flight is directly proportional to *d*-spacing, as seen below.[6]

$$t = \left(\frac{2m}{h}\right) L \sin\theta \, d \tag{2.4}$$

Where m is the neutron mass, h is the Planck constant, L is the distance between the moderator and the detector, via the sample, and θ is the scattering angle.

In preparation for the neutron scattering experiment samples were desiccated in a vacuum oven at 100 °C for 12 hours, so that incoherent scattering resulting from the protons associated with surface water found on synthesised materials could be kept to a minimum. Samples were then loaded into either 6 or 8 mm diameter vanadium cans. Vanadium is used because it is virtually invisible to neutrons with a scattering length of -0.38 fm. To obtain patterns suitable for Rietveld refinement, typically 150 μA (1 hours) worth of data were collected per sample. Typically data from Bank 5 were used for refinement as it yielded data over a suitable d-spacing range for the materials studied.

2.2.3 Total Scattering

Total scattering experiments take into account both the Bragg and diffuse scattering. While the Bragg scattering typically yields sharp peaks related to long range periodicity, diffuse scattering yields features many orders of magnitude less intense, which are related to short and medium range order and in particular deviations from the ideal crystal structure. Owing to the low intensity of the diffuse scattering it is typically treated as background when doing a Rietveld refinement of the crystal structure and fitted as a smooth function. To get statistics of high enough quality for total scattering analysis, typically between 750-900 μA (5-6 hours) worth of data were collected per sample. In addition to the data from the sample, data must be collected for a vanadium rod, the empty instrument and an empty sample container. This is done so the data can be normalised and background subtraction performed. Each of these data sets typically comprises 150 μA (1 hours) worth of data. The data from the rod are used to normalise the data to the flux distribution of the moderator and put the sample data on an absolute scale. The empty instrument and sample container measurements are both used to background subtraction. A simplified method for the correction can be found below.

$$Corrected\ Data = \frac{Sample - Empty\ Container}{Vanadium\ Rod - Empty\ Instrument} \tag{2.5}$$

Through Fourier transform, the reciprocal space i(Q) is converted into the correlation function, a real space distribution of interatomic distances, Figure 2.3.

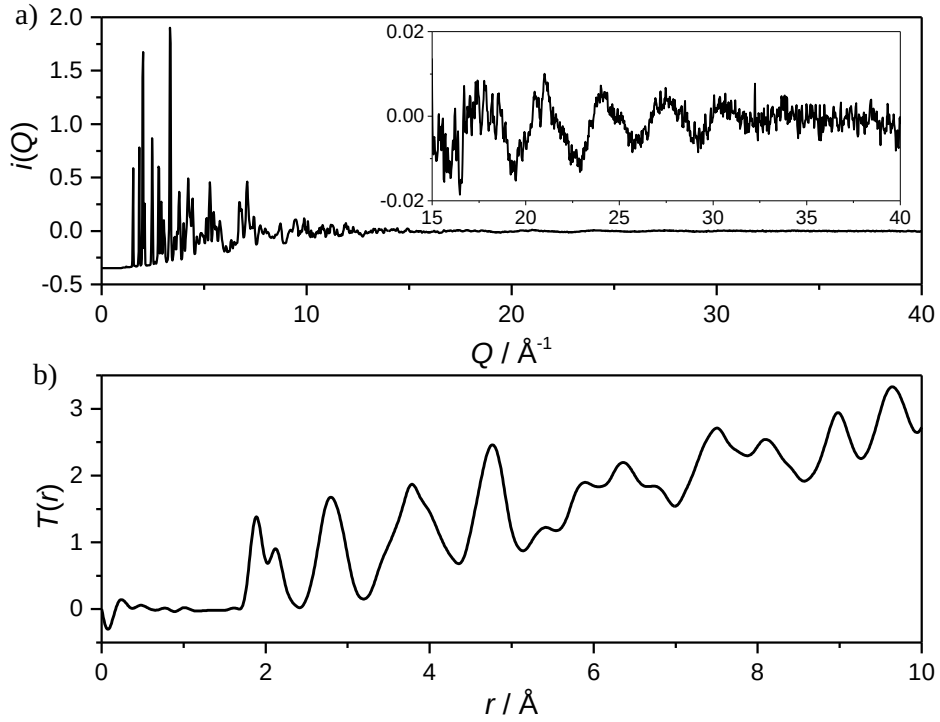

Figure 2.3: a) Corrected *i*(*Q*) for α-TeO2.b) Result of Fourier transform into *T*(*r*). Reproduced from Barney *et al.*[7]

There are two common forms of correlation function, *T*(*r*) and *D*(*r*), throughout this project *D*(*r*) is used, as it can be calculated without data regarding sample composition and density, and is related to *i*(*Q*) by the function below.

$$D(r) = \frac{2}{\pi}\int_{Q_{min}}^{Q_{max}} Qi(Q)\sin r(Q)dQ \tag{2.6}$$

The wide scattering angle covered by the detectors ensures that the Q-range of the data is maximised, which is essential for maximising the real-space resolution of the correlation function. Q-space is a wavelength independent method for describing diffraction data and can be calculated using the following equation, where λ is the wavelength of a particular source.

$$Q = \frac{4\pi \sin\theta}{\lambda} \; or \frac{2\pi}{d} \tag{2.7}$$

2.2.4 Data Fitting

For refinement of the unit cell of a material, Le Bail refinements were undertaken.[8] A least squares approach is taken to fit the unit-cell parameters, instrumental zero error and peak

shape/width parameters. The main advantage of this method is knowledge of the crystal structural parameters is not required, as calculated intensities are unconstrained as such should fit the data. However, a candidate unit cell must be known.

If high quality data were obtained and unit cell parameters had been extracted from Le Bail fitting, then Rietveld refinements could be undertaken,[9] and a starting model that resembles that of the phase under investigation is required. Like the Le Bail method, the Rietveld model adopts a least squares approach to data fitting, however there are more degrees of freedom than that of the Le Bail model, including atomic positions, site occupancies, and atomic displacement parameters (ADPs), all of which have an effect on the calculated peak intensity. It should be noted that this is a method for structural refinement not solution.

2.2.5 Software Used

Rietveld and Le Bail fits were carried out using the software GSAS,[10] and was visualised using the EXPGUI interface.[11]

GudrunN was used to normalise and merge neutron diffraction data acquired on GEM.[12] The Fourier transform was then carried out using the StoG function of RMC profile.[13] The resulting pair distribution function was then analysed using PDFgui.[14]

2.2.6 Scanning Electron Microscopy (SEM)

Samples were either sprinkled on sticky carbon tape or a silicon wafer for imaging. Those samples that were not conducting were then also coated in carbon using an Emitech Evaporator, to prevent charging of the particles under the beam.

SEM was used to study the crystal morphology of synthesised materials. Images were collected on a Zeiss Supra 55-VP scanning electron microscope, using a field emission gun with an accelerating voltage between 5 and 20 kV to generate an electron beam. For high resolution images, the inlens camera was used with a working distance of 3 mm. For general imaging and use of the attached energy dispersive X-ray analysis system, secondary electron imaging was done at a working distance of 7 mm. Energy-dispersive X-ray Analysis

(EDXA) was used extensively throughout this thesis to gather approximate molar ratios of metals in the materials, while simultaneously checking for possible inhomogeneity. The metal ratios extracted were used as a starting point in the refinement of diffraction data.

Throughout Chapter 4, metal ratios in mixed pyrochlores are calculated using the data from EDXA. It assumed that calcium and sodium were found on the A-site of the pyrochlore and iridium and the substituent metal were exclusively found on the B-site. The substitution percentage of metal M was calculated using the equation below:

$$M\ Substitution\ \% = (Ir\ mol\%/M\ mol\% + Ir\ mol\%) * 100 \quad (2.8)$$

2.2.7 Transmission Electron Microscopy (TEM)

TEM was used to examine the crystal morphology and obtaining EDX spectra on individual particles. Micrographs were collected on either a JEOL 2100 TEM or a JEOL ARM200F TEM, both operating at 200 kV using LaB_6 filaments. Samples were prepared by sonication in methanol followed by dropwise deposition on 3 mm lacy carbon grids supplied by Agar.

Elemental mapping and EDXA line scans where collected on a JEOL ARM200F, to gain a better understanding of the distribution of elements in selected materials. Line scan data were normalised for each element under investigation as to better understand the metal distribution.

All TEM was performed either by Dr Reza Kashtiban or Daniel Cook.

2.2.8 Raman Spectroscopy

Raman spectroscopy exploits the inelastic scattering of monochromatic photons incident on the sample. Different crystal lattices have different active photon modes and these can be used to identify the space group of the material being studied. Measurements were carried out on a Renishaw inVia Reflex Raman Microscope employing a 633 nm HeNe laser. The microscope uses a Leica N Plan 50x/0.75 BD objective, and the measurements were carried out in a back scattering geometry. Laser power was sample dependant, but typically 0.5 % of

the available power was used to minimise thermal effects, that could be observed in the collected spectra.

2.2.9 Fourier Transform Infra-Red Spectroscopy

FT-IR was used to determine the presence of water, hydroxide and peroxide groups, in the synthesised oxides and hydroxides. It is a useful spectral technique for the identification of bonds with significant covalent character. Unlike Raman spectroscopy only those modes with a permanent change in dipole when excited are detected. Spectra were collected on a Bruker alpha platinum AT-IR instrument between 450 and 4000 cm^{-1}.

2.2.10 X-ray Absorption Spectroscopy

X-ray absorption spectroscopy (XAS) was carried out on Beamline B18[15] (Diamond Light Source, U.K.), yielding spectra that can be split into two regions, Figure 2.3.

X-ray absorption near edge structure (XANES) is dependent on the local environment and valance state of an element, as such using appropriate reference material of known structure and valence this was employed to obtain information on the oxidation state of the metals contained the synthesised materials.

The incoming X-rays generate photoelectrons at absorption edges, act as waves, which subsequently are scattered from the surrounding atoms producing an interference pattern between the outgoing and incoming electrons. This causes the ripples observed in the Extended X-Ray Absorption Fine Structure (EXAFS) region, analysis of which can yield information regarding the local environment of the absorbing atom, such as interatomic distances, coordination number and thermal parameters.

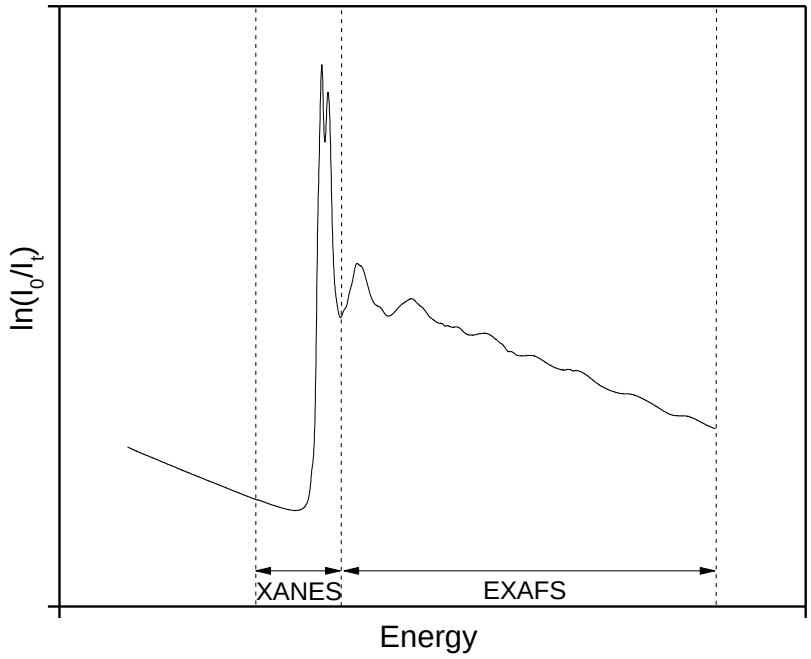

Figure 2.4: An X-ray absorption spectrum defining the XANES and EXAFS regions.

Sample preparation involved diluting the sample, typically 10 mg, in spectroscopic grade polyethylene powder (Aldrich), 100 mg. These were ground together in acetone until homogenised. The mixtures were then pressed into a 13 mm diameter pellet with a thickness of approximately 1 mm. Data were collected in transmission mode around the K or L_{III}-edges of the studied elements. Data were normalised by subtracting linear pre-edge and polynomial post-edge backgrounds using the ATHENA software.[16]

Most reference materials for XANES oxidation state calibration were purchased, however it was necessary to synthesise some. $BaNa_{0.5}Ir_{0.5}O_{2.5}$ was synthesised by grinding $BaCO_3$, Na_2CO_3 and IrO_2 in the appropriate ratio, and heating at 850 °C in pure oxygen for 12 hours, the reground and fired again under the same conditions.[17] Sb_2O_4 was synthesised by heating Sb_2O_3 in air at 500 °C for 6 hours.[18] $La_{4.87}Ru_2O_{12}$ was synthesised by grinding together La_2O_3 and RuO_2 in the appropriate ratio then firing at 1050 °C for 12 hours.[19] $SrRu_2O_6$ was synthesised hydrothermally via the reaction of SrO_2 and $KRuO_4$ in the appropriate ratio at 200 °C for 24 hours in water.[20] $SrRuO_4$ was produced in the same way using the same reagents but at 100 °C for 24 hours. Sr_3NaRhO_6 was made using a SrOH flux in a silver crucible, with NaOH and $RhCl_3$, at 600 °C for 24 hours.[21]

2.2.11 Thermal Analysis

Thermogravimetric analysis (TGA) combined with differential scanning calorimetry (DSC) was used to probe the thermal decomposition and water and/or hydroxide content of the synthesised oxides and reagents used in their synthesis. Data were collected using a Mettler-Toledo TGA/DSC1 instrument. This was carried out using 10-40 mg of sample in an alumina crucible, then under a constant flow of N_2 the sample was taken to 1000 °C at 10 °C per minute. For selected experiments a mass spectrometer monitored the exhaust gases, facilitating a more accurate description of the decomposition steps in the TGA.

Some TGA data were collected by Dr Luke Daniels and Alex Dunn. TGA-MS experiments were carried out by David Hammond.

2.2.12 Pycnometry

Pycnometry was used to determine the density of the samples studied using neutron diffraction, as this is needed in the analysis of total scattering data. Densities of the samples were collected using a micromeritics AccuPyc 1330 gas pycnometer with helium gas. In preparation for these measurements the samples were placed in a vacuum oven at 80 °C for 24 Hours, to minimise surface contamination. Once in the pycnometer, the samples were allowed to soak in helium for an hour prior to measurement. Measurements were carried out until the pressure reading had stabilised. A 1 cm^3 inset as used for all measurements and a stainless steel ball bearing of known volume was used for calibration.

2.2.13 Magnetometry

A Quantum Design MPMS XL7 SQUID magnetometer was used to collect magnetisation data as a function of temperature. 10-20 mg of sample was loaded into a gel capsule, which was in turn loaded into a plastic straw. This was then placed inside the magnetometer. Data were collected between 5 and 400 K in an applied field of 1000 Oe.

2.2.14 Surface Area Measurement

Surface area measurements were carried out using a Micromeritics Tristar 3000 porosimeter. Sample preparation involved adding the material to a Brunauer-Emmett-Teller (BET) tube then degassing it under flowing nitrogen at 200 °C for 12 hours. Once degassed, known volumes of nitrogen were added at cryogenic temperature until the material was saturated. The amount of gas absorbed at a given pressure allows the surface to be calculated from the absorption isotherms using BET theory.[22] This is a theory of multilayer absorption of gases on solids, building on Langmuir theory, which describes monolayer absorption.

2.2.15 Inductively Coupled Plasma Optical Emission Spectroscopy

The ratios of metals were determined utilising inductively coupled plasma optical emission spectroscopy (ICP-OES). This was performed by the analytical department at Johnson Matthey Technology Centre.

2.2.16 X-ray Fluorescence

X-ray fluorescence was used to determine the ratios of metals in catalyst coated membranes prior to MEA testing. This was carried out under supervision of fuel cells group at Johnson Matthey Technology Centre.

References

1 W. H. Bragg and W. L. Bragg, *Proc. R. Soc. London A Math. Phys. Eng. Sci.*, 1913, **88**, 428–438.
2 A. Kelly and K. M. Knowles, in *Crystallography and Crystal Defects*, John Wiley & Sons, Ltd, 2012, pp. 469–472.
3 A. L. Patterson, *Phys. Rev.*, 1939, **56**, 978–982.
4 W. G. Williams, R. M. Ibberson, P. Day and J. E. Enderby, *Phys. B Condens. Matter*, 1997, **241**, 234–236.
5 A. C. Hannon, *Nucl. Instruments Methods Phys. Res. Sect. A Accel. Spectrometers, Detect. Assoc. Equip.*, 2005, **551**, 88–107.
6 G. Barone, L. Bartoli, C. M. Belfiore, V. Crupi, F. Longo, D. Majolino, P. Mazzoleni and V. Venuti, *J. Anal. At. Spectrom.*, 2011, **26**, 1060–1067.
7 E. R. Barney, A. C. Hannon and D. Holland, *J. Phys. Chem. C*, 2012, **116**, 3707–3718.
8 A. Le Bail, H. Duroy and J. L. Fourquet, *Mater. Res. Bull.*, 1988, **23**, 447–452.
9 H. Rietveld, *J. Appl. Cryst.*, 1969, **2**, 65–71.
10 A. C. Larson and R. B. Von Dreele, *Los Alamos Natl. Lab. Rep.*, 2004, 86.
11 B. H. Toby, *J. Appl. Cryst.*, 2001, **34**, 210–221.
12 A. K. Soper, *GudrunN GudrunX. Programs correcting raw neutron x-ray Total Scatt. data to Differ. cross Sect. (http//purl. org/net/epubs/work/56240)*.

13 M. G. Tucker, D. A. Keen, M. T. Dove, A. L. Goodwin and Q. Hui, *J. Phys. Condens. Matter*, 2007, **19**, 335218.
14 C. L. Farrow, P. Juhas, J. W. Liu, D. Bryndin, E. S. Božin, J. Bloch, T. Proffen and S. J. L. Billinge, *J. Phys. Condens. Matter*, 2007, **19**, 335219.
15 P. E. Dent, A. J.; Cibin, G.; Ramos, S.; Smith, A. D.; Scott, S. M.; Varandas, L.; Pearson, M. R.; Krumpa, N. A.; Jones, C. P.; Robbins, *J. Phys. Conf. Ser.*, 2009, **190**, 12039.
16 B. Ravel and M. Newville, *J. Synchrotron Radiat.*, 2005, **12**, 537–541.
17 D.-Y. Jung, G. Demazeau, J. Etourneau and M. A. Subramanian, *Mater. Res. Bull.*, 1995, **30**, 113–123.
18 N. Greenwood, *Chemistry of the Elements (2nd ed.).*, New York, Butterworth–Heinemann, 1997.
19 P. Khalifah, Q. Huang, D. M. Ho, H. W. Zandbergen and R. J. Cava, *J. Solid State Chem.*, 2000, **155**, 189–197.
20 C. I. Hiley, M. R. Lees, J. M. Fisher, D. Thompsett, S. Agrestini, R. I. Smith and R. I. Walton, *Angew. Chemie Int. Ed.*, 2014, **53**, 4423–4427.
21 B. A. Reisner and and Angelica M. Stacy, *J. Am. Chem. Soc.*, 1998, **120**, 9682–9683.
22 S. Brunauer, P. H. Emmett and E. Teller, *J. Am. Chem. Soc.*, 1938, **60**, 309–319.

Chapter 3 – Substituted Ruthenium Rutiles

3.1 Introduction and Scope of Chapter

Rutile structured RuO_2 and materials based on it are some of the most active oxygen evolution reaction catalysts under acidic conditions.[1–3] In this chapter, an investigation into the synthesis and subsequent characterisation of substituted ruthenium oxide rutiles and the peroxide precursors required to synthesise them is reported. Conventionally +4 metals are the ones found in atomically substituted RuO_2, like Sn^{4+}, V^{4+}, Ti^{4+} and Ir^{4+}.[4–8] However, using peroxides and a Ru^{7+} precursor to maintain an oxidising atmosphere, a method for the synthesis of substituted RuO_2 has been devised where the substituents have a valence lower than +4. The metals replacing the ruthenium are zinc, magnesium, nickel, cobalt and copper. The synthesis was based on work by Hiley *et al.*,[9] who prepared new calcium, strontium and barium ruthenates from alkaline earth peroxides and potassium perruthenate.

3.2 Synthesis

3.2.1 Peroxide Synthesis

Zinc Peroxide

$Zn(NO_3)_2 \cdot 6H_2O$ (4.0 g) was added to a plastic bottle with a volume of approximately 250 ml. The minimal volume of ammonium hydroxide 35 % was added to the zinc nitrate to allow dissolution under constant stirring, and upon complete dissolution hydrogen peroxide 30 % was added until the solution turned white and opaque. The bottle was then sealed and heated at 100 °C for 24 hours. The resulting white solid was retrieved via vacuum filtration, and washed with water. The solid was then dried in an oven at 70 °C for 24 hours.

Magnesium Peroxide

$Mg(NO_3)_2 \cdot 6H_2O$ (3.45g) was added to a 100 ml conical flask. The minimal volume of ammonium hydroxide 35 % was added to this to allow dissolution under constant stirring, and upon complete dissolution hydrogen peroxide 30 % was added until the solution turned

white and opaque. The flask was then stored in a fridge at 5 °C for 72 hours. The resulting white solid was retrieved via centrifugation. The solid was then dried in an oven at 70 °C for 24 hours.

Copper and Cobalt "Peroxides"

Adapting the procedure of Pankratov *et al.*,[10] either $Cu(NO_3)_2 \cdot 2.5H_2O$ (2.0 g) or $Co(NO_3)_2 \cdot 2.5H_2O$ (2.0 g) was added to a 250 ml conical flask. To this the minimum volume of methanol was added to facilitate dissolution under constant stirring and upon complete dissolution, solid potassium hydroxide was added to the mixture, enough to make an approximately 1 M $KOH_{(MeOH)}$ solution. To this hydrogen peroxide 30 % was added until the solution had turned completely brown. The flask was then stored in a fridge at 5 °C for 72 hours. The resulting brown was then retrieved via centrifugation. The collected materials were then washed in 50 ml of distilled water for 24 hours to remove excess potassium nitrate before a final vacuum filtration. The solids were then dried in an oven at 70 °C for 24 hours.

Nickel "Peroxide"

Nickel peroxide was purchased from Sigma Aldrich. No information was given regarding purity.

3.2.2 Synthesis of Substituted Ruthenate Rutiles

The substituted rutile materials were synthesised using potassium perruthenate (Alfa Aesar, 98 %) and metal peroxide in 10 ml H_2O, these were added in a molar ratio of 1 : 0.5 respectively based on 2.45 mmol Ru. In all the substituted materials it was later found that only 15 % of the ruthenium was substituted, thus the 1 : 0.5 ratio of perruthenate to peroxide provides an excess of peroxide. This was done to ensure the maximum amount of substituent was incorporated into the synthesised material. The reaction was then carried out at 240 °C for three days. The black powders were then collected via vacuum filtration and stirred in 50 ml of 3 M nitric acid, to remove and hydroxide or oxide byproducts. The duration of the acid treatment was dependant on the substituent metal. The magnesium substituted material

only needed 5 minutes, zinc substituted material needed two hours, and the copper, cobalt and nickel substituted materials needed twenty four hours. The materials were then collected via vacuum filtration, and washed with water and then acetone.

The ruthenium oxide used for comparison against these substituted materials was supplied by Johnson Matthey. It was produced through the hydrolysis of ruthenium chloride, and the hydrolysis product was then fired at 300 °C.

3.3 Characterisation of Peroxide Precursors

Powder XRD patterns of the zinc and magnesium peroxides reveals phase pure materials adopting cubic structures with the space group $Pa\bar{3}$ have been synthesised. Rietveld refinements reveal structures very close to those in the literature, Figure 3.1 and Table 3.1. The magnesium material shows considerable peak broadening suggesting very small crystallite size.

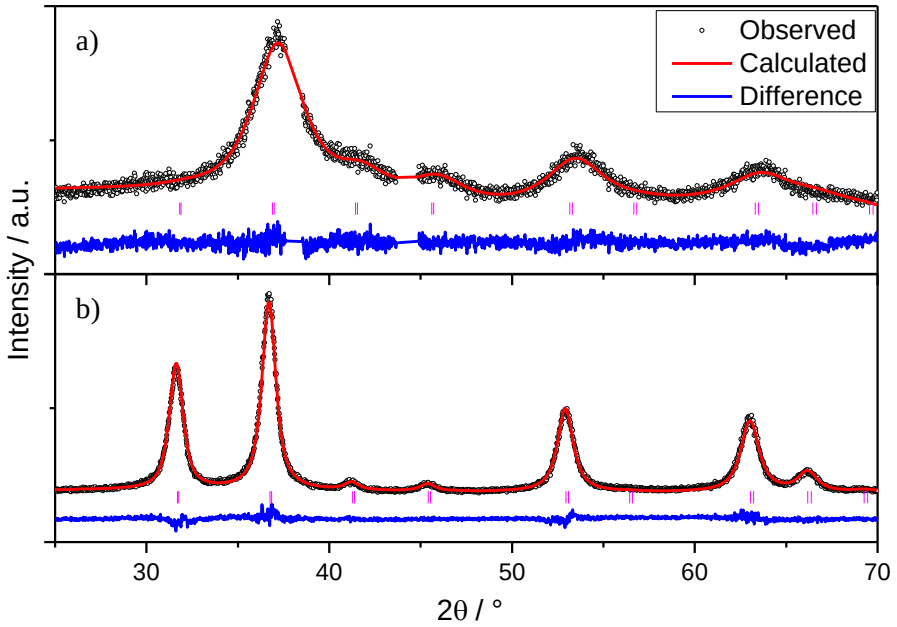

Figure 3.1: Rietveld refinements of powder XRD data (λ = 1.5418 Å), a) Magnesium and b) Zinc Peroxides.

Table 3.1: Structural details of ZnO_2 and MgO_2 obtained from Rietveld refinement of powder XRD data.

Atom	Site	*x y z*	Occ	U_{iso}*100 / Å^2
MgO_2: Space Group = $Pa\bar{3}$ *a* = 4.8685(12) Å Lit = 4.839 Å[11]				
Mg	4*a*	0	1.000(3)	2.99(5)
O	8*c*	0.4151(2) Lit = 0.4110[11]	1.000(5)	1.819(8)
ZnO_2: Space Group = $Pa\bar{3}$ *a* = 4.88744(13) Å Lit = 4.871 Å[12]				
Zn	4*a*	0	1.000(1)	1.472(19)
O	8*c*	0.4144(2) Lit = 0.4130[12]	1.000(4)	3.44(11)

FT-IR spectroscopy reveals a very weak peak at ~ 870 cm^{-1} in MgO_2, and a possible peak ~835 cm^{-1} in ZnO_2 similar to that of the O - O stretching of the peroxy groups reported in $K_3Ta(O_2)_4$ and $K_3Nb(O_2)_4$.[13] Broad features in are observed both spectra around 3500 cm^{-1} and a sharper feature around 1450 cm^{-1}, which can be attributed to O-H stretching and bending modes respectively, likely from surface water, Figure 3.2.

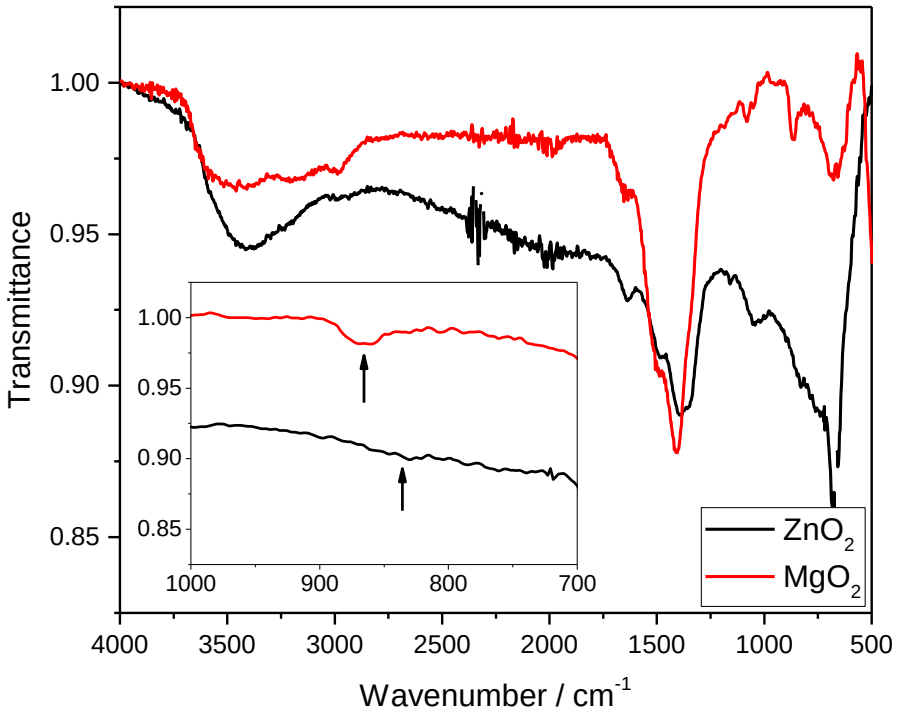

Figure 3.2: FT-IR spectra of zinc and magnesium peroxides.

Thermal analysis, Figure 3.3, shows that the mass losses and thermal events occur at the same temperature as found in the literature for ZnO_2.[14] Initially a small mass loss of 1.6 % is observed over the first hundred degrees, which can be attributed to surface water. The major

mass loss and endothermic event around 230 °C of 17.0 % is close to the expected loss of 16.4 %, corresponding to the release of O_2, following reaction below.

$$2ZnO_2 \rightarrow 2ZnO + O_2$$

The mass losses and thermal events also occur at the same temperature as found in the literature for MgO_2.[15] The initial mass loss is greater than that observed for ZnO_2, and again is attributed to surface water, consistent with the smaller crystallite size observed by XRD, which would imply a higher surface area for MgO_2. The mass loss and small endothermic peak at 340 °C of 31.1 % is close to the expected loss of 29.4 %, corresponding to the release of O_2, following reaction below.

$$2MgO_2 \rightarrow 2MgO + O_2$$

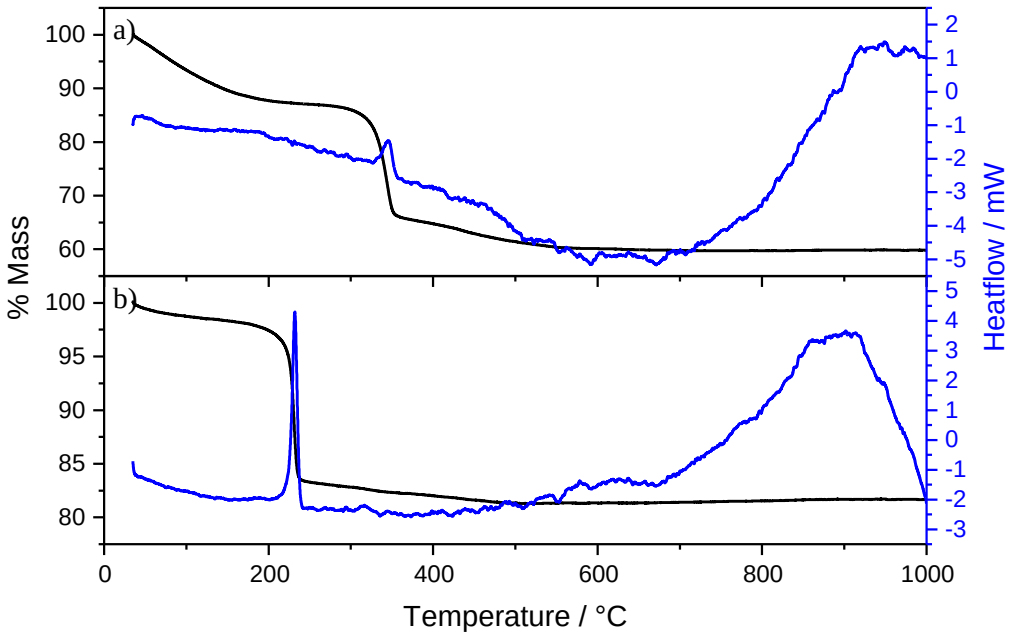

Figure 3.3: Thermogravimetric analysis data of, a) Magnesium and b) Zinc Peroxides.

To the best of the authors knowledge there is no literature containing structural data for nickel, cobalt or copper peroxide, as such there are no data to compare the collected XRD data with.

The powder XRD pattern of the "nickel peroxide" purchased from Sigma Aldrich is almost completely amorphous with the only peak centred around 38 °, Figure 3.4, as such information related to the structure of the material could not be obtained.

The powder XRD of the “cobalt peroxide” reveals a one set of Bragg peaks, arising from poorly crystalline Co_3O_4, Figure 3.4. However this material is brown, where as Co_3O_4 is black, so it seems likely there is an amorphous phase as well.

The powder XRD of the “copper peroxide” reveals the material to be mixed phased, as there are Bragg peaks arising from both CuO and Cu_2O, as well as another unidentified phase, likely some hydroxide or nitrate given the reagents used, Figure 3.4. It seems unlikely that either CuO or Cu_2O is the major phase as the material is brown and CuO is grey/black and Cu_2O is red.

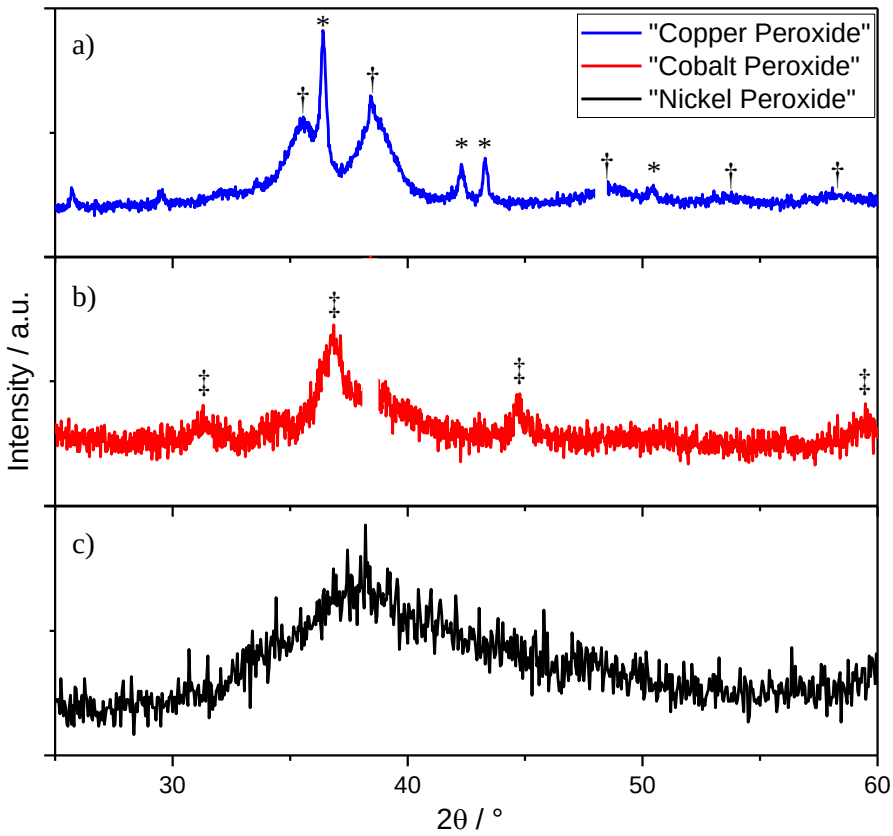

Figure 3.4: Powder XRD patterns (λ = 1.5418 Å) of, a) "Copper Peroxide" where † indicates peaks arising from CuO and * from Cu_2O, b) "Cobalt Peroxide" where ‡ indicates peaks arising from Co_3O_4, and c) "Nickel Peroxide". In all patterns the feature observed at approximately 19 ° 2θ is a result of the sample holder.

A broad feature at 3500 cm^{-1} and the peak at 1500 cm^{-1}, are observed in IR spectra of all three materials, which can be attributed to O-H stretching and bending modes respectively, likely from surface water, Figure 3.5. There is no obvious band similar to that of the O - O stretching of the peroxy groups reported in $K_3Ta(O_2)_4$ and $K_3Nb(O_2)_4$,[13] in any of the materials.

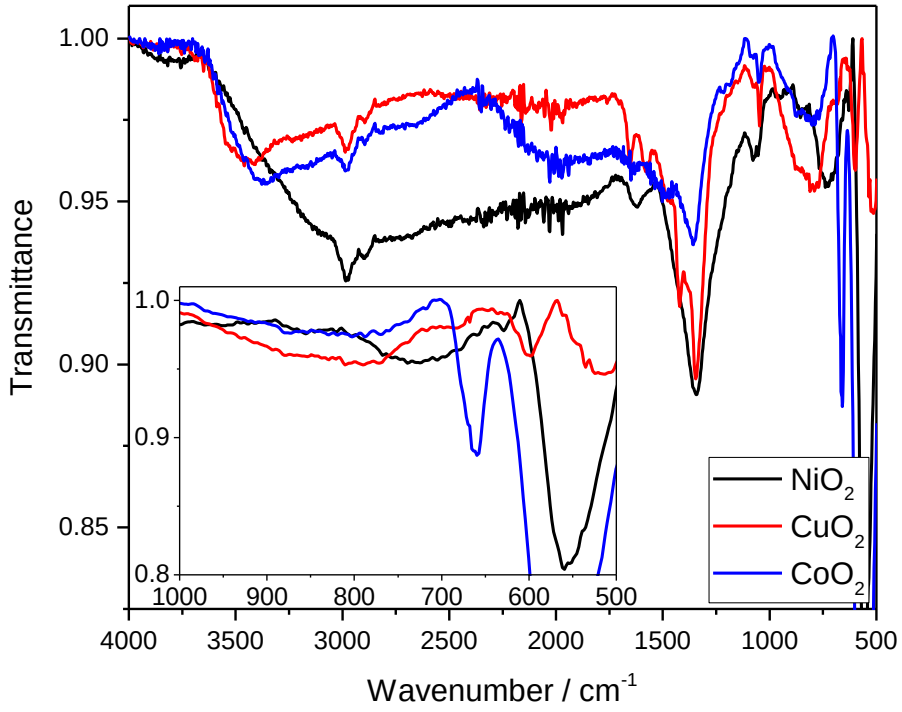

Figure 3.5: FT-IR spectra of nickel, copper and cobalt "peroxides".

Thermal analysis of "nickel peroxide", Figure 3.6, shows a steady mass loss between room temperature and 400 °C, with a couple of inflections. The first occurs at roughly 160 °C, by which point 8.7 % of the total mass has been lost and this can be attribute to the loss of surface water. Past 160 °C the rate of mass loss increases and a further 13.2 % of the total mass is lost by the time 400 °C is reached, which could be due to liberation of oxygen. Assuming the formula $NiO_2 \cdot xH_2O$ as Sigma Aldrich claimed, one would expect a mass loss of 32.3 %, assuming x = 1 and that the peroxide decomposes into NiO. Assuming fraction of water is the only variable then the true value of x can be calculated, and is found to be 0.38.

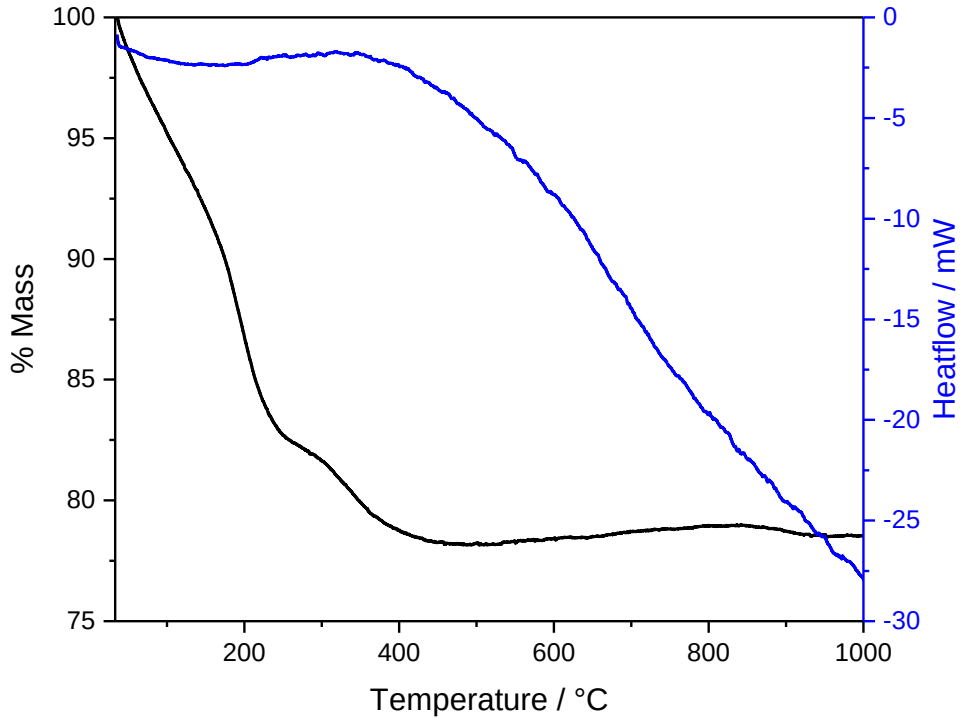

Figure 3.6: Thermogravimetric analysis data of "Nickel Peroxide".

Figure 3.7 shows the thermal analysis data of copper and cobalt "peroxides". The following analysis assumes that given these are heated under flowing N_2 the decomposition products are Cu_2O and CoO respectively.

In the TGA of the cobalt material an initial mass loss of 5.0 % is observed between room temperature and 125 °C, this is probably due to surface water. The next major loss of 11.8 % of the occurs around 175 °C, a similar temperature observed for the release of oxygen in both the zinc and nickel peroxides, at this stage it is probable Co_3O_4 has been produced. The final loss of 7.5 % occurs at 800 °C at which point the Co_3O_4 is converted to CoO, the expected loss for which is 6.7 %. The mass loss observed at 175 °C is 50 % greater than the loss at 800 °C, meaning more oxygen is liberated during the decomposition. The initial mass loss up until 175 °C is poorly defined. As such the material could likely be an oxy-hydroxide, which is probable given that the TGA data is the same shape as observed for CoO(OH) in the literature.[16]

In the TGA of the copper material an initial mass loss of 1.6 % is observed between room temperature and 100 °C, this is probably due to surface water. The next major loss of 7.2 %

of the occurs around 180 °C, a similar temperature observed for the release of oxygen in both the zinc and nickel "peroxides", at this stage it is probable CuO has been produced. The final loss of 7.9 % of the starting mass occurs at 800 °C at which point the CuO is converted to Cu_2O, the expected loss which is 10 %. From XRD this material is known to be mixed phase, which introduces some error into the mass losses, but given how similar the shape of the TGA data is to that of the cobalt material, it could be possible that this is also an oxyhydroxide.

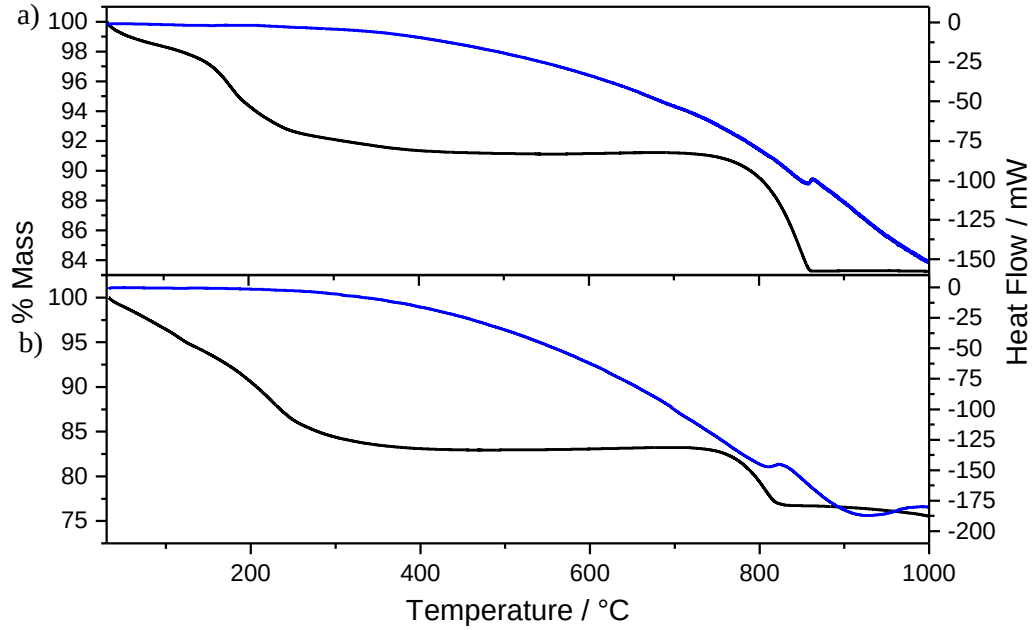

.**Figure 3.7:** Thermogravimetric analysis data of a) copper "peroxide" and b) cobalt "peroxide".

The Ni K-edge XANES spectrum of the purchased "nickel peroxide" aligns very well with nickel (II) acetate, however it does not line up well with nickel (II) oxide, Figure 3.8. In both reference materials the coordination geometry is octahedral, however there is a clear shift in the edge energy. Despite the expectation of having nickel in the same oxidation state, nickel oxide and acetate have edge energies approximately 2 eV apart. The difference between Ni^{2+} and Ni^{3+} in literature seems to also be approximately 2 eV, with the Ni^{3+} edge being shifted to higher energy with respect to the Ni^{2+} edge.[17,18] Given how difficult is it to produce Ni^{3+} materials, it seems likely that the "nickel peroxide" has a nickel oxidation state of +2.

However, the synthesis of peroxide requires to use of very oxidising conditions, so it remains possible, that it could contain Ni^{3+}.

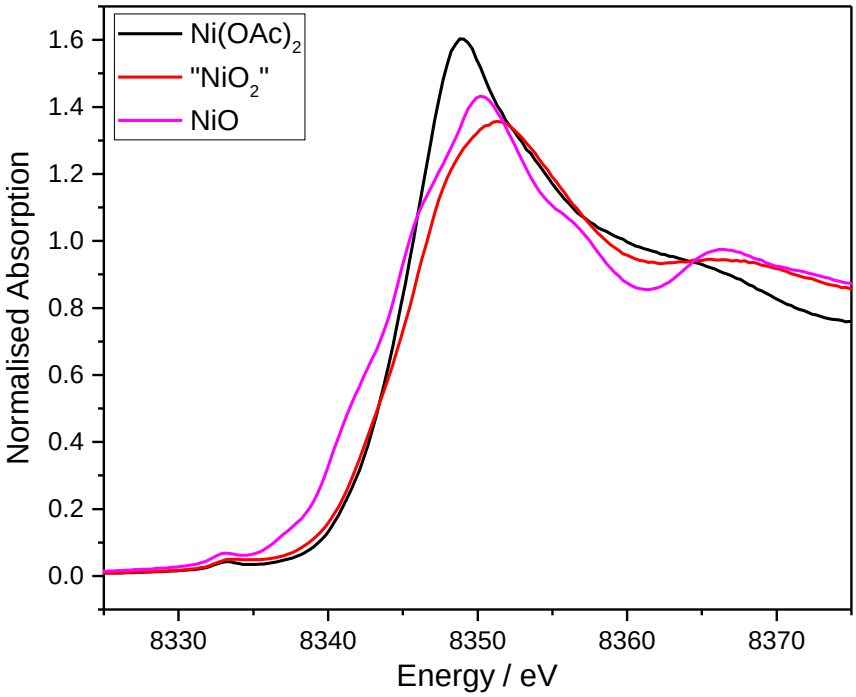

Figure 3.8: Nickel K-edge XANES spectra of nickel oxide, nickel acetate and "nickel peroxide".

Figure 3.9 shows the Co K-edge position in the XANES spectra of the "cobalt peroxide" material. There is known to be a linear increase in edge energy with cobalt oxidation state, as long as any pre-edge features are minimal in size.[17] The average cobalt oxidation state of approximately +2.75 this is higher than +2.66, which would be expected if there were only Co_3O_4 present. There is also a difference in line shape compared to Co_3O_4 suggesting a second phase is present. This increase in average cobalt oxidation state could be due to the presence of CoO(OH), which is brown, like the material synthesised.[19]

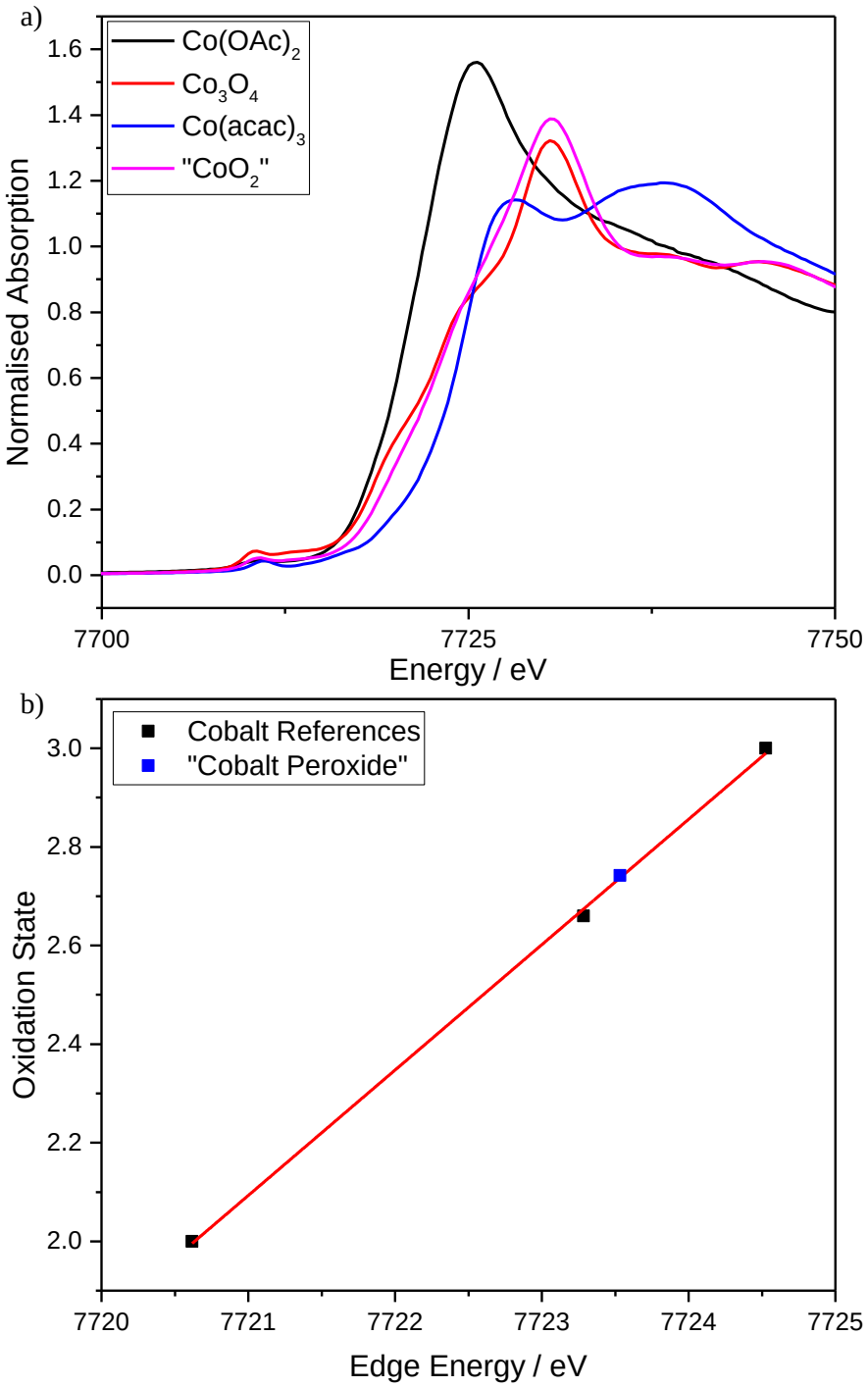

Figure 3.9: a) Cobalt K-edge XANES spectra of cobalt precursor and cobalt reference materials for calibration. b) Edge position against cobalt oxidation state.

The Cu K-edge XANES position is known to follow a linear increase in energy with oxidation state.[20] and the copper in "copper peroxide" is shown to have an oxidation state of +2, Figure 3.10.

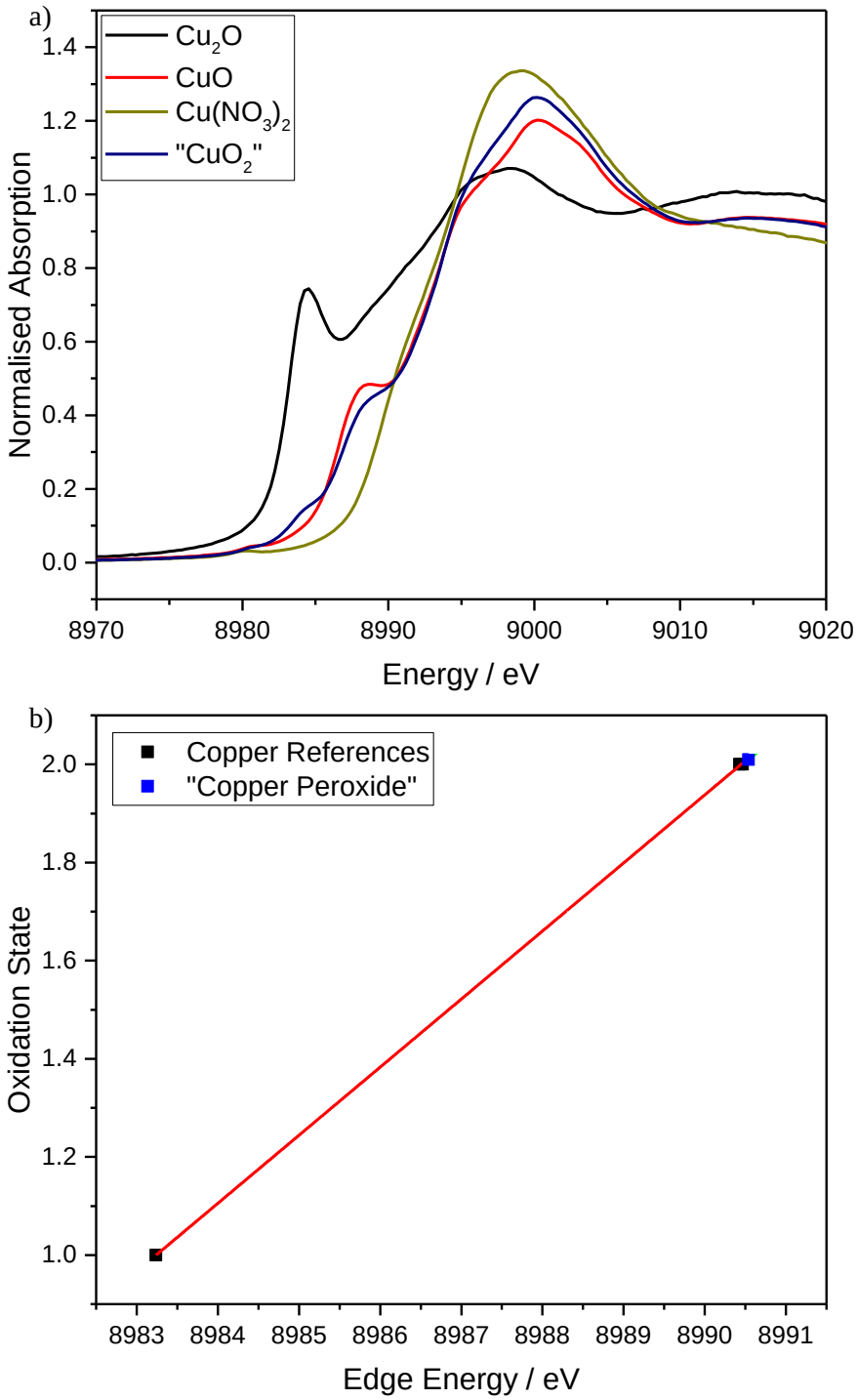

Figure 3.10: a) Copper K-edge XANES spectra of copper precursor and copper reference materials for calibration. b) Edge position against copper oxidation state.

3.4 Powder XRD of Substituted Rutiles

Powder XRD data from all materials could be indexed to a tetragonal rutile phase adopting the space group $P4_2/mnm$, Figure 3.11. All substituted materials have an expanded *a* axis, and a contracted *c* axis, when compared to RuO_2, Table 3.2. However, there is always an

increase of unit cell volume upon substitution of the divalent metal as the increases in *a* outweigh the decrease in *c*.

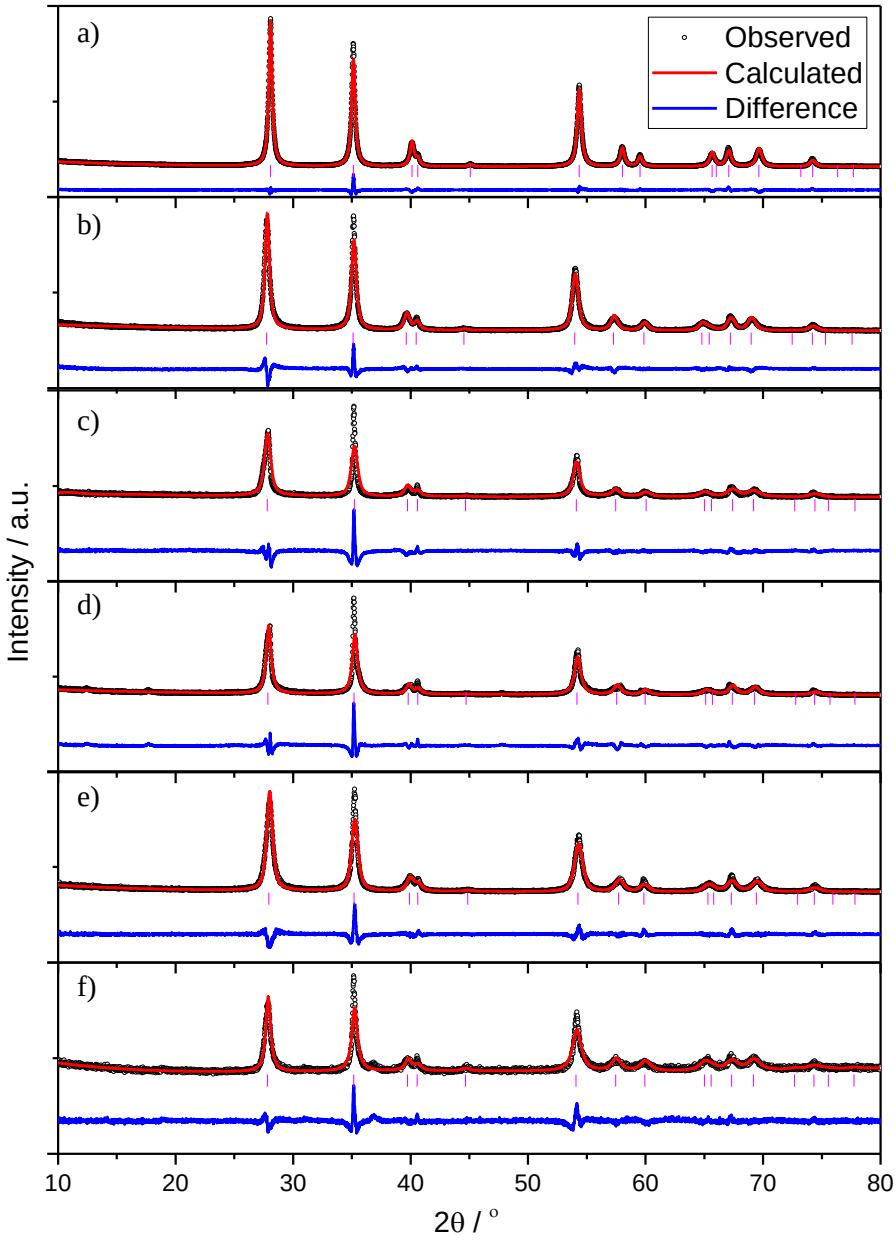

Figure 3.11: Le Bail refinements of powder XRD data (λ = 1.54056 Å), a) RuO_2, b) $Zn_{0.15}Ru_{0.85}O_2$, c) $Mg_{0.15}Ru_{0.85}O_2$, d) $Ni_{0.15}Ru_{0.85}O_2$, e) $Cu_{0.15}Ru_{0.85}O_2$ and f) $Co_{0.15}Ru_{0.85}O_2$

Table 3.2: Lattice parameters of RuO_2 and substituted rutiles from Le Bail refinement of powder XRD data.

Material	*a* / Å	*c* / Å	*V* / Å^3
RuO_2	4.49365(4)	3.10407(5)	62.680(1)
RuO_2[21]	4.4919	3.1066	62.682
$Zn_{0.15}Ru_{0.85}O_2$	4.54210(11)	3.08536(11)	63.653(4)
$Mg_{0.15}Ru_{0.85}O_2$	4.5342(2)	3.0798(2)	63.319(7)
$Ni_{0.15}Ru_{0.85}O_2$	4.5274(2)	3.0836(2)	63.207(6)
$Cu_{0.15}Ru_{0.85}O_2$	4.5153(2)	3.0887(2)	62.973(6)
$Co_{0.15}Ru_{0.85}O_2$	4.5342(3)	3.0846(3)	63.421(10)

The unit cell data of the substituted ruthenium oxide rutiles synthesised in this study were compared with a wide range of binary rutile oxides, from Bolzan *et al.*[22] and the mixed-metal rutile oxides $Zn_{0.15}Nb_{0.3}Ti_{0.55}O_2$, $Al_{0.2}Nb_{0.2}Ti_{0.6}O_2$, and $Li_{0.15}Nb_{0.45}Ti_{0.4}O_2$ produced by Abrahams *et al.*,[23] Figure 3.12. The materials in Abrahams' work show the same *a* axis expansion and *c* axis contraction observed here, when compared to the parent material TiO_2. The average ionic radius of the metals in the rutile materials from this study was calculated using the ratios of metals observed in, EDXA, Section 3.6, neutron diffraction, Section 3.8, and ionic radii from Shannon *et al.*[24]

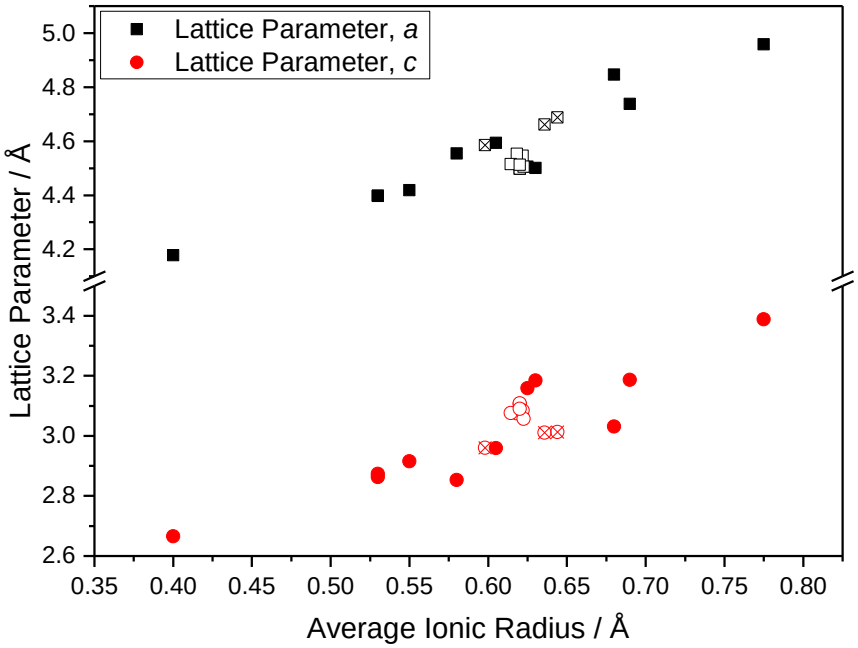

Figure 3.12: Lattice parameters of various rutile oxides. Materials from Bolzan's study are marked with block symbols, those from Abraham's study with crossed symbols and those from this study with open symbols.

The 101 reflection, at approximately 30 ° 2θ, is not fitted well for the substituted materials, which could be due to preferred orientation effects in flat plate geometry of X-ray measurement. It is also possible that the space group differs from $P4_2/mnm$. Hence the literature was searched for likely distortions of the rutile structure. It was found at high pressure, exceeding 5.3 GPa RuO_2 becomes orthorhombic adopting the β-PtO_2 structure with space group *Pbcm*.[25] There are also the possibilities of unusual metal and oxygen positions and possible reduction in oxygen occupancy; however since the XRD patterns are dominated by the scattering from the ruthenium atoms, these possibilities will be further explored in the neutron diffraction section.

3.5 Raman Spectroscopy

There are four Raman active bands in RuO_2, the B_{1g} at 165 cm^{-1}, the E_g and 526 cm^{-1} the A_{1g} at 646 cm^{-1} and the B_{2g} at 715 cm^{-1}.[26] The B_{1g} mode is extremely weak in comparison to the other bands and due to the limited signal observed this region of the spectrum was not analysed. The other three peaks can all be observed in both RuO_2 and the substituted materials, Figure 3.13.

The reason to use Raman spectroscopy as a probe for these materials is when 11 GPa of pressure is applied to RuO_2 the unit cell converts from tetragonal rutile type to an orthorhombic β-PtO_2 type, which leads to a distinctive splitting of the E_g band.[27] This was looked for as it was possible that that the inclusion of large divalent metals into the rutile structure may induce this transformation, and Raman spectroscopy would be much more sensitive to this transformation on the local scale than X-ray diffraction where static disorder may make its long-range detection difficult.

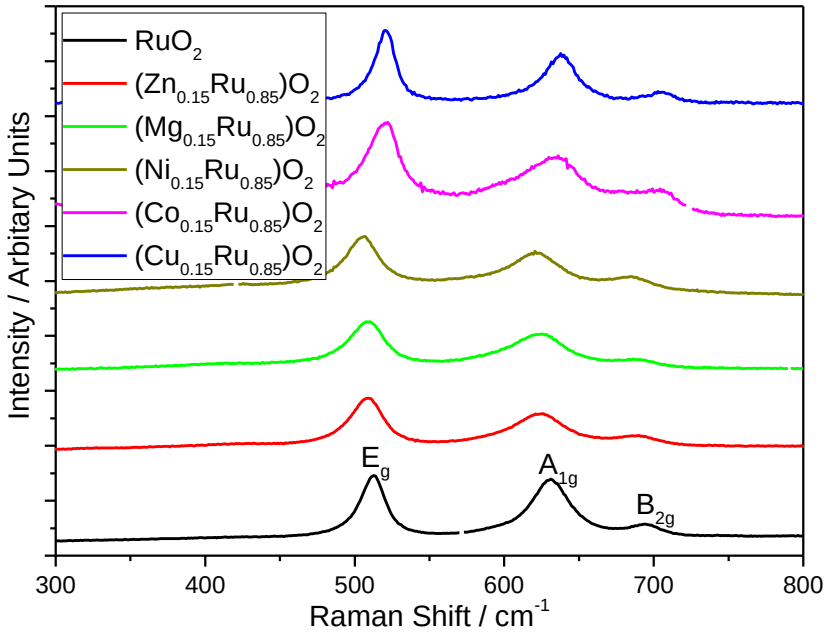

Figure 3.13: Raman spectra of RuO_2 and other substituted rutiles.

To determine whether an orthorhombic cell was present, the Raman bands were fitted and FWHM values were determined, Table 3.3. The ratio of the FWHMs of the E_g and A_{1g} modes should reveal whether any splitting in the E_g peak has taken place, since the singly degenerate A_{1g} band will not split. Table 3.3 shows that while there is some deviation in the E_g / A_{1g} ratios there is no positive correlation, and so no evidence for orthorhombic distortion.

Table 3.3: FWHM data from fitting of E_g and A_{1g} peaks for RuO_2 and substituted rutile materials.

Material	E_g FWHM	A_{1g} FWHM	E_g / A_{1g}
RuO_2	20.1	32.4	0.62
$Zn_{0.15}Ru_{0.85}O_2$	27.3	46.2	0.59
$Mg_{0.15}Ru_{0.85}O_2$	32.1	46.8	0.69
$Ni_{0.15}Ru_{0.85}O_2$	26.7	46.3	0.58
$Cu_{0.15}Ru_{0.85}O_2$	24.4	54.2	0.54
$Co_{0.15}Ru_{0.85}O_2$	18.7	26.6	0.70

3.6 Electron Microscopy

TEM reveals that the zinc and magnesium substituted rutiles both have particles adopting a rod shaped morphology, Figure 3.14. SEM shows that the nickel, cobalt and copper

substituted materials all adopt the same morphology, Figure 3.15, with cube shaped particles. EDXA reveals in all cases the approximate M : Ru ratio is 1 : 5, Table 3.4.

Table 3.4: EDXA results for substituted ruthenium oxide materials obtained from SEM.

Material	M / Atomic %	Ru / Atomic %
$Zn_{0.15}Ru_{0.85}O_2$	17.4	82.6
$Mg_{0.15}Ru_{0.85}O_2$	18.2	81.8
$Ni_{0.15}Ru_{0.85}O_2$	16.3	83.7
$Cu_{0.15}Ru_{0.85}O_2$	14.8	85.2
$Co_{0.15}Ru_{0.85}O_2$	13.2	86.8

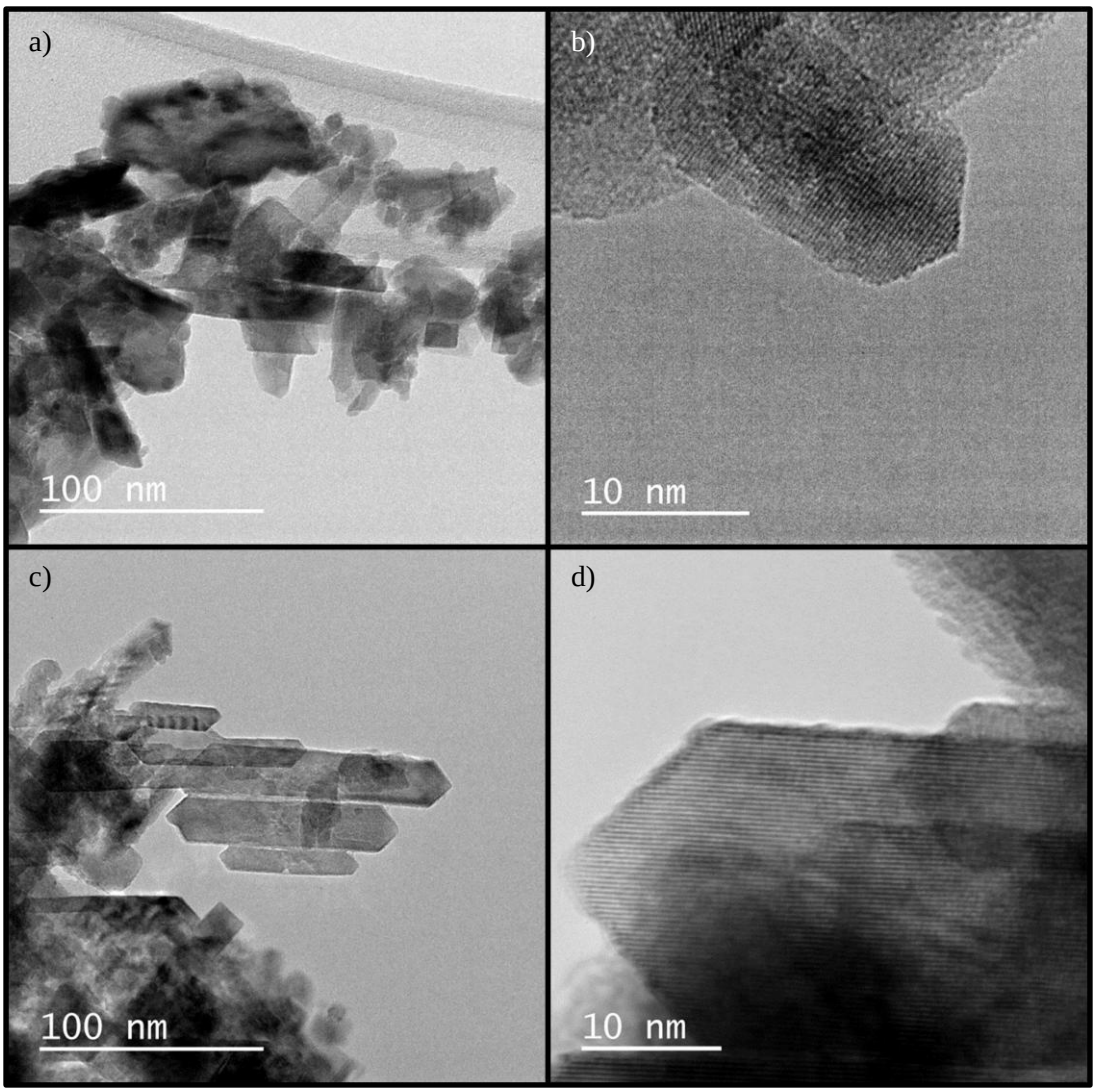

Figure 3.14: TEM micrographs of a) + b) $Zn_{0.15}Ru_{0.85}O_2$, c) + d) $Mg_{0.15}Ru_{0.85}O_2$.

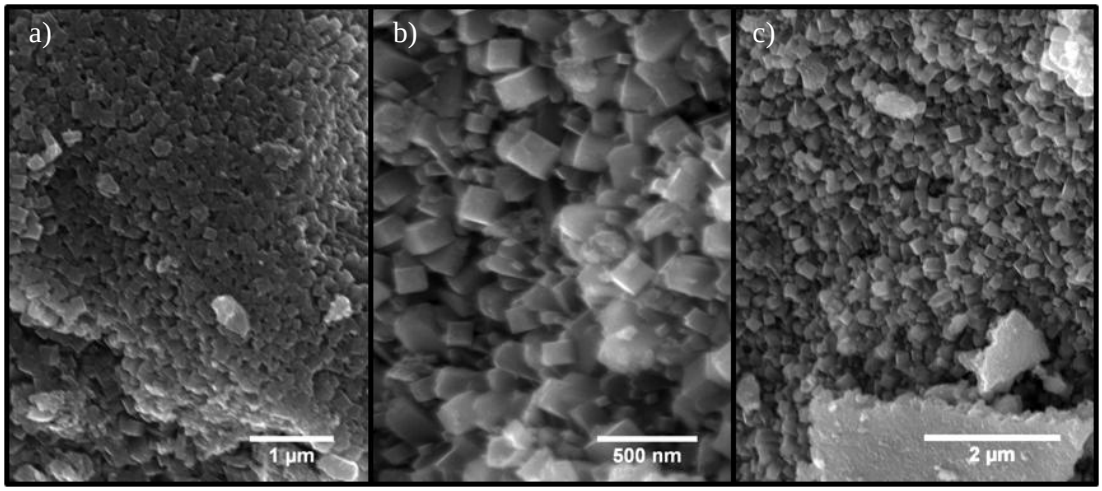

Figure 3.15: SEM micrographs of a) $Ni_{0.15}Ru_{0.85}O_2$, b) $Co_{0.15}Ru_{0.85}O_2$ and c) $Cu_{0.15}Ru_{0.85}O_2$.

3.7 X-ray Absorption Spectroscopy

The Ru K-edge position, taken at when the normalised absorption is equal to 0.5, in the XANES spectrum is known to show a linear increase in energy with oxidation state, as long as any pre-edge features are minimal in size.[9] Thus XANES was employed to probe the oxidation state of the ruthenium contained within the synthesised materials, Figure 3.16. By comparing the edge position of the doped rutile materials against those of known valence it is observed that in all cases there is an oxidation of the ruthenium above the +4 state. Assuming the substituent metal has an oxidation state of +2, that the 15% substitution level observed from EDXA is accurate and that there are no oxygen vacancies, the ruthenium would be expected to have an oxidation state to approximately +4.3. In all the synthesised materials except the cobalt substituted material a ruthenium oxidation state between +4.2 and +4.25 is extracted from the XANES data, consistent with the formula $M_{0.15}^{2+}Ru_{0.85}^{4.3+}O_2$. The cobalt substituted material yields a ruthenium oxidation state of +4.14, suggesting the cobalt found in the substituted rutile has a valance greater than +2, this possibility is explored with Co K-edge XANES see below.

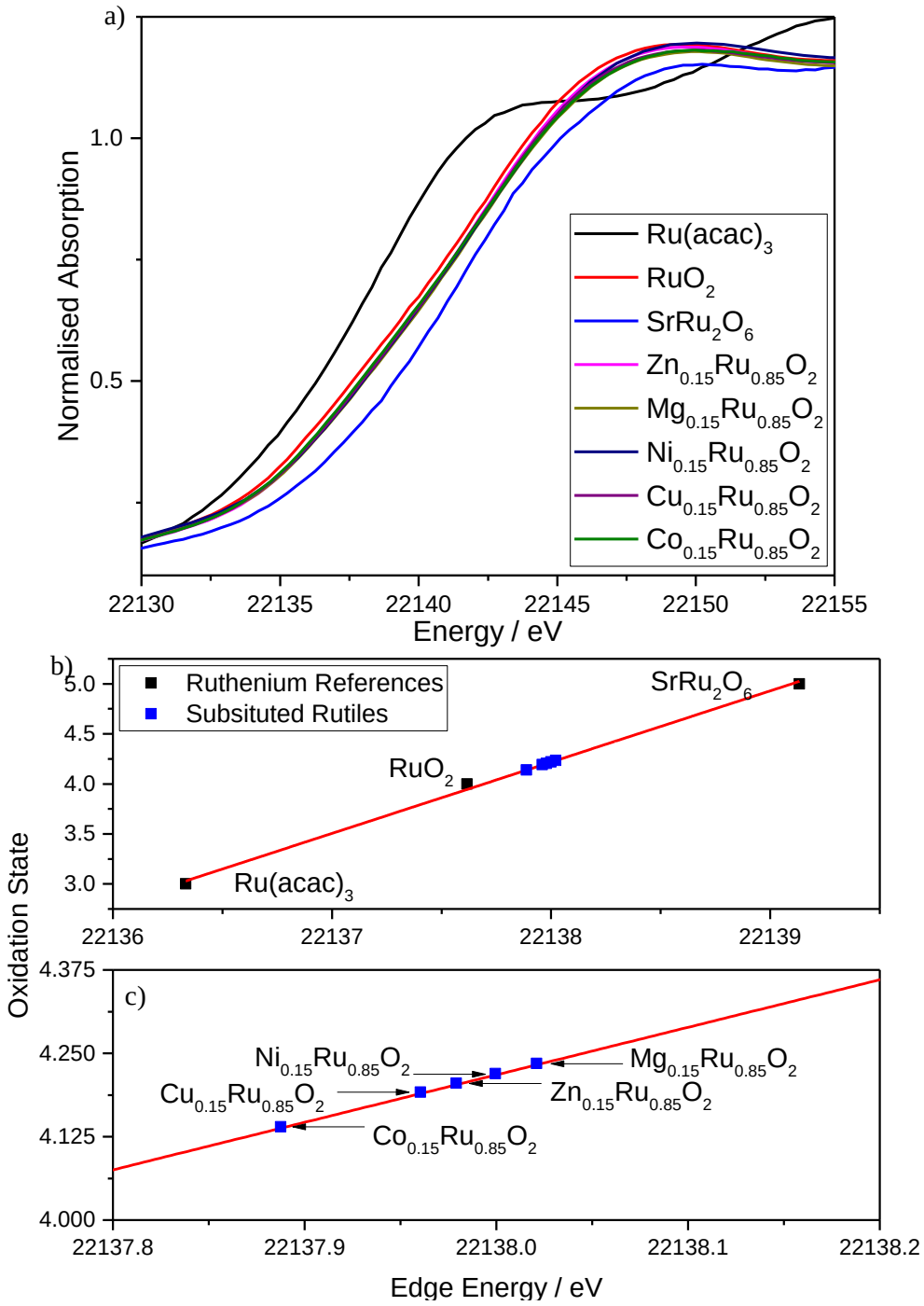

Figure 3.16: a) Ruthenium K-edge XANES spectra of substituted rutiles and ruthenium reference materials for calibration. b) Edge position against ruthenium oxidation state. c) zoom of b) on substituted materials.

Zinc and magnesium are limited to the +2 oxidation state, however in the rest of the materials the situation is not as simple. This Ni K-edge, Co K-edge and Cu K-edge XANES were utilised to check the oxidation states of these metals, Figures 3.17, 3.18 and 3.19 respectively. While nickel is most commonly found in the +2 state, it is possible to have Ni^{3+}, however the nickel edge of the substituted ruthenium oxide lies on top of that of both

nickel acetate and "nickel peroxide" and given the oxidation state of ruthenium extracted from the Ru K-edge XANES there is strong evidence for the nickel being Ni^{2+}. This supports the conclusion drawn from the ruthenium edge data.

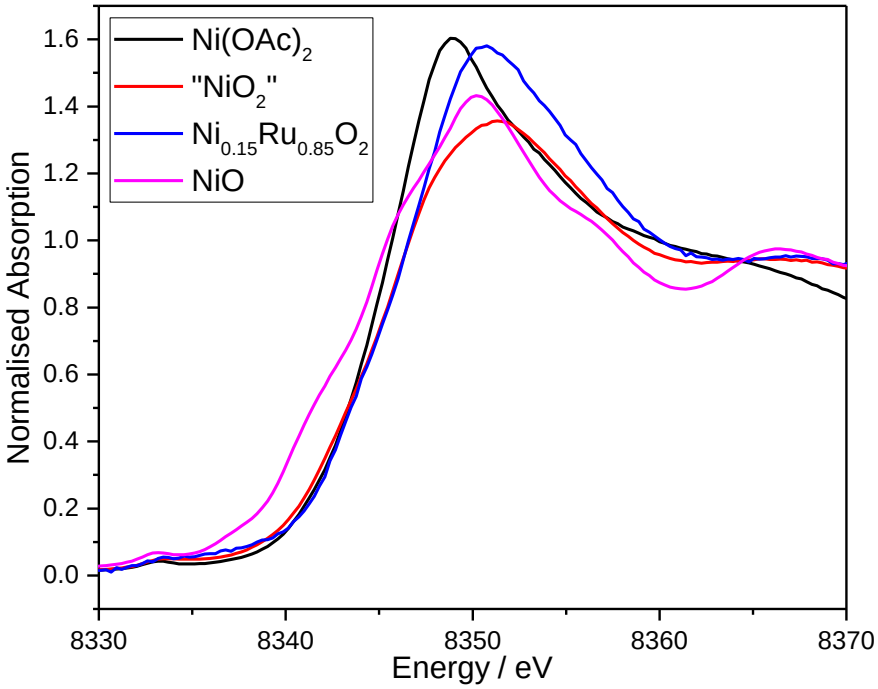

Figure 3.17: Nickel K-edge XANES spectra of nickel substituted rutile and nickel reference materials for calibration.

Copper has several stable oxidation states with both Cu^{+} and Cu^{2+} compounds being common place, whist Cu^{3+} is rarer but still possible.[28] Like the other edges studied, Cu K-edge XANES show a linear increase in edge energy with oxidation state,[20] so it was used to probe the oxidation state of the copper in the copper substituted ruthenium oxide, Figure 3.18. This shows Cu to be in the +2 oxidation state, consistent with the Ru K-edge XANES.

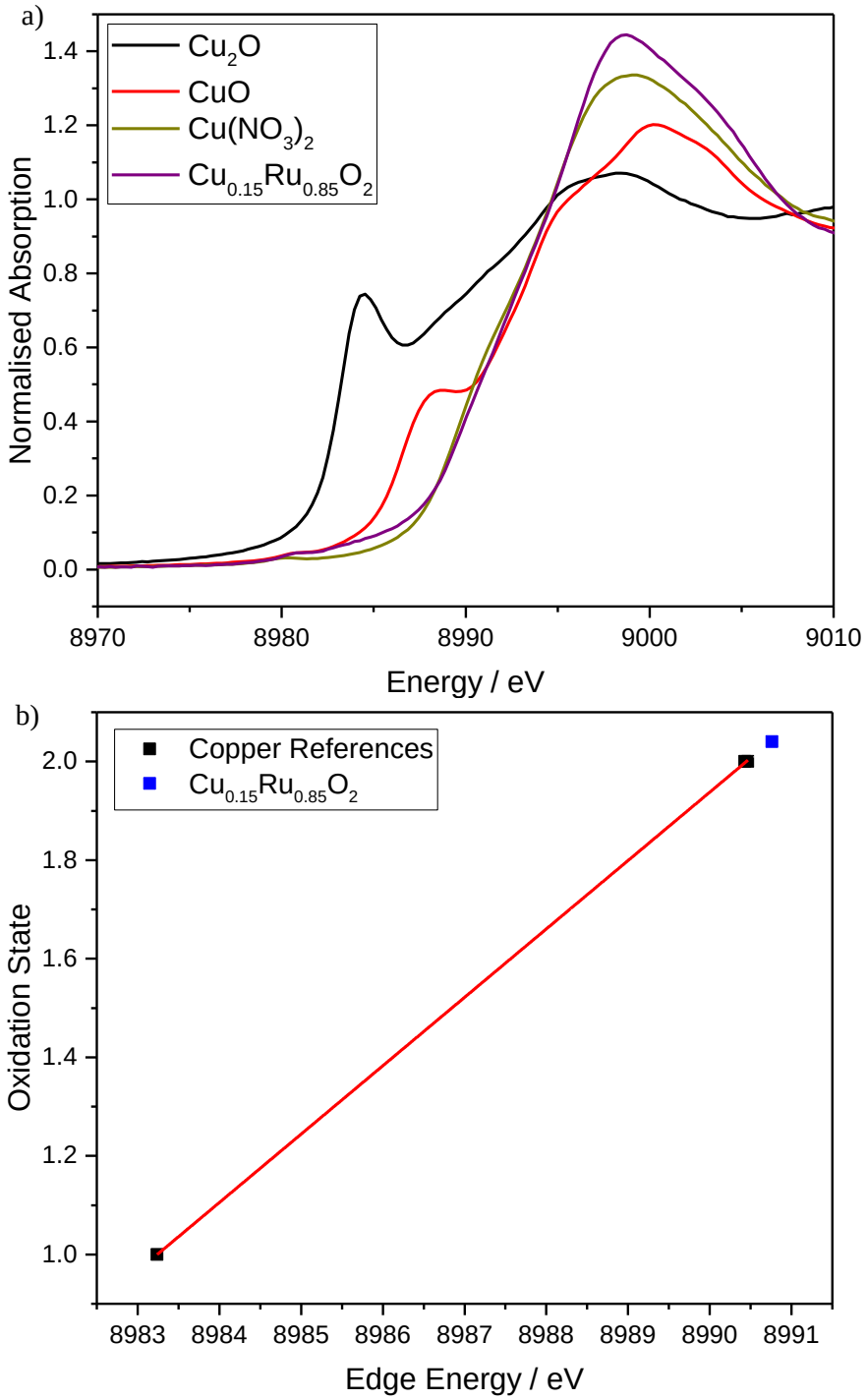

Figure 3.18: a) Copper K-edge XANES spectra of copper substituted rutile and copper reference materials for calibration. b) Edge position against copper oxidation state.

The slight reduction in the ruthenium oxidation state observed in the Ru K-edge XANES for the cobalt substituted ruthenium oxide when compared to the other substituted ruthenium oxide materials suggests the presence of trivalent metal substituent rather than a divalent one. This is entirely possible cobalt has two common oxidation states, Co^{2+} and Co^{3+}. The

Co K-edge XANES spectra reveal cobalt to be in the +3 state, Figure 3.19. This supports the conclusion drawn from the ruthenium K-edge data.

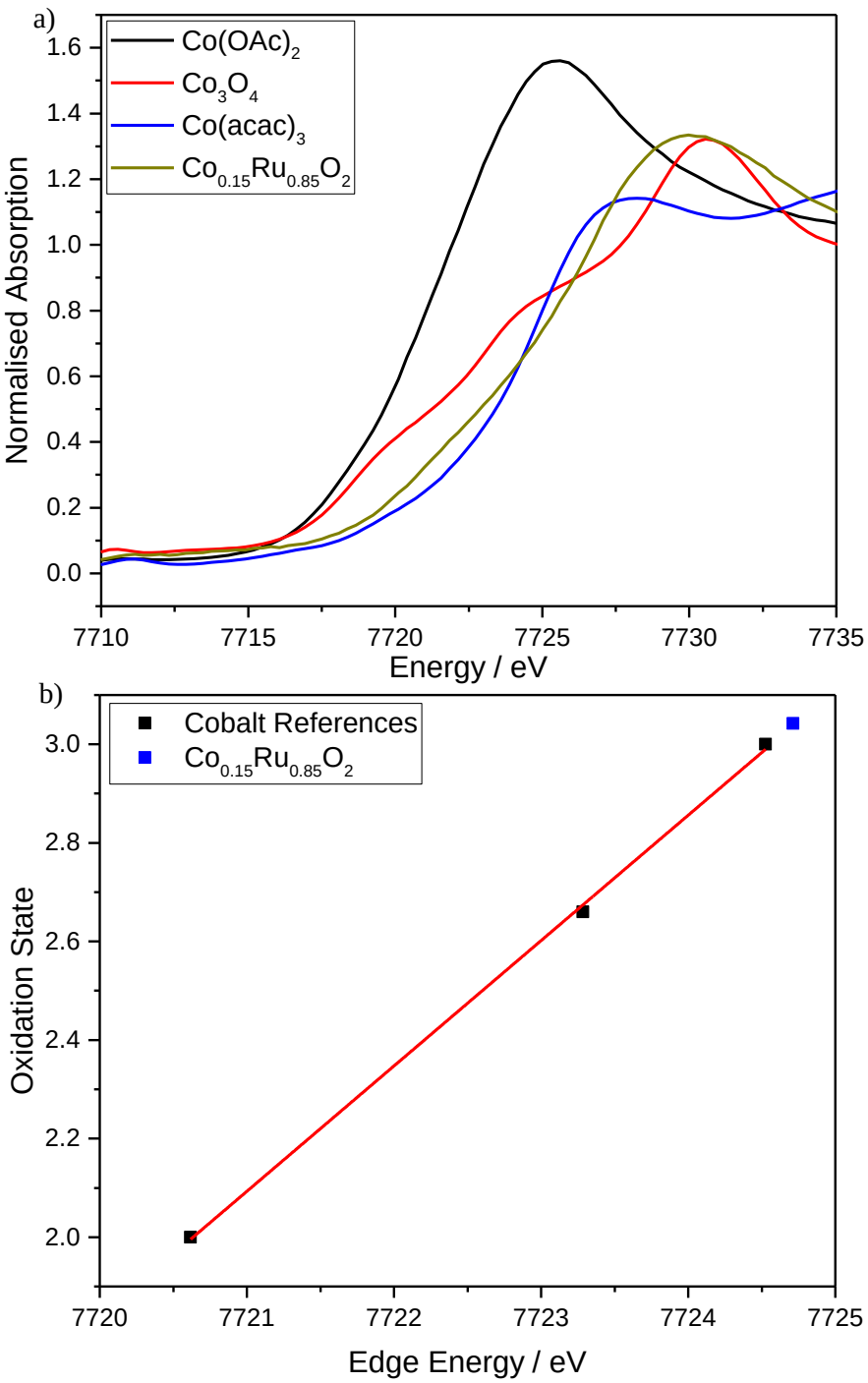

Figure 3.19: a) Cobalt K-edge XANES spectra of cobalt substituted rutile and cobalt reference materials for calibration. b) Edge position against cobalt oxidation state.

3.8 Powder Neutron Diffraction

Powder neutron diffraction data were collected on GEM (ISIS, UK) and proved vital for the proper characterisation of this set of materials, as there was a possibility for some oxygen

disorder, most likely in the form of vacancies due to the inclusion of the divalent cations. This can be better elucidated via neutrons rather than by X-rays, as the neutron scattering length is not dependant on atomic number like in X-ray diffraction, allowing the oxygen positions to be better defined. Figure 3.20 shows the fits to the data collect on bank 3 of GEM, and Table 3.5 shows the atomic parameters extracted from the Rietveld refinement against the data. All the synthesised materials could be indexed to a tetragonal rutile phases, adopting the space group $P4_2/mnm$, the lattice parameters extracted are consistent with those extracted from PXRD data. There is now strong agreement between the peak intensities in the calculated and observed patterns, since now the effects of preferred orientation have been eliminated .

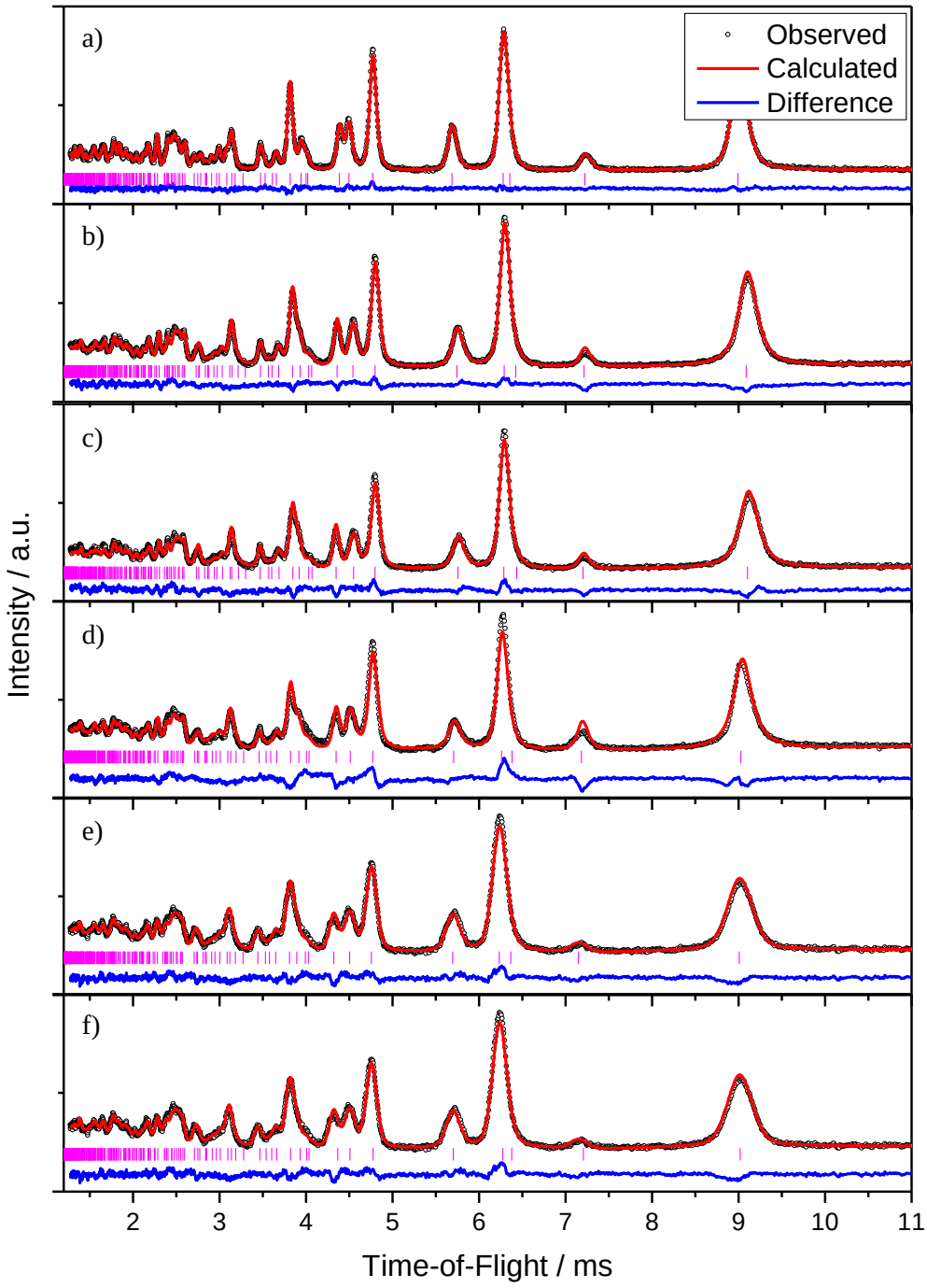

Figure 3.20: Rietveld refinements of powder neutron diffraction data from bank 3 of GEM for, a) RuO_2, b) $Zn_{0.15}Ru_{0.85}O_2$, c) $Mg_{0.15}Ru_{0.85}O_2$, d) $Ni_{0.15}Ru_{0.85}O_2$, e) $Cu_{0.15}Ru_{0.85}O_2$ and f) $Co_{0.15}Ru_{0.85}O_2$.

Table 3.5: Structural details of rutiles obtained from Rietveld fits to neutron powder diffraction data, for RuO_2 and $M_{0.15}Ru_{0.85}O_2$ materials using space group $P4_2/mnm$.

Atom	Site	*x*	*y*	*Z*	Occ	U_{iso} / Å^2
RuO_2: *a* = 4.49280(4) Å / c = 3.10337(4) Å						
Ru	2*a*	0	0	0	0.999(1)	0.0107(8)
O	4*f*	0.30490(12)	0.30490(12)	0	1.002(2)	0.0505(9)
$Zn_{0.15}Ru_{0.85}O_2$: *a* = 4.5461(2) Å / c = 3.0848(2) Å						
Zn	2*a*	0	0	0	0.187(11)	0.00137(11)
Ru	2*a*	0	0	0	0.813(11)	0.00137(11)
O	4*f*	0.3031(2)	0.3031(2)	0	1.002(2)	0.00481(10)
$Mg_{0.15}Ru_{0.85}O_2$: *a* = 4.54168(19) Å / c = 3.08022(18)Å						
Mg	2*a*	0	0	0	0.171(11)	0.00348(17)
Ru	2*a*	0	0	0	0.829(11)	0.00348(17)
O	4*f*	0.30299(19)	0.30299(19)	0	1.004(2)	0.00320(11)
$Ni_{0.15}Ru_{0.85}O_2$: *a* = 4.52541(14) Å / c = 3.08247(13) Å						
Ni	2*a*	0	0	0	0.141(6)	0.00161(15)
Ru	2*a*	0	0	0	0.859(6)	0.00161(15)
O	4*f*	0.3031(3)	0.3031(3)	0	1.000(2)	0.00535(19)
$Co_{0.15}Ru_{0.85}O_2$: *a* = 4.5057(3) Å / c = 3.0565(3) Å						
Co	2*a*	0	0	0	0.153(2)	0.00191(15)
Ru	2*a*	0	0	0	0.847(2)	0.00191(15)
O	4*f*	0.30251(17)	0.30251(17)	0	1.000(2)	0.00270(10)
$Cu_{0.15}Ru_{0.85}O_2$: *a* = 4.5132(2) Å / c = 3.0901(2) Å						
Cu	2*a*	0	0	0	0.173(2)	0.00965(19)
Ru	2*a*	0	0	0	0.827(2)	0.00965(19)
O	4*f*	0.30247(16)	0.30247(16)	0	1.000(2)	0.00404(11)

The refined compositions of all the materials agree with the EDXA, and the resulting models charge balance in the way the XANES data predicts. The oxygen *x*/*y* parameter is also reduced for all substituted materials when compared with ruthenium oxide. If the composition of the new materials written as $M_{0.15}{}^{2+}Ru_{0.55}{}^{4+}Ru_{0.30}{}^{5+}O_2$, then the analogy with the mixed-metal material of Abrahams et al. can be seen, namely $Li_{0.15}Ti_{0.4}Nb_{0.45}O_2$, $Zn_{0.15}Ti_{0.55}Nb_{0.3}O_2$ and $Al_{0.2}Ti_{0.6}Nb_{0.2}O_2$. And in these materials the x/y parameter is lowered in the same way, when compared with TiO_2.[22,23] The thermal parameter for the metals in the copper substituted material is higher than in the other materials, suggesting some distortion of the metal sites, and this is likely to be the result of a Jahn-Teller distortion around the Cu^{2+}

centres. The thermal parameters in the remaining materials are all much smaller and suggest there is little distortion from the ideal rutile structure.

3.9 Pair Distribution Function Analysis

By analysing both the Rietveld and PDFs the aim was to produce a much more complete picture of how the long range order suggested by powder XRD is compatible with the local order preferred by some of the substituents: for example, the Jahn-Teller distortion expected for Cu^{2+} and the possibility of Zn^{2+} being displaced from its octahedral location to give lower coordination number, as what is observed in both polymorphs of ZnO.

The PDF for ruthenium oxide and the substituted materials were then fitted using the model from the Bragg scattering, with refinement of the lattice parameters, ADPs and oxygen *x* coordinates, Figure 3.21 and Table 3.6. For all the studied materials there is strong agreement between the structural parameters extracted from the Bragg scattering and the PDF. All the fits are good, even at low *r*, Figure 3.22, where the distortions described above should be visible. Despite fitting well, the copper in the copper substituted material still has a very large thermal parameter, and the oxygen x parameter is significantly different from what is observed in the Bragg scattering. Thus it is entirely possible that the copper oxygen octahedra are Jahn-Teller distorted, however the substitution level of copper is so low the splitting is been overwhelmed by the signal from the Ru - O bond at 1.96 Å.

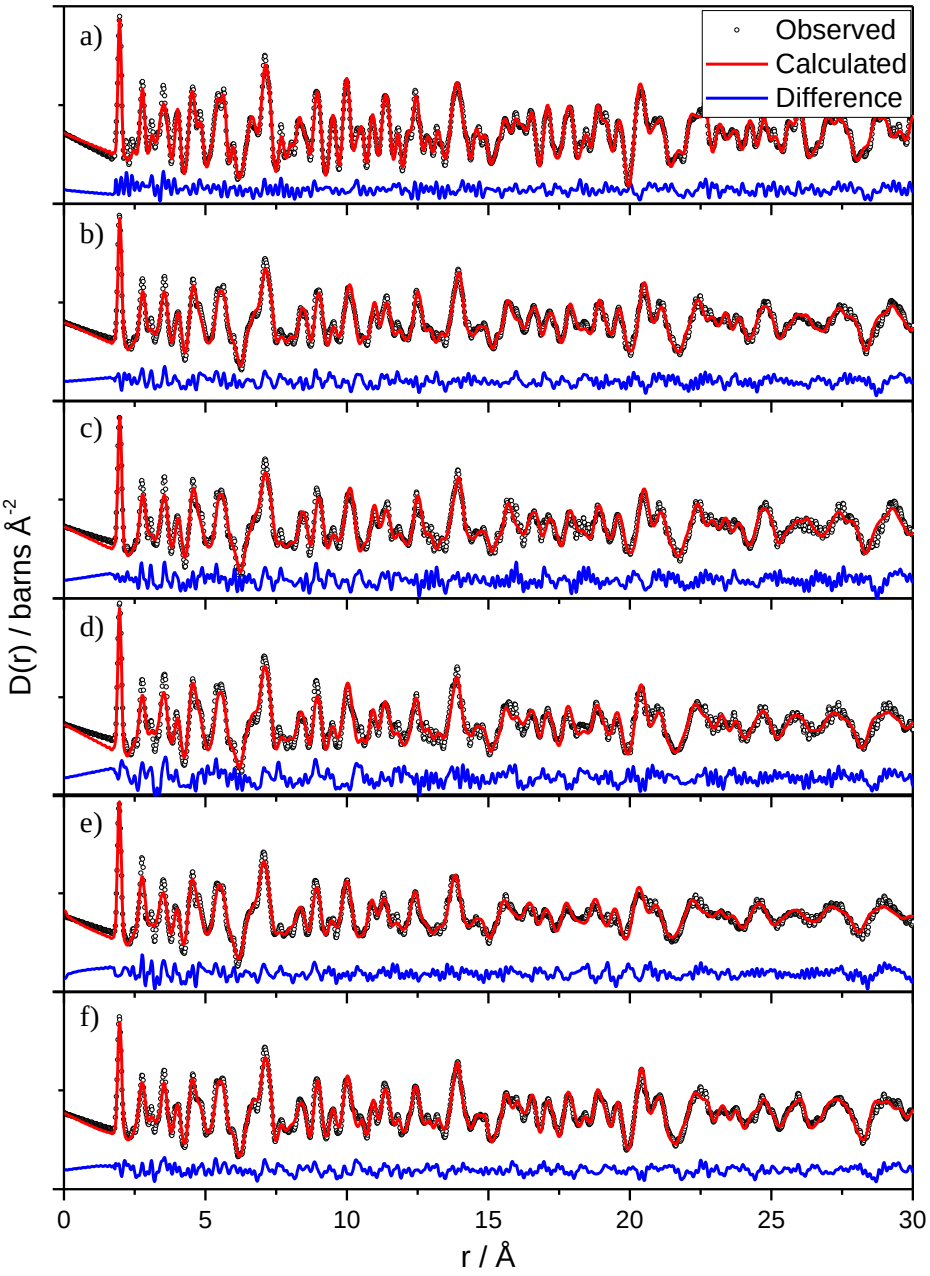

Figure 3.21: Fits to pair distribution function using the model extracted from Rietveld refinement of neutron diffraction data for, a) RuO_2, b) $Zn_{0.15}Ru_{0.85}O_2$, c) $Mg_{0.15}Ru_{0.85}O_2$, d) $Ni_{0.15}Ru_{0.85}O_2$, e) $Co_{0.15}Ru_{0.85}O_2$ and f) $Cu_{0.15}Ru_{0.85}O_2$.

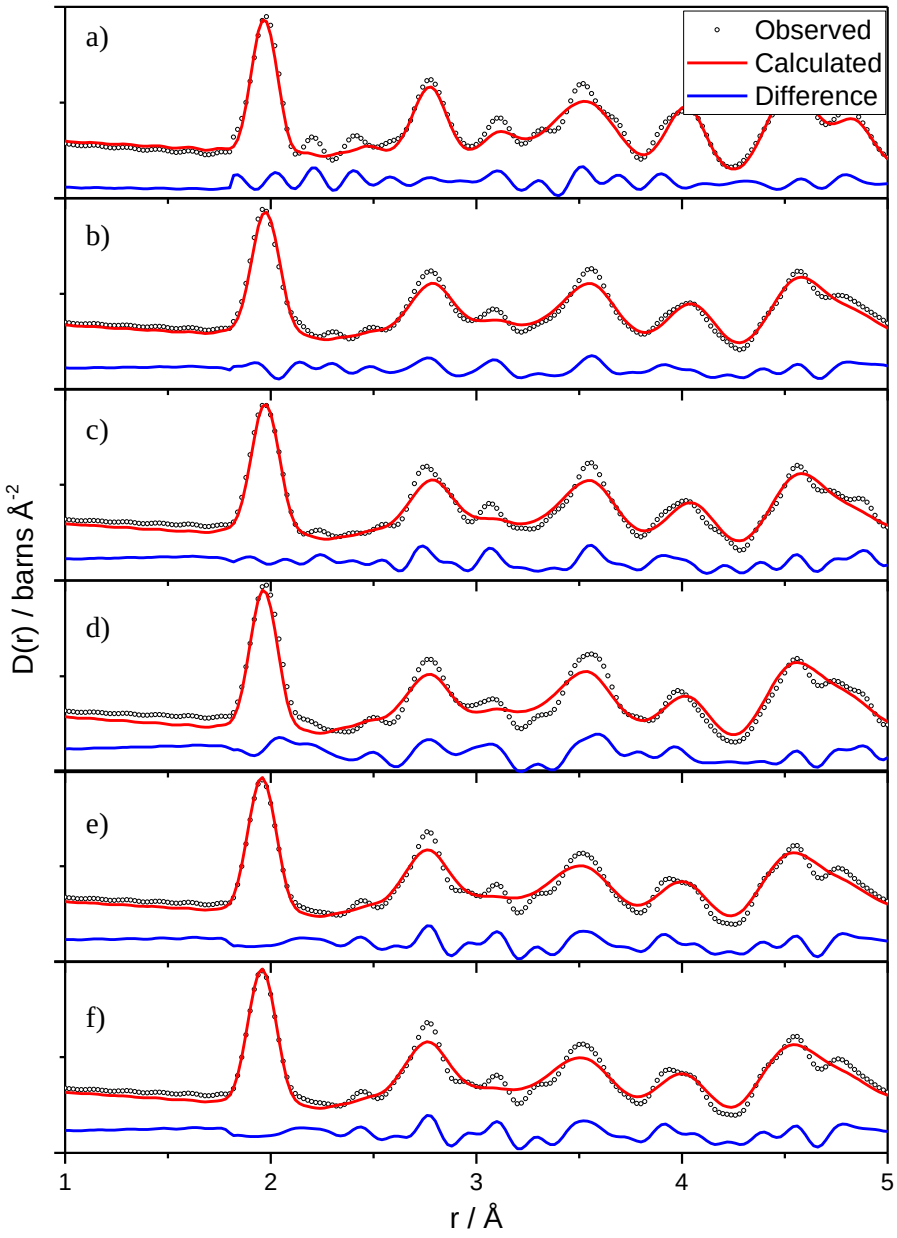

Figure 3.22: Low *r* region of fits to pair distribution function using the model extracted from Rietveld refinement of neutron diffraction data for, a) RuO_2, b) $Zn_{0.15}Ru_{0.85}O_2$, c) $Mg_{0.15}Ru_{0.85}O_2$, d) $Ni_{0.15}Ru_{0.85}O_2$, e) $Co_{0.15}Ru_{0.85}O_2$ and f) $Cu_{0.15}Ru_{0.85}O_2$.

Table 3.6: Structural details of rutiles from least squares fitting of PDF data, for RuO_2 and $M_{0.15}Ru_{0.85}O_2$ materials using space group $P4_2/mnm$.

Atom	Site	*x*	*y*	*Z*	Occ	U_{iso} / Å^2
RuO_2: *a* = 4.495(4) Å / c = 3.104(5) Å						
Ru	2*a*	0	0	0	1.000	0.0042(15)
O	4*f*	0.30(5)	0.30(5)	0	1.000	0.0054(16)
$Zn_{0.15}Ru_{0.85}O_2$: *a* = 4.539(4) Å / c = 3.087(5) Å						
Zn	2*a*	0	0	0	0.150	0.039(9)
Ru	2*a*	0	0	0	0.850	0.0053(17)
O	4*f*	0.30(6)	0.30(6)	0	1.000	0.010(3)
$Mg_{0.15}Ru_{0.85}O_2$: *a* = 4.539(4) Å / c = 3.087(5) Å						
Mg	2*a*	0	0	0	0.150	0.03(7)
Ru	2*a*	0	0	0	0.850	0.0051(19)
O	4*f*	0.295(12)	0.295(12)	0	1.000	0.009(2)
$Ni_{0.15}Ru_{0.85}O_2$: *a* = 4.510(4) Å / c = 3.081(4) Å						
Ni	2*a*	0	0	0	0.150	0.02(3)
Ru	2*a*	0	0	0	0.850	0.0055(16)
O	4*f*	0.30(2)	0.30(2)	0	1.000	0.010(2)
$Co_{0.15}Ru_{0.85}O_2$: *a* = 4.501(4) Å / c = 3.091(5) Å						
Co	2*a*	0	0	0	0.150	0.02(7)
Ru	2*a*	0	0	0	0.850	0.0029(8)
O	4*f*	0.30(4)	0.30(4)	0	1.000	0.0088(16)
$Cu_{0.15}Ru_{0.85}O_2$: *a* = 4.509(4) Å / c = 3.092(4) Å						
Cu	2*a*	0	0	0	0.150	0.51(9)
Ru	2*a*	0	0	0	0.850	0.0044(12)
O	4*f*	0.31(3)	0.31(3)	0	1.000	0.010(2)

3.10 Thermal Stability

Figure 3.23 shows thermodiffraction that highlights the thermal stability of RuO_2. With the *in situ* heating under flowing nitrogen show showing that up to 900 °C only a rutile phase is observed. However the material does display an increase in crystallinity with increasing temperature, illustrated increasing sharpness of the Bragg peaks.

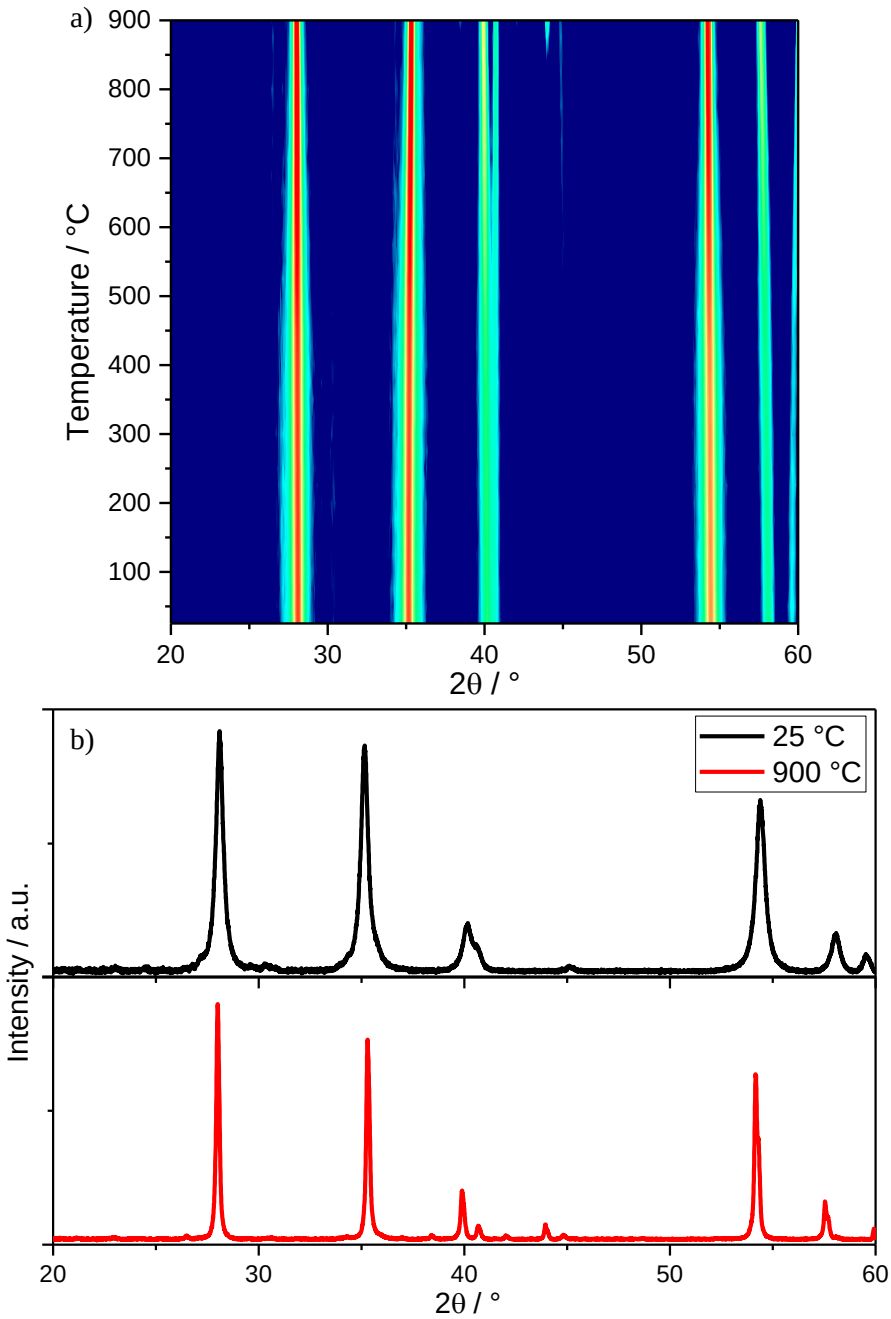

Figure 3.23: a) Thermodiffractometry (λ = 1.5418 Å) of RuO_2, under flowing N_2. b) Powder patterns obtained at 25 and 900 °C.

The zinc substituted material decomposes at 800 °C, phase separating, producing zinc oxide and ruthenium oxide, Figure 3.24. When the zinc oxide peaks appear there is an clear shift in the lattice parameter of the rutile phase, indicating the conversion of the zinc substituted phase to ruthenium oxide.

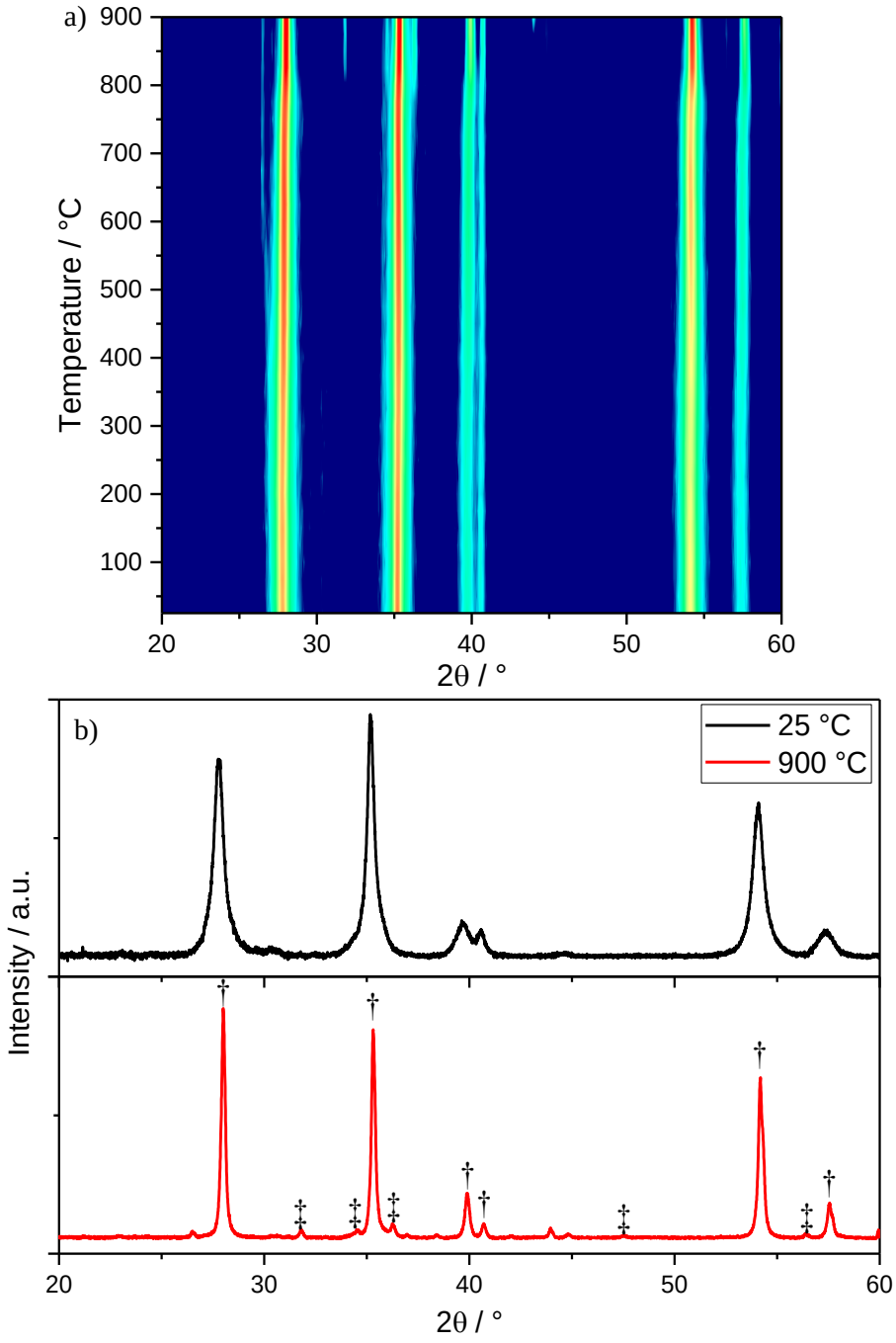

Figure 3.24: a) Thermodiffractometry (λ = 1.5418 Å) of $Zn_{0.15}Ru_{0.85}O_2$, under flowing N_2. b) Diffraction patterns acquired at 25 and 900 °C with RuO_2 marked with † and ZnO marked with ‡.

Figure 3.25 shows the thermogravimetric analysis data of the zinc substituted ruthenium oxide. From room temperature to 230 °C there is a mass loss of 1.8 %, which is attributed to the loss of surface water. Between 300 and 500 °C there is a further loss of 1.8 %, this is attributable to the phase separation of the zinc substituted material to zinc oxide and ruthenium oxide, with the reduction of $Ru^{4.3+}$ to Ru^{4+}, which agrees with the predicted loss of

1.9 %. At this stage no further loss is expected, unless ruthenium oxide is reducing to the metal. If all the ruthenium were to be reduced only 75.4 % of the initial mass would remain, thus if this is what is happening then it must be a partial reduction.

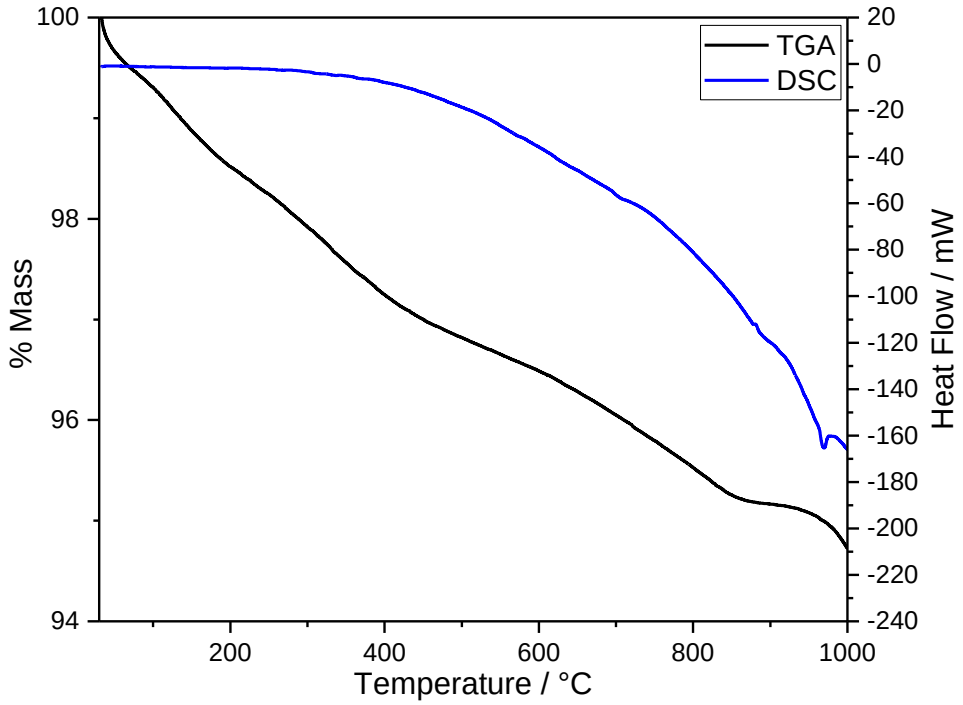

Figure 3.25: Thermogravimetric analysis of zinc substituted ruthenium oxide.

The magnesium substituted material decomposes between 800 and 850 °C, phase separating, producing magnesium oxide and ruthenium oxide, Figure 3.26. When the magnesium oxide peaks appear there is an clear shift in the lattice parameter of the rutile phase, indicating the conversion of the magnesium substituted phase to ruthenium oxide.

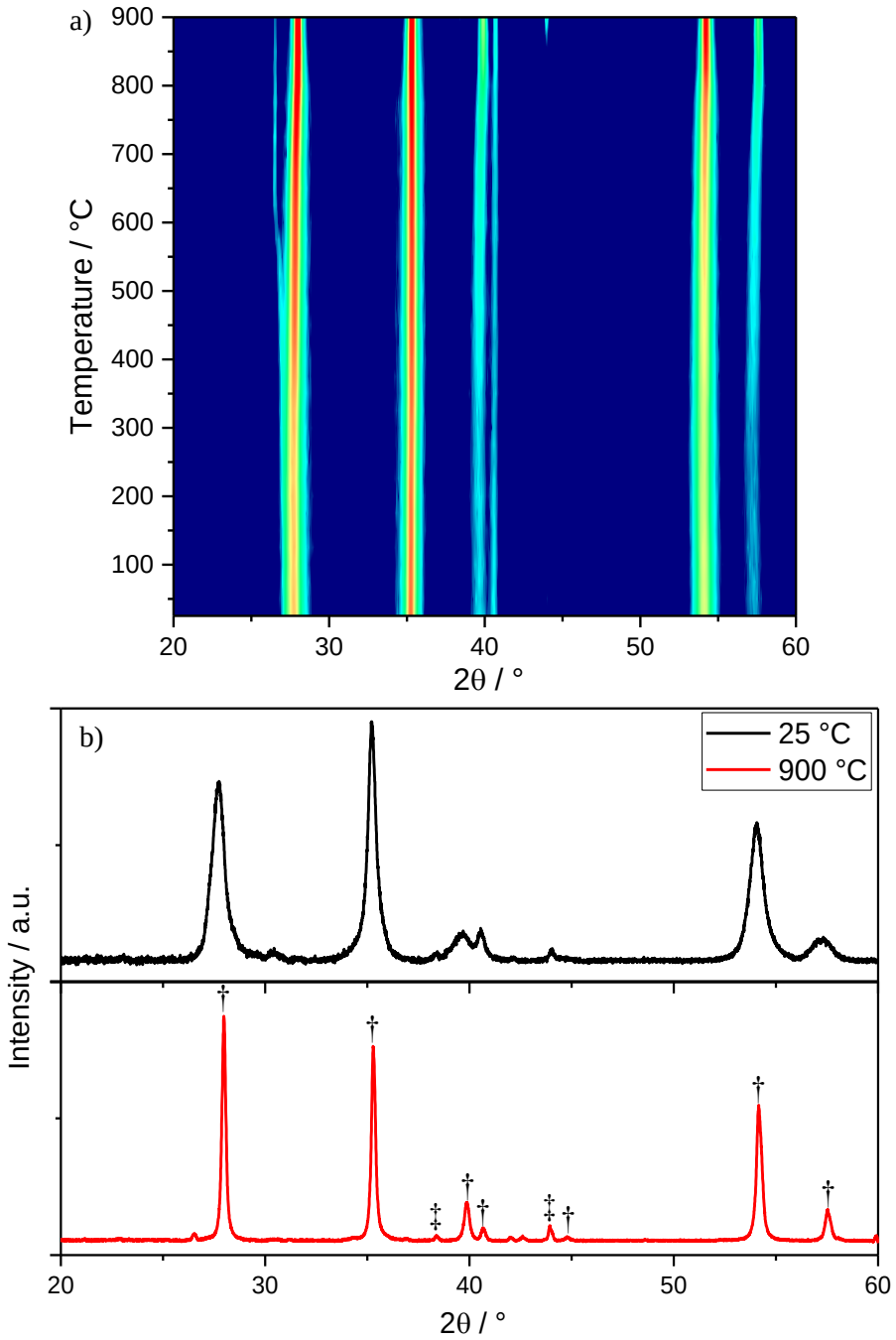

Figure 3.26: a) Thermodiffractometry (λ = 1.5418 Å) of $Mg_{0.15}Ru_{0.85}O_2$, under flowing N_2. b) Diffraction patterns acquired at 25 and 900 °C with RuO_2 marked with † and MgO marked with ‡.

Figure 3.27 shows the thermogravimetric analysis data of the magnesium substituted ruthenium oxide. From room temperature to 240 °C there is a mass loss of 1.5 %, which is attributed to the loss of surface water. Between 300 and 600 °C there is a further loss of 1.8 %, this is attributable to the phase separation of the magnesium substituted material to magnesium oxide and ruthenium oxide, with reduction of ruthenium, which agrees with the

predicted loss of 2.0 %. Further losses are likely caused by partial reduction of ruthenium oxide to ruthenium metal.

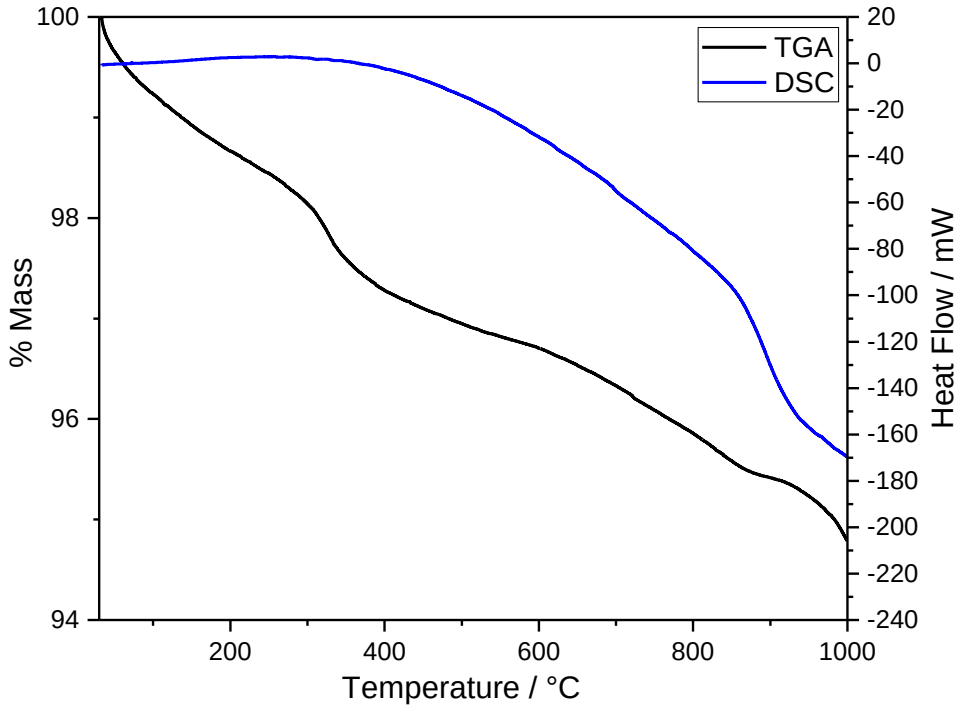

Figure 3.27: Thermogravimetric analysis of magnesium substituted ruthenium oxide.

The nickel substituted material decomposes at 650 °C, phase separating, producing nickel oxide and ruthenium oxide, Figure 3.28. When the nickel oxide peaks appear there is an slight shift in the lattice parameter of the rutile phase, indicating the conversion of the nickel substituted phase to ruthenium oxide.

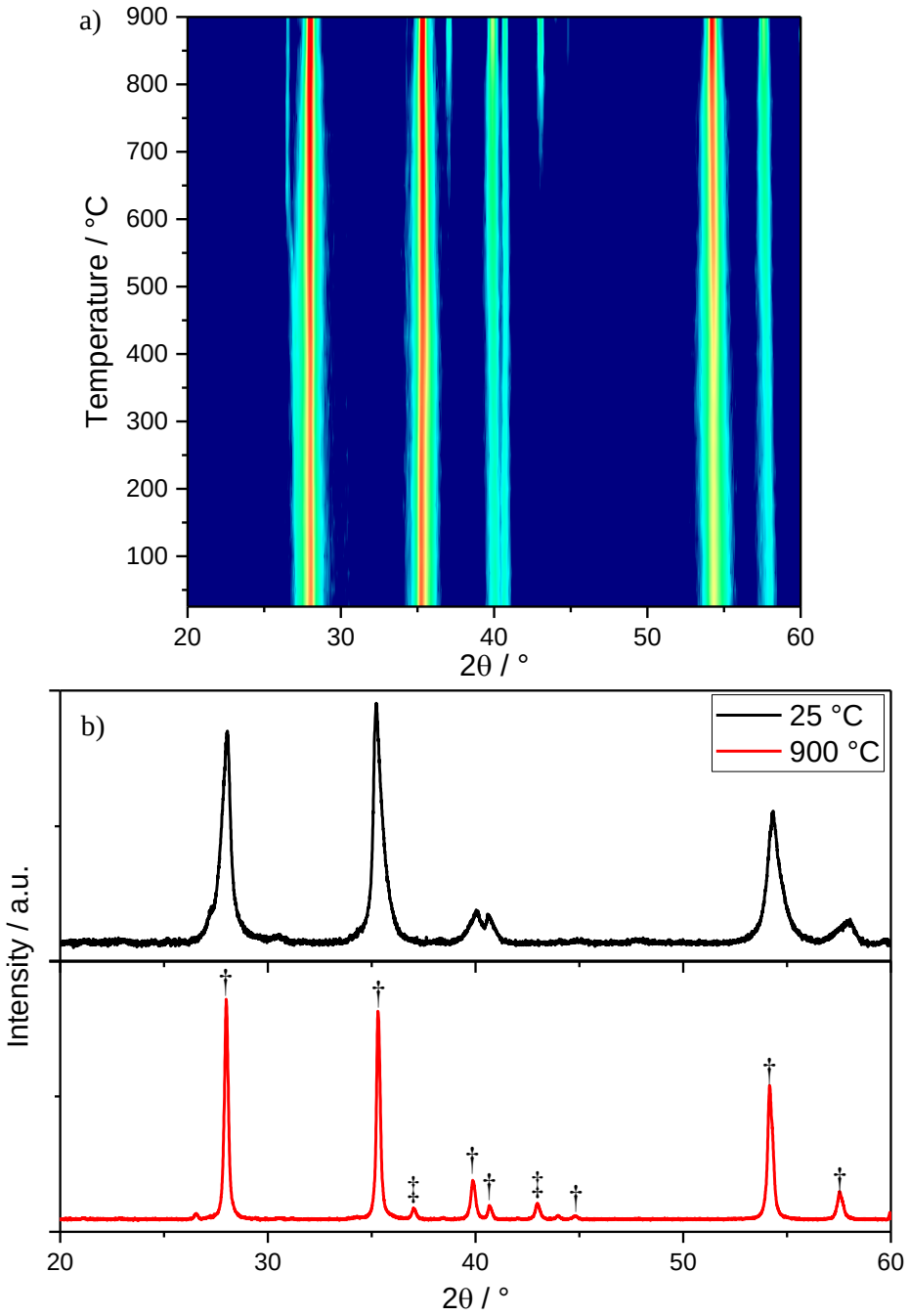

Figure 3.28: a) Thermodiffractometry (λ = 1.5418 Å) of $Ni_{0.15}Ru_{0.85}O_2$, under flowing N_2. b) Diffraction patterns acquired at 25 and 900 °C with RuO_2 marked with † and NiO marked with ‡.

Figure 3.29 shows the thermogravimetric analysis data of the nickel substituted ruthenium oxide. From room temperature to 230 °C there is a mass loss of 1.2 %, which is attributed to the loss of surface water. Between 250 and 500 °C there is a further loss of 2.4 %, this is attributable to the phase separation of the nickel substituted material to nickel oxide and ruthenium oxide, with reduction of ruthenium, which agrees well with the predicted loss of

2.1 %. Further losses are likely caused by partial reduction of ruthenium oxide to ruthenium metal.

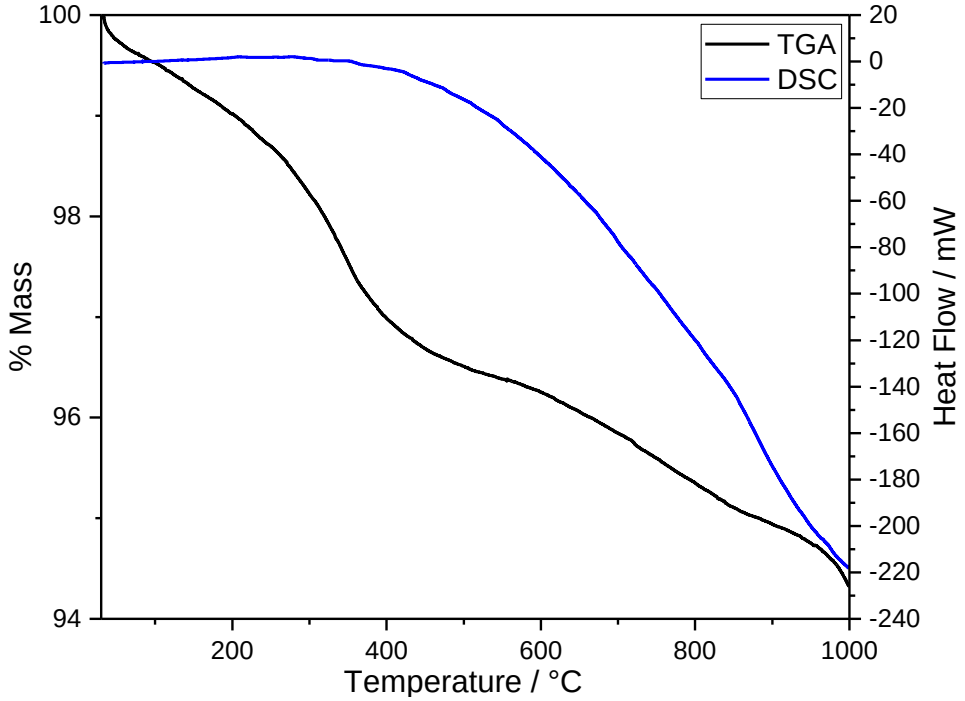

Figure 3.29: Thermogravimetric analysis of nickel substituted ruthenium oxide.

The cobalt substituted material decomposes at 700 °C, phase separating, forming cobalt oxide and ruthenium oxide, Figure 3.30. When the cobalt oxide peaks appear there is an slight shift in the lattice parameter of the rutile phase, indicating the conversion of the cobalt substituted phase to ruthenium oxide.

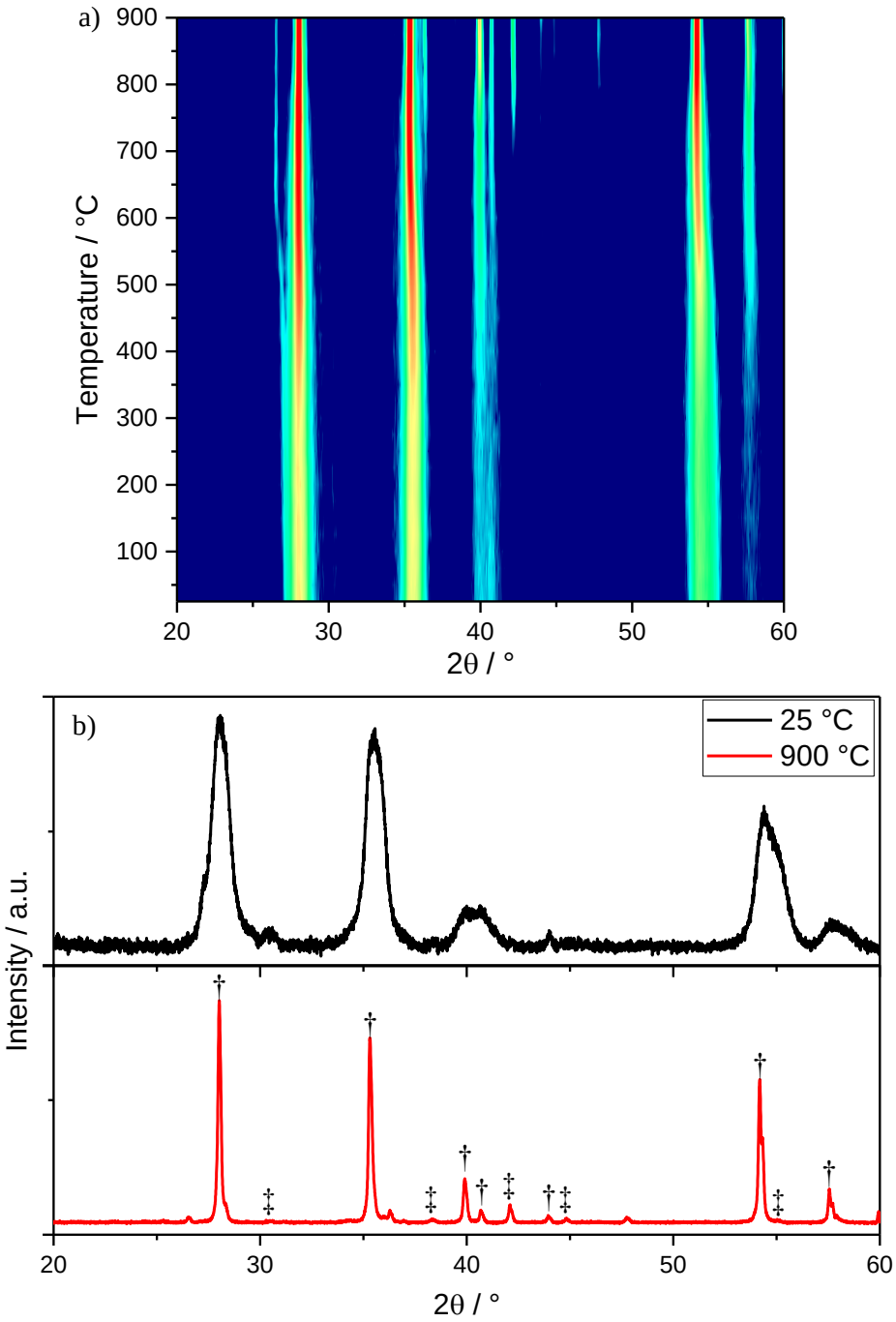

Figure 3.30: a) Thermodiffractometry (λ = 1.5418 Å) of $Co_{0.15}Ru_{0.85}O_2$, under flowing N_2. b) Diffraction patterns acquired at 25 and 900 °C with RuO_2 marked with † and Co_3O_4 marked with ‡.

Figure 3.31 shows the thermogravimetric analysis data of the cobalt substituted ruthenium oxide. From room temperature to 250 °C there is a mass loss of 1.8 %, which is attributed to the loss of surface water. Between 250 and 450 °C there is a further loss of 1.4 %, this is attributable to the phase separation of the cobalt substituted material to cobalt oxide and ruthenium oxide, with reduction of ruthenium, which agrees with the theoretical loss of

1.3 %. At this stage there are two further losses could occur: the conversion of cobalt (II,III) oxide to cobalt (II) oxide, and the reduction of ruthenium oxide to the metal. The reduction of the cobalt oxide would give an additional 0.6 % mass loss, as such this can not account for the total of the remaining loss. Further losses are likely caused by partial reduction of ruthenium oxide to ruthenium metal.

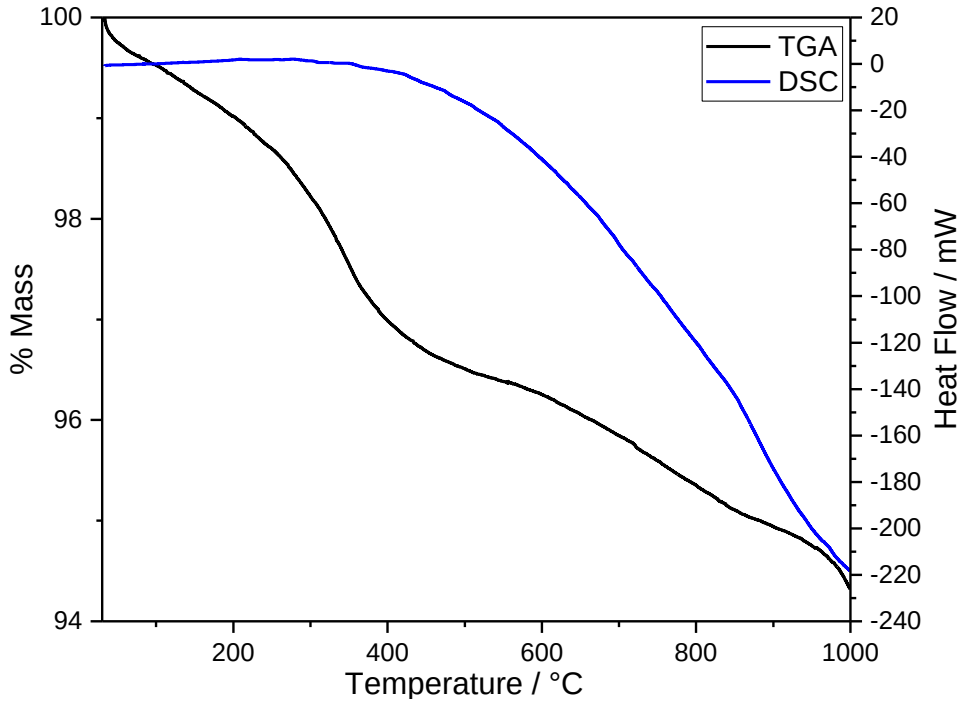

Figure 3.31: Thermogravimetric analysis of cobalt substituted ruthenium oxide.

The copper substituted material decomposes at 650 °C, phase separating, copper nickel oxide and ruthenium oxide, Figure 3.32. When the copper oxide peaks appear there is an slight shift in the lattice parameter of the rutile phase, indicating the conversion of the copper substituted phase to ruthenium oxide.

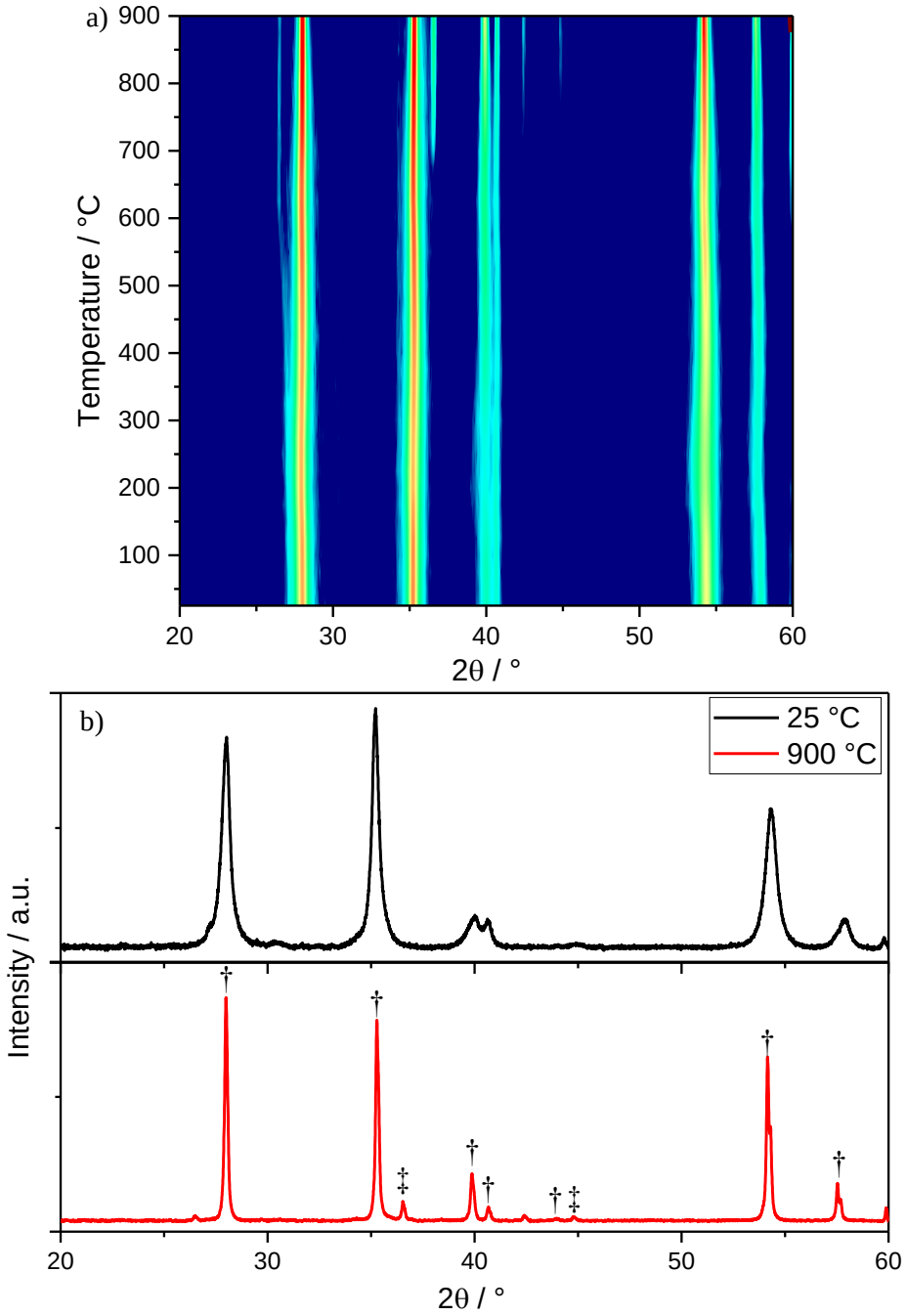

Figure 3.32: a) Thermodiffractometry (λ = 1.5418 Å) of $Cu_{0.15}Ru_{0.85}O_2$, under flowing N_2. b) Diffraction pattern acquired at 900 °C with RuO_2 marked with † and CuO marked with ‡.

Figure 3.33 shows the thermogravimetric analysis data of the copper substituted ruthenium oxide. From room temperature to 250 °C there is a mass loss of 1.0 %, which is attributed to the loss of surface water. Between 250 and 530 °C there is a further loss of 1.9 %, this is attributable to the phase separation of the copper substituted material to copper (II) oxide and ruthenium oxide, with reduction of ruthenium, which agrees perfectly with the expected loss of 1.9 %. At this stage there are two further losses that could occur, the conversion of copper

(II) oxide to copper (I) oxide, and the reduction of ruthenium oxide to the metal. The reduction of the copper oxide would give an additional 0.9 % mass loss, so this would account for the observed loss between 500 and 750 °C. Further losses are likely caused by partial reduction of ruthenium oxide to ruthenium metal.

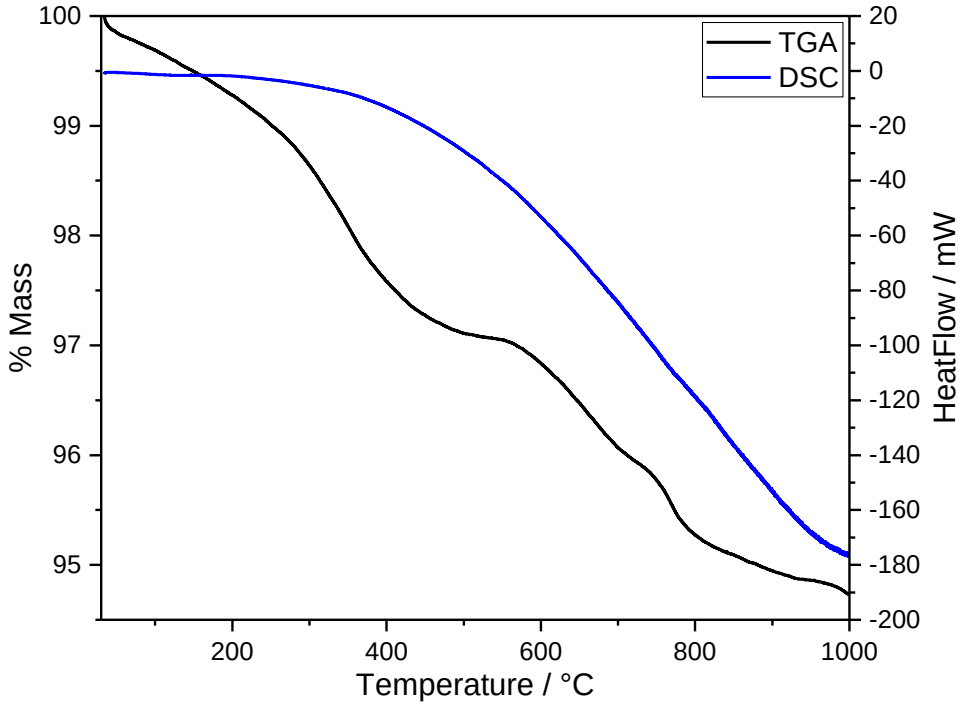

Figure 3.33: Thermogravimetric analysis of copper substituted ruthenium oxide.

3.10 Magnetic Susceptibility Studies

Ruthenium dioxide is a Pauli paramagnet,[29] and all the substituted materials behave in the same fashion. In the ZFC data of the zinc and magnesium materials there is a small feature around 75 K; this can be attributed to the response from condensed oxygen. The apparent transition at 25 K for the cobalt substituted material can be attributed to a small Co_3O_4 impurity.[30] Substituting Zn and Mg into RuO_2 has little effect on the susceptibility per mol Ru; this is unsurprising as all there are no valence electron associated with by Zn and Mg so no extra contribution to the measured moment should be detected. However, given a small portion of Ru^{4+} is replaced by Ru^{5+}, a small decrease in susceptibility might be expected, as some of the ruthenium valence electrons are being removed from the system. Ni^{2+}, Co^{3+} and Cu^{2+} can have both unpaired electrons; as such the increases in susceptibility for these

materials is expected. Due to the very weak response to the applied field fitting to a Curie-Weiss function gave unreasonable values for Weiss temperature. Paramagnetic materials such as RuO_2 should have a Weiss temperature of 0 K, however in this study the Weiss temperature ranged from -70 to -3200 K.

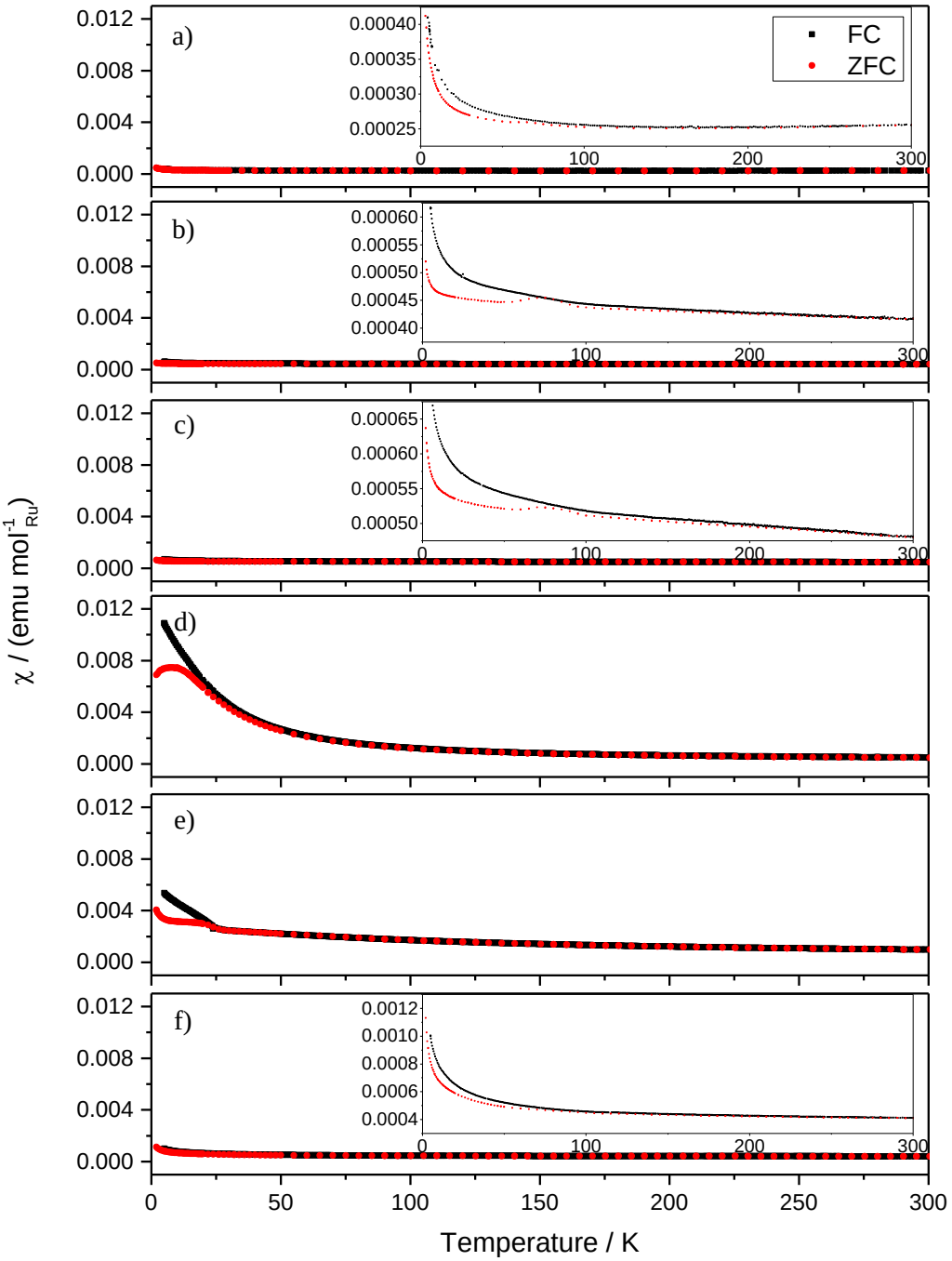

Figure 3.34: FC and ZFC magnetic susceptibility studies as a function of temperature for, a) RuO_2, b) $Zn_{0.15}Ru_{0.85}O_2$, c) $Mg_{0.15}Ru_{0.85}O_2$, d) $Ni_{0.15}Ru_{0.85}O_2$, e) $Co_{0.15}Ru_{0.85}O_2$ and f) $Cu_{0.15}Ru_{0.85}O_2$.

3.10 Summary

In this chapter a number of metal peroxides have been synthesised and subsequently used as reagents for the production of substituted ruthenium oxides. Using these oxidising precursors it has been demonstrated that ruthenium can be substituted with a metal of lower valence to give materials formulated as $M_{0.15}Ru_{0.85}O_2$. It has been proven that in order to accommodate metals of lower valence the ruthenium is oxidised above +4, and the degree to which it is oxidised is dependent on the oxidation state of the substituent metal. Neutron diffraction proves that there are no bulk oxide vacancies present in the structure of any of the synthesised materials. Additionally it has been shown, through the use of total neutron scattering, that accommodating these unusual metals into the rutile structure does not affect the local structure to any significant degree. The materials synthesised in this study appear to have the substituents randomly distributed throughout the rutile structure, unlike in the substituted ruthenium oxide materials synthesised by Ktril and coworkers.[31–33] This group prepared materials in which magnesium, zinc, nickel, cobalt and iron had been substituted into ruthenium oxide, Table 3.7, the substituents forming localised clusters/layers within the ruthenium oxide structure. There is no evidence of this clustering observed in the materials synthesised as part of this study.

Table 3.7: Comparison of Lattice parameters between Ktril's substituted ruthenium oxides, $M_{0.2}Ru_{0.8}O_2$ and those synthesised here

	Ktril's $M_{0.2}Ru_{0.8}O_2$		$M_{0.15}Ru_{0.85}O_2$	
M	*a* / Å	*c* / Å	*a* / Å	*c* / Å
Mg	4.50	3.10	4.54210(11)	3.08536(11)
Zn	4.49	3.10	4.5342(2)	3.0798(2)
Ni	4.48	3.10	4.5274(2)	3.0836(2)
Co	4.48	3.08	4.5153(2)	3.0887(2)
Cu	N/A	N/A	4.5342(3)	3.0846(3)
Fe	4.48	3.10	N/A	N/A

Recently β-Ag_3RuO_4 has been synthesised hydrothermally using silver oxide and potassium perruthenate as reagents.[34] This suggests it is likely the substituted rutile materials could be produced using metal oxides as precursors instead of the poorly defined cobalt and copper peroxide materials. It is probable that small particle size oxides would be required as

precursors to produce homogeneously substituted materials, as cobalt and copper oxides are most likely insoluble in water even at reaction temperature, 240 °C.

References

1 Y. Lee, J. Suntivich, K. J. May, E. E. Perry and Y. Shao-Horn, *J. Phys. Chem. Lett.*, 2012, **3**, 399–404.
2 R. Kötz and S. Stucki, *Electrochim. Acta*, 1986, **31**, 1311–1316.
3 R. Tunold, A. T. Marshall, E. Rasten, M. Tsypkin, L.-E. Owe and S. Sunde, *ECS Trans.*, 2010, **25**, 103–117.
4 J. Gaudet, A. C. Tavares, S. Trasatti and D. Guay, *Chem. Mater.*, 2005, **17**, 1570–1579.
5 W. Sugimoto, T. Shibutani, Y. Murakami and Y. Takasu, *Electrochem. Solid-State Lett.*, 2002, **5**, 170–172.
6 J. Málek, A. Watanabe and T. Mitsuhashi, *J. Therm. Anal. Calorim.*, 2000, **60**, 699–705.
7 F. I. Mattos-Costa, P. de Lima-Neto, S. A. S. Machado and L. A. Avaca, *Electrochim. Acta.*, 1998, **44**, 1515–1523.
8 E. N. Balko and C. R. Davidson, *J. Inorg. Nucl. Chem.*, 1980, **42**, 1778–1781.
9 C. I. Hiley, M. R. Lees, J. M. Fisher, D. Thompsett, S. Agrestini, R. I. Smith and R. I. Walton, *Angew. Chemie Int. Ed.*, 2014, **53**, 4423–4427.
10 D. A. Pankratov, T. A. Portachenko and Y. D. Perfil'ev, *Moscow Univ. Chem. Bull.*, 2008, **63**, 292–296.
11 N. G. Vannerberg, *Arkiv Kemi*, 1959, **14**, 99–105.
12 M. Puselj, Z. Ban and J. Morvaj, *Chemi. Inform.*, 1986, **17**.
13 D. Bayot and M. Devillers, *Coord. Chem. Rev.*, 2006, **250**, 2610–2626.
14 M. Sun, W. Hao, C. Wang and T. Wang, *Chem. Phys. Lett.*, 2007, **443**, 342–346.
15 A. A. Rywak, J. M. Burlitch and T. M. Loehr, *Chem. Mater.*, 1995, **7**, 2028–2038.
16 J. Yang, H. Liu, W. N. Martens and R. L. Frost, *J. Phys. Chem. C*, 2010, **114**, 111–119.
17 J.-W. Kim and S.-M. Park, *J. Electrochem. Soc.*, 2003, **150**, 560–566.
18 M. Risch, K. Klingan, J. Heidkamp, D. Ehrenberg, P. Chernev, I. Zaharieva and H. Dau, *Chem. Commun.*, 2011, **47**, 11912–11914.
19 N. Greenwood, *Chemistry of the Elements (2nd ed.).*, New York, Butterworth–Heinemann, 1997.
20 Y. Deng, A. D. Handoko, Y. Du, S. Xi and B. S. Yeo, *ACS Catal.*, 2016, **6**, 2473–2481.
21 C.-E. Boman, *Acta Chem. Scand.*, 1970, **24**, 116–122.
22 A. A. Bolzan, C. Fong, B. J. Kennedy and C. J. Howard, *Acta Crystallogr. Sect. B*, 1997, **53**, 373–380.
23 I. Abrahams, P. G. Bruce, W. I. David and A. R. West, *Chem. Mater.*, 1989, **1**, 237–240.
24 R. D. Shannon, *Acta Crystallogr. Sect. A*, 1976, **32**, 751–767.
25 J. Haines, J. M. Léger, O. Schulte and S. Hull, *Acta Crystallogr. Sect. B*, 1997, **53**, 880–884.
26 Y. S. Huang and F. H. Pollak, *Solid State Commun.*, 1982, **43**, 921–924.
27 S. S. Rosenblum, W. H. Weber and B. L. Chamberland, *Phys. Rev. B*, 1997, **56**, 529.
28 A. S. Moskvin, A. A. Gippius, A. V Tkachev, A. V Mahajan, T. Chakrabarty, I. A. Presniakov, A. V Sobolev and G. Demazeau, *Phys. Rev. B*, 2012, **86**, 241107.
29 Y. Kimishima, M. Matsuo, K. Homma, M. Uehara and K. Irie, *J. Magn. Soc. Japan*, 2007, **31**, 149–152.
30 P. Dutta, M. S. Seehra, S. Thota and J. Kumar, *J. Phys. Condens. Matter*, 2008, **20**, 15218.
31 V. Petrykin, K. Macounova, O. A. Shlyakhtin and P. Krtil, *Angew. Chemie*, 2010,

122, 4923–4925.
32 D. F. Abbott, V. Petrykin, M. Okube, Z. Bastl, S. Mukerjee and P. Krtil, *J. Electrochem. Soc.*, 2015, **162**, 23–31.
33 D. F. Abbott, S. Mukerjee, V. Petrykin, Z. Bastl, N. B. Halck, J. Rossmeisl and P. Krtil, *RSC Adv.*, 2015, **5**, 1235–1243.
34 B. E. Prasad, P. Kazin, A. C. Komarek, C. Felser and M. Jansen, *Angew. Chemie Int. Ed.*, 2016, **55**, 4467–4471.

Chapter 4 – Iridate Pyrochlores

4.1 Introduction and Scope of Chapter

In this chapter an investigation into the synthesis and subsequent characterisation of iridium oxide pyrochlores is reported. The chapter is then divided into two major sections, B-site substitution and A-site substitution. This work starts from the synthesis of the solid solution $(Ce_{0.67},Na_{0.33})_2(Ir_{1-x},Ru_x)_2O_7$,[1] as it had previously been shown to be an excellent electrocatalyst for the OER, in PEMFCs. This chapter begins with the synthesis of another iridate pyrochlore $(Ca,Na)_{2-x}Ir_2O_6{\cdot}H_2O$, which was reported in the group previously[2] and contains no cerium, whose own redox chemistry may complicate the electrochemistry. Work on the optimisation of other acid-resilient OER catalysts (rutile type, IrO_2 and RuO_2) showed that in some cases incorporating another metal into the material either atomically or physically improved their performance,[3] so B-site substitution was a starting point for attempting to investigate optimising the properties of $(Ca,Na)_{2-x}Ir_2O_6{\cdot}H_2O$. Since it was shown that the A-site metals in these types of oxides were leachable under operational conditions, substituting the A-site metals was a second strategy for catalytic optimisation. Chapter 6 will describe the electrocatalysis results from these materials.

4.2 Materials Synthesis

To prepare $(Ca,Na)_{2-x}Ir_2O_6{\cdot}H_2O$, $Ca(NO_3)_2{\cdot}4H_2O$, $IrCl_3.5H_2O$ and Na_2O_2 in a 1:1:4 molar ratio based on 0.6 mmol of Ir, were added to 10 ml of 10 M NaOH solution. The reaction was carried out in a hydrothermal bomb at 240 °C for a period of 96 hours. Difficulties were encountered when scaling up this synthesis to prepare larger amounts of solid, using 1.4 mmol of Ir. It was assumed the increase in nitrate anion concentration interfered with the crystallisation of the pyrochlore phase instead yielding rutile IrO_2, thus $Ca(NO_3)_2{\cdot}4H_2O$ was replaced with CaO_2, which was found to be more reliable. It was subsequently observed that increasing the CaO_2 : $IrCl_3$ ratio in favour of the calcium improved the reliability of the

synthesis. This increased the amount of $Ca(OH)_2$ by product, which was removed by washing with 3 M HNO_3.

Attempts were made to control the particle size of $(Ca,Na)_{2-x}Ir_2O_6{\cdot}H_2O$. Previous work on $Bi_2Ir_2O_7$ showed that changing the pH of the reaction influenced the particle size of the synthesised material.[2] This proved somewhat ineffective for $(Ca,Na)_{2-x}Ir_2O_6{\cdot}H_2O$, so changing the reaction temperature was explored. It was found that $(Ca,Na)_{2-x}Ir_2O_6{\cdot}H_2O$ with a variety of particle sizes could be synthesised, when the reaction temperature was varied between 170-240 °C, with lower temperatures producing materials with smaller particle sizes, see Section 4.5.2.

To substitute iridium with other metals, $IrCl_3{\cdot}5H_2O$ must be partially substituted with another metal salt. Substituting iridium with antimony was possible using, $SbCl_3$, $SbCl_5$ and $NaSbO_3{\cdot}3H_2O$, however, $NaSbO_3$ was chosen as it was the easiest to handle, as $SbCl_3$ is extremely hygroscopic and $SbCl_5$ is a liquid that readily reacts with water. When substituting iridium with zirconium, ruthenium, osmium and rhodium, respectively; $ZrOCl_2{\cdot}8H_2O$, $RuCl_3{\cdot}4H_2O$, $OsCl_3{\cdot}4H_2O$ and $RhCl_3{\cdot}3H_2O$ were found to be effective reagents. It was found, however, that unless the NaOH concentration of the reaction was reduced to 2 M in the ruthenium and osmium substitution reactions, a significant proportion of the metal was found to be left in solution, resulting in an orange filtrate. Manganese doping proved most effective using $KMnO_4$ when the molarity of the hydroxide solution was reduced to 2 M; and this will be discussed in more detail in the manganese substitution section.

The substitution of iridium by several other metals was also attempted, including titanium, hafnium, niobium, tantalum, chromium, rhenium, iron, cobalt, platinum and tin. However, all of these reactions either yielded materials containing multiple phases or the replacement metal remained in solution, and only the unsubstituted pyrochlore was formed.

To synthesise a material without sodium incorporated onto the A-site, all sodium needed to be eliminated from the reaction, thus Na_2O_2 and NaOH needed to be replaced. It was found

that both Li_2O_2 and KO_2 proved suitable replacements for Na_2O_2, upon scale up, the reactions utilising KO_2 as an oxidiser were more reliable. KOH was the most suitable replacement for NaOH, as it proved impossible to produce a LiOH solution concentrated enough to produce the pyrochlore phase. RbOH and CsOH both produce the desired pyrochlore phase however, they are considerably more expensive than KOH. When NH_4OH was used as a solvent, the iridium chloride reduced forming iridium metal.

All solid products were isolated by suction filtration after cooling. Prior to filtration the reaction mixture was added to 100 ml of deionised water to dilute the NaOH solution to prevent damage to the filter paper. The product was then washed with 50 ml of dilute HNO_3 (approximately 3 M) to remove any $Ca(OH)_2$ produced due to the excess CaO_2 in the synthesis. The product was then re-washed with 20 ml of deionised water to wash away any residual acid, followed by acetone and dried at 80 °C in air for characterisation.

Post synthesis removal of the alkali and alkaline earth metals from the A-site of the pyrochlore using concentrated H_2SO_4, 98 % (approximately 18 M) was investigated. This was achieved by adding 500 mg of either $(Ca,Na)_{2-x}Ir_2O_6 \cdot H_2O$ or $Ca_{2-x}Ir_2O_6 \cdot H_2O$ to 10 ml of conc. H_2SO_4, then stirring the suspension and heating it to either 80 or 110 °C, depending on the degree of leaching desired.

4.3 Pyrochlores with A = Ca, Na and B = Ir

The powder XRD patterns of $(Ca,Na)_{2-x}Ir_2O_6 \cdot H_2O$ materials prepared using $Ca(NO_3)_2$ or CaO_2 can both be indexed and fitted using space group $Fd\bar{3}m$, Figure 4.1, with very similar compositions and lattice parameters, Table 4.1. Those materials produced using $Ca(NO_3)_2$ all contain a small fraction of IrO_2 as a secondary phase.

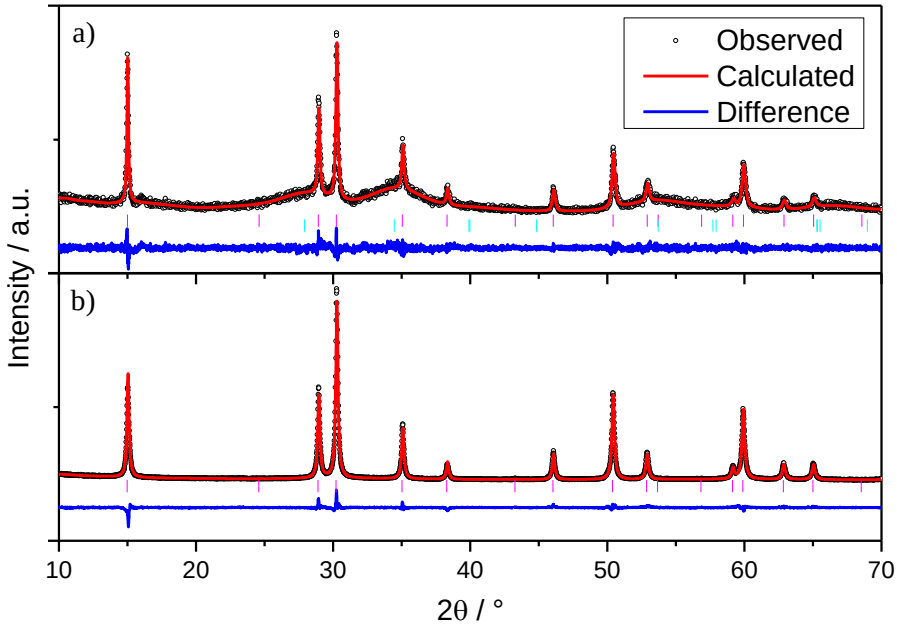

Figure 4.1: Rietveld refinements made against powder XRD data (λ = 1.54056 Å) of a) the $(Ca,Na)_{2-x}Ir_2O_6{\cdot}H_2O$ material using $Ca(NO_3)_2$ as calcium source and b) using CaO_2 as calcium source. Pink tick marks indicate peaks attributed to pyrochlore phase and cyan those attributed to rutile-IrO_2.

Table 4.1: Structural details of $(Ca,Na)_{2-x}Ir_2O_6{\cdot}H_2O$ pyrochlores obtained from Rietveld refinement of powder XRD data, produced from $Ca(NO_3)_2$ or CaO_2 as calcium source respectively.

Atom	Site	*x*	*y*	*z*	Occ	U_{iso} / Å^2
$Ca(NO_3)_2$ Pyrochlore: *a* = 10.2333(2) Å/ Crystallite Size = 27.8 ± 6.4 nm						
Ca	16*d*	0.5	0.5	0.5	0.640(11)	0.034(3)
Na	16*d*	0.5	0.5	0.5	0.23(2)	0.034(3)
Ir	16*c*	0	0	0	1.000(3)	0.015(1)
O	48*f*	0.3322(14)	0.125	0.125	1.00(3)	0.045(7)
O'	8*b*	0.375	0.375	0.375	1.00(5)	0.008(13)
CaO_2 Pyrochlore: *a* = 10.23978(5) Å/ Crystallite Size = 36.2 ± 2.4 nm						
Ca	16*d*	0.5	0.5	0.5	0.704(3)	0.0132(8)
Na	16*d*	0.5	0.5	0.5	0.239(5)	0.0132(8)
Ir	16*c*	0	0	0	1.000(1)	0.00313(14)
O	48*f*	0.3380(3)	0.125	0.125	1.000(7)	0.0024(13)
O'	8*b*	0.375	0.375	0.375	1.002(8)	0.032(4)

Table 4.1 shows the synthesised materials have very similar lattice parameters, O(48*f*) *x* co-ordinates and site occupancies, which are similar to those reported for $(Ca_{0.587}Na_{0.273})_2Ir_2O_6{\cdot}0.66H_2O$,[2] the differences between the materials are negligible however they could be accounted for by the differences observed on the A-site of the materials. The

(48*f*) *x* co-ordinate can have any value between 0.3125 and 0.375 in the pyrochlore structure.[4] Generally this tends towards the 0.3125, at which point the B site octahedra are comprised of six B-O bonds all of equal bond length with O-B-O angles of 90 °. As the value of *x* increases the octahedron becomes distorted, the B-O bond lengths all remain the same however the O-B-O angles vary, with half becoming more acute and more obtuse. The synthesised calcium sodium iridates have O(48*f*) *x* co-ordinates greater than 0.3125, however, they have very similar values to other pyrochlore iridates $Bi_2Ir_2O_7$,[5] $Eu_2Ir_2O_7$[6] and $Pr_2Ir_2O_7$.[6]

Scherrer analysis reveals a difference in the crystallite size between the materials produced via the two reactions, with the materials produced from CaO_2 having larger crystallites. The refined formulae for the materials synthesised using calcium nitrate and peroxide are $(Ca_{0.64}Na_{0.23})_2Ir_2O_6{\cdot}O$ and $(Ca_{0.70}Na_{0.24})_2Ir_2O_6{\cdot}O$, respectively. Compared with the literature material the A : B site occupancy ratio is higher, and the occupancy of the O' site is greater, it is likely that these variations are due to the differences in reaction conditions. While it can not be proven using XRD it is likely the oxygen on the O' is water rather than an oxide anion. If the O' was occupied by O^{2-} to maintain charge balance the iridium in these materials would need to have an oxidation state exceeding +5.5 and anything above +5 is extraordinarily difficult to achieve for iridium.[7]

Electron micrographs, Figure 4.2, correlate well with what is observed in the XRD patterns. For the material synthesised from calcium nitrate, a poorly-defined phase is observable on the surface of octahedron shaped particles, which may be attributed to the rutile IrO_2 phase observed in the XRD patterns. This poorly defined phase is not observable in the micrographs from the material produced from calcium peroxide. The particle size agrees relatively well with what is extracted from the Scherrer analysis of the XRD.

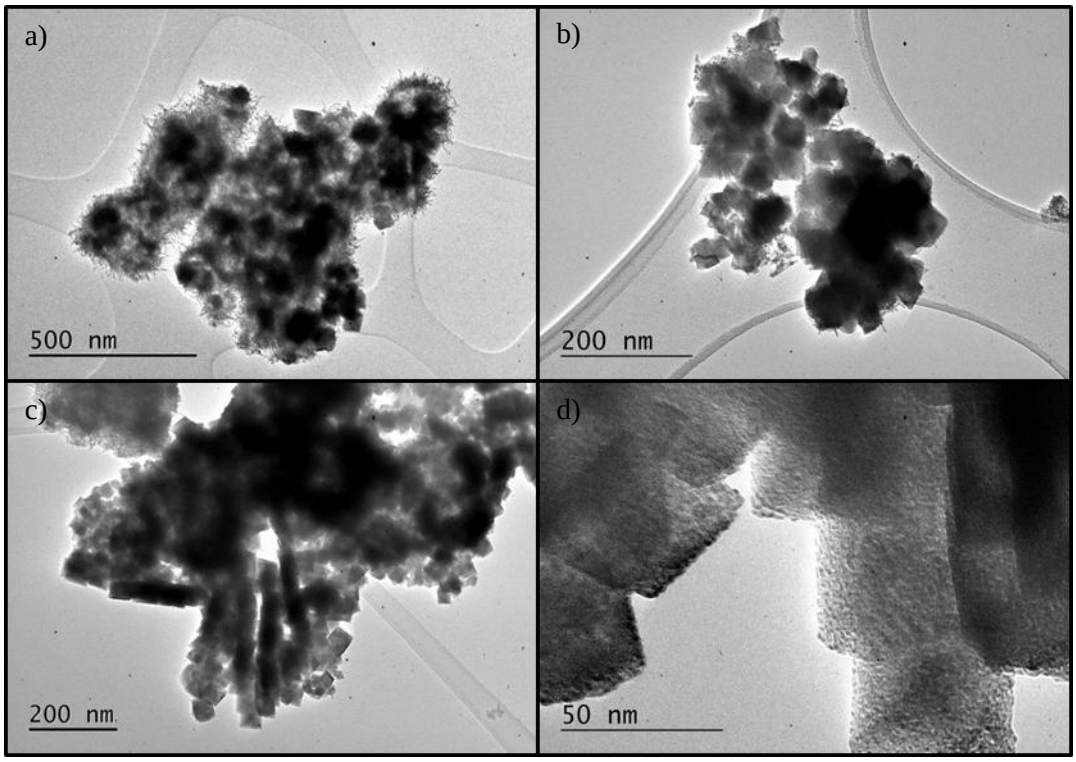

Figure 4.2: TEM micrographs of materials produced from a) + b) $Ca(NO_3)_2$ synthesis, and c) + d) CaO_2 synthesis.

XANES measurements were carried out at the Ir-L_{III} edge, Figure 4.3, to determine the oxidation state of the iridium found within the synthesised materials. The white line position was used to determine the oxidation state,[2] which was revealed to be approximately +4.5 regardless of whether calcium nitrate or peroxide was the calcium source. The model produced from fitting the XRD data yielded an Ir-O bond length of 2.024 Å for the pyrochlore synthesised from CaO_2 and 1.995 Å for the material synthesised from $Ca(NO_3)_2$, and using bond valence sums these distances correspond to an iridium valence of +4.5 and +4.8, respectively. The valence of the material synthesised from CaO_2 agrees well with the analysis of the XANES data, however the material synthesised from $Ca(NO_3)_2$ has a greater than anticipated derived iridium oxidation state from bond valence sums.

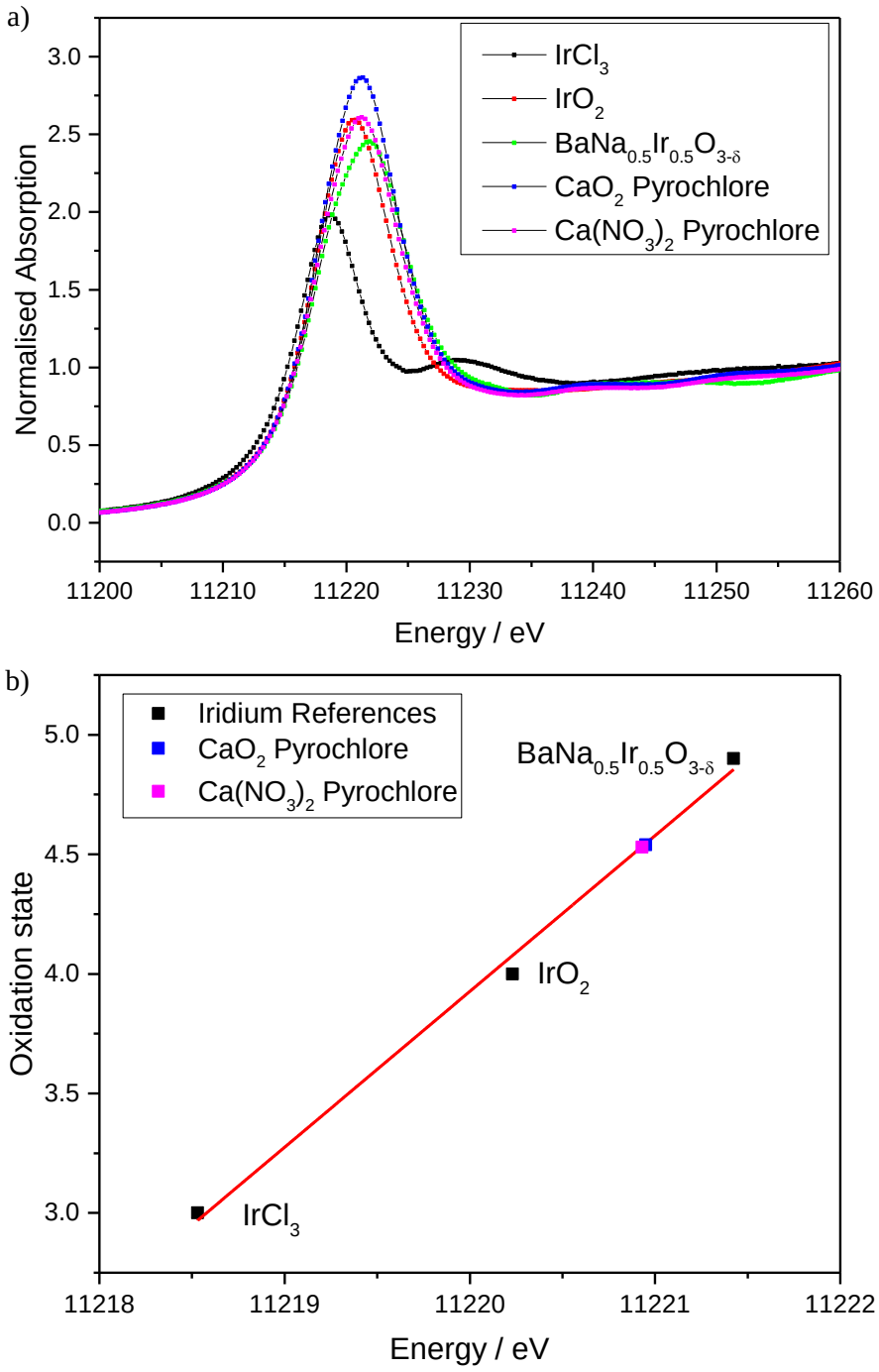

Figure 4.3: a) Ir L_{III}-edge XANES spectra of calcium sodium iridium oxides made from calcium nitrate and calcium peroxide and reference materials for calibration. b) White line energy against iridium oxidation state.

Due to the small IrO_2 impurity phase in the material synthesised from $Ca(NO_3)_2$ it was not further characterised in this study. The structural data presented below for the pyrochlore produced using $Ca(NO_3)_2$ comes from Sardar et al.[2] Refinement of structure against powder neutron diffraction data gives a model consistent with the results of powder XRD, Figure 4.4 and Table 4.2. The materials produced from both calcium sources produce materials that can

be indexed as a cubic pyrochlore with space group $Fd\bar{3}m$. The major differences between the two materials are the occupancy of the O′ oxygen site, and their lattice parameters. Additionally there is some small variation in the A-site composition. Prior to the collection of neutron diffraction data the samples were treated under vacuum at elevated temperature to remove any surface water. This was done as hydrogen is a strong incoherent scatter towards neutrons, giving greater background noise. TGA clearly shows the presence of water in these materials, Figure 4.6. Thus the oxygen on the O′ site can be attributed to crystal water, with protons situated on the 32*e* site, giving O-H bond distances of ~1 Å, following the model reported by Dickens and Weller for hydrated tantalum pyrochlores.[8] It is conceivable that in addition to any surface water, some of the water from the O′ site could be removed from the material by treatment in the vacuum oven, causing the lattice parameter shift. This is confirmed by thermodiffractometry, Figure 4.7, which shows a lattice parameter decrease upon heating. Given the O' oxygen coordination to the A site metals, differences in occupancy on either site would likely result in materials with different lattice parameters.

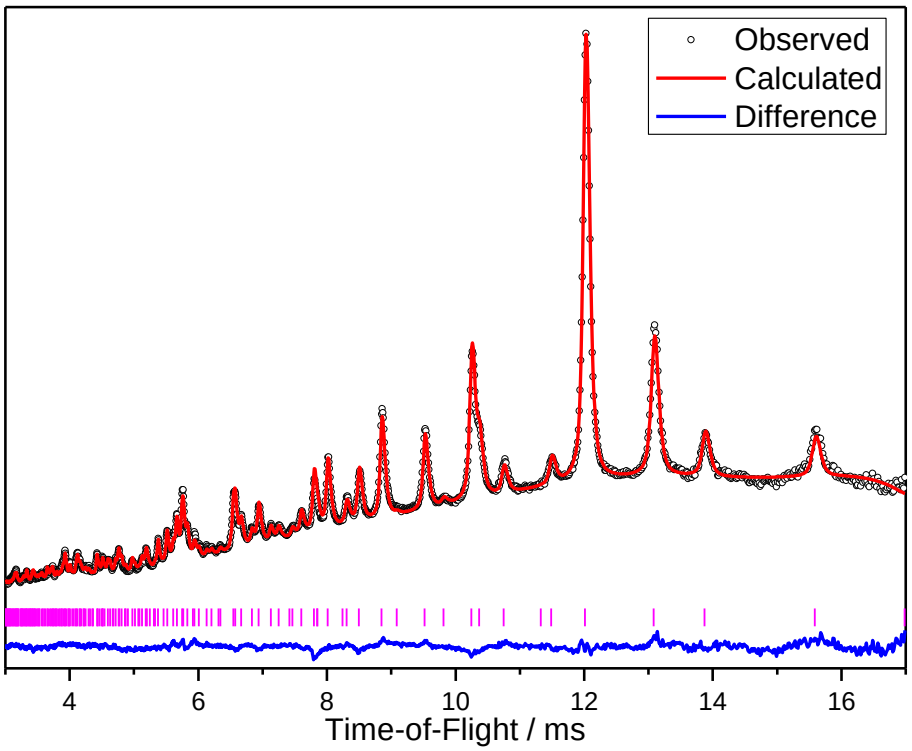

Figure 4.4: Rietveld refinements against time-of-flight neutron data from bank 5 of GEM for calcium sodium iridium oxide produced from CaO_2.

Table 4.2: Structural details of pyrochlores obtained from Rietveld refinement against powder neutron diffraction data, of materials produced using $Ca(NO_3)_2$ by Sardar *et.al.*[2] and CaO_2 as calcium source respectively.

Atom	Site	*x*	*y*	*z*	Occ	U_{iso} / Å$_2$
$Ca(NO_3)_2$ Pyrochlore: [2] *a* = 10.2589(1) Å						
Ca	16*d*	0.5	0.5	0.5	0.587(6)	0.016(6)
Na	16*d*	0.5	0.5	0.5	0.27(3)	0.160(18)
Ir	16*c*	0	0	0	1.000(1)	0.012(1)
O	48*f*	0.3262(1)	0.125	0.125	1.000(1)	0.013(1)
O'	8*b*	0.375	0.375	0.375	0.662(11)	0.024(1)
H	32*e*	0.3289	0.3289	0.3289	0.34(2)	*
CaO_2 Pyrochlore: *a* = 10.21572(19) Å						
Ca	16*d*	0.5	0.5	0.5	0.597(6)	0.0127(6)
Na	16*d*	0.5	0.5	0.5	0.267(5)	0.0127(6)
Ir	16*c*	0	0	0	1.000(1)	0.00940(12)
O	48*f*	0.3244(1)	0.125	0.125	1.000(2)	0.00827(12)
O'	8*b*	0.375	0.375	0.375	0.950(7)	0.0282(10)
H	32*e*	0.3289	0.3289	0.3289	0.476(14)	**

* U11 = 0.75(3), U22 =0.28(3) , U33 = 0.75(3), U12 = -0.250(15), U13 = -0.400(15), U23= -0.250(15)
** U11 = 0.76(3), U22 =0.30(3) , U33 = 0.76(3), U12 = -0.253(19), U13 = -0.40(2), U23= -0.253(19)

To obtain a useable pair distribution function (PDF), the Q space data had been truncated prior to the Fourier Transform. This was due to a combination of the high incoherent scattering of hydrogen, from crystal water and the nuclear absorption of iridium, which both result in a large background and unphysical features observed at low *r* upon Fourier Transformation. The truncation results in data below *r* = 1.7 Å been masked, unfortunately this region contains the first atomic correlation, that of the O-H bonds in crystal water, which should be observed around 1.0 Å.

The resulting PDF for the synthesised material was then fitted using the model produced from the Bragg scattering, Figure 4.5, with refinement of the lattice parameter, the occupancies and the ADPs, Table 4.3. The *r* > 10 Å region fits very well, however there are some discrepancies in the low *r* region. The first observable atomic correlation is at ~1.96 Å and agrees well with the B-O distance between the metal on the 16*c* site and co-ordinating oxygen on the 48*f* site. The next broader feature between 2.3-3.2 Å has multiple contributions from A-O and O-O correlations, however these fit less well, suggesting some deviation from the average pyrochlore structure at the local scale. Overall the fit to the ideal

cubic pyrochlore is quite good, much more so than was found for $(Na_{0.33}Ce_{0.53}Ti_{0.14})_2Ti_2O_7$ by Playford et al, [9] where to fit the low *r* region of the PDF, oxide anions had to be displaced from the positions allowed by relaxing the symmetry of the space group $Fd\bar{3}m$ to the sub-group $F\bar{4}3m$. This variability in the position of the 48*f* oxygen is well established, been observed in the pyrochlore materials $Pb_2Ru_2O_{6.5}$[10] and $(Bi_{1-x}Y_x)_2Sn_2O_7$.[11]

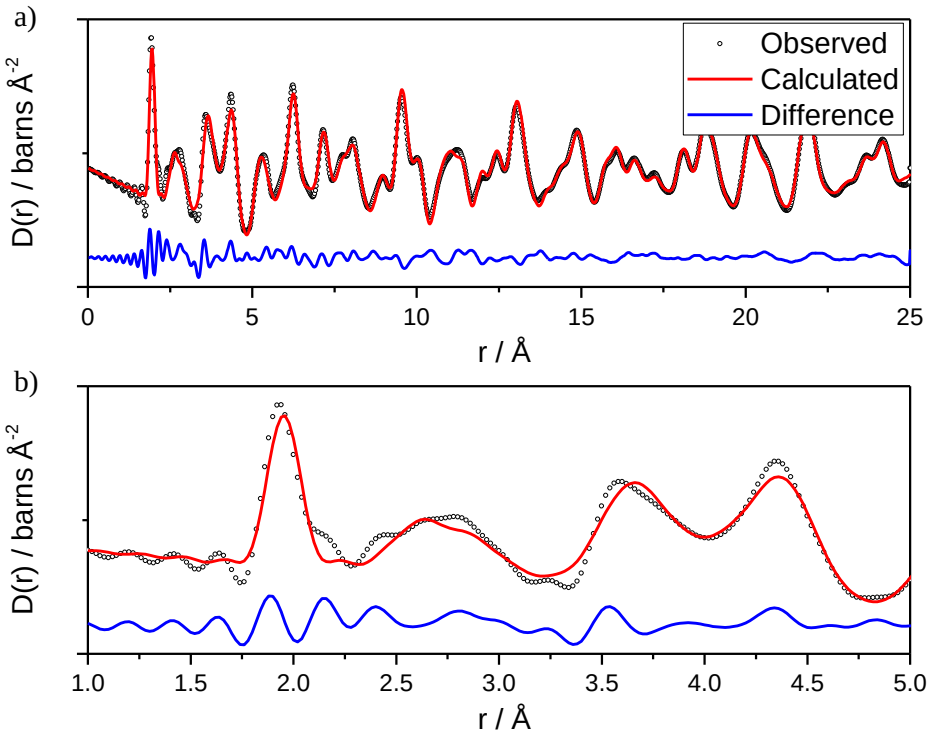

Figure 4.5: Fits of the Rietveld models against PDF data a) up to r = 25 Å and b) up to r = 5 Å of calcium sodium iridium oxide pyrochlore.

Table 4.3: Structural details of calcium sodium iridium oxide obtained from least-squares fitting of PDF data.

Atom	Site	*x*	*y*	*z*	Occ	U_{iso} / Å^2
		CaO_2 Pyrochlore: *a* = 10.196(3) Å				
Ca	16*d*	0.5	0.5	0.5	0.597	0.024(4)
Na	16*d*	0.5	0.5	0.5	0.267	0.024(4)
Ir	16*c*	0	0	0	1.000	0.0118(8)
O	48*f*	0.3244	0.125	0.125	1.000	0.0127(8)
O'	8*b*	0.375	0.375	0.375	1.000	0.031(4)
H	32*e*	0.3289	0.3289	0.3289	0.500	0.7626

TGA-MS was employed to further explore the presence of crystal water, Figure 4.6. In this experiment the sample was held at 120 °C before continued heating to attempt to observe

loss of surface water separately from crystal water. An initial mass loss of 4.8 % is observed, up to the end of the 4 hour hold at 120 °C, and can be attributed to the loss of surface water, as confirmed by the MS response and also shown by an exothermic feature in the DSC. At this point if it can be assumed that all the surface water has been removed, any further loss must be due to crystal water. Hence the next loss of 3.6 % of the remaining mass, can be attributed to the loss of crystal water, which is similar to the 3.2 % loss expected if the O' site is fully occupied by H_2O, there is a small endothermic feature in the DSC overlapping this loss, meaning this is bound differently to the surface water lost at 120 °C, requiring an input of energy to remove water from within the crystal structure. There is a sharp endothermic peak in the DSC right after the loss of crystal water indicative of a second distinct mass loss, likely due to partial phase separation to a stoichiometric pyrochlore and IrO_2, like what is observed in $Ca_{1.5}Ru_2O_7$,[12] the theoretical mass loss associated with reduction of iridium from +4.5 to +4 can account for approximately 3 % through loss of oxygen, not enough to match the observed loss. It is possible that during the phase change sodium is volatilised this would account for a further 2 % mass loss. Combining these two losses we come close to the loss observed experimentally. The loss observed at 750 °C can then be attributed to the formation of $CaIr_2O_4$ and reduction of the remaining iridium to metal.

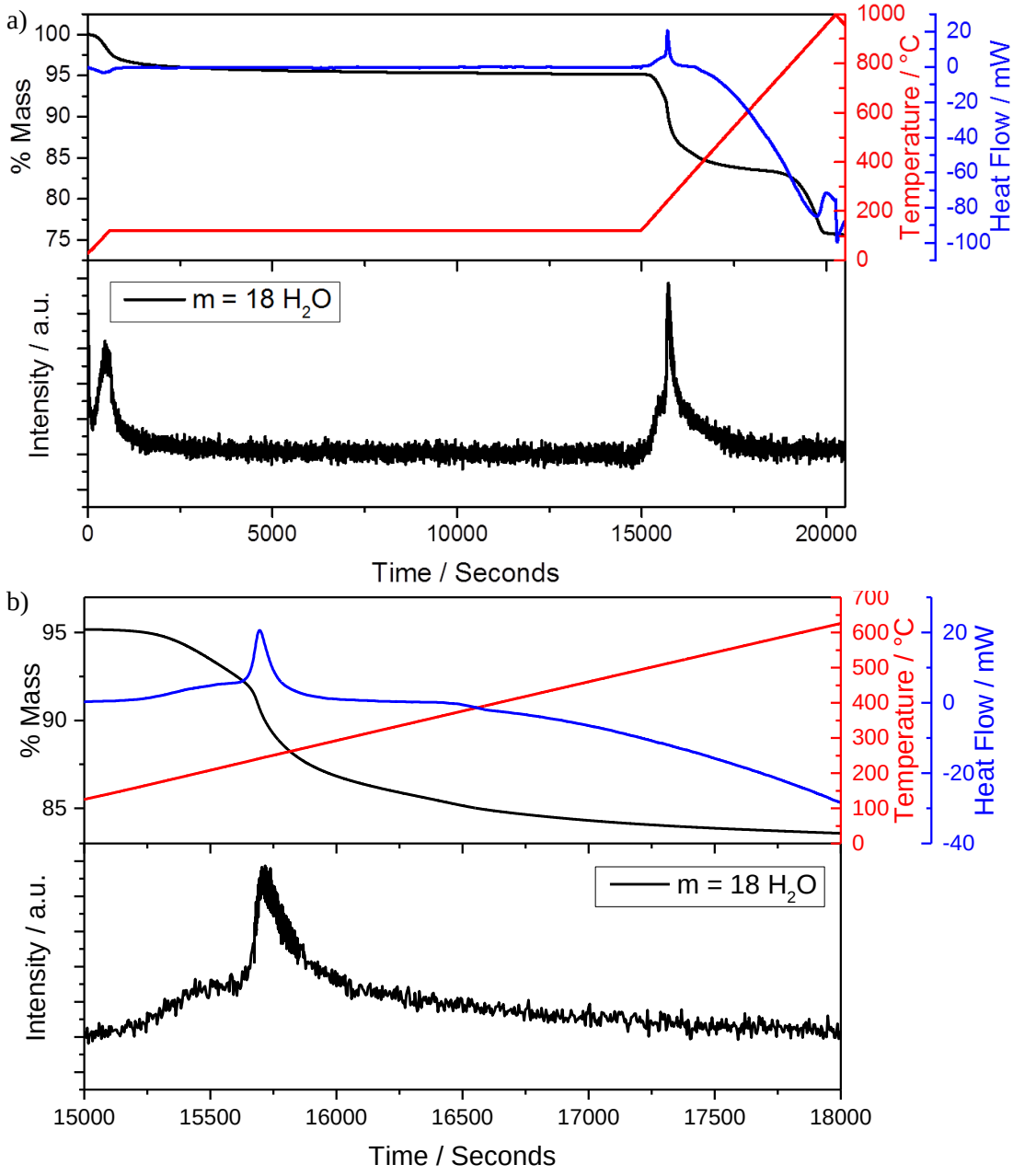

Figure 4.6: TGA-MS plots a) complete range and b) zoom of region with loss of crystal water of calcium sodium iridium oxide.

Thermodiffractometry, Figure 4.7, shows the pyrochlore phase to be thermally stable up to around 600 °C at which point iridium metal starts forming as a separate phase. Upon closer inspection however, a lattice parameter decrease of the pyrochlore phase between 250 and 300 °C is seen, which occurs at the same time as the loss of crystal water observed in the TGA. Even though we might expect thermal expansion in a pyrochlore, the contraction seen is evidently related to the loss of crystal water. Once 300 °C is exceeded, a consistent loss of crystallinity up until 650 °C is observed, at which point iridium metal starts to form a

separate phase. Then between 750 and 800 °C a complete breakdown of the pyrochlore phase is seen yielding Ca_2IrO_4 and even more iridium metal.

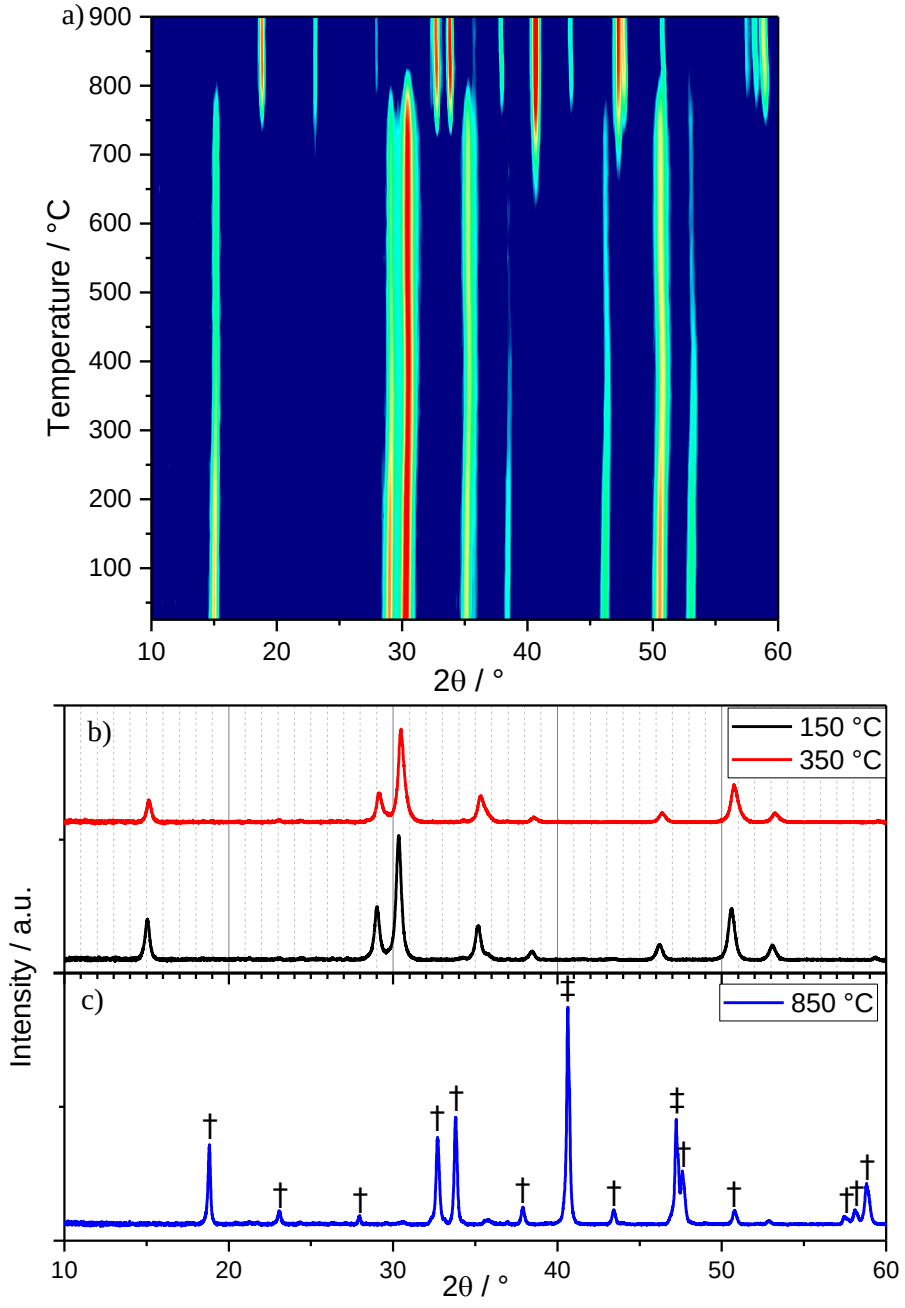

Figure 4.7: a) Thermodiffractometry (λ = 1.5418 Å) of calcium sodium iridium oxide synthesised from CaO_2. b) XRD patterns either side of temperature at which crystal water is lost. c) XRD pattern after phase change, † denotes peaks arising from Ca_2IrO_4 and ‡ denoting peaks arising from Ir metal.

4.4 B-site Substitution in A = Ca and Na and B = Ir and M

4.4.1 Antimony Substitution

The powder XRD patterns, Figure 4.8 and 4.9, of materials synthesised with the assumed formula $(Ca,Na)_{2-x}(Ir_{1-y}Sb_y)_2O_6 \cdot H_2O$, can be indexed and fitted to a cubic pyrochlore cell using space group $Fd\bar{3}m$ across the range $0.1 \leq y \leq 1$. High resolution XRD data were collected from y = 0.25, 0.5 and 1.0 materials and Rietveld refinements were carried out; the remaining materials were fitted using the Le Bail method and lattice parameters were extracted. Across the solid solution the lattice parameter increase with antimony content, Figure 4.10, consistent with the relative ionic radii of the B-site metals, with octahedral Ir(IV) 0.625 Å and Ir(V) 0.57 Å being smaller than octahedral Sb(III) 0.76 Å and Sb(V) 0.6 Å.[13] In all instances there is a reduction in crystallite size compared to the unsubstituted material when antimony is substituted into the structure.

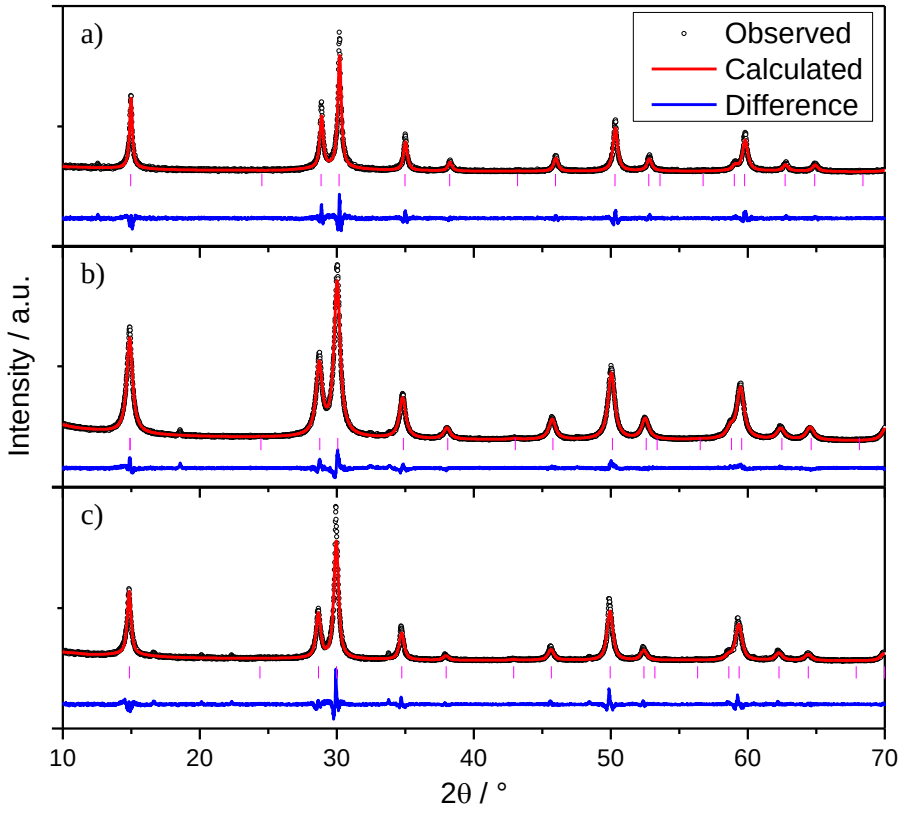

Figure 4.8: Rietveld refinements to powder XRD data (λ = 1.54056 Å) from $(Ca,Na)_{2-x}(Ir_{1-y}Sb_y)_2O_6 \cdot H_2O$, a) y = 0.25, b) y = 0.50 and c) y = 1.00.

Table 4.4: Structural details of $(Ca,Na)_{2-x}(Ir_{1-y}Sb_y)_2O_6 \cdot H_2O$ pyrochlores obtained from Rietveld refinement against powder XRD data.

Atom	Site	*x*	*y*	*z*	Occ	U_{iso} / Å^2
25 % Sb Pyrochlore: *a* = 10.2561(2) Å / Crystallite Size = 17.8 ± 3.4 nm						
Ca	16*d*	0.5	0.5	0.5	0.666(7)	0.0369(19)
Na	16*d*	0.5	0.5	0.5	0.322(12)	0.0369(19)
Ir	16*c*	0	0	0	0.708(4)	0.0062(3)
Sb	16*c*	0	0	0	0.292(4)	0.0062(3)
O	48*f*	0.3391(8)	0.125	0.125	1.000(14)	0.021(3)
O'	8*b*	0.375	0.375	0.375	1.064(18)	0.026(7)
50 % Sb Pyrochlore: *a* = 10.29167(11) Å / Crystallite Size = 13.2 ± 1.4 nm						
Ca	16*d*	0.5	0.5	0.5	0.610(3)	0.0568(8)
Na	16*d*	0.5	0.5	0.5	0.356(5)	0.0568(8)
Ir	16*c*	0	0	0	0.467(2)	0.0149(2)
Sb	16*c*	0	0	0	0.533(2)	0.0149(2)
O	48*f*	0.3277(2)	0.125	0.125	1.002(5)	0.0092(9)
O'	8*b*	0.375	0.375	0.375	1.001(7)	0.067(3)
100 % Sb Pyrochlore: *a* = 10.3214(2) Å / Crystallite Size = 16.5 ± 2.1 nm						
Ca	16*d*	0.5	0.5	0.5	0.621(4)	0.0181(11)
Na	16*d*	0.5	0.5	0.5	0.336(7)	0.0181(11)
Sb	16*c*	0	0	0	1.000(1)	0.0111(2)
O	48*f*	0.3323(4)	0.125	0.125	1.000(8)	0.0145(19)
O'	8*b*	0.375	0.375	0.375	1.010(9)	0.065(7)

The data extracted from Table 4.4 would suggest the materials have the following formulae, $(Ca_{0.67}Na_{0.32})_2(Ir_{0.71}Sb_{0.29})_2O_7$, $(Ca_{0.61}Na_{0.36})_2(Ir_{0.47}Sb_{0.53})_2O_7$ and $(Ca_{0.62}Na_{0.34})_2Sb_2O_7$, so in all cases the proposed material is not charge balanced. It is assumed the antimony in these materials is found in the +5 state, as at high substitution levels the presence of Sb^{3+} would be impossible to account for. So much like the calcium sodium iridium oxide, the charge is probably balanced by the presence of water on the O' site instead of O^{2-}. This creates another issue as at high levels of antimony substitution the net positive charge is too high, It is possible that instead of complete occupancy by water a portion of the O' site could be occupied with hydroxide, similar to defect pyrochlore $KTa_2O_5OH \cdot 1.4H_2O$,[14] with the degrees of hydroxylation being proportional to the degree of antimony substitution.

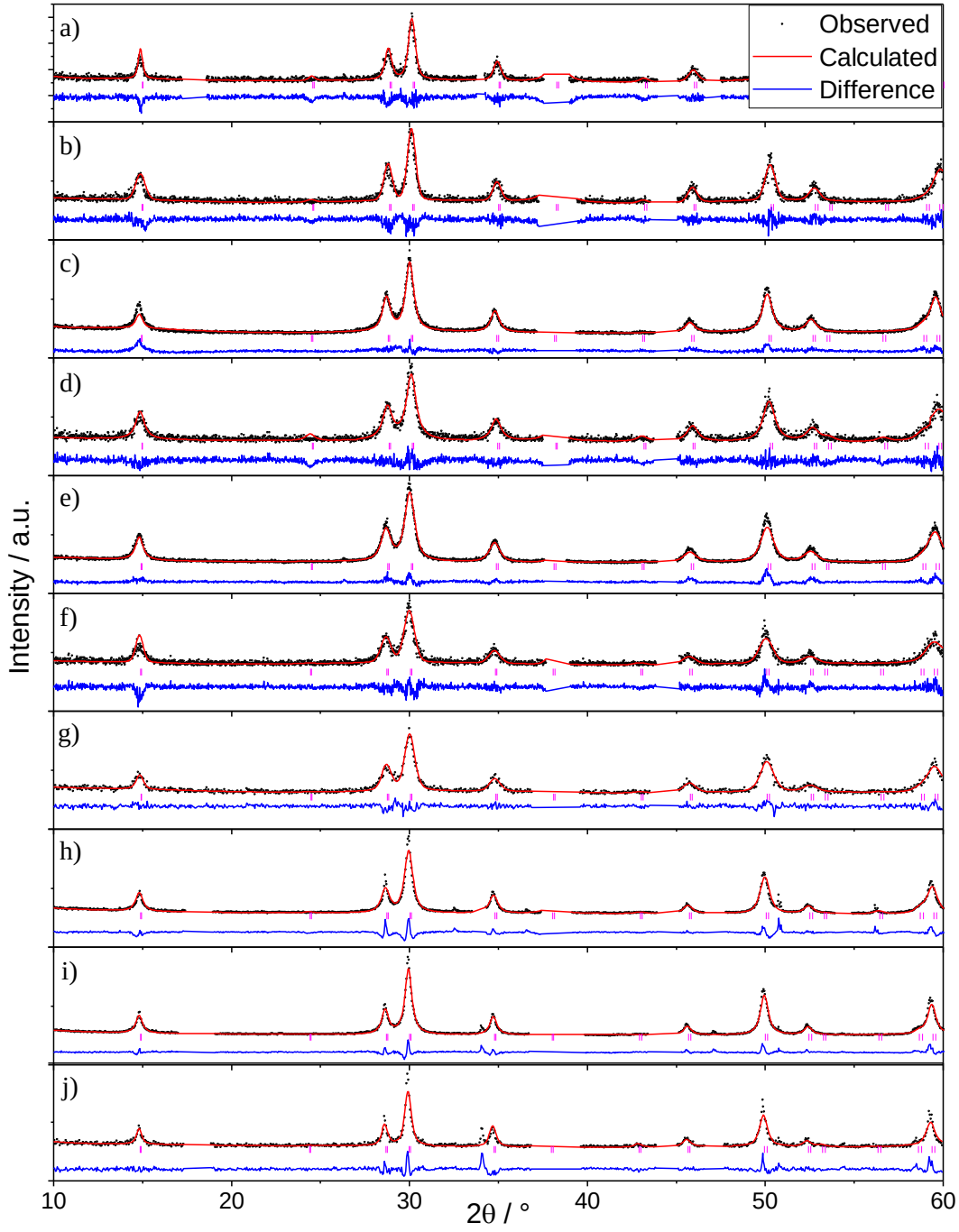

Figure 4.9: Le Bail fits to powder XRD data (λ = 1.5418 Å) from $(Ca,Na)_{2-x}(Ir_{1-y}Sb_y)_2O_6 \cdot H_2O$, a) y = 0.1, b) y = 0.2, c) y = 0.3, d) y = 0.4, e) y = 0.5, f) y = 0.6, g) y = 0.7, h) y = 0.8, i) y = 0.9 and j) y = 1.0. Peaks resulting from aluminium sample holder at 38 and 44 ° 2θ are excluded.

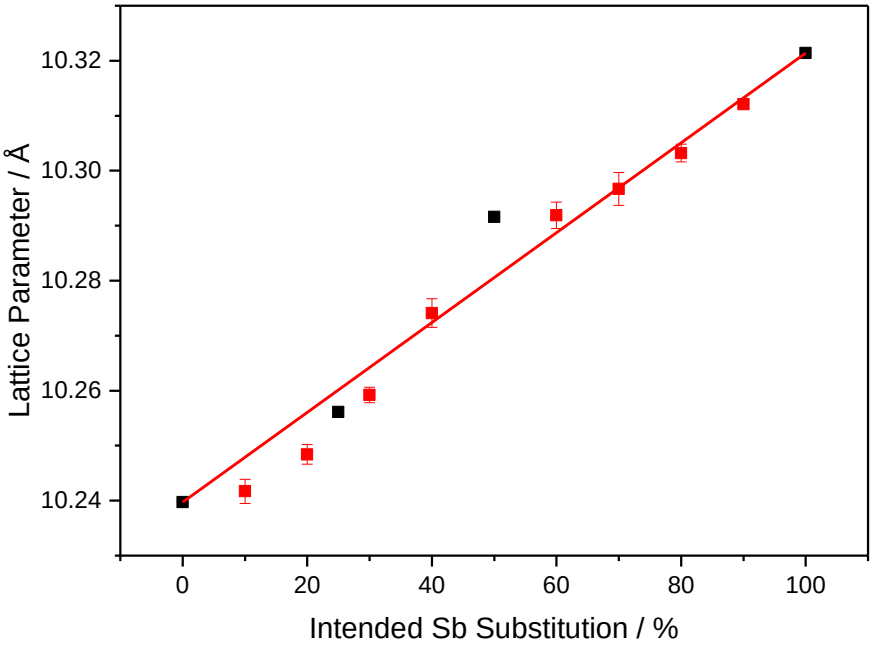

Figure 4.10: Refined lattice parameter as a function of nominal antimony substitution. Black points from Rietveld fits and red points from Le Bail fits. Red line is an extrapolation between the two extremes in composition.

Analysis of the EDXA data, as described in Chapter 2, revealed a linear increase in the level of antimony substitution across the solid solution, Figure 4.11, consistent with the linear increase in lattice parameter. A linear change in lattice parameter is also observed in the pyrochlore solid solutions $(Y_{1-x}Bi_x)_2Sn_2O_7$[15] and $Y_2(Hf_{1-x}Ti_x)_2O_7$.[16]

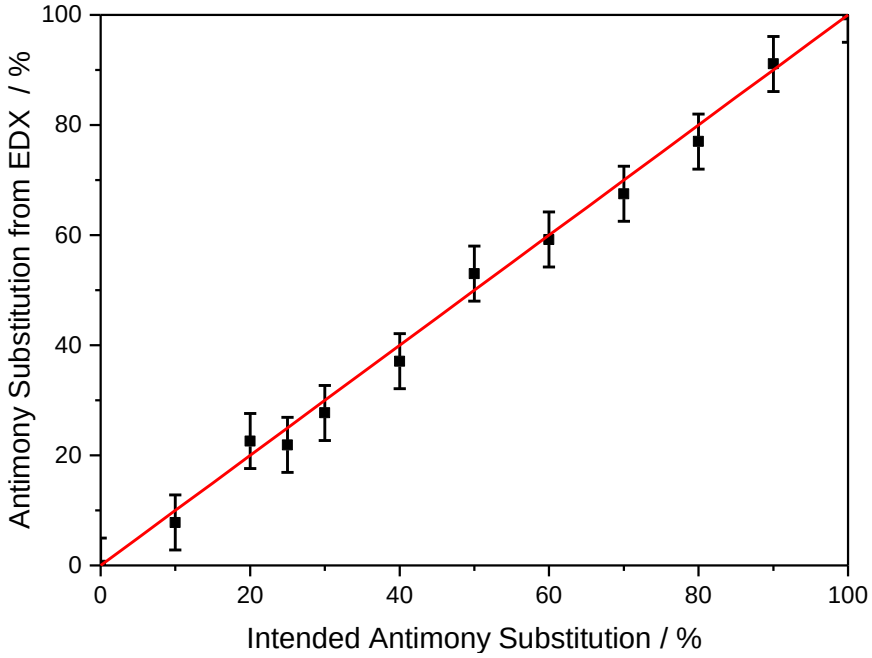

Figure 4.11: Measured antimony content from EDXA as a function of intended antimony substitution.

XANES measurements were carried out at both the Sb K-edge and the Ir L_{III}-edge to determine the oxidation state of the metals within the synthesised materials. The white line position was used to determine the iridium oxidation state, Figure 4.12,which was found to be between +4.25-4.5 with no correlation to the antimony substitution level, Table 4.5. This apparently random variation could be due to uncharacterised differences between the A-site occupancies and the species found on the O' site. The edge position at a normalised absorption of 0.5 was used to calculate the antimony oxidation state, Figure 4.13, and the antimony in all these materials was found in the +5 state.

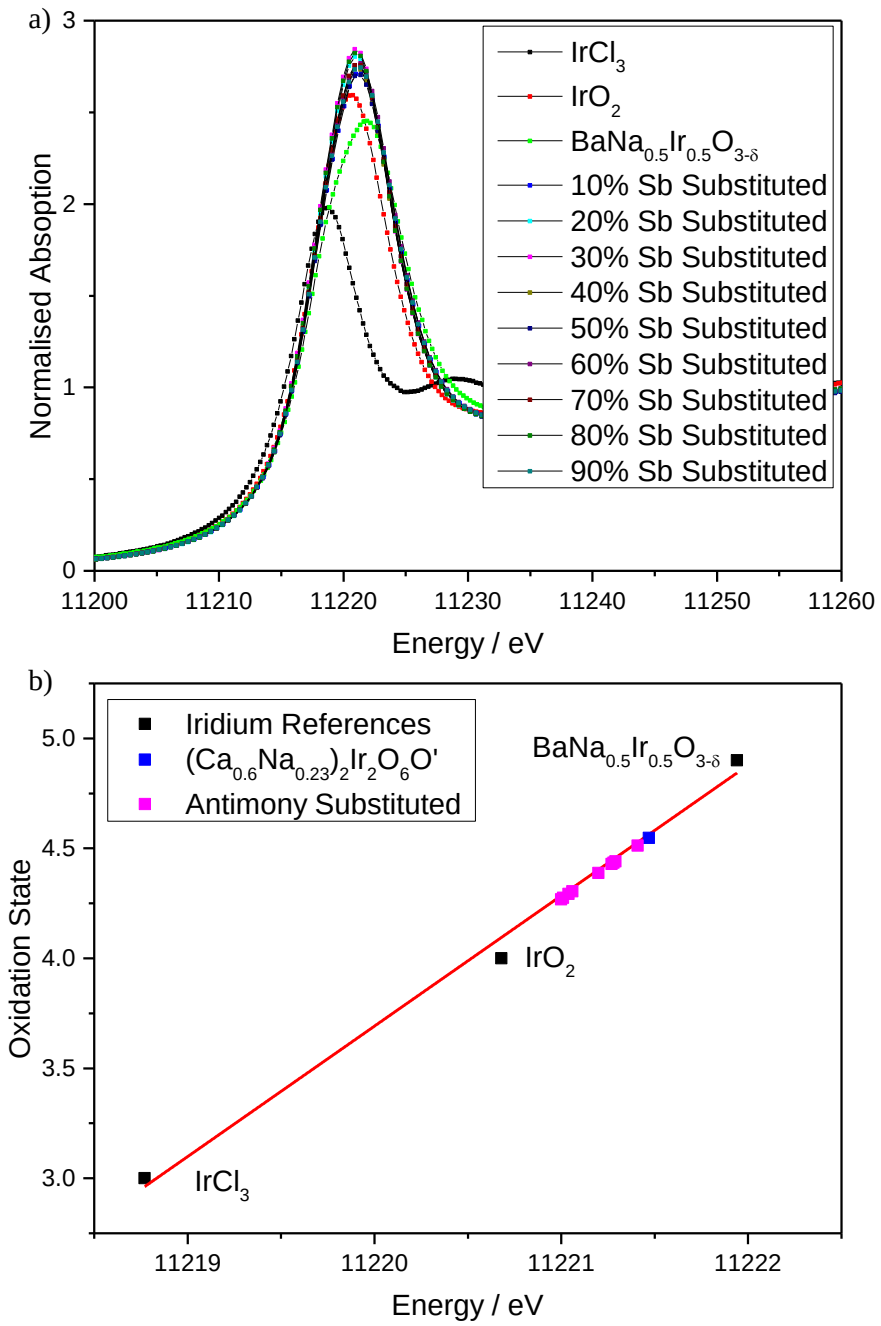

Figure 4.12: a) Ir L_{III}-edge XANES spectra of calcium sodium iridium antimony oxide materials and reference materials for calibration. b) White line position against iridium oxidation state.

Table 4.5: Iridium oxidation of calcium sodium iridium antimony oxide materials against intended antimony fraction y.

y	0.10	0.20	0.30	0.40	0.50	0.60	0.70	0.80	0.90
Ir Oxidation State	4.51	4.29	4.27	4.39	4.44	4.43	4.30	4.27	4.43

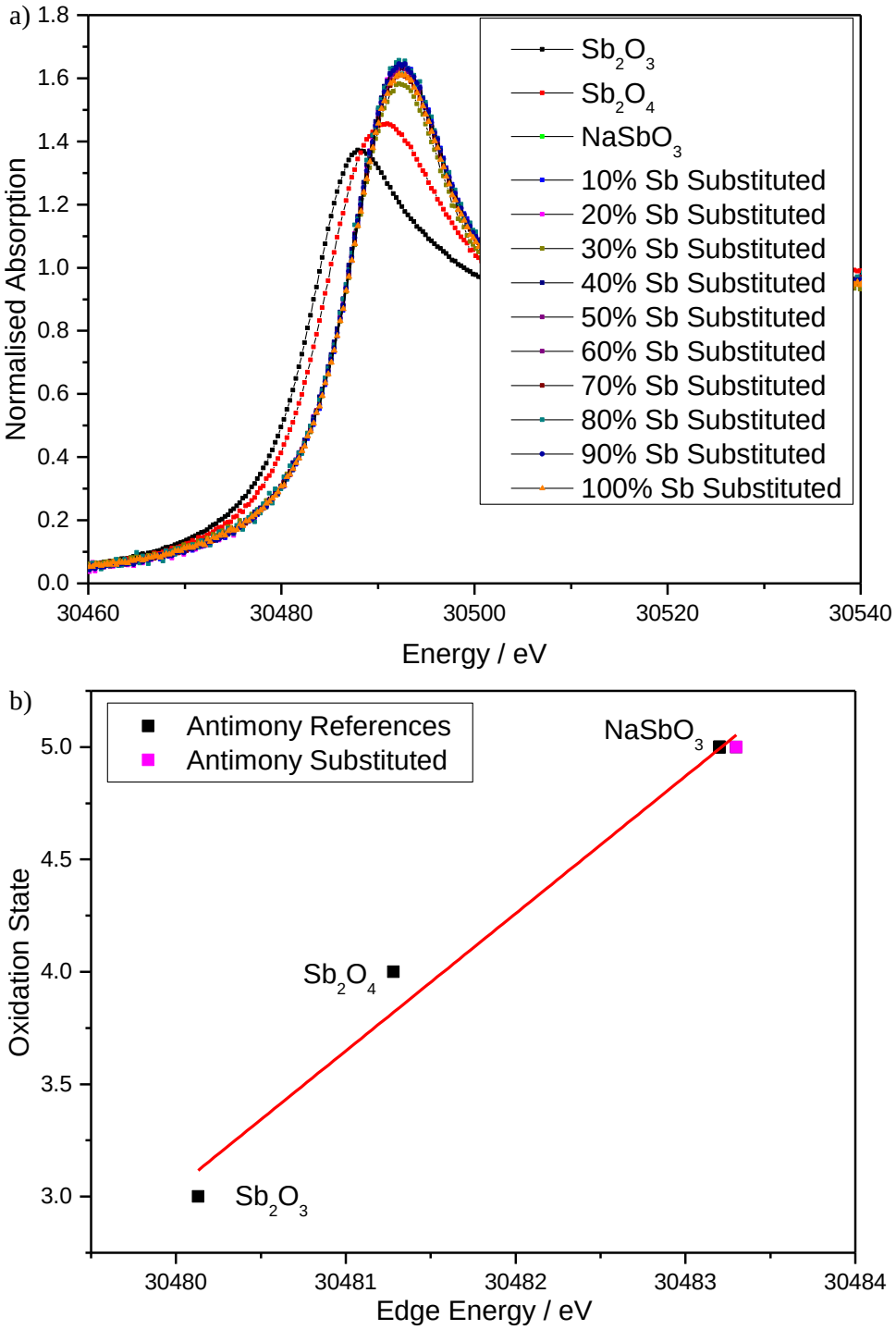

Figure 4.13: a) Sb K-edge XANES spectra of antimony calcium sodium iridium antimony oxide materials and reference materials for calibration. b) Edge position against antimony oxidation state.

The powder neutron diffraction data of the 50 % antimony substituted material can be fitted in the same manner as the pure iridium material, Figure 4.14, with split occupancy on the B-site between antimony and iridium. The crystal structure parameters refined from the data agree well with those determined from powder XRD, however using neutron diffraction it is

possible to locate the protons required for charge balance. These were modelled in the same manner as in the unsubstituted material.

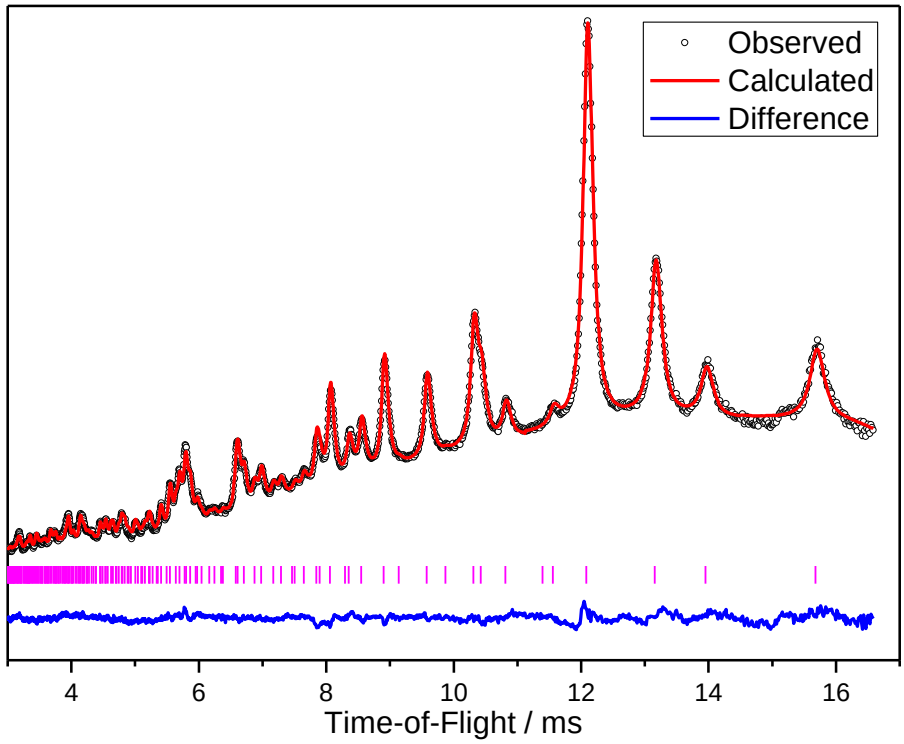

Figure 4.14: Rietveld refinement against time-of-flight neutron data from bank 5 of GEM for 50 % antimony substituted calcium sodium iridium oxide.

Table 4.6: Structural details of 50 % antimony substituted calcium sodium iridium oxide, obtained from Rietveld refinement of powder neutron diffraction data.

Atom	Site	*x*	*y*	*z*	Occ	U_{iso} / Å^2
50 % Sb Substituted Pyrochlore: *a* = 10.2749(2) Å						
Ca	16*d*	0.5	0.5	0.5	0.589(7)	0.0212(7)
Na	16*d*	0.5	0.5	0.5	0.324(10)	0.0212(7)
Ir	16*c*	0	0	0	0.489(5)	0.00899(16)
Sb	16*c*	0	0	0	0.511(5)	0.00899(16)
O	48*f*	0.32355(10)	0.125	0.125	1.000(2)	0.0099(11)
O'	8*b*	0.375	0.375	0.375	1.000(6)	0.0367(10)
H	32*e*	0.3289	0.3289	0.3289	0.334(12)	*

* U11 = 0.752(2), U22 =0.303(2) , U33 = 0.753(2), U12 = -0.253(3), U13 = -0.400(12), U23= -0.253(3)

For the same reasons as the unsubstituted material the Q space data for the 50 % antimony substituted material had to be truncated prior to the Fourier Transformation. The resulting PDF was then fitted using the model produced from the Bragg scattering, with refinement of the lattice parameter and the ADPs, Table 4.7. The r > 10 Å region fits very well, however the low r region does not fit quite as well, Figure 4.15. This is probably due to disorder in the

oxide anion positions as a result of the material having a mixed metal B-site. Much like the unsubstituted material, however, this fit is much better than many other pyrochlores whose structure is distorted from the ideal at the local scale.

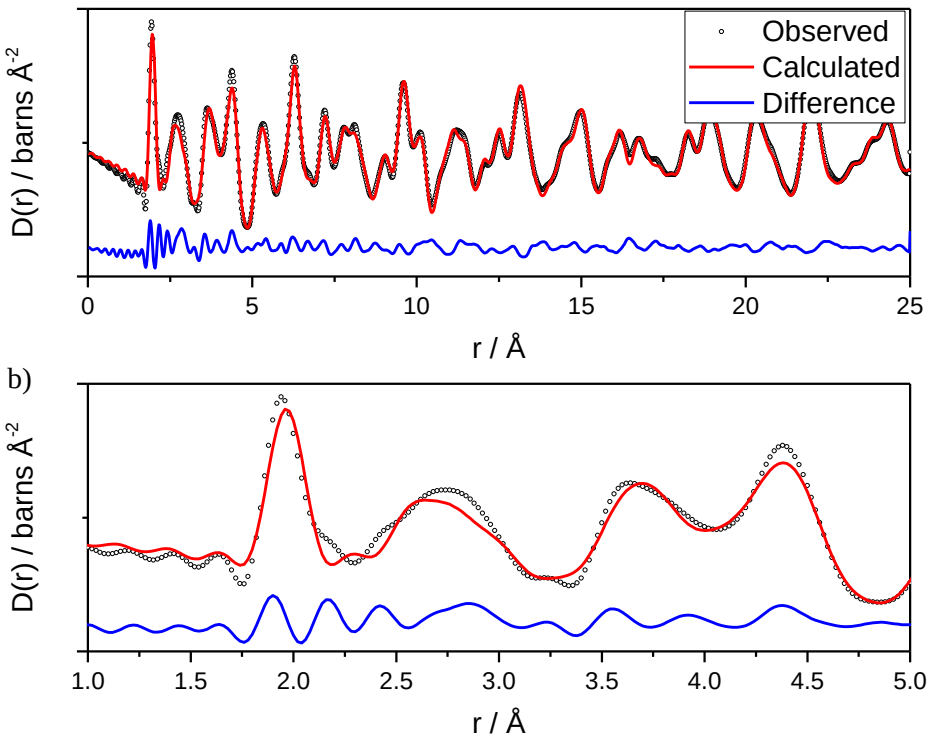

Figure 4.15: Fits of the Rietveld models against PDF data a) up to r = 25 Å and b) up to r = 5 Å of 50 % antimony substituted calcium sodium iridium oxide.

Table 4.7: Structural details of 50 % antimony substituted calcium sodium iridium oxide obtained from least-squares fitting of PDF data.

Atom	Site	*x*	*y*	*z*	Occ	U_{iso} / Å^2
50 % Sb Substituted Pyrochlore: *a* = 10.260(3) Å						
Ca	16*d*	0.5	0.5	0.5	0.589	0.029(4)
Na	16*d*	0.5	0.5	0.5	0.342	0.029(4)
Ir	16*c*	0	0	0	0.489	0.0107(9)
Sb	16*c*	0	0	0	0.511	0.0107(9)
O	48*f*	0.3236	0.125	0.125	1.000	0.0130(7)
O'	8*b*	0.375	0.375	0.375	1.000	0.039(5)
H	32*e*	0.3289	0.3289	0.3289	0.344	0.762

Like the unsubstituted material, Figure 4.16, TGA-MS was employed to look for the crystal water proposed from fitting the neutron diffraction data. An initial mass loss of 1.8 % is observed, up to the end of the 4 hour hold at 120 °C, and can be attributed to the loss of

surface water. Next is observed a loss of 2.1 % of the remaining mass, which can be attributed to the loss of crystal water. However this is lower than the theoretical losses of 3.5 and 3.7 % we expect if the O’ site is fully occupied by OH^- or H_2O, respectively. Although difficult to accurately estimate, it can be assumed the temperature at which the lattice parameter stops shifting in the thermodiffractometry, Figure 4.17, corresponds to the temperature at which all the water or hydroxide is expelled from the O' site. As such the mass loss of 3.7 % recorded up until 300 °C, corresponds to the complete expulsion of water and hydroxide from the O' site. The slightly inflated mass loss could be explained by incomplete loss of surface water from the sample after the hold, evidence for which can be seen in the small exothermic peak observed in the DSC after the four hour hold. Further losses are less well defined than that of the unsubstituted material, however this is expected as it is likely various oxide phase changes and separations happen as the temperature increases.

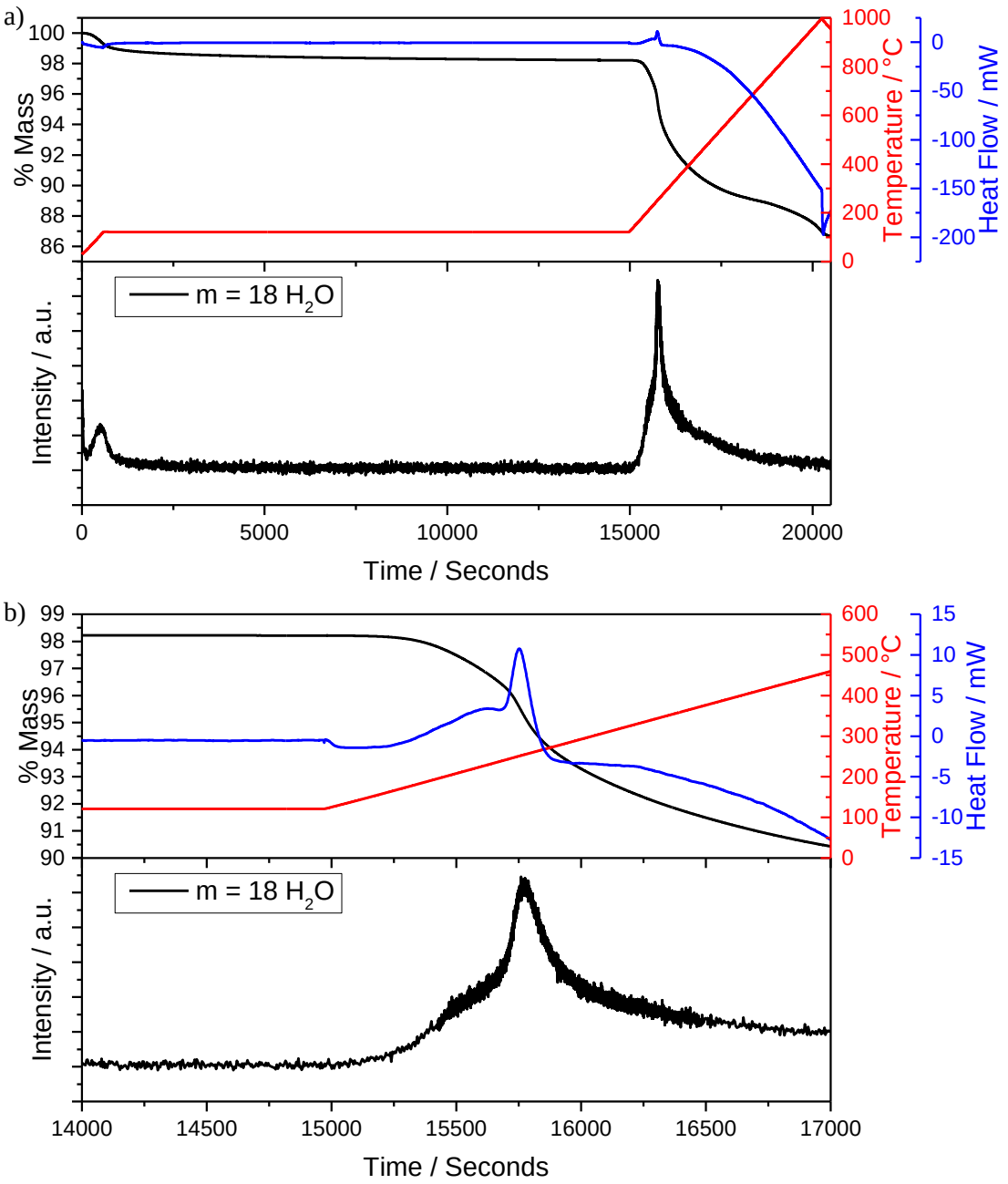

Figure 4.16: TGA-MS plots a) complete range and b) zoom of region with loss of crystal water of calcium sodium iridium antimony oxide, y = 0.50.

Thermodiffractometry, Figure 4.17, reveals the pyrochlore phase to be thermally stable up to roughly 500 °C at which point iridium metal starts forming as a separate phase, making this material less thermally stable than the unsubstituted material. Like the unsubstituted material a decrease in lattice parameter is observed for the pyrochlore phase between 250 and 300 °C due to the loss of crystal water as seen in the TGA. The only oxide phase observed up to 900 °C is a pyrochlore phase, unlike the unsubstituted material, where Ca_2IrO_4 is formed.

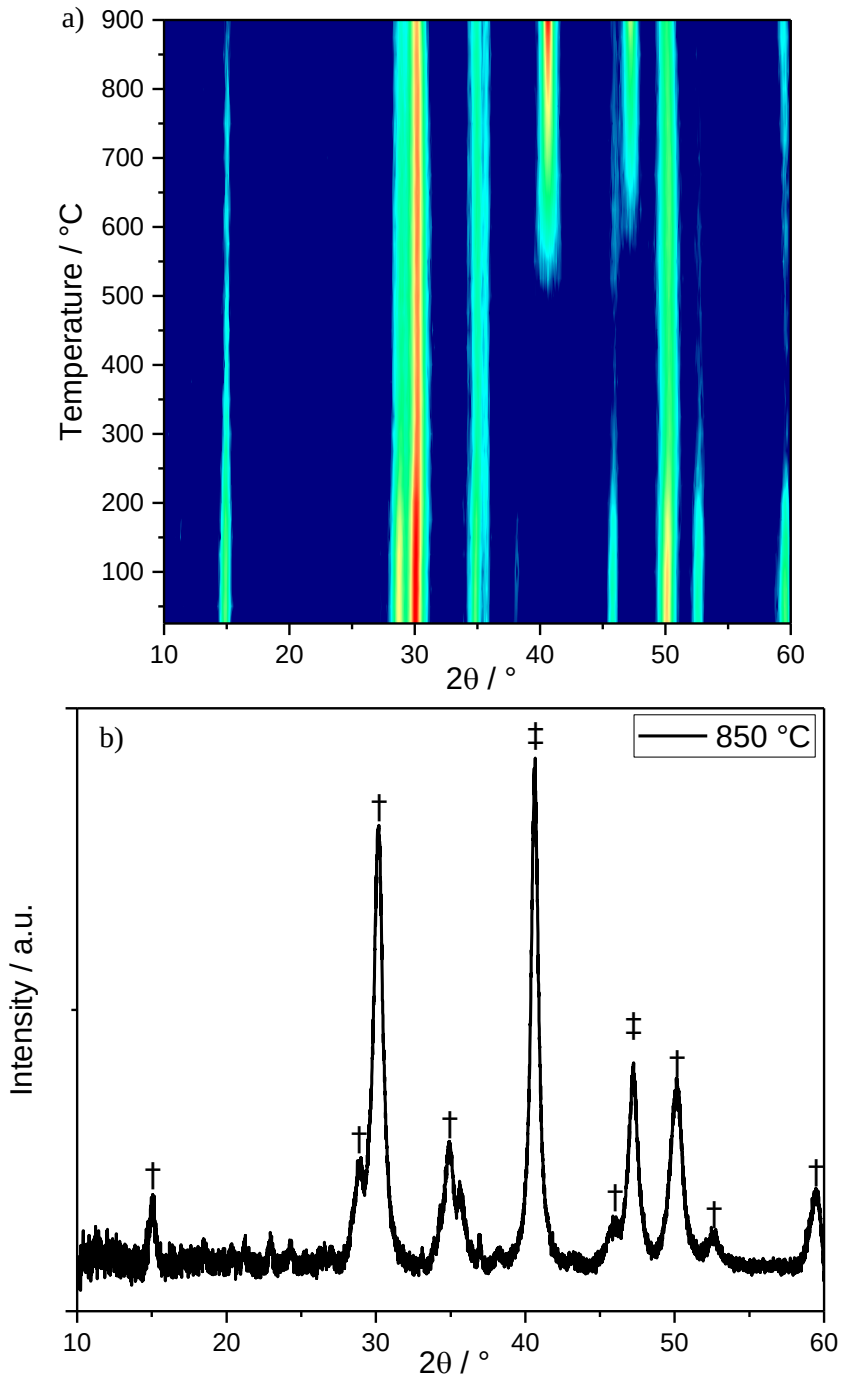

Figure 4.17: a) Thermodiffractometry (λ = 1.5418 Å) of 50 % antimony substituted calcium sodium iridium oxide. b) XRD pattern at 850 °C, † denoting peaks arising from a pyrochlore phase and ‡ denotes peaks arising from Ir metal.

4.4.2 Zirconium Substitution

The powder XRD patterns of the materials synthesised with initially assumed formulae $(Ca,Na)_{2-x}(Ir_{1-y}Zr_y)_2O_6 \cdot H_2O$, can be indexed and fitted to a cubic pyrochlore cell using space group $Fd\bar{3}m$ within the range $0.1 \leq y \leq 0.5$, Figures 4.18, 4.19 and Table 4.8. Attempting to increase the Zr content beyond y = 0.5 results in the formation of the cubic phase, $CaZr_4O_9$,

which is the same material produced when y = 1.0, Figure 4.21. As y increases the lattice parameter increases, Figure 4.20, consistent with Ir(IV) 0.625 Å and Ir(V) 0.57 Å been smaller than six co-ordinate Zr(IV) 0.72 Å.[13] However this substitution does not follow Vegards law, probably due to the zirconium in these materials been able to occupy either the A or B site. In a similar fashion to the antimony substituted material it is found that the crystallite size derived from the Scherrer analysis is much smaller than that of the unsubstituted material.

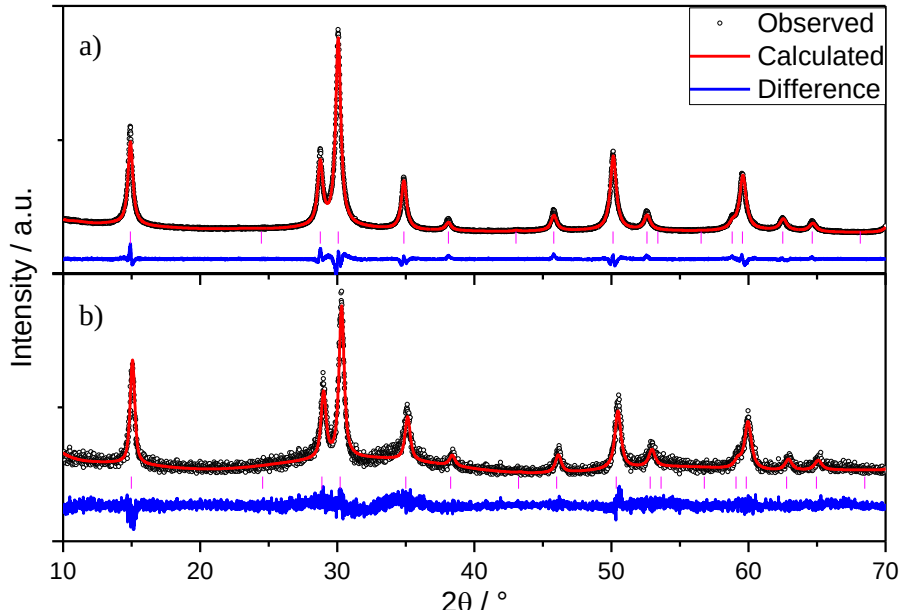

Figure 4.18: Rietveld refinements to powder XRD data (λ = 1.54056 Å), from $(Ca,Na)_{2-x}(Ir_{1-y}Zr_y)_2O_6 \cdot H_2O$, a) y = 0.25 and b) y = 0.50.

Table 4.8: Structural details of pyrochlores obtained from Rietveld refinement of powder XRD data of Zr substituted materials.

Atom	Site	*x*	*y*	*z*	Occ	U_{iso} / Å^2
25 % Zr Pyrochlore: *a* = 10.2471(5) Å / Crystallite Size = 15.4 ± 1.8 nm						
Ca	16*d*	0.5	0.5	0.5	0.594(13)	0.24(4)
Na	16*d*	0.5	0.5	0.5	0.24(2)	0.24(4)
Zr	16*d*	0.5	0.5	0.5	0.061(6)	0.24(4)
Ir	16*c*	0	0	0	0.795(3)	0.082(6)
Zr	16*c*	0	0	0	0.205(5)	0.082(6)
O	48*f*	0.3236(14)	0.125	0.125	0.99(2)	0.16(7)
O'	8*b*	0.375	0.375	0.375	1.00(5)	0.40(18)
50 % Zr Pyrochlore: *a* = 10.26542(11) Å / Crystallite Size = 14.4 ± 1.5 nm						
Ca	16*d*	0.5	0.5	0.5	0.579(3)	0.0315(5)
Na	16*d*	0.5	0.5	0.5	0.300(5)	0.0315(5)
Zr	16*d*	0.5	0.5	0.5	0.120(1)	0.0315(5)
Ir	16*c*	0	0	0	0.560(1)	0.0226(2)
Zr	16*c*	0	0	0	0.440(1)	0.0226(2)
O	48*f*	0.3328(2)	0.125	0.125	1.001(5)	0.0286(14)
O'	8*b*	0.375	0.375	0.375	0.998(6)	0.076(5)

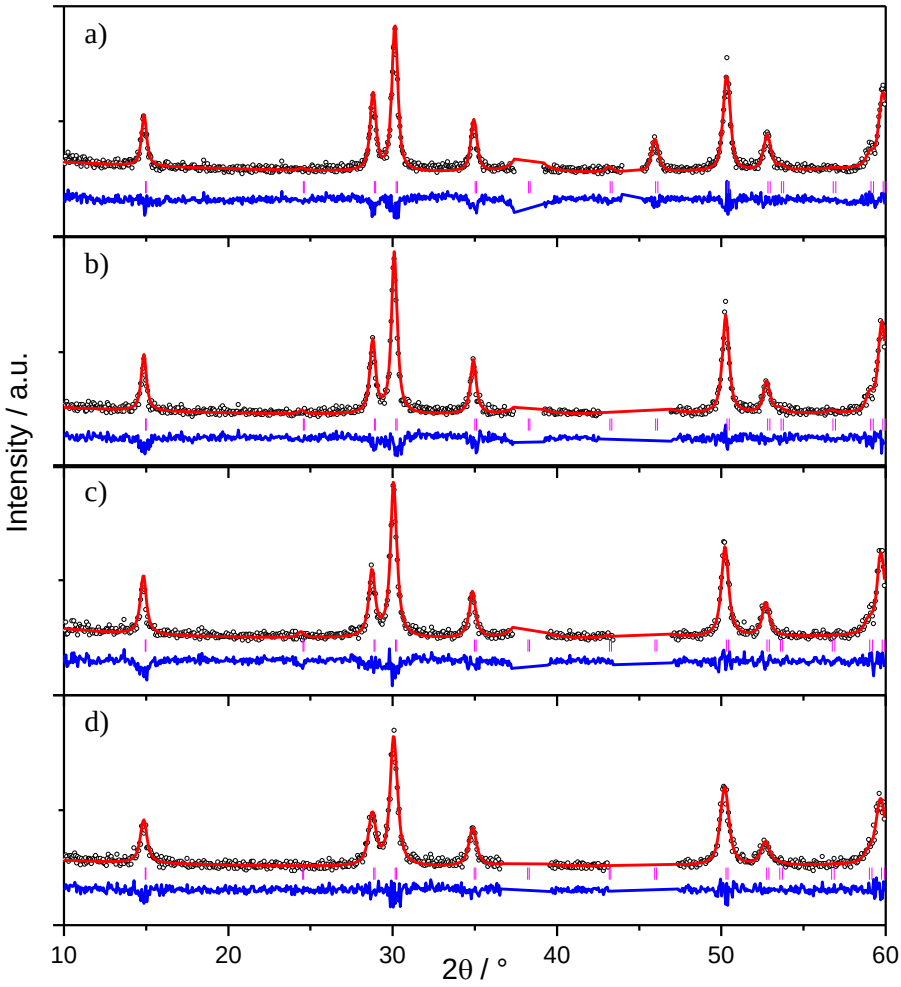

Figure 4.19: Le Bail fits to powder XRD data (λ = 1.5418 Å) from $(Ca,Na)_{2-x}(Ir_{1-y}Zr_y)_2O_6 \cdot H_2O$, a) y = 0.10, b) y = 0.20, c) y = 0.30 and d) y = 0.40.

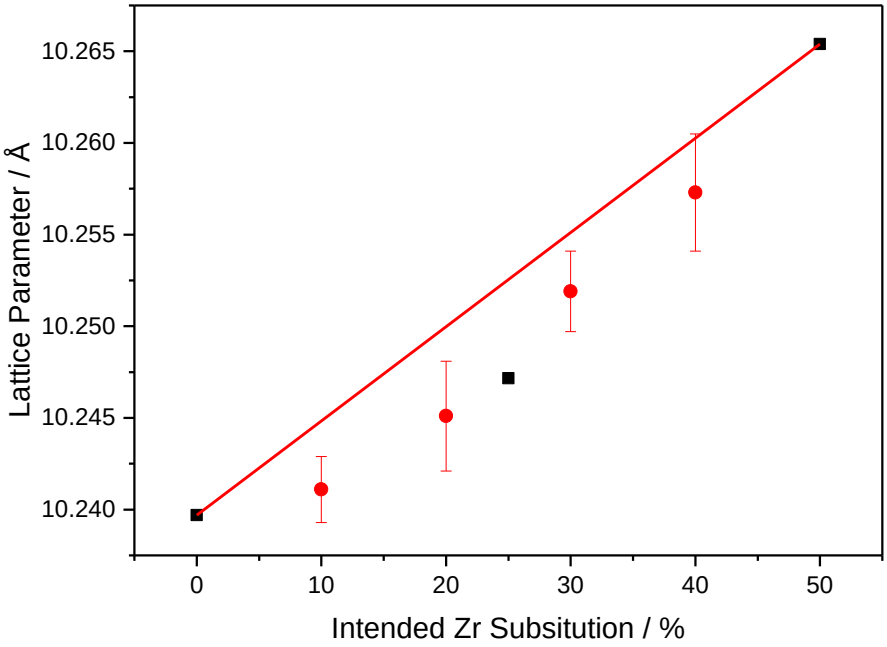

Figure 4.20: Refined lattice parameter as a function of intended zirconium substitution. Black points from Rietveld fits and red points from Le Bail fits. Red line is an extrapolation between the two extremes in composition.

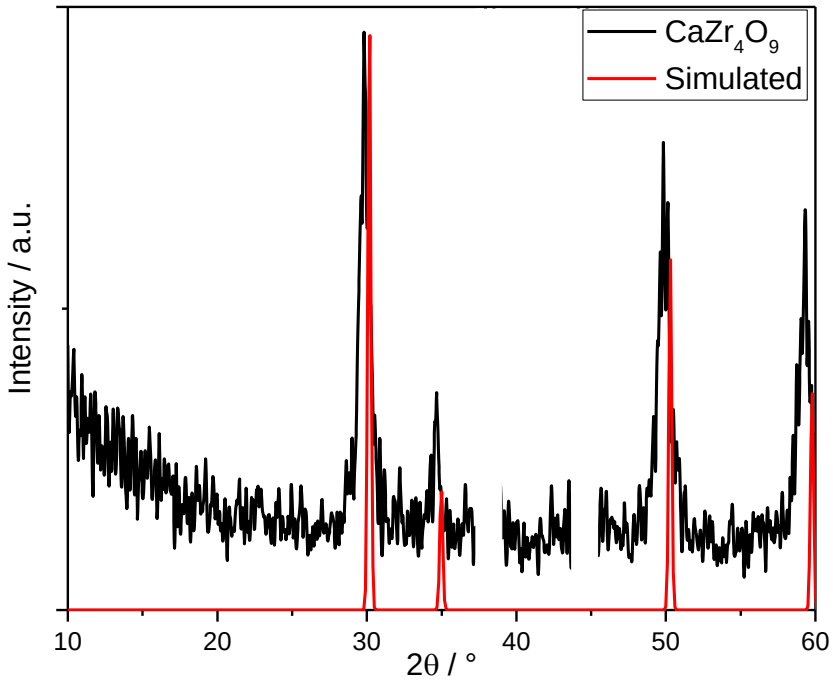

Figure 4.21: Powder XRD data (λ = 1.5418 Å) from $CaZr_4O_9$. Peaks arising from aluminium sample holder at 38 and 44 ° have been masked. Simulated pattern for same phase in red.

EDX analysis across the series of materials shows a linear increase in zirconium concentration, Figure 4.22, consistent with the powder XRD data.

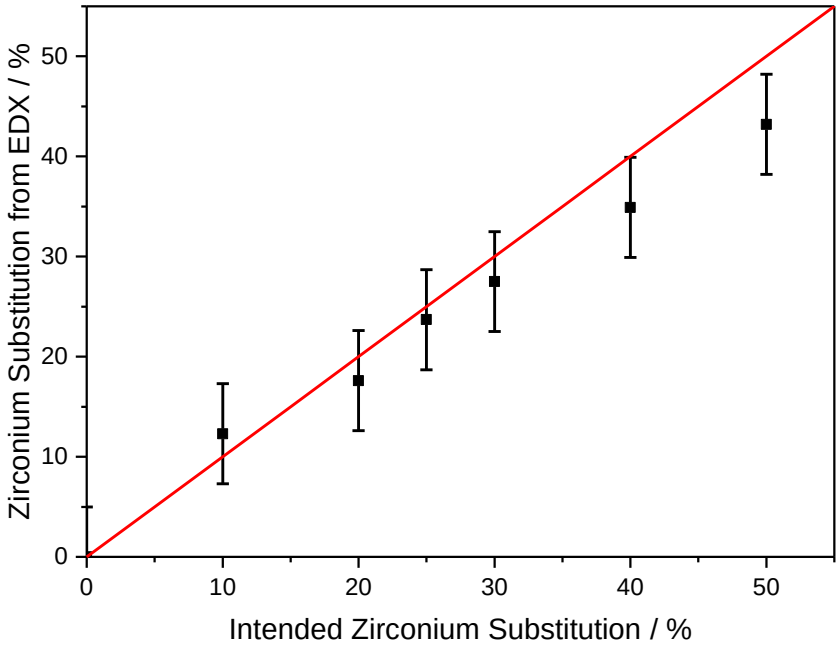

Figure 4.22: Measured zirconium content from EDX as a function of intended zirconium substitution.

XANES measurements were carried out to determine the oxidation state of the iridium found within the zirconium substituted materials. The white line position was used to determine the oxidation state, which was revealed to consistently be approximately +4.5 regardless of the level of zirconium substitution, Figure 4.23.

It was assumed that all the zirconium in the materials would be found in the +4 state, as this is the most stable oxidation state for non-metallic zirconium with electron configuration [Kr] $4d^2 5s^2$.

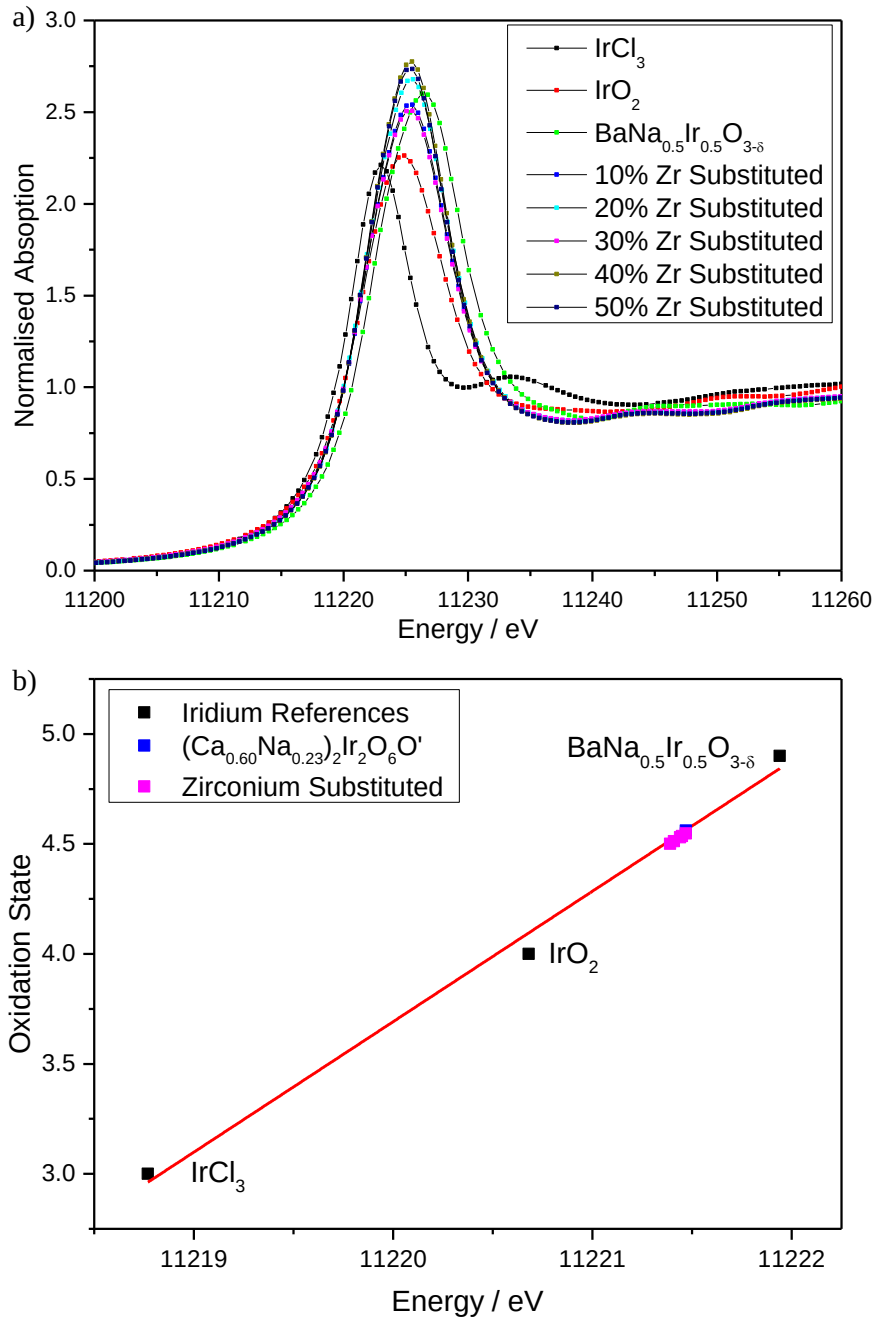

Figure 4.23: a) Ir L_{III}-edge XANES spectra of zirconium substituted pyrochlore materials and reference materials for calibration. b) White line Position against iridium oxidation state.

The powder neutron diffraction of the 50 % zirconium substituted material was initially fitted in the same manner as the pure iridium material, with zirconium occupying the same site as iridium, however this resulted in a poor fit, Figure 4.24, however when a small fraction of the total zirconium was placed on the 16*d* site a far superior fit was achieved, like in $(Na_{0.33}Ce_{0.53}Ti_{0.14})_2Ti_2O_7$, $(Bi_{1.88}Fe_{0.12})(Fe_{1.42}Te_{0.58})O_{6.87}$, $Lu_2Ti_2O_{6+x}$ and

$(Bi_{0.75}Zn_{0.25})_2(Zn_{0.25}Nb_{0.75})_2O_7$, where some of the B-site metal has been found on the A-site.[9,17–19]

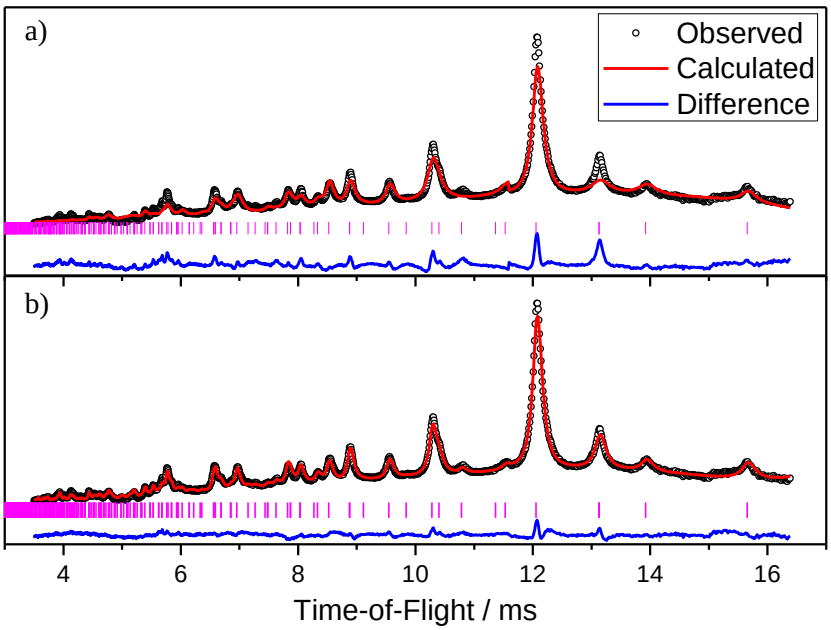

Figure 4.24: Rietveld refinements against time-of-flight neutron data from bank 5 of GEM for 50 % zirconium substituted calcium sodium iridium oxide. a) With all zirconium on 16*c* site. b) With a small fraction of zirconium on 16*d* site.

Table 4.9: Structural details of 50 % zirconium substituted calcium sodium iridium oxide pyrochlore obtained from Rietveld refinement of powder neutron diffraction data.

Atom	Site	*x*	*y*	*z*	Occ	U_{iso} / Å^2
50 % Zr Substituted Pyrochlore: *a* = 10.2318(3) Å						
Ca	16*d*	0.5	0.5	0.5	0.568(11)	0.0243(10)
Na	16*d*	0.5	0.5	0.5	0.315(15)	0.0243(10)
Zr	16d	0.5	0.5	0.5	0.120(7)	0.0243(10)
Ir	16*c*	0	0	0	0.560(3)	0.0095(2)
Zr	16*c*	0	0	0	0.440(3)	0.0095(2)
O	48*f*	0.3303(2)	0.125	0.125	1.000(3)	0.0152(2)
O'	8*b*	0.375	0.375	0.375	0.965(12)	0.0233(14)
H	32*e*	0.3289	0.3289	0.3289	0.48(3)	*

* U11 = 0.4342(16), U22 = 0.4342(16), U33 = 0.4342(16), U12 = -0.238(2), U13 = -0.238(2), U23 = -0.238(2)

The PDF for the 50 % zirconium substituted material was then fitted using the model produced from the Bragg scattering, Figure 4.25, with refinement for the lattice parameter and ADPs. The first observable atomic correlation is at ~2 Å and is considerably broader than the calculated, appearing to be comprised of two distinct correlations, suggesting significant deviation from the Rietveld pyrochlore structure at the local scale. Additionally

the remainder of the PDF fits poorly, and once r > 15 Å it becomes obvious that the model provided by average pyrochlore structure doesn't fit the data. This is likely due to the mismatch of ionic radius of zirconium, compared with every other metal in the structure. Eight co-ordinate zirconium has a radius of 0.84 Å, which is considerably smaller than eight co-ordinate calcium and sodium whose radii are 1.12 and 1.18 Å, respectively. On the other hand six co-ordinate zirconium with a radius of 0.72 Å is considerably larger than that of six co-ordinate iridium where Ir(IV) and Ir(V) have radii of 0.625 and 0.57 Å respectively. This is reflected in the ADPs of zirconium where for both the A and B sites they are much higher than the other atoms in the model, Table 4.10.

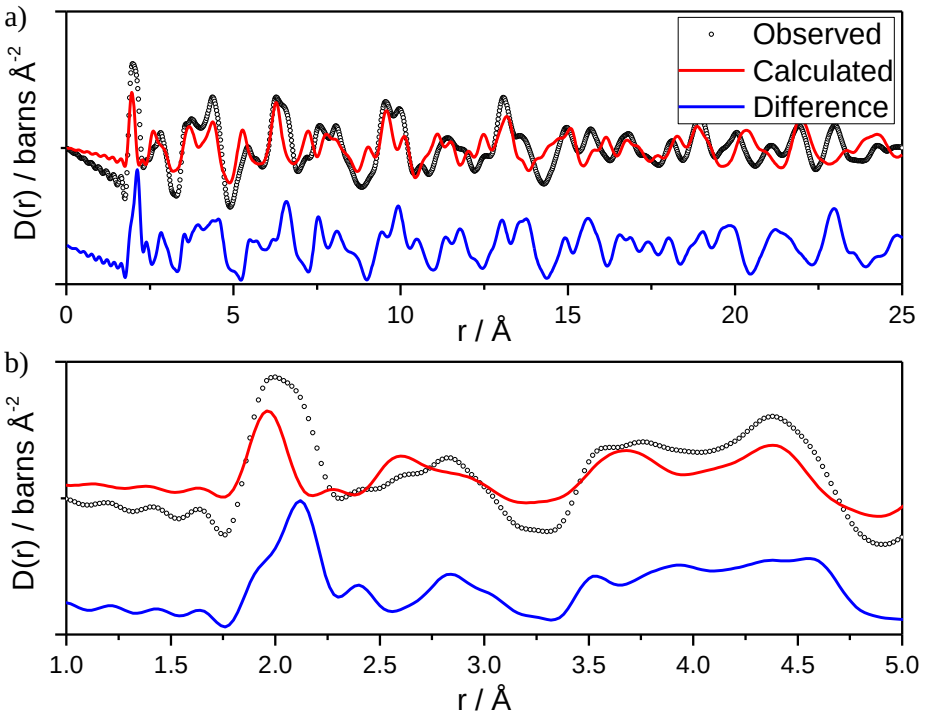

Figure 4.25: Fits of the Rietveld models against PDF data up to r = 25 Å and b) up to r = 5 Å of 50 % zirconium substituted calcium sodium iridium oxide pyrochlore.

Table 4.10: Structural details of 50 % zirconium substituted pyrochlore obtained from least squares refinement against PDF data.

Atom	Site	*x*	*y*	*z*	Occ	U_{iso} / Å^2
50 % Zr Substituted Pyrochlore: *a* = 10.250(6) Å						
Ca	16*d*	0.5	0.5	0.5	0.568	0.009(3)
Na	16*d*	0.5	0.5	0.5	0.315	0.009(3)
Zr	16*d*	0.5	0.5	0.5	0.120	0.009(3)
Ir	16*c*	0	0	0	0.560	0.020(3)
Zr	16*c*	0	0	0	0.440	0.020(3)
O	48*f*	0.3294	0.125	0.125	1.000	0.043(6)
O'	8*b*	0.375	0.375	0.375	0. 965	0.030(8)
H	32*e*	0.3289	0.3289	0.3289	0.482	0.7626

Like the unsubstituted material, TGA-MS was employed to look for the crystal water proposed from fitting the neutron diffraction data, Figure 4.26. An initial mass loss of 2.3 % is observed, up to the end of the 4 hour hold at 120 °C, and can be attributed to the loss of surface water. Any further loss can be attributed to crystal water, assuming this is lost by 300 °C, the temperature at which the pyrochlore phase collapses, as observed in the thermodiffractometry, Figure 4.27. At this point 3.6 % of the remaining mass is lost, slightly less than the theoretical loss of 3.7 % expected if the O' site is fully occupied by H_2O, however this reduced value supports the model produced by neutron diffraction data where there is a small vacancy on the O' site. Further losses are less well defined than that of the unsubstituted material, however this is somewhat expected as various oxide phase changes and phase separations are happening as the temperature increases.

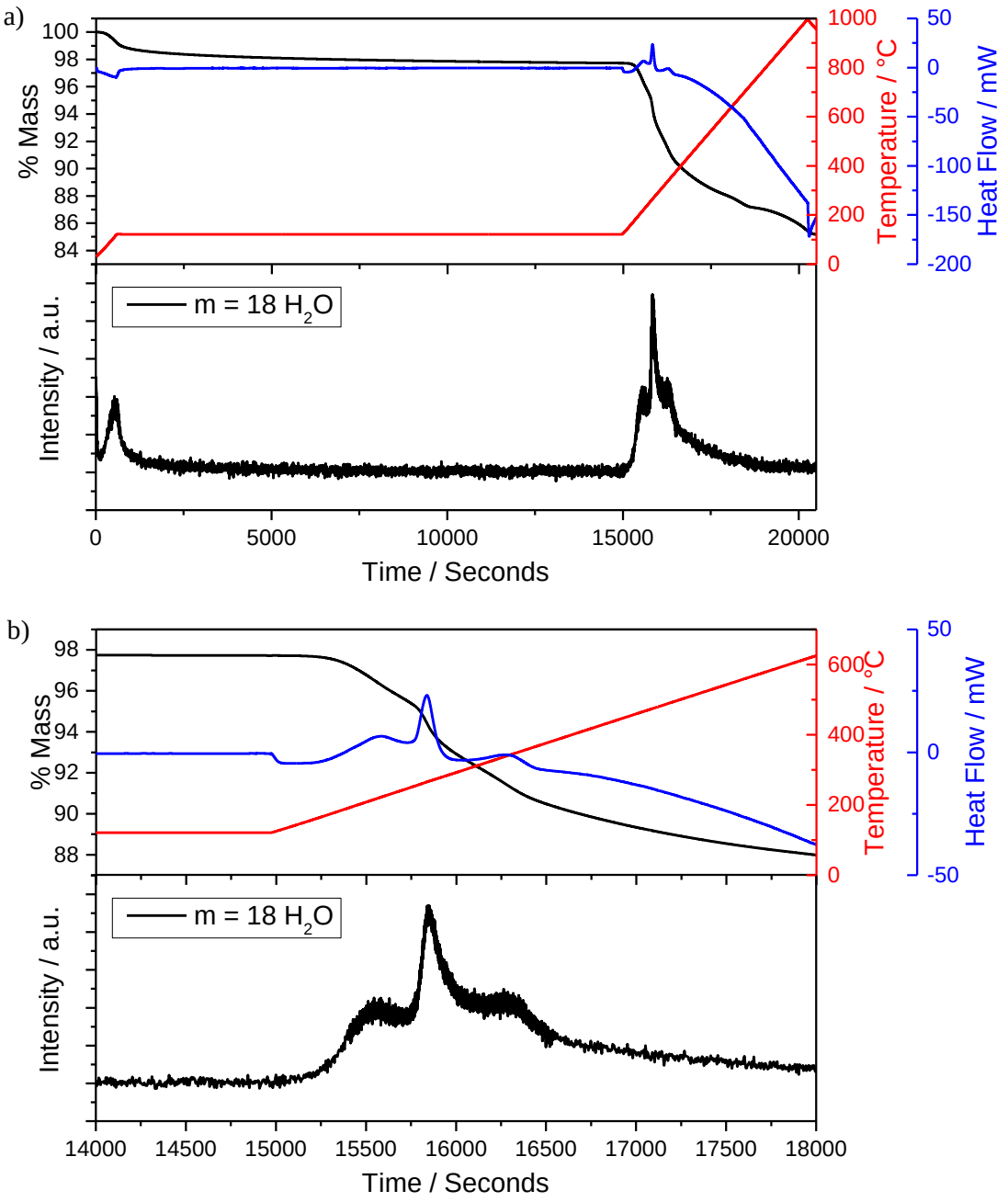

Figure 4.26: TGA-MS plots a) complete range and b) zoom of region with loss of crystal water of 50 % zirconium substituted calcium sodium iridium oxide.

Thermodiffractometry reveals that up to 200 °C there is no apparent change in the material. Above this there is a decrease in lattice parameter, however unlike the unsubstituted material as the material loses this water the pyrochlore phase collapses, separating into ZrO_2 and IrO_2. At 400 °C the iridium oxide starts to further reduce to iridium metal.

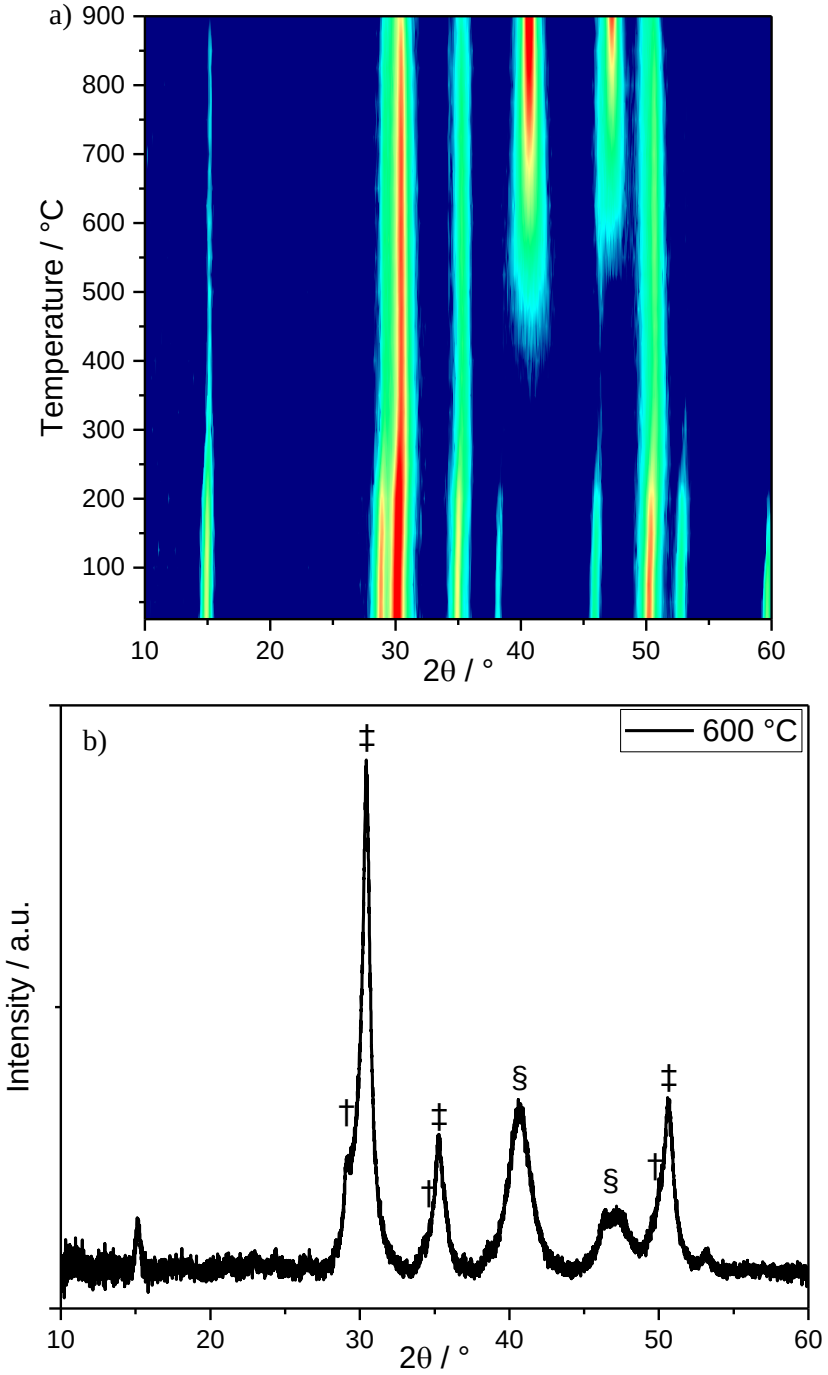

Figure 4.27: a) Thermodiffractometry (λ = 1.5418 Å) of 50 % zirconium substituted calcium sodium iridium oxide. b) XRD pattern at 600 °C, † denoting peaks arising from IrO_2, ‡ denoting peaks arising from ZrO_2 and § denoting peaks arising from Ir metal.

4.4.3 Ruthenium Substitution

The powder XRD patterns of the materials synthesised with the assumed formula $(Ca,Na)_{2-x}(Ir_{1-y}Ru_y)_2O_6 \cdot H_2O$, can be indexed and fitted to a cubic pyrochlore cell using space group $Fd\bar{3}m$ within the range $0.25 \leq y \leq 1$, Figure 4.28 and Table 4.11. Across the solid solution the lattice parameter decreases, Figure 4.29, which is unsurprising considering

Ir(IV) 0.625 Å and Ir(V) 0.57 Å are slightly larger than Ru(IV) 0.62 Å and Ru(V) 0.565 Å.[13] The IrO_2 observed in the 25% substituted pattern can be explained by the tendency not to form pure iridate pyrochlore phase at lower NaOH concentrations, see Section 4.5.2. The y = 1.0 material (a = 10.2207 Å), has a larger lattice parameter than $Ca_{1.5}Ru_2O_7$ (a = 10.1997 Å),[12] which is another calcium ruthenium oxide synthesised hydrothermally using $KRuO_4$ as a ruthenium source, highlighting how reagent choice and reaction conditions can affect the final material.

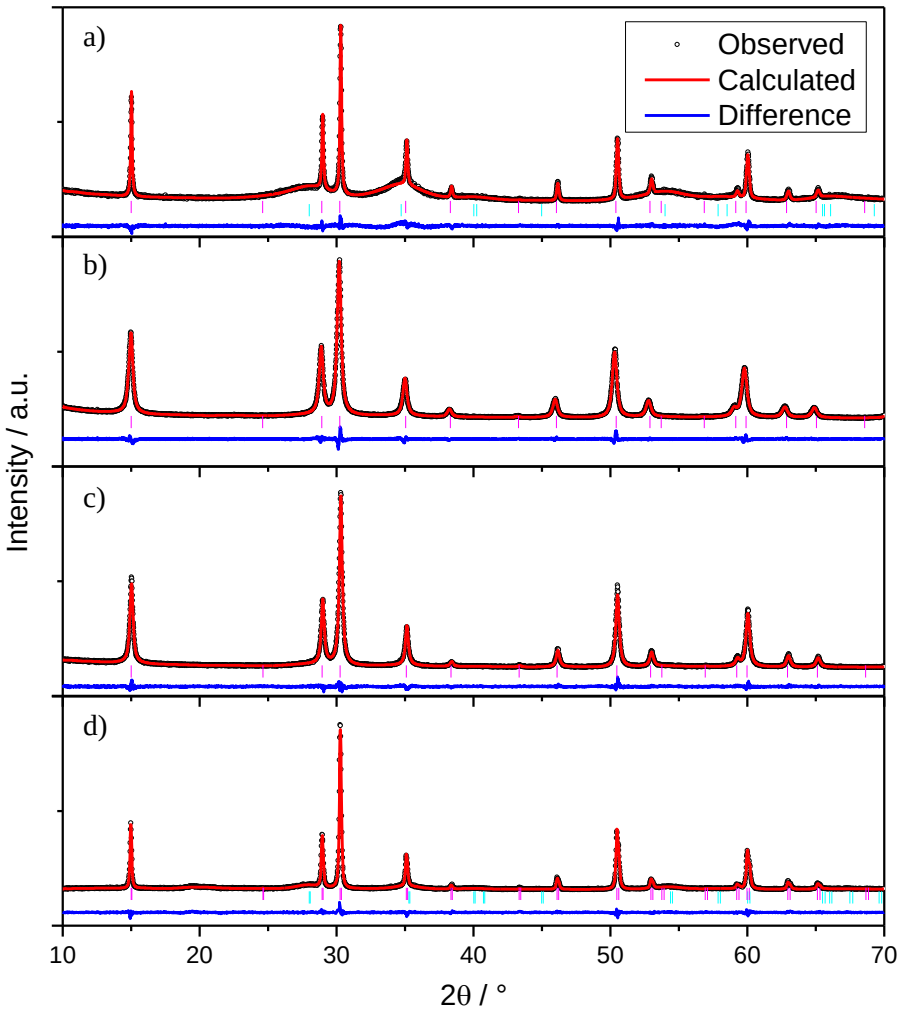

Figure 4.28: Rietveld refinements to powder XRD data (λ = 1.54056 Å) from $(Ca,Na)_{2-x}(Ir_{1-y}Ru_y)_2O_6 \cdot H_2O$, a) y = 0.25, b) y = 0.50, c) y = 0.75 and d) y = 1.00.

Table 4.11: Structural details of pyrochlores obtained from Rietveld refinement of powder XRD data, of ruthenium substituted materials.

Atom	Site	*x*	*y*	*z*	Occ	U_{iso} / Å^2
25 % Ru Pyrochlore: a = 10.23528(8) Å / Crystallite Size = 35.2 ± 10.0 nm						
Ca	16*d*	0.5	0.5	0.5	0.637(5)	0.020(2)
Na	16*d*	0.5	0.5	0.5	0.362(9)	0.020(2)
Ir	16*c*	0	0	0	0.748(3)	0.0164(4)
Ru	16*c*	0	0	0	0.252(3)	0.0164(4)
O	48*f*	0.3327(7)	0.125	0.125	0.998(13)	0.027(3)
O'	8*b*	0.375	0.375	0.375	1.00(2)	0.012(7)
50 % Ru Pyrochlore: *a* = 10.23414(9) Å / Crystallite Size = 19.2 ± 2.1 nm						
Ca	16*d*	0.5	0.5	0.5	0.669(3)	0.0888(9)
Na	16*d*	0.5	0.5	0.5	0.321(1)	0.0888(9)
Ir	16*c*	0	0	0	0.444(1)	0.0151(2)
Ru	16*c*	0	0	0	0.556(1)	0.0151(2)
O	48*f*	0.3266(3)	0.125	0.125	1.000(5)	0.0053(8)
O'	8*b*	0.375	0.375	0.375	1.001(11)	0.018(3)
75 % Ru Pyrochlore: *a* = 10.22500(7) Å / Crystallite Size = 25.9 ± 2.2 nm						
Ca	16*d*	0.5	0.5	0.5	0.619(2)	0.0150(7)
Na	16*d*	0.5	0.5	0.5	0.325(4)	0.0150(7)
Ir	16*c*	0	0	0	0.229(1)	0.0131(6)
Ru	16*c*	0	0	0	0.771(1)	0.0131(6)
O	48*f*	0.3239(3)	0.125	0.125	1.000(5)	0.0017(9)
O'	8*b*	0.375	0.375	0.375	1.001(11)	0.025(3)
100 % Ru Pyrochlore: *a* = 10.22067(9) Å / Crystallite Size = 50.4 ± 3.7 nm						
Ca	16*d*	0.5	0.5	0.5	0.651(4)	0.0443(6)
Na	16*d*	0.5	0.5	0.5	0.351(8)	0.0443(6)
Ru	16*c*	0	0	0	1.000(2)	0.0138(4)
O	48*f*	0.3372(5)	0.125	0.125	1.000(9)	0.041(2)
O'	8*b*	0.375	0.375	0.375	1.001(11)	0.045(6)

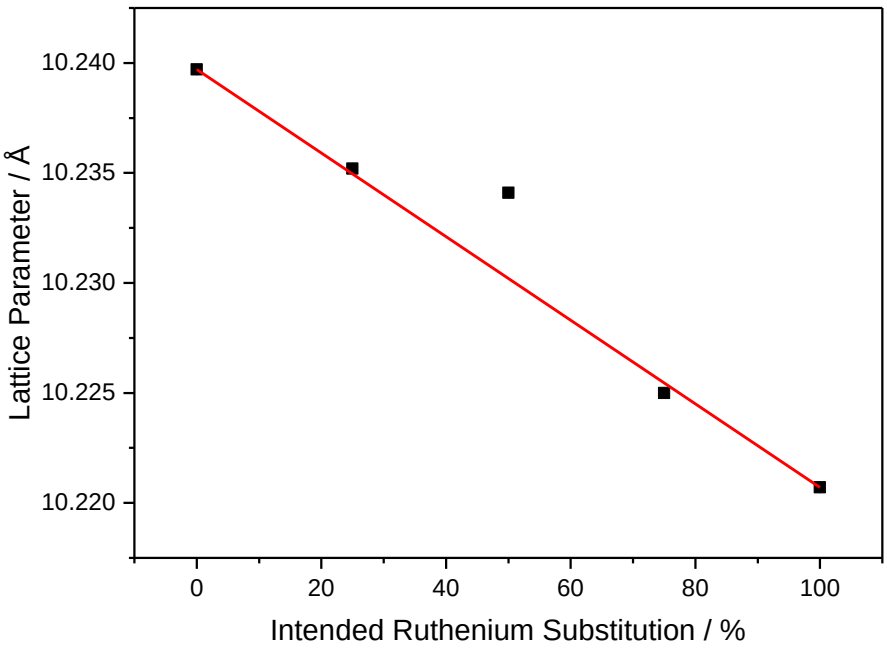

Figure 4.29: Refined lattice parameter as a function of intended ruthenium substitution.

EDX analysis across the series of materials produced from the optimised reactions shows a linear increase in ruthenium concentration across the solid solution, Figure 4.30. With the observed ruthenium concentration been almost identical to the intended amount, suggesting the reagent is being fully utilised. This is in contrast to the materials produced in 10 M sodium hydroxide where the filtrate has a distinctive orange colour, suggesting the presence of Na_2RuO_4 in solution.

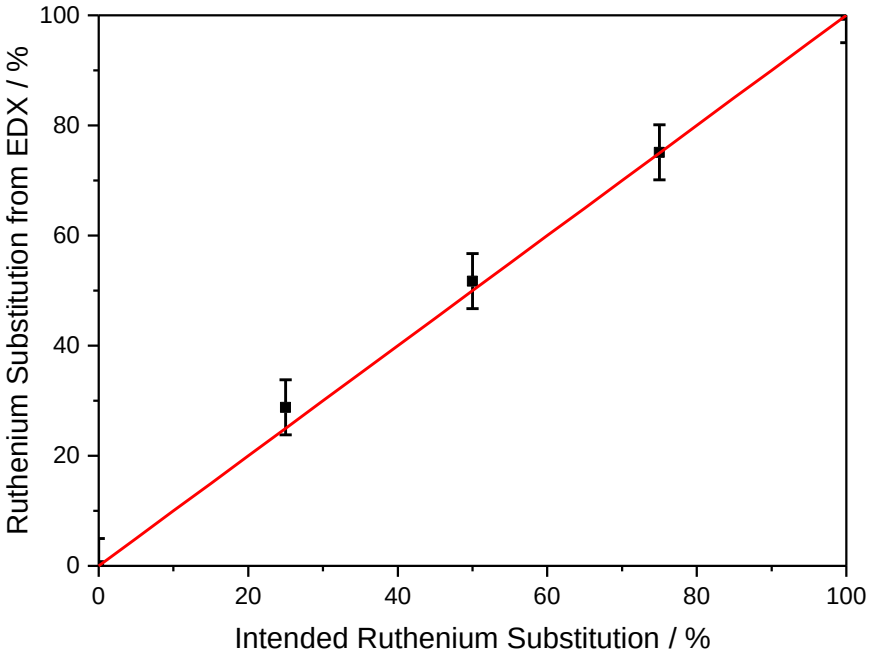

Figure 4.30: Measured ruthenium content from EDX as a function of nominal ruthenium substitution.

XANES measurements were carried out at both the Ru K-edge and the Ir L_{III}-edge to determine the oxidation state of both the ruthenium and iridium in the synthesised materials. The white line position was used to determine the oxidation state, which was revealed to be approximately +4.5 in all the synthesised materials, Figure 4.31. The edge position, when the normalised absorption is equal to 0.5, was used to calculate the ruthenium oxidation state. In the mixed metal materials the oxidation state was always found to be approximately +5, however in the pure ruthenium material the ruthenium appears to be further oxidised, tending towards +5.5 much like the previously reported $Ca_{1.5}Ru_2O_7$, [12] Figure 4.32.

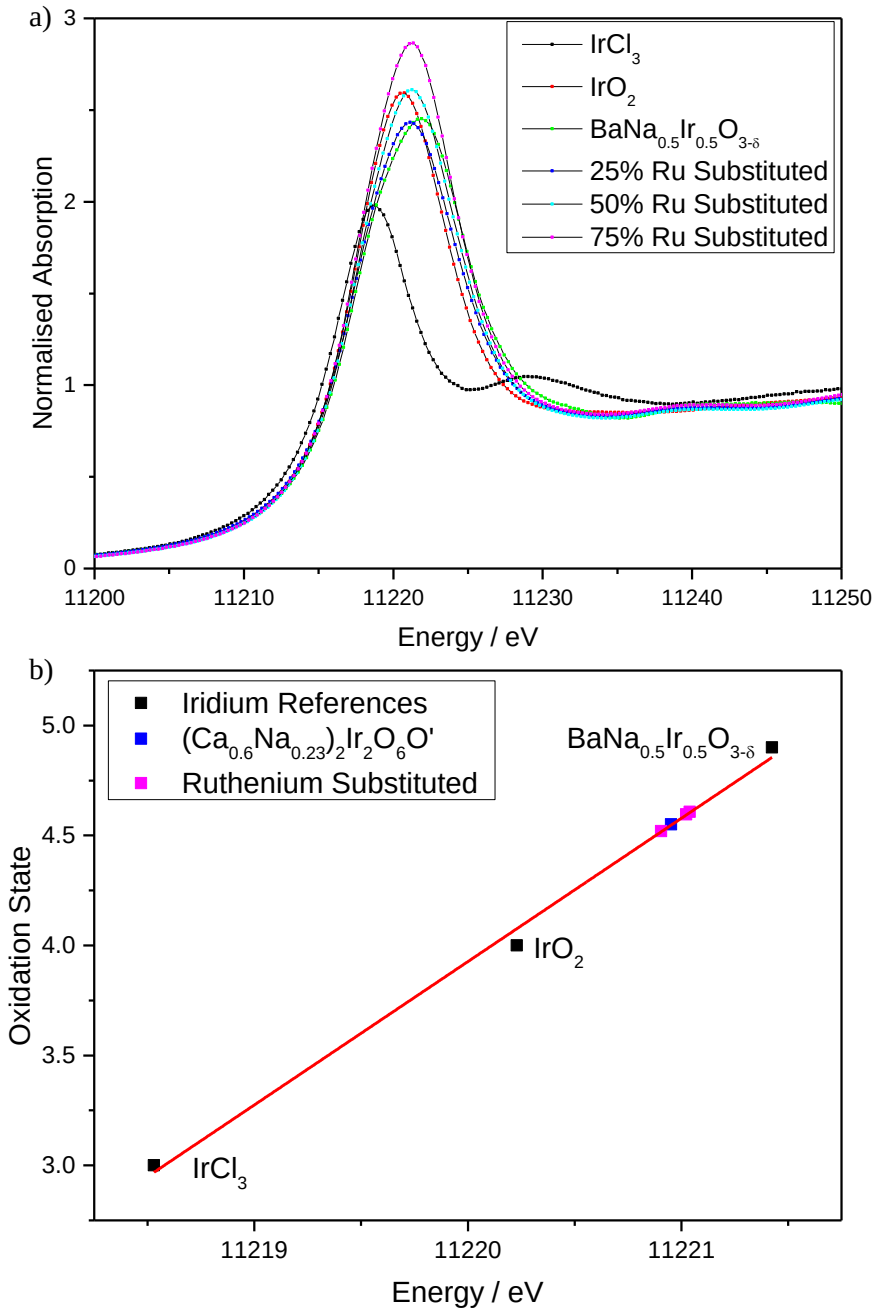

Figure 4.31: a) Ir L_{III}-edge XANES spectra of ruthenium substituted pyrochlore materials and reference materials for calibration. b) White line position against iridium oxidation state.

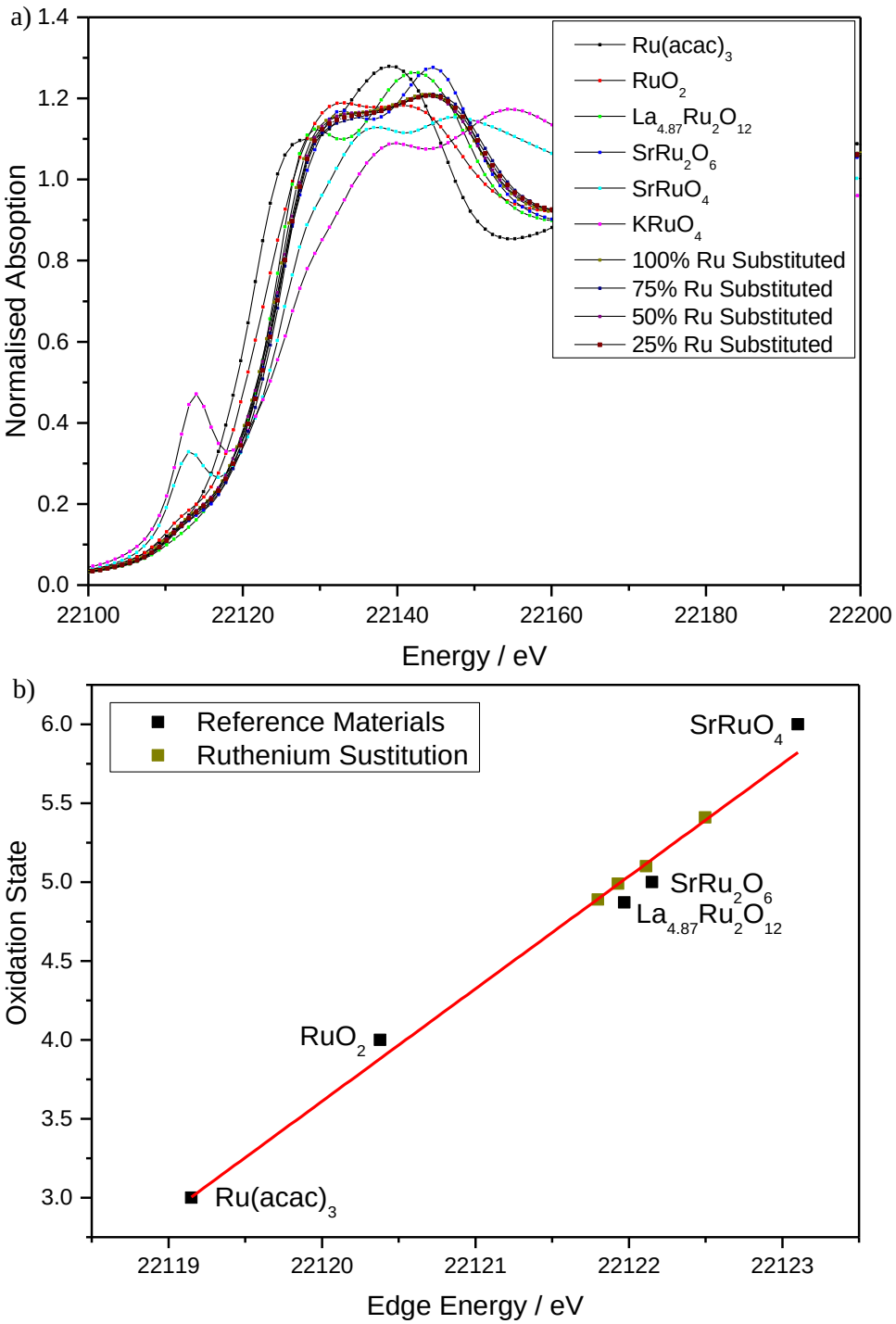

Figure 4.32: a) Ru K-edge XANES spectra of ruthenium substituted pyrochlore materials and reference materials for calibration. b) Edge Position against ruthenium oxidation state.

The neutron diffraction of the 50 % ruthenium substituted material can be fitted in the same manner as the pure iridium material, with ruthenium occupying the same site as iridium, Figure 4.33.

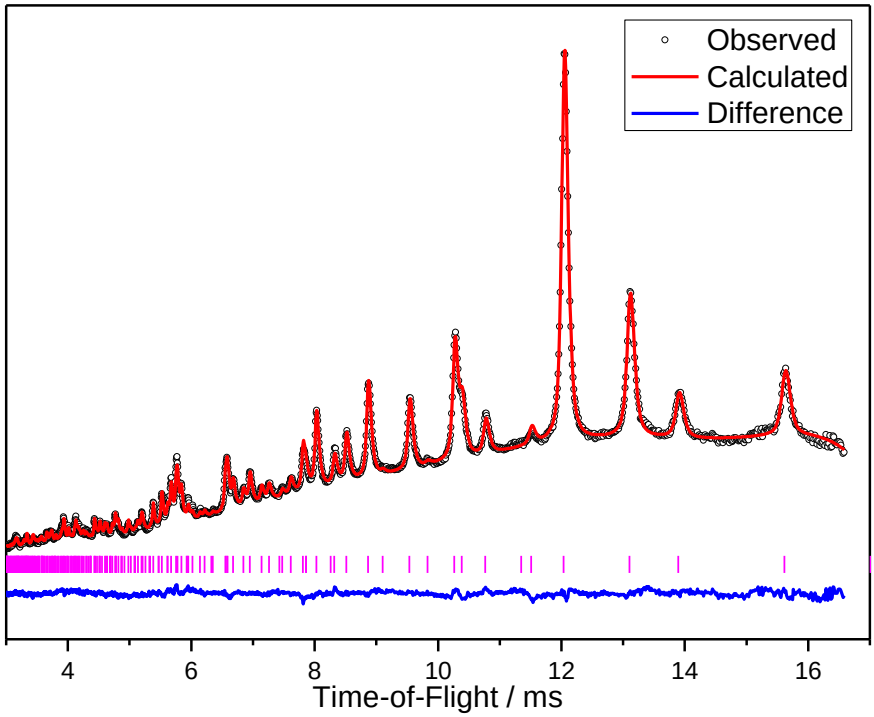

Figure 4.33: Rietveld refinements against time-of-flight neutron data from bank 5 of GEM for 50 % ruthenium substituted calcium sodium iridium oxide.

Table 4.12: Structural details of 50 % ruthenium substituted calcium sodium iridium oxide pyrochlore obtained from Rietveld refinement of powder neutron diffraction data.

Atom	Site	*x*	*Y*	*z*	Occ	U_{iso} / Å^2
50 % Ru Substituted Pyrochlore: *a* = 10.23360(17) Å						
Ca	16*d*	0.5	0.5	0.5	0.594(5)	0.0310(8)
Na	16*d*	0.5	0.5	0.5	0.320(9)	0.0310(8)
Ir	16*c*	0	0	0	0.496(6)	0.00726(5)
Ru	16*c*	0	0	0	0.504(6)	0.00726(5)
O	48*f*	0.32304(10)	0.125	0.125	1.000(2)	0.1072(12)
O'	8*b*	0.375	0.375	0.375	0.990(6)	0.0280(9)
H	32*e*	0.3289	0.3289	0.3289	0.495(13)	*

* U11 = 0.7970(9), U22 = 0.3669(9) , U33 = 0.7970(9), U12 = -0.2911(7), U13 = -0.3972(7), U23 = -0.2911(7)

The PDF for the 50 % ruthenium substituted material was then fitted using the model produced from the Bragg scattering, Figure 4.34, with refinement of the lattice parameter and the ADPs, Table 4.3 The r > 10 Å region fits very well and the low r region fits reasonably well. The first observable atomic correlation is at ~1.96 Å and agrees well with the B-O distance extracted from the Bragg scattering. The next feature between 2.3-3.2 Å has multiple contributions and fits less well, however like the unsubstituted material the fit to the PDF is much better than other pyrochlores using the ideal structure model.[9]

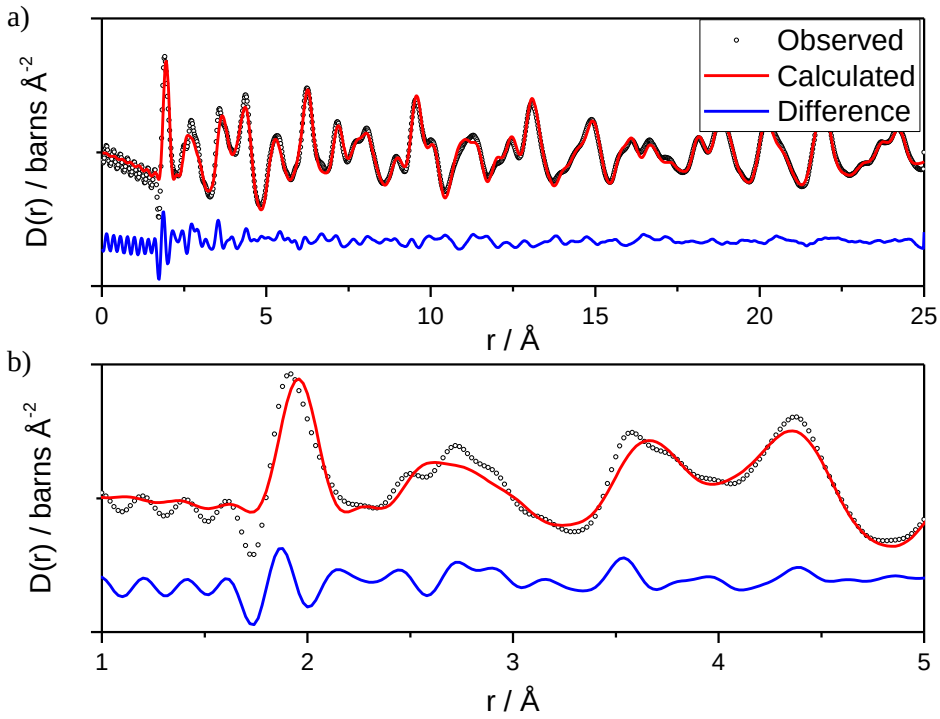

Figure 4.34: Fits of the Rietveld models against PDF data a) up to r = 25 Å and b) up to r = 5 Å of 50 % ruthenium substituted calcium sodium iridium oxide pyrochlore

Table 4.13: Structural details of 50 % ruthenium substituted pyrochlore obtained from least squares fitting of PDF data.

Atom	Site	*x*	*Y*	*z*	Occ	U_{iso} / Å^2
50 % Ru Substituted Pyrochlore: *a* = 10.217(3) Å						
Ca	16*d*	0.5	0.5	0.5	0.594	0.024(4)
Na	16*d*	0.5	0.5	0.5	0.321	0.024(4)
Ir	16*c*	0	0	0	0.496	0.0113(10)
Ru	16*c*	0	0	0	0.504	0.0113(10)
O	48*f*	0.3230	0.125	0.125	1.000	0.0144(9)
O'	8*b*	0.375	0.375	0.375	0.990	0.031(5)
H	32*e*	0.3289	0.3289	0.3289	0.495	0.7627

Like the unsubstituted material, TGA-MS was employed to look for the crystal water proposed from fitting the neutron diffraction data, Figure 4.35. An initial mass loss of 1.7 % is observed, up to the end of the 4 hour hold at 120 °C, and is attributed to the loss of surface water. Using the mass loss at 300 °C the temperature the lattice parameter stops shifting in the thermodiffractometry, a loss of 4.0 % of the remaining mass is observed slightly greater the theoretical loss of 3.8 % we expect if the O' site is fully occupied by H_2O. Exceeding

300 °C results in the conversion of pyrochlore oxide to rutile oxide. At 450 °C we then observe the initial reduction of oxide to iridium and or ruthenium metal. Then between 700-800 °C we see the complete collapse of the rutile phase to metal and $CaRuO_3$. All these phase changes correspond with the mass losses observed in the TGA.

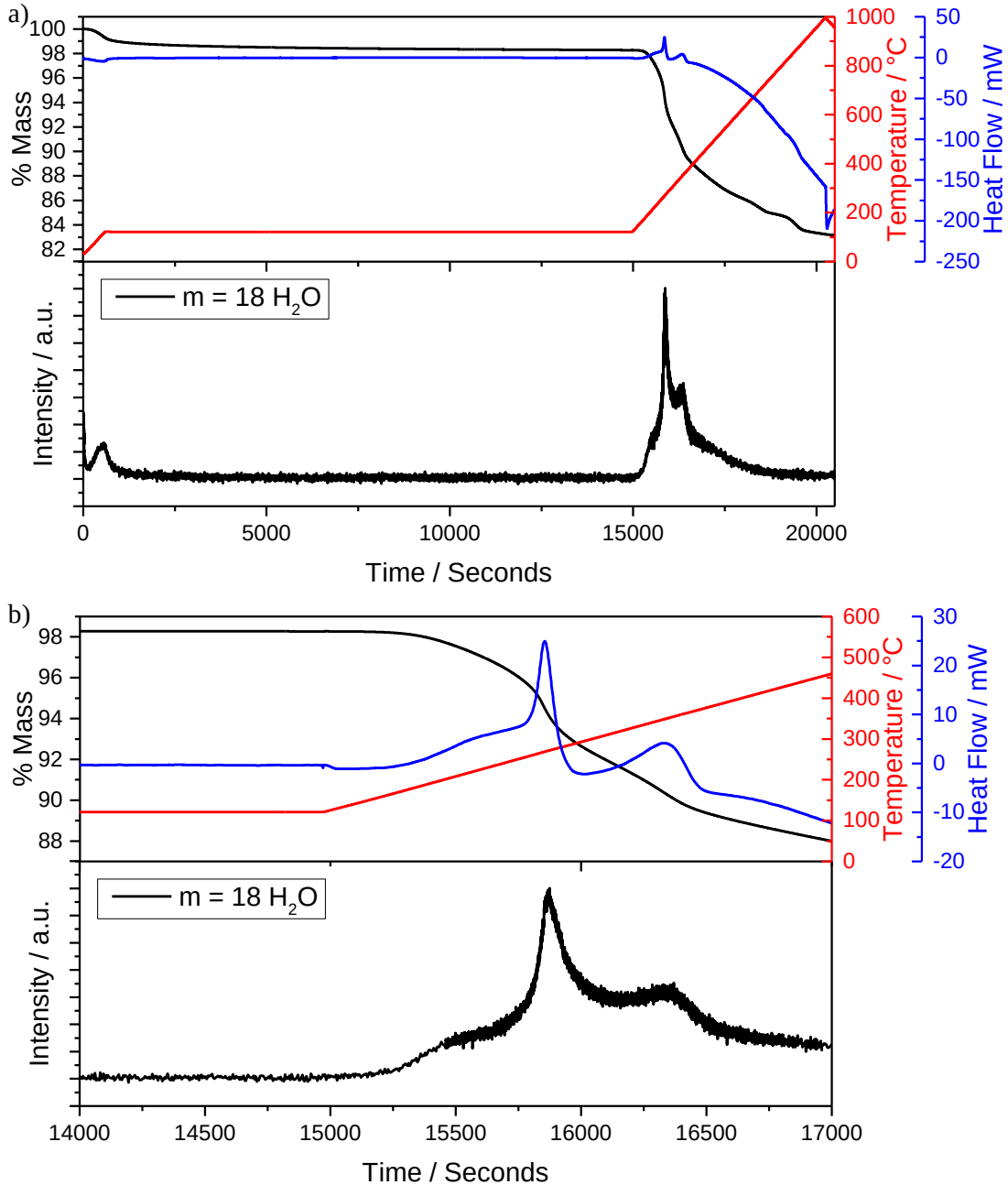

Figure 4.35: TGA-MS plots a) complete range and b) zoom of region with loss of crystal water of 50 % ruthenium substituted calcium sodium iridium oxide.

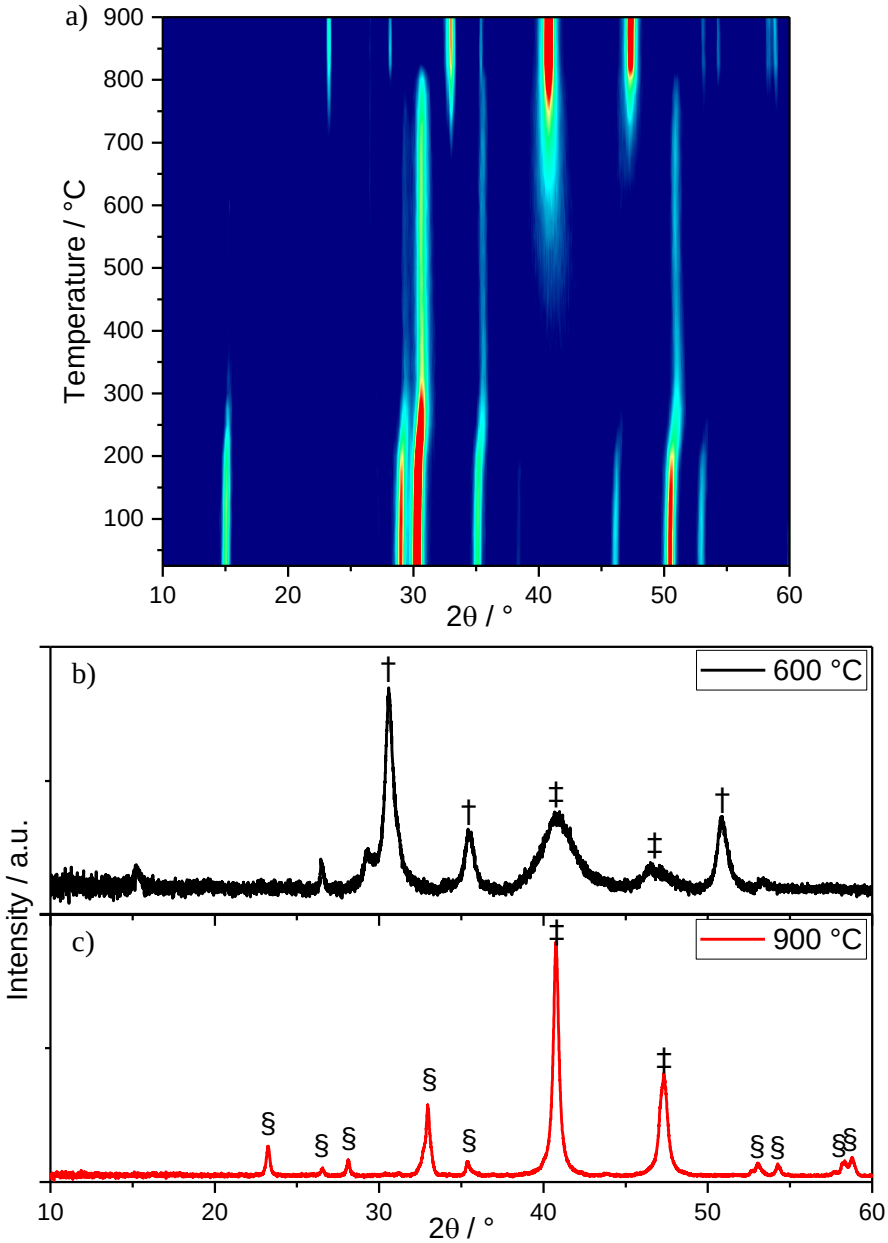

Figure 4.36: a) Thermodiffractometry (λ = 1.5418 Å) of 50 % ruthenium substituted calcium sodium iridium oxide. b) XRD pattern at 600 °C, † denoting peaks arising from $(Ru,Ir)O_2$, ‡ denoting peaks arising from Ir metal. c) XRD pattern at 900 °C, § denoting peaks arising from $CaRuO_3$, ‡ denoting peaks arising from Ir metal.

4.4.4 Osmium Substitution

The powder XRD patterns of the materials synthesised with the assumed formula $(Ca,Na)_{2-x}(Ir_{1-y}Os_y)_2O_6 \cdot H_2O$, can be indexed and fitted to a cubic pyrochlore cell using space group $Fd\bar{3}m$ within the range $0.25 \leq y \leq 1$, Figure 4.37. There is an initial drop in lattice parameter as osmium is substituted with iridium, however once $y \geq 0.25$ the lattice parameter

increases across the solid solution, Figure 4.38, consistent with Ir(IV) 0.625 Å and Ir(V) 0.57 Å having smaller ionic radii than Os(IV) 0.63 Å and Os(V) 0.575 Å.[13]

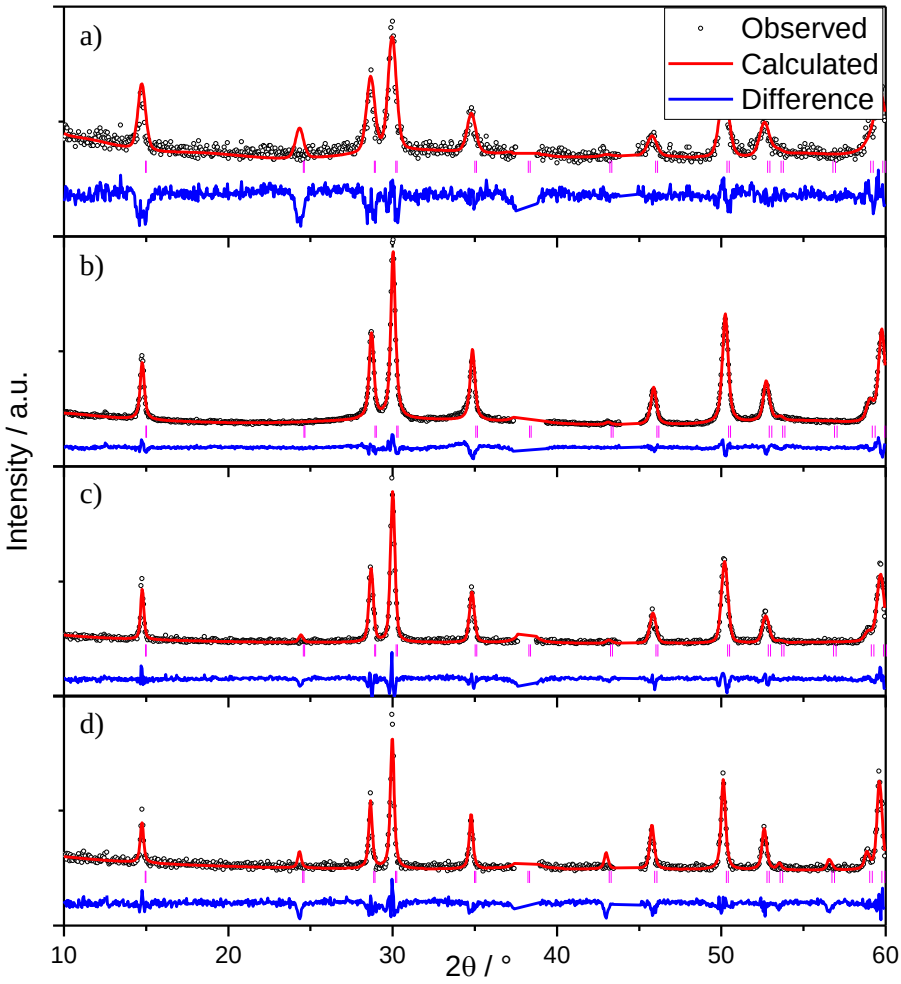

Figure 4.37: Le Bail fits to powder XRD data (λ = 1.5418 Å) from $(Ca,Na)_{2-x}(Ir_{1-y}Os_y)_2O_6 \cdot H_2O$, a) y = 0.25, b) y = 0.5, c) y = 0.75 and d) y = 1.00. Regions at 38° and 44° are excluded as peaks are due to aluminium sample holder.

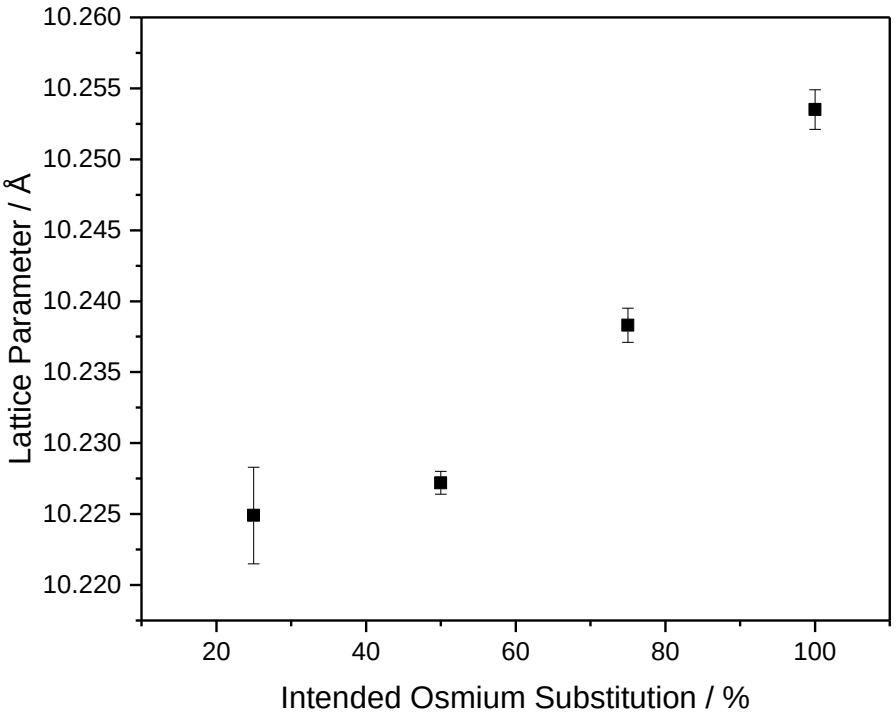

Figure 4.38: Refined lattice parameter as a function of intended osmium substitution.

EDX analysis across the series of materials produced from the reactions shows a linear increase in osmium concentration across the solid solution, Figure 4.39. The micrographs of the $(Ca,Na)_{2-x}Os_2O_6O'$ material present predominantly particles adopting a octahedral geometry, Figure 4.40, a common particle shape among hydrothermally synthesised pyrochlores.[12,14]

Characterisation of the osmium substituted materials was not continued as it became apparent that osmium was leaching out of the materials under ambient conditions, with staining of the sample containers. The route of osmium leaching likely involves the volatilisation of osmium in the form of OsO_4, a white solid or pale yellow liquid that readily volatilises. The highly toxic nature of osmium tetroxide made it unwise to consider scale up synthesis of the osmium substituted pyrochlore materials for electrocatalytic testing.

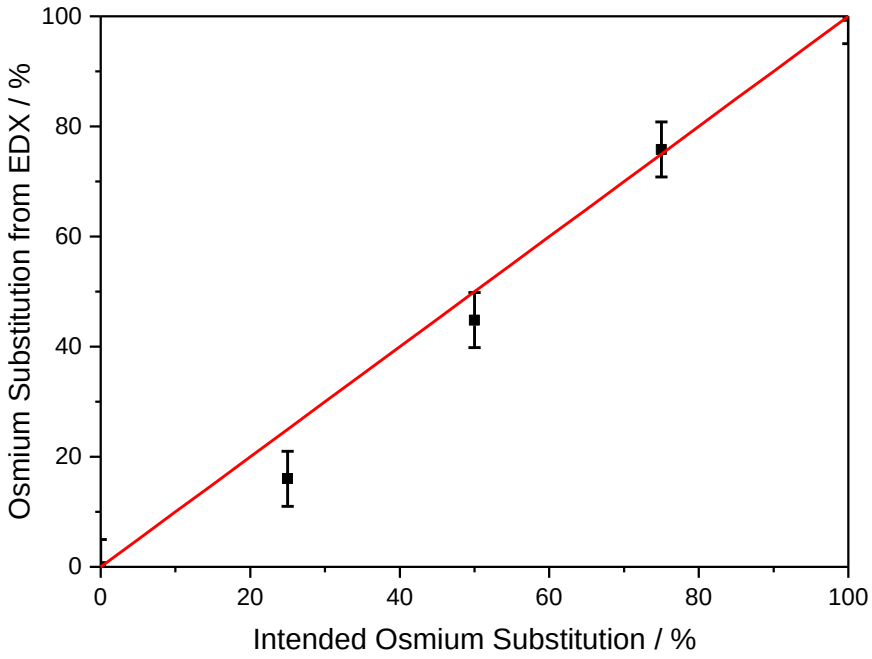

Figure 4.39: Measured osmium content from EDX as a function of intended osmium substitution.

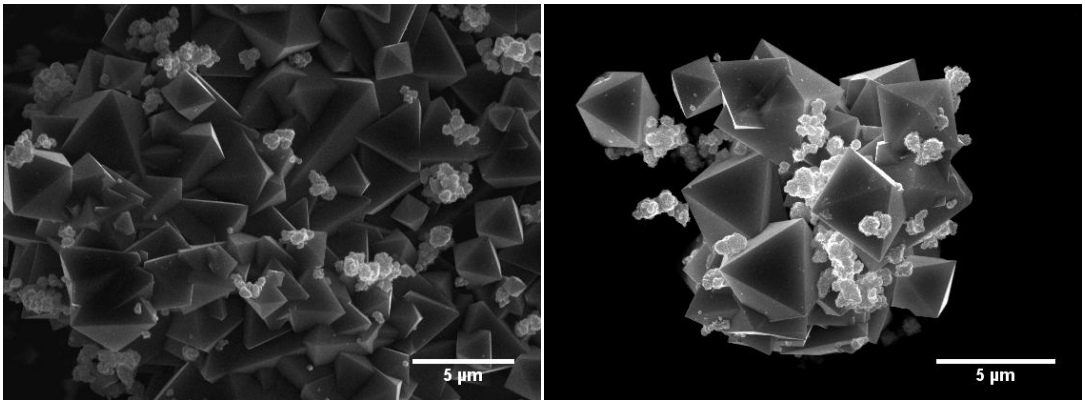

Figure 4.40: Typical Scanning electron micrographs of $(Ca,Na)_{2-x}Os_2O_6O'$.

4.4.5 Rhodium Substitution

The powder XRD patterns of the materials synthesised with the assumed formula $(Ca,Na)_{2-x}(Ir_{1-y}Rh_y)_2O_6{\cdot}H_2O$, can be indexed and fitted to a cubic pyrochlore cell using space group $Fd\bar{3}m$ where y = 0.15 and 0.3, Figure 4.41. When rhodium is substituted into the material the lattice parameter increases, Figure 4.42, consistent with Ir(IV) 0.625 Å and Ir(V) 0.57 Å being smaller than Rh(III) 0.665 Å and Rh(IV) 0.6 Å.[13] Rhodium is extremely hard to oxidise beyond the +3 state and as such the literature on the synthesis and characterisation of Rh^{4+} and Rh^{5+} oxides is somewhat sparse.[20,21] Given it is substituting $Ir^{4.5+}$ in the synthesised

materials, initially it was believed that all the rhodium was found in at least the +4 state, however given the extreme conditions needed to oxidise rhodium, it is possible the rhodium could have an oxidation state as low as +3. Substituting rhodium in place of iridium in these materials has little effect on the crystallite size, however there is a slight reduction for the y = 0.3 material.

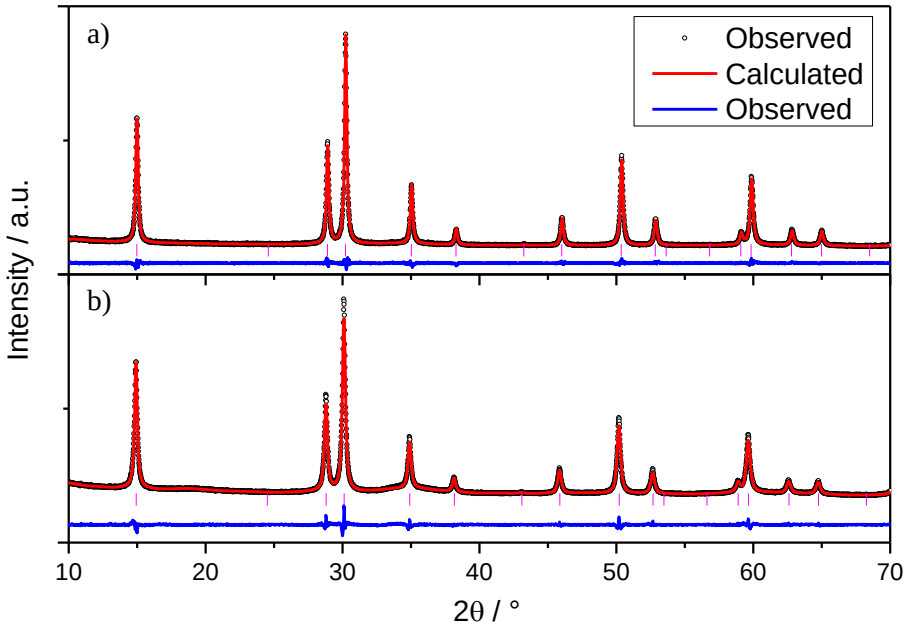

Figure 4.41: Rietveld refinements against powder XRD data (λ = 1.54056 Å) from $(Ca,Na)_{2-x}(Ir_{1-y}Rh_y)_2O_6 \cdot H_2O$, a) y = 0.15 and b) y = 0.3.

Table 4.14: Structural details of pyrochlores obtained from Rietveld refinement of powder XRD data, of Rh substituted materials.

Atom	Site	*x*	*y*	*z*	Occ	U_{iso} / Å^2
15 % Rh Pyrochlore: *a* = 10.24467(5) Å / Crystallite Size = 32.4 ± 3.5 nm						
Ca	16*d*	0.5	0.5	0.5	0.630(3)	0.0327(9)
Na	16*d*	0.5	0.5	0.5	0.352(6)	0.0327(9)
Ir	16*c*	0	0	0	0.830(2)	0.0109(2)
Rh	16*c*	0	0	0	0.170(2)	0.0109(2)
O	48*f*	0.3284(3)	0.125	0.125	1.000(6)	0.0119(14)
O'	8*b*	0.375	0.375	0.375	1.001(8)	0.018(3)
30 % Rh Pyrochlore: *a* = 10.27437(7) Å / Crystallite Size = 25.8 ± 2.2 nm						
Ca	16*d*	0.5	0.5	0.5	0.594(3)	0.0304(9)
Na	16*d*	0.5	0.5	0.5	0.269(5)	0.0304(9)
Ir	16*c*	0	0	0	0.707(2)	0.0165(2)
Rh	16*c*	0	0	0	0.293(2)	0.0165(2)
O	48*f*	0.3280(3)	0.125	0.125	1.000(6)	0.0268(15)
O'	8*b*	0.375	0.375	0.375	1.000(8)	0.038(4)

The lattice expansion recorded for the rhodium substituted material does not scale linearly with increasing rhodium content, this could be caused by the substituted rhodium being mixed valent, with greater proportion of Rh^{3+} been in the y = 0.3 material than the y = 0.15.

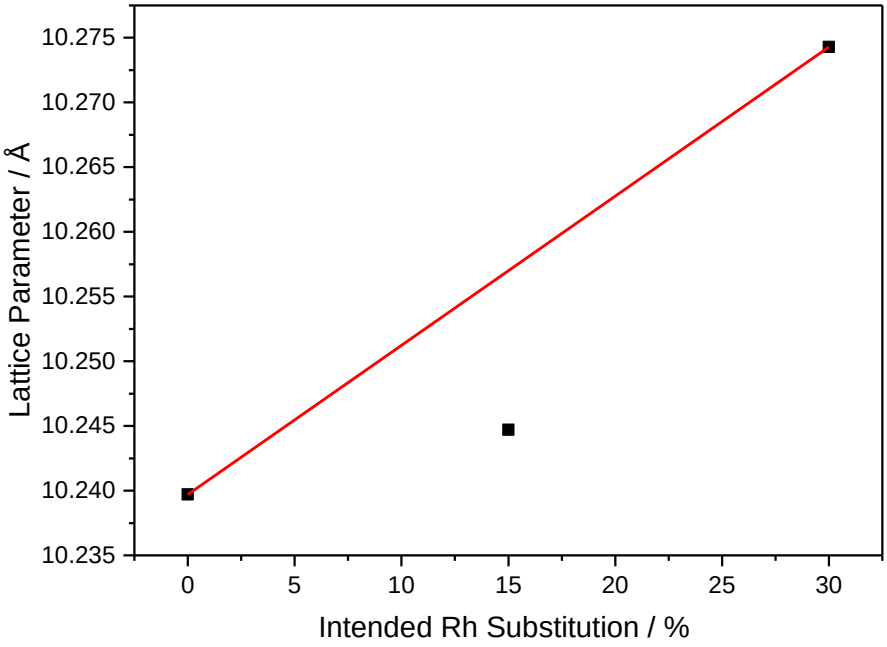

Figure 4.42: Refined Lattice Parameter as a function of intended rhodium substitution.

EDX analysis, Figure 4.43, shows an increase in rhodium concentration across the series, consistent with the intended substitution.

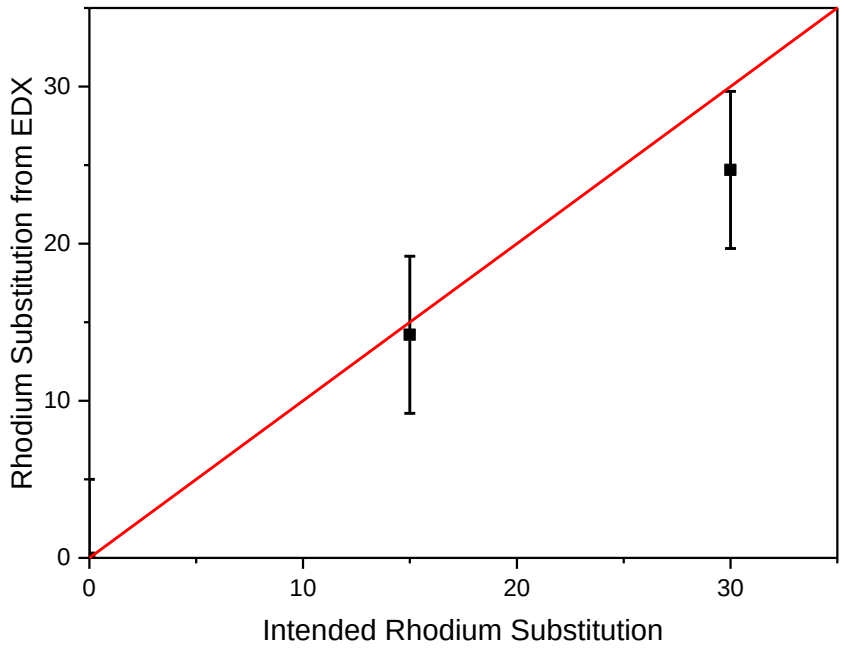

Figure 4.43: Measured rhodium content from EDX as a function of nominal rhodium substitution.

XANES measurements were carried out at both the Ir L_{III}-edge, Figure 4.44, and the Rh K-edge, Figure 4.45, to determine the oxidation state of both the rhodium and iridium found within the synthesised material. The white line position was used to determine the iridium oxidation state, which was revealed to be ≈+4.3, roughly the same as the pure iridium material. The edge position, when the normalised absorption was equal to 0.5, was used to calculate the rhodium oxidation state and was found to be +3.6. RhO_2 should have a rhodium oxidation state of +4, however a common impurity in RhO_2 is RhO(OH),[22] resulting in a decrease in the average valance of rhodium in RhO_2. BVS completed using the fit obtained from powder neutron diffraction data, Figure 4.46, suggest an average rhodium oxidation state of +3.84, supporting the assumptions made in the XANES analysis.

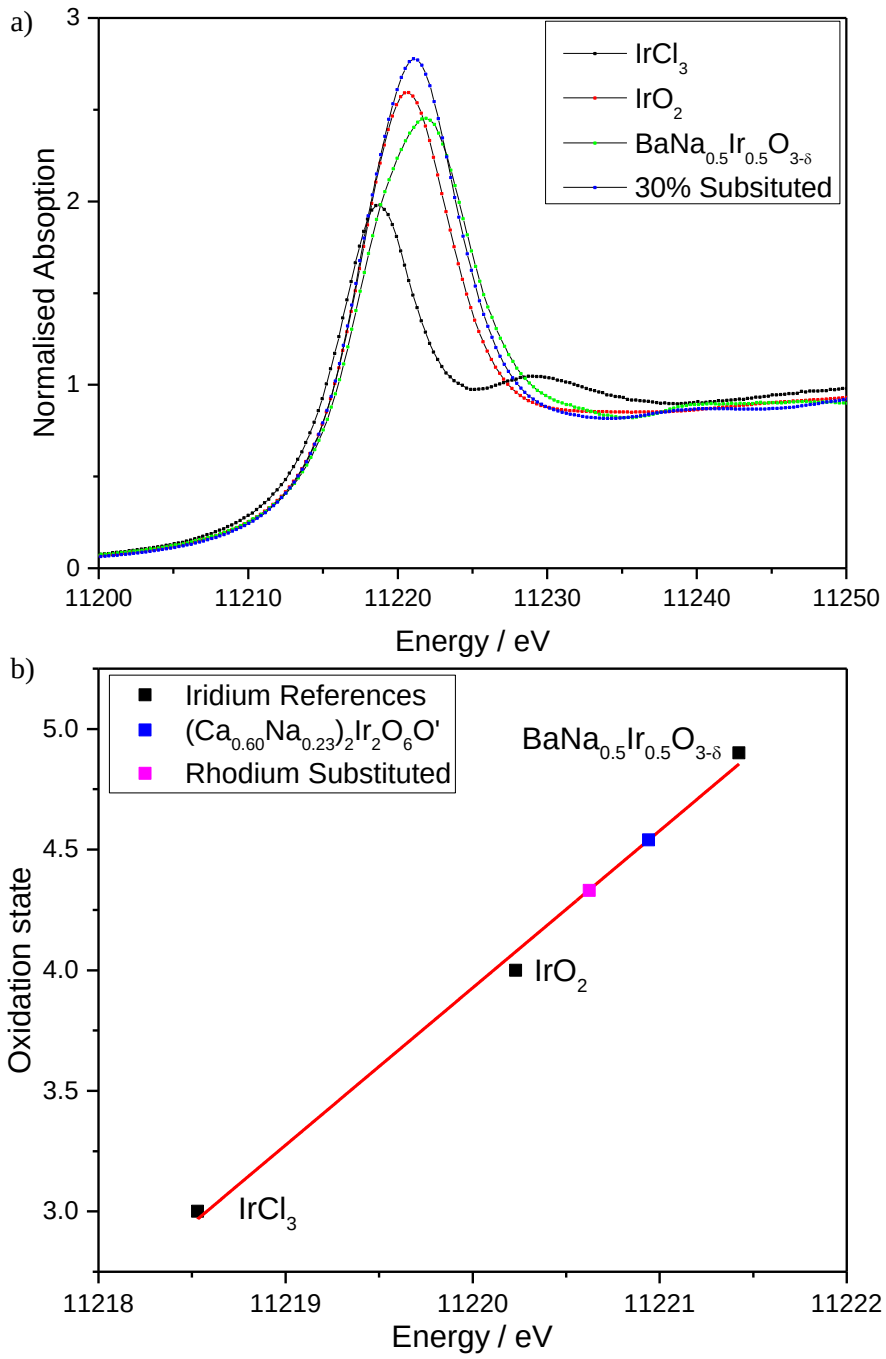

Figure 4.44: a) Ir L_{III}-edge XANES spectra of rhodium substituted pyrochlore materials and reference materials for calibration. b) White line position against iridium oxidation state.

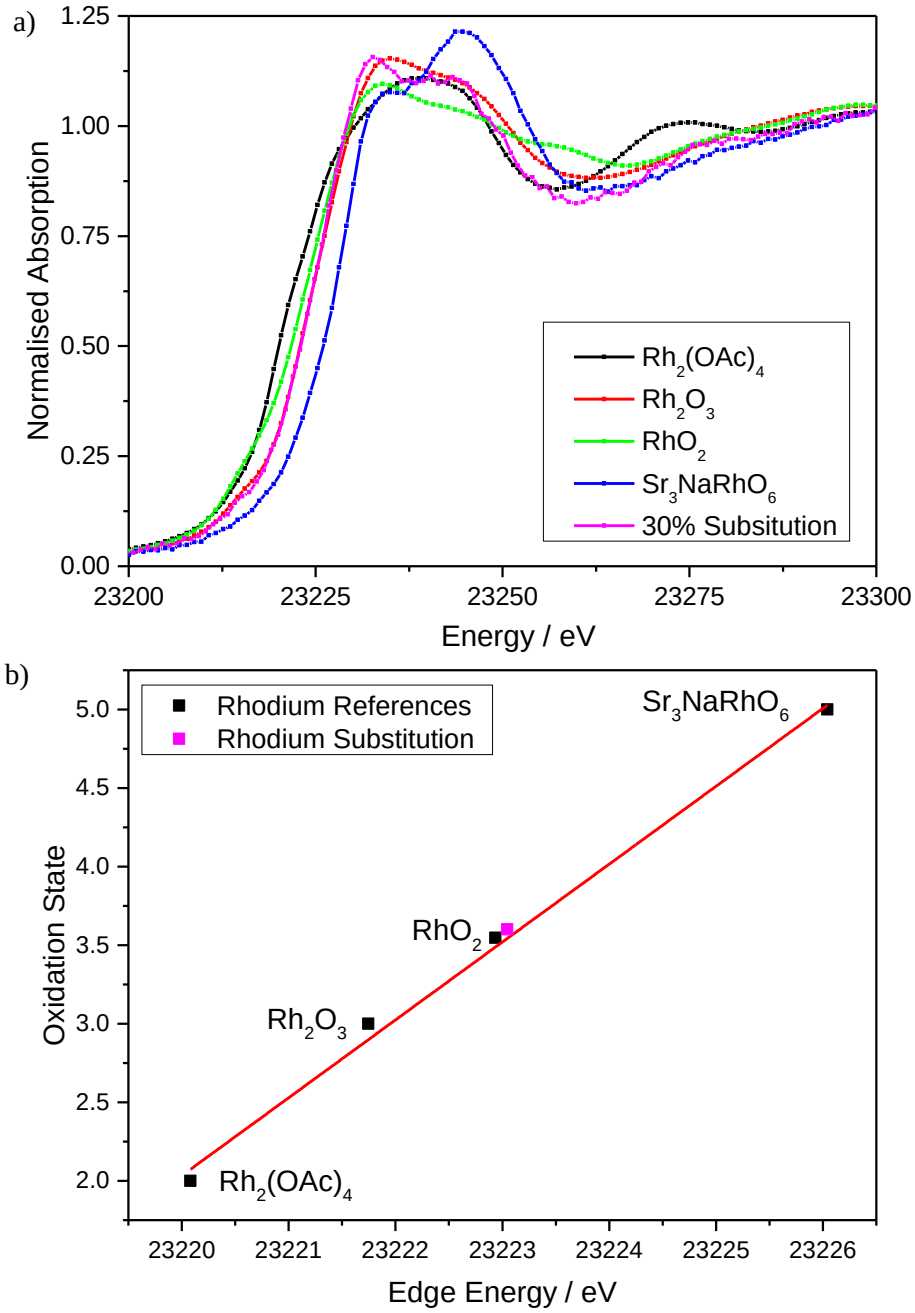

Figure 4.45: a) Rh K-edge XANES spectra of rhodium substituted pyrochlore materials and reference materials for calibration. b) Edge Position against rhodium oxidation state, assuming RhO_2 is mixed valent, as discussed in the text.

The neutron diffraction of the 30 % rhodium substituted material can be fitted in the same manner as the pure iridium material, Figure 4.46, with rhodium occupying the same site as iridium.

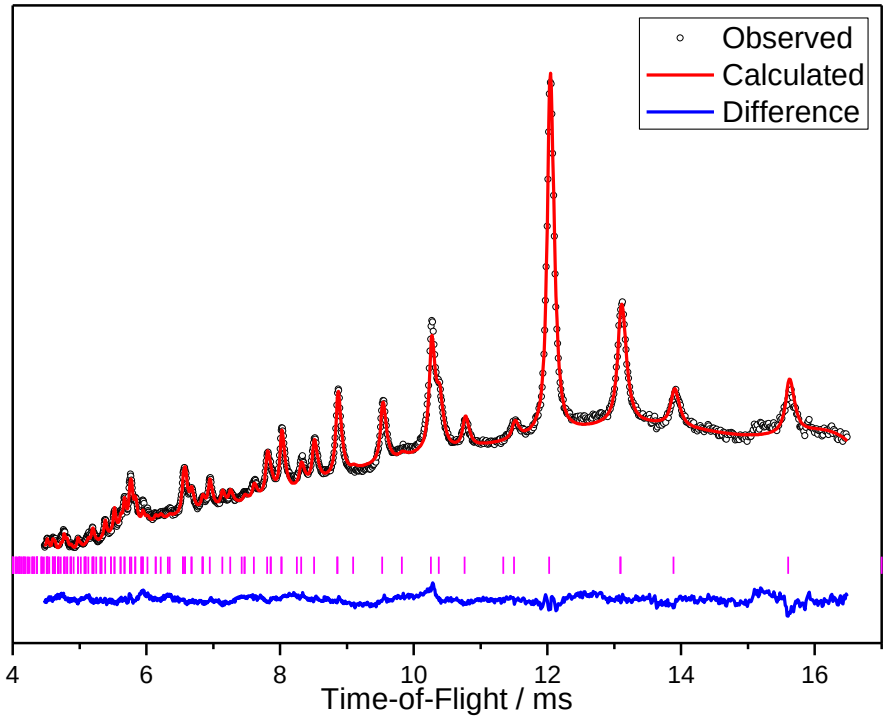

Figure 4.46: Rietveld refinements against time-of-flight neutron data from bank 5 of GEM for 30 % rhodium substituted calcium sodium iridium oxide.

Table 4.15: Structural details of 30 % rhodium substituted calcium sodium iridium oxide pyrochlore obtained from Rietveld refinement of powder neutron diffraction data.

Atom	Site	*x*	*Y*	*z*	Occ	U_{iso} / Å^2
30 % Rh Substituted Pyrochlore: *a* = 10.2263(2) Å						
Ca	16*d*	0.5	0.5	0.5	0.571(10)	0.0267(12)
Na	16*d*	0.5	0.5	0.5	0.303(13)	0.0267(12)
Ir	16*c*	0	0	0	0.729(7)	0.0096(2)
Rh	16*c*	0	0	0	0.271(7)	0.0096(2)
O	48*f*	0.3229(2)	0.125	0.125	1.000(3)	0.0123(2)
O'	8*b*	0.375	0.375	0.375	0.999(10)	0.0238(12)
H	32*e*	0.3289	0.3289	0.3289	0.50(2)	*

* U11 = 0.659(14), U22 = 0.659(14) , U33 = 0.659(14), U12 = -0.327(7), U13 = -0.327(7), U23= -0.327(7)

The PDF for the 30 % rhodium substituted material was then fitted using the model produced from the Bragg scattering, Figure 4.47, with slight with refinement of the lattice parameter, some of the occupancies and the ADP's. The r > 10 Å region fits very well and he first observable atomic correlation is at ~1.96 Å and agrees well with the B-O distance extracted from the Bragg scattering. However the shoulder on the first correlation, and the next feature between 2.3-3.2 Å has multiple contributions that do not fit perfectly, suggesting

some deviation from the average pyrochlore structure. But like the unsubstituted material the fit to the PDF is much better than other pyrochlores using the average structure model.

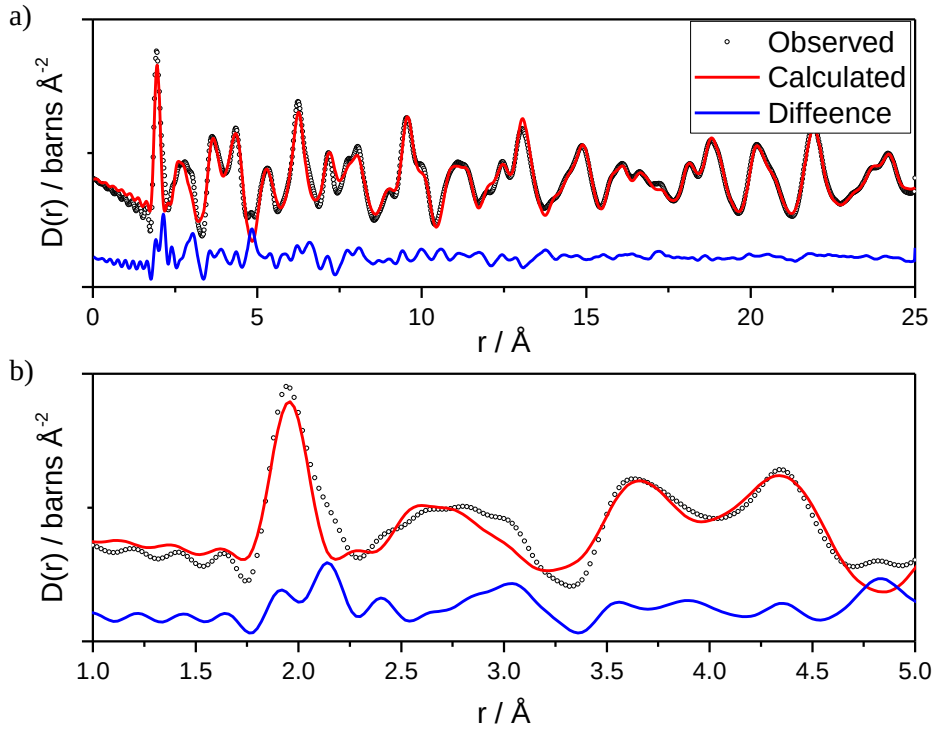

Figure 4.47: Fits of the Rietveld models against PDF data a) up to r = 25 Å and b) up to r = 5 Å of 30 % ruthenium substituted calcium sodium iridium oxide pyrochlore.

Table 4.16: Structural details of 30 % rhodium substituted pyrochlore obtained from least squares fitting of PDF data.

Atom	Site	*x*	*Y*	*z*	Occ	U_{iso} / Å^2
30 % Rh Substituted Pyrochlore: *a* = 10.215(5) Å						
Ca	16*d*	0.5	0.5	0.5	0.571	0.027(7)
Na	16*d*	0.5	0.5	0.5	0.303	0.027(7)
Ir	16*c*	0	0	0	0.729	0.0137(15)
Rh	16*c*	0	0	0	0.271	0.0137(15)
O	48*f*	0.3229	0.125	0.125	1.000	0.0183(16)
O'	8*b*	0.375	0.375	0.375	0.999	0.035(6)
H	32*e*	0.3289	0.3289	0.3289	0.499	0.7627

Like the unsubstituted material, TGA-MS was employed to look for the crystal water proposed from fitting the neutron diffraction data, Figure 4.48. An initial mass loss of 2.5 % is observed, up to the end of the 4 hour hold at 120 °C, and can be attributed to the loss of surface water. Taking the mass loss at 250 °C, the temperature at which the lattice parameter

decrease finishes in the thermodiffractometry, Figure 4.49, a mass loss of 3.0 % is observed, lower than to the theoretical loss of 3.5 % we expect if the O' site is fully occupied by H_2O. Subsequent mass losses then happen simultaneously with the phase changes observed in the thermodiffractometry.

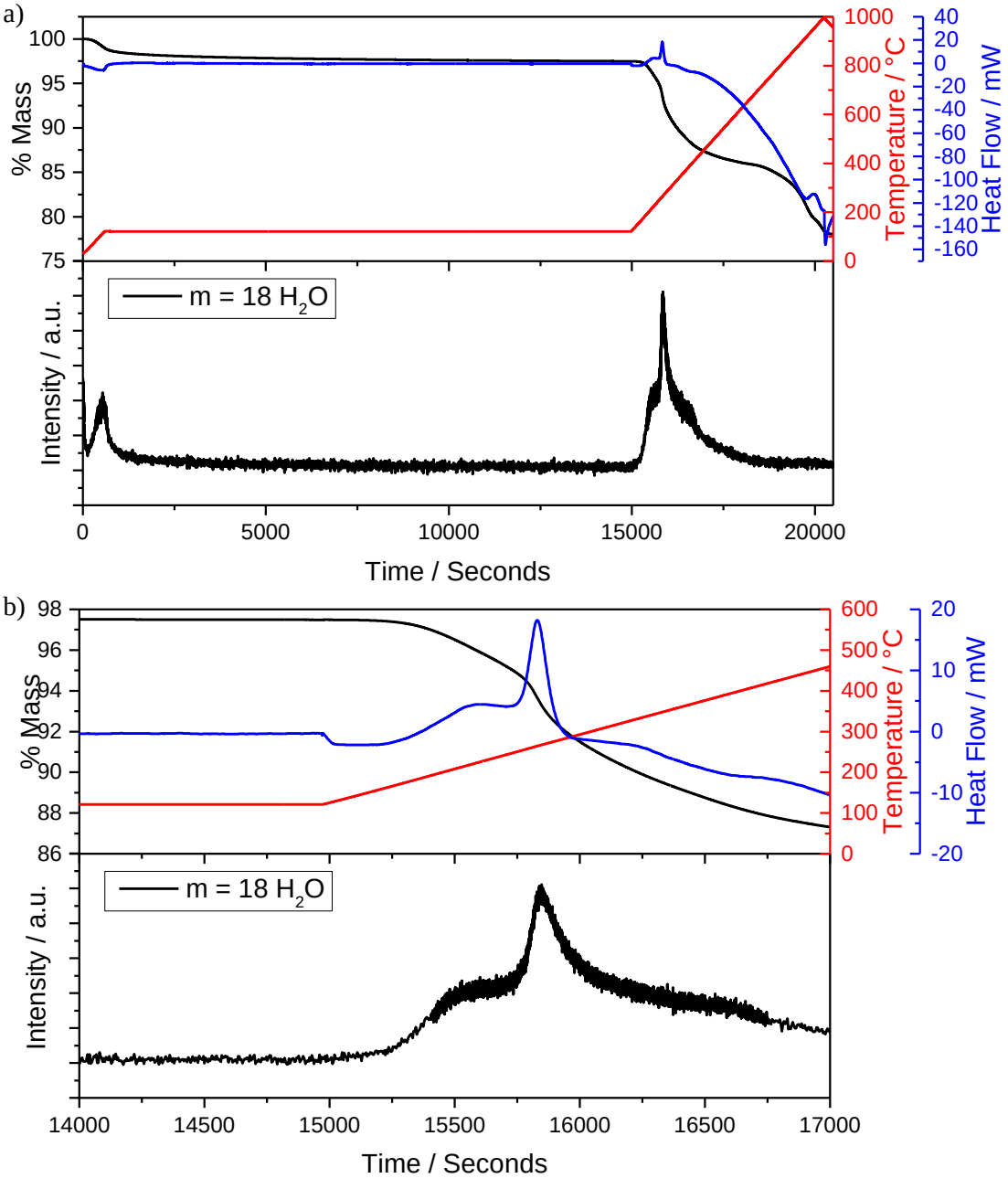

Figure 4.48: TGA-MS plots a) complete range and b) zoom of region with loss of crystal water of 30 % rhodium substituted calcium sodium iridium oxide.

Thermodiffractometry, Figure 4.49, shows the decrease in lattice parameter associated with the loss of crystal water begins at 150 °C, ending at 250 °C, considerably lower temperatures

that the unsubstituted material. Once 250 °C is exceeded a phase change to rutile type oxide is observed, and then at 400 °C the oxide begins its reduction to metal. However the oxide phase isn't completely reduced until 800 °C at which point only metal remains.

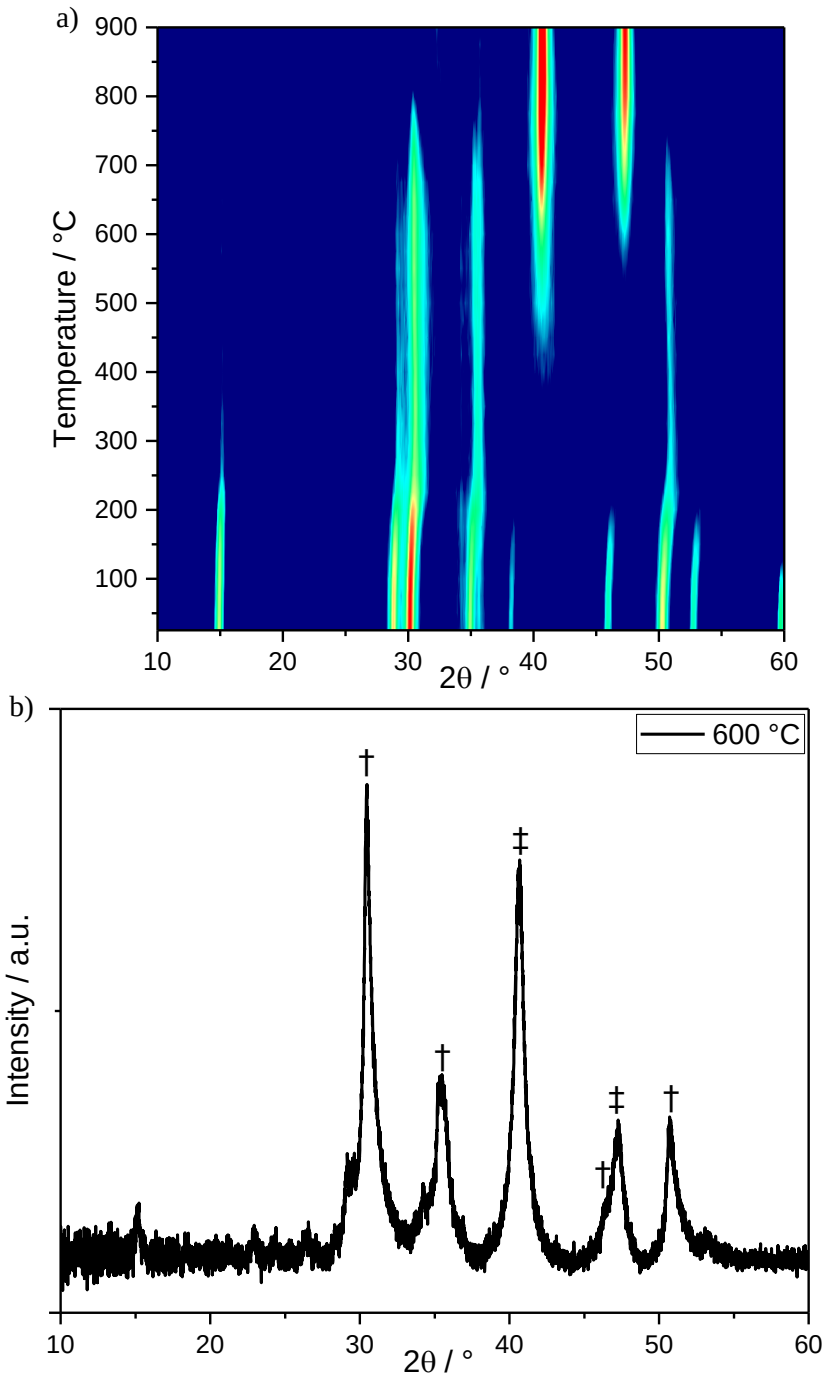

Figure 4.49: a) Thermodiffractometry (λ = 1.5418 Å) of 30 % rhodium substituted calcium sodium iridium oxide. b) XRD pattern at 600 °C, † denotes peaks arising from (Rh,Ir)O_2, ‡ denoting peaks arising from Ir,Rh metal.

4.4.6 Manganese Substitution

In the initial exploratory reactions it was observed that both the manganese reagent and sodium hydroxide concentration play a role in the level of manganese substitution in the final material, but that all synthesised materials could be indexed to the cubic pyrochlore cell with space group $Fd\bar{3}m$, Figure 4.50. Only a small variation in lattice parameter was observed using $MnCl_2$ and $KMnO_4$ as manganese sources in 10 M sodium hydroxide. When manganese is substituted into the material the lattice parameter decreases with respect to the unsubstituted material, consistent with octahedral Mn(IV) 0.53 Å being smaller than Ir(IV) 0.625 Å and Ir(V) 0.57 Å. Like the ruthenium and osmium substitution reactions it was found that the hydroxide concentration has an effect on the synthesised materials. As the molarity of the hydroxide is decreased from 10 M, a divergence in lattice parameter is observed, Figure 4.51. Those materials synthesised using $MnCl_2$ as a manganese source show an increase in the lattice parameter with decreasing hydroxide concentration, while those materials using $KMnO_4$ as the manganese source show a decrease in lattice parameter with decreasing hydroxide concentration. This suggests the amount of manganese incorporated into the pyrochlore phase is directly correlated to the molarity of the NaOH and dependant on the oxidation state of the manganese precursor used. When using $MnCl_2$ as a manganese source, a smaller proportion of the manganese in the reaction is incorporated into the pyrochlore phase as the molarity of the hydroxide is reduced. Whereas, when using $KMnO_4$ as a manganese source, a greater proportion of the manganese in the reaction is incorporated into the pyrochlore phase as the molarity of the hydroxide is reduced. Upon filtration, the filtrate in the 6 and 10 M NaOH reactions was always green/turquoise in colour suggesting the presence of MnO_4^{2-} in solution.[23] A second possibility is the presence of a poorly crystalline or amorphous type phase.

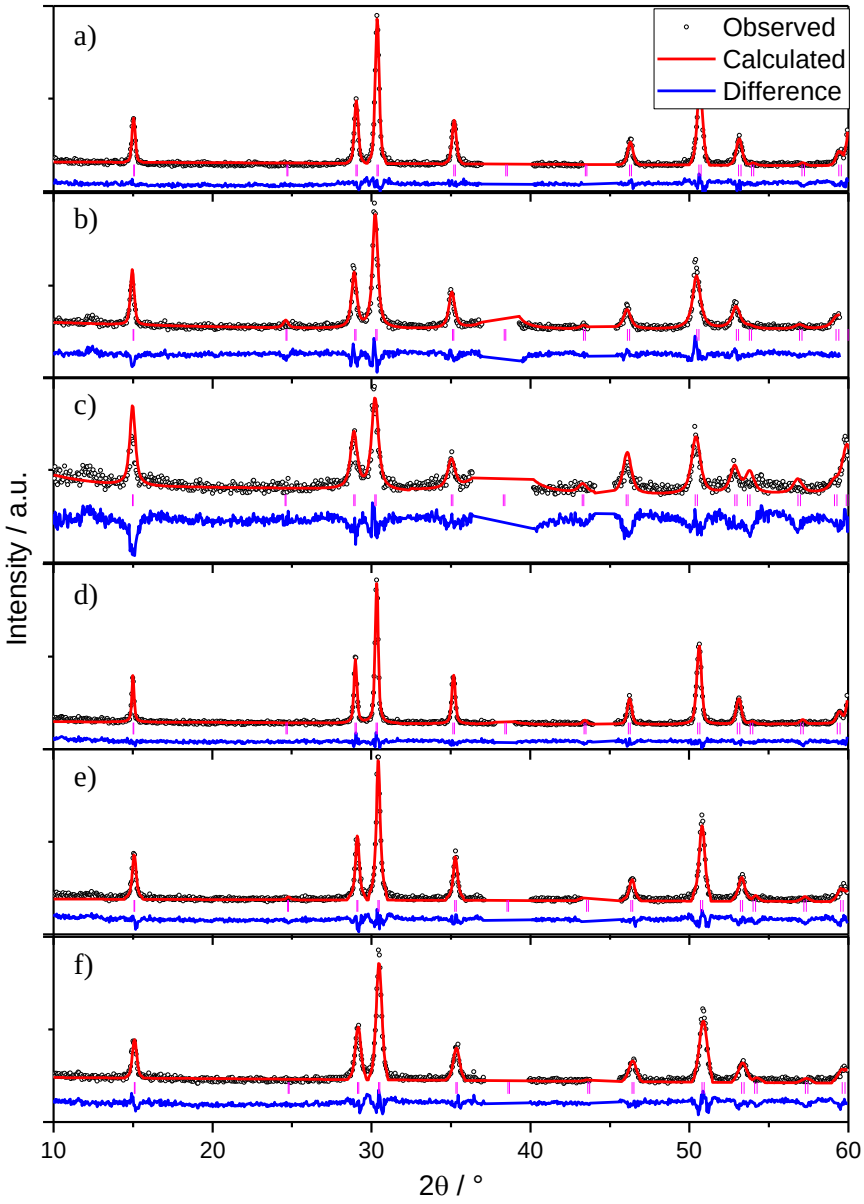

Figure 4.50: Le Bail fits to powder XRD data (λ = 1.5418 Å) from $(Ca,Na)_{2-x}(Ir_{1-y}Mn_y)_2O_6{\cdot}H_2O$ where y = 0.30. Mn source was $MnCl_2$ with NaOH concentration of, a) 10 M, b) 6 M and c) 2 M. Mn source was $KMnO_4$ with NaOH concentration of, d) 10 M, e) 6 M and f) 2 M. Regions at 38 ° and 44 ° are excluded as peaks are due to aluminium sample holder.

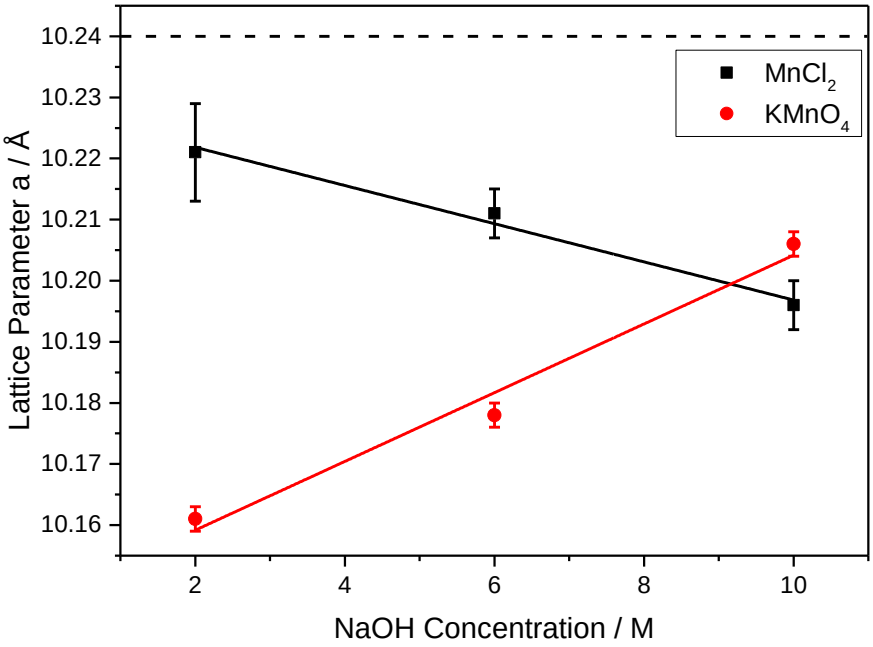

Figure 4.51: Refined Lattice Parameters for y = 0.30 materials, as a function of NaOH concentration and Mn source. Dashed line indicating lattice parameter of unsubstituted material.

EDX analysis, Figure 4.52, shows a linear increase in manganese concentration, with decreasing hydroxide concentration, consistent with the intensity of the colour of the filtrate observed during their filtration. However the observed manganese concentration is much higher than expected in those reactions using $MnCl_2$ as a reagent. Given the surface bias of EDX in SEM, this is likely due to the formation of a manganese rich phase on the surface of the pyrochlore.

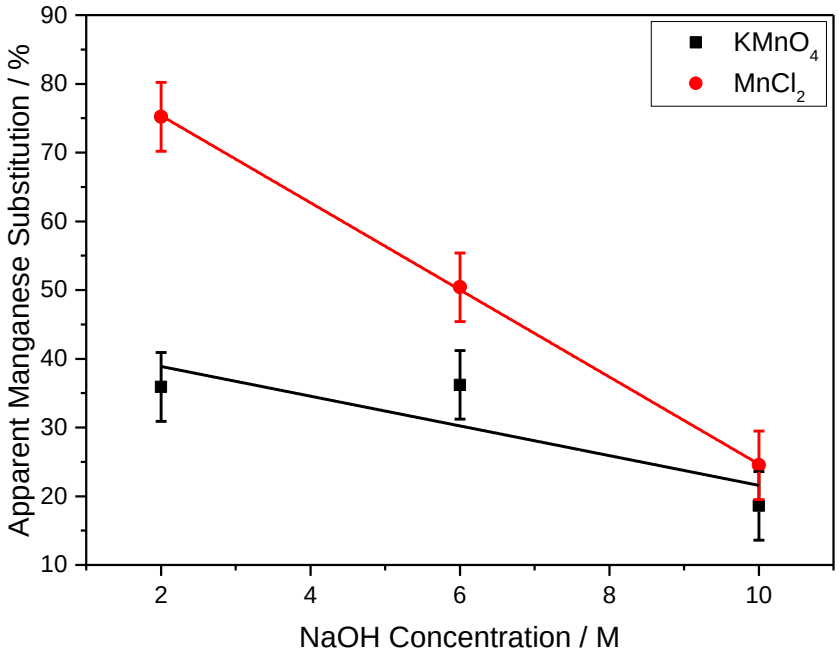

Figure 4.52: Effect of reaction conditions on apparent manganese substitution of B-site from EDX.

The powder XRD patterns of the materials synthesised utilising $KMnO_4$ as a manganese source in 2 M NaOH with the assumed formula $(Ca,Na)_{2-x}(Ir_{1-y}Mn_y)_2O_6 \cdot H_2O$, can be indexed and fitted to a cubic pyrochlore cell using space group $Fd\bar{3}m$ where y = 0.15 and 0.3, Figure 4.53. At both substitution levels we observe the presence of a poorly crystalline rutile phase. This is likely to be iridium oxide as observed in section 4.5.2, however this phase could also be manganese substituted. The rutile phase is much more prevalent in the y = 0.15 material, meaning the manganese is aiding the crystallisation of the pyrochlore phase at low NaOH concentrations.

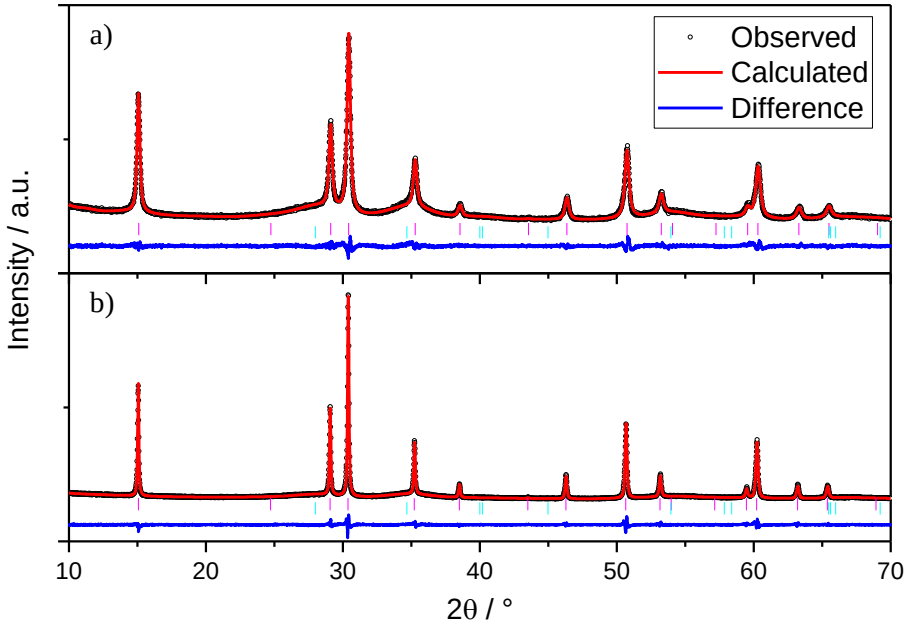

Figure 4.53: Rietveld refinements to powder XRD data (λ = 1.54056 Å) from $(Ca,Na)_{2-x}(Ir_{1-y}Mn_y)_2O_6 \cdot H_2O$, a) y = 0.15 and b) y = 0.30.

Table 4.17: Structural details of pyrochlores obtained from Rietveld refinement of powder XRD data, of Mn substituted materials.

Atom	Site	*x*	*y*	*z*	Occ	U_{iso} / Å^2
15 % Mn Pyrochlore: *a* = 10.17275(10) Å / Crystallite Size = 19.4 ± 3.6 nm						
Ca	16*d*	0.5	0.5	0.5	0.612(4)	0.0497(13)
Na	16*d*	0.5	0.5	0.5	0.313(7)	0.0497(13)
Ir	16*c*	0	0	0	0.694(1)	0.0081(2)
Mn	16*c*	0	0	0	0.306(1)	0.0081(2)
O	48*f*	0.3247(4)	0.125	0.125	0.993(8)	0.027(2)
O'	8*b*	0.375	0.375	0.375	1.001(10)	0.013(4)
30 % Mn Pyrochlore: *a* = 10.18777(5) Å / Crystallite Size = 44.3 ± 10.5 nm						
Ca	16*d*	0.5	0.5	0.5	0.668(4)	0.0575(13)
Na	16*d*	0.5	0.5	0.5	0.321(8)	0.0575(13)
Ir	16*c*	0	0	0	0.727(1)	0.0062(2)
Mn	16*c*	0	0	0	0.273(1)	0.0062(2)
O	48*f*	0.3307(4)	0.125	0.125	1.000(8)	0.028(2)
O'	8*b*	0.375	0.375	0.375	1.001(11)	0.039(5)

EDX analysis shows a linear increase in manganese concentration across the composition range consistent with the intended substitution.

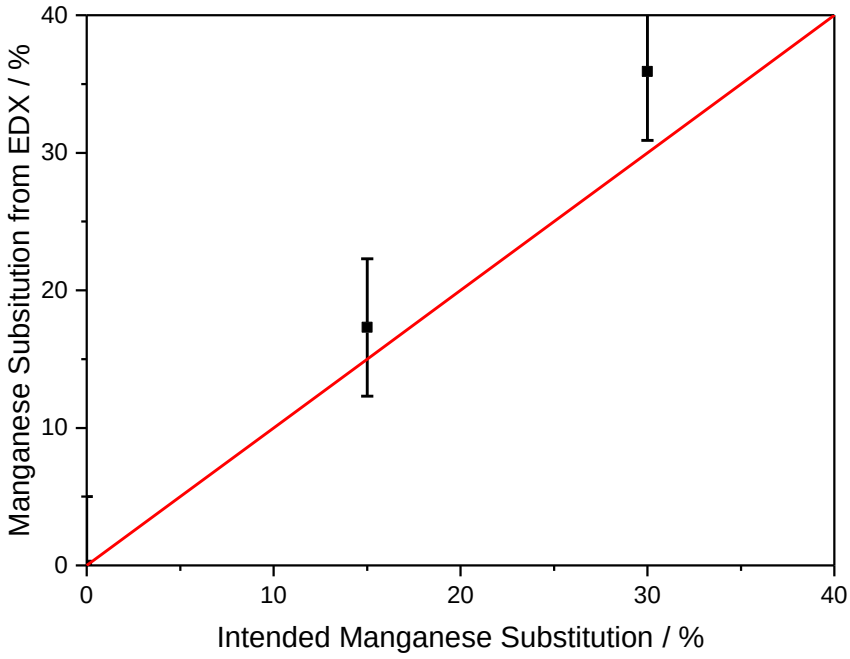

Figure 4.54: Measured manganese content from EDX as a function of intended manganese substitution.

XANES measurements were carried out at both the Ir L_{III}-edge, Figure 4.55, and the Mn K-edge, Figure 4.56, to determine the oxidation state of both the iridium and manganese found within the y = 0.30 material. The white line position was used to determine the Ir oxidation state, which was revealed to be approximately +4.5. The edge position, where the normalised absorption was equal to 0.5, was used to calculate the manganese oxidation state and was found to be in the +4 state.

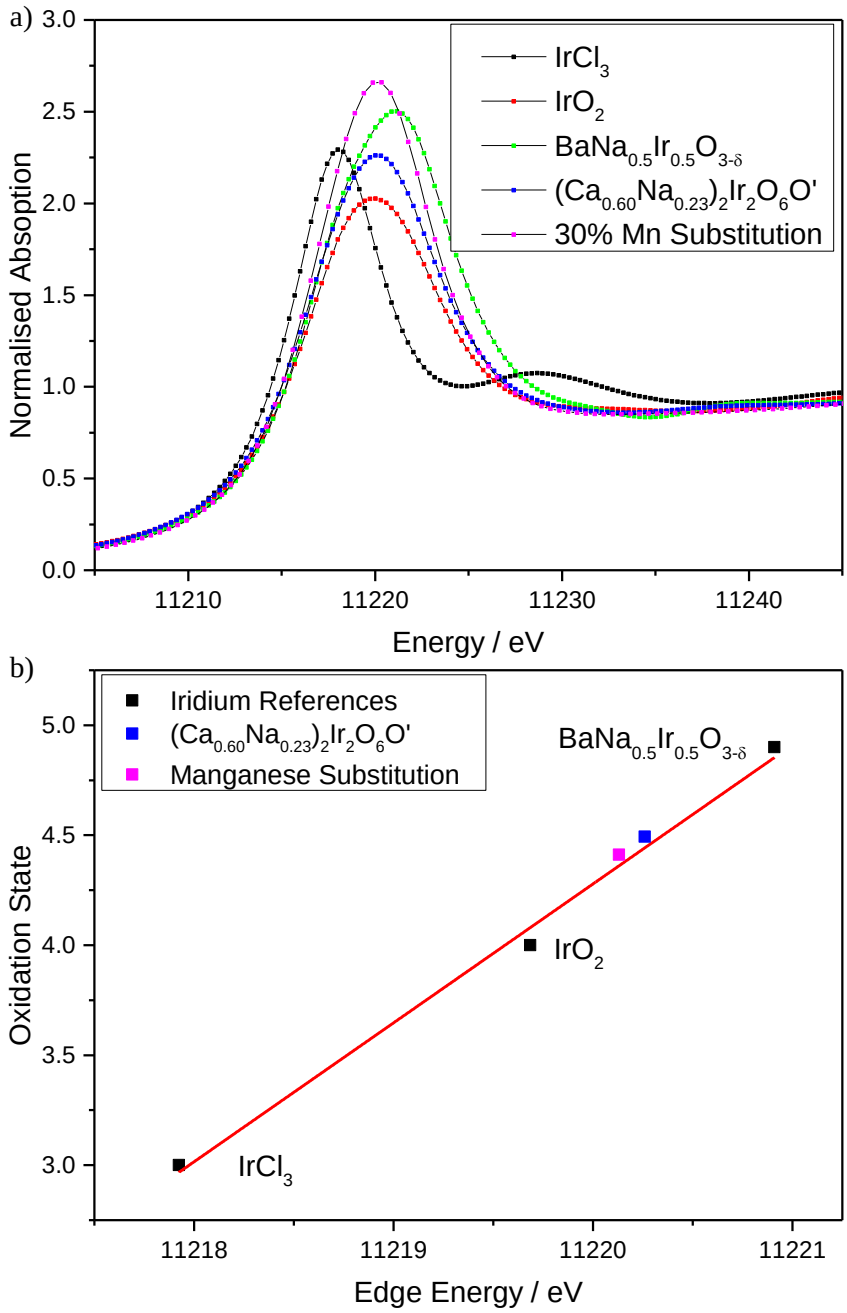

Figure 4.55 a) Ir L_{III}-edge XANES spectra of manganese substituted pyrochlore material and reference materials for calibration. b) White line position against iridium oxidation state.

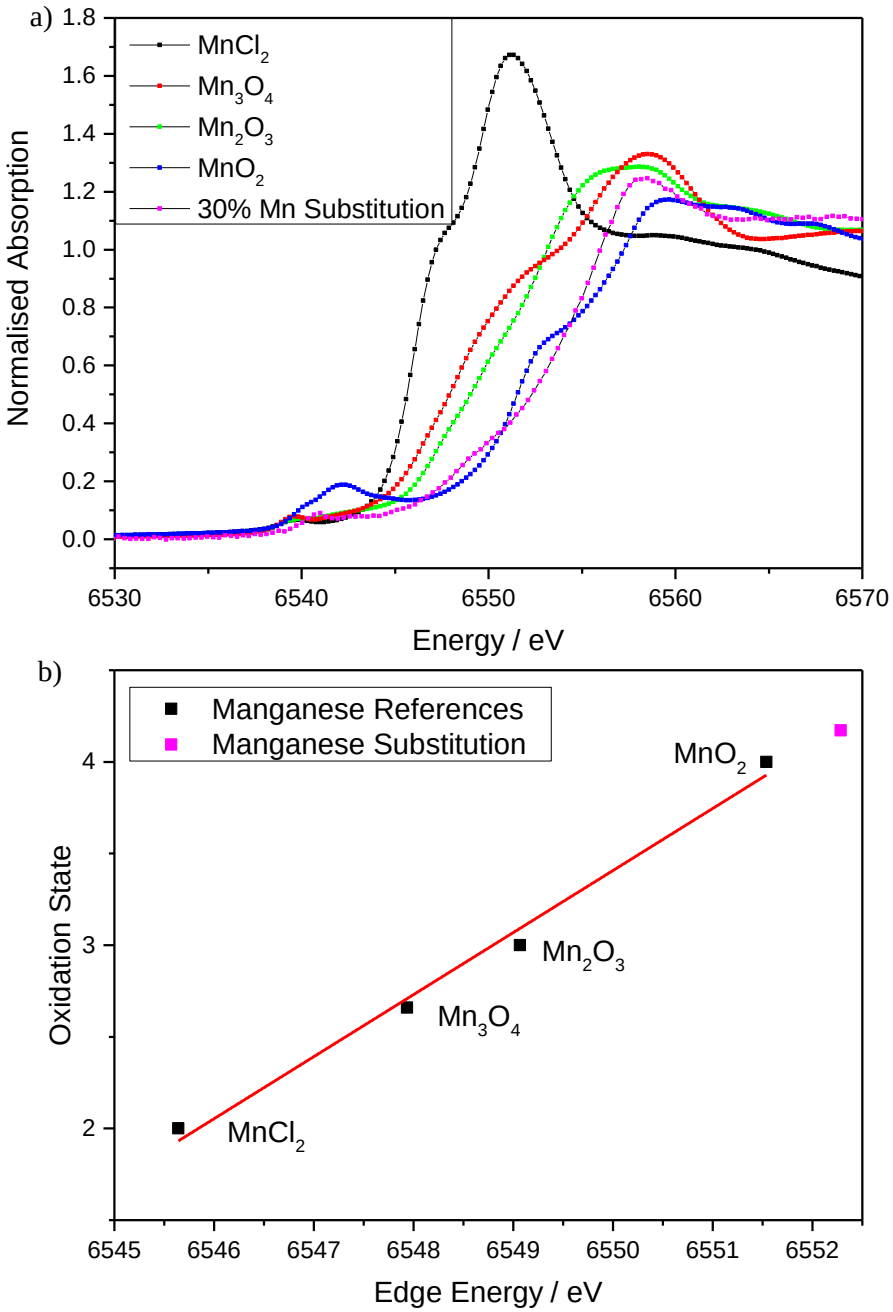

Figure 4.56: a) Mn K-edge XANES spectra of manganese substituted pyrochlore material and reference materials for calibration. b) Edge position against manganese oxidation state.

4.4.7 B-site Substitution Discussion

In this section we have shown how a range of metals can be substituted into the pyrochlore structure of calcium sodium iridium oxide. Several possibilities exist for how charge is balanced in these materials and the experimental data do not necessarily allow these to be distinguished:

- Reduction or oxidation of iridium, depending on whether the substituted metal has a valence greater than or less than 4.5^{+}.
- The inclusion of extra A-site cations, or additional vacancies on the same site.
- The possibility that the H_2O on the O' site could be instead present as OH^- or O^{2-} when metals of higher valence are substituted.

Iridium oxides can contain iridium with a wide range of oxidation states ranging from +3.75 through +6.[7,24–26] The iridium L_{III}-edge XANES of all the substituted materials shows an iridium oxidation state between +4.25-4.60. However we see no trend in oxidation state vs substitution level of dopant metal, although it is possible it could be related to particle size effects, it is more likely this variation is due to the error associated with the experimental technique. If it is assumed this is limited by the energy difference between two adjacent points on the measured spectra then an error of ± 0.27 of an oxidation state can be estimated, agreeing with the range of oxidation states observed in XANES measurements.

A great deal of variation in A-site occupancy across the synthesised materials is observed when fitting the XRD, ranging from 85 % occupied to fully occupied. The occupancies extracted from fitting the neutron diffraction data show much less variation, with 87 - 92 % occupancy, with the exception of the zirconium substituted material, whose A-site is fully occupied, Table 4.18.

Table 4.18: Structural composition of pyrochlores obtained from Rietveld refinement of powder neutron diffraction data.

Material	Composition
Unsubstituted	$(Ca_{0.60}Na_{0.27})_2Ir_2O_6{\cdot}0.95H_2O$
50% Sb Substituted	$(Ca_{0.59}Na_{0.32})_2(Ir_{0.49}Sb_{0.51})_2O_6{\cdot}H_2O$
50% Zr Substituted	$(Ca_{0.58}Na_{0.32}Zr_{0.12})_2(Ir_{0.56}Zr_{0.44})_2O_6{\cdot}0.97H_2O$
50% Ru Substituted	$(Ca_{0.59}Na_{0.32})_2(Ir_{0.50}Ru_{0.50})_2O_6{\cdot}0.99H_2O$
30% Rh Substituted	$(Ca_{0.57}Na_{0.30})_2(Ir_{0.73}Rh_{0.27})_2O_6{\cdot}H_2O$

Any small charge imbalances arising from the substitution of iridium can be dealt with by conversion of the O' oxygen from H_2O to either OH^- or O^{2-}, like in $NaW_{2-x}Mo_xO_{6+\delta}{\cdot}nH_{2-y}O$.[27]

However this is exceedingly hard to prove, as small variations are hard to detect especially when multiple species co-exist.

The local structure analysis of these materials agrees well with the model from the Bragg scattering, except in the zirconium substituted material with only the slightest deviation from the average pyrochlore at the local scale, specifically in the r < 5 Å region. As previously stated it is possible that this could be remedied by refining the local data using the space group $F\bar{4}3m$, which would allow displacement of the oxygen anions from their ideal positions used in the higher symmetry system of $Fd\bar{3}m$.[9] It is likely that Reverse Monte Carlo modelling would need to be implemented to obtain a more accurate picture of the local disorder present in these systems. In the case of the zirconium substituted material, where there is significant deviation from the ideal pyrochlore structure, the use further modelling techniques would certainly be required.

4.5 Calcium Sodium Iridium Oxide Variations

4.5.1 Sodium Free Pyrochlore

In an attempt to stabilise the unsubstituted material towards the OER conditions, see Chapter 6, synthesis of the iridate pyrochlore with only calcium on the A-site was attempted. This was achieved by removing sodium from the reaction, and although a concern was other group I metals would be incorporated into the pyrochlore structure, this was not found to occur, most likely due to a mismatch of ionic radii of larger K^+ or smaller Li^+. The materials synthesised were fitted using the cubic pyrochlore cell using space group $Fd\bar{3}m$, Figure 4.57 and Table 4.19, and the lattice parameters of the materials synthesised using Li_2O_2 and KO_2 in KOH were found not to be significantly different from those of $(Ca,Na)_{2-x}Ir_2O_6{\cdot}H_2O$. Eight coordinate Na(I) has an ionic radius of 1.18 Å, similar to 1.12 Å of eight coordinate Ca(II). If sodium was replaced by lithium the lattice parameter would be expected to decrease as eight coordinate Li(I) has an ionic radius of 0.92 Å. Alternatively if sodium was replaced with potassium the lattice parameter would be expected to increase as eight

coordinate K(I) has an ionic radius of 1.51 Å. In addition EDX analysis shows no evidence of potassium in the materials regardless of whether lithium peroxide or potassium superoxide is used as the oxidiser. There is one major difference between the synthesised materials, which is the crystallite size; the material produced using KO_2 has considerably smaller crystallites than both $(Ca,Na)_{2-x}Ir_2O_6{\cdot}H_2O$ and the material produced using Li_2O_2, Table 4.19.

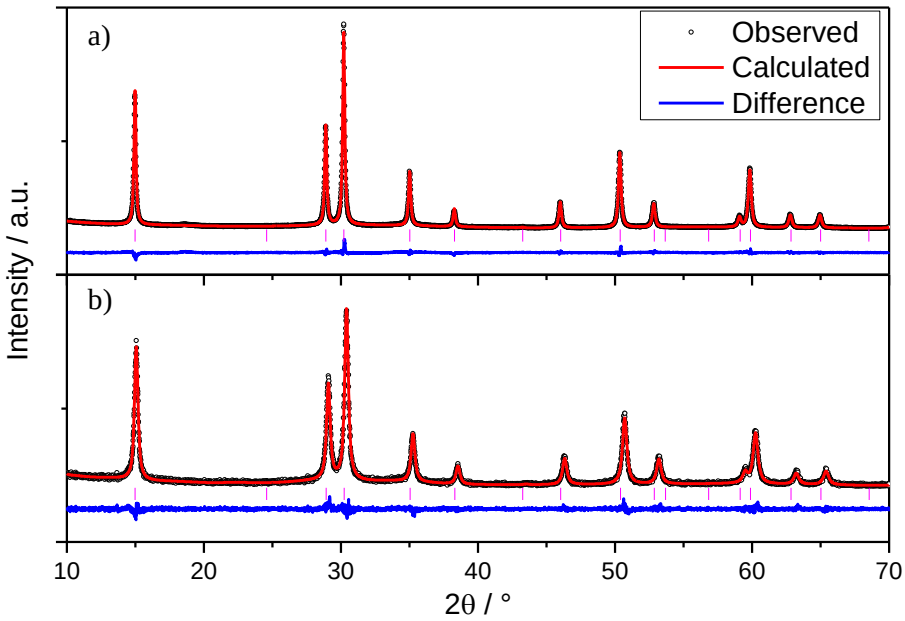

Figure 4.57: Rietveld refinements to powder XRD data (λ = 1.54056 Å) from $Ca_{2-x}Ir_2O_6O'$, a) Using Li_2O_2 as an oxidiser and b) using KO_2 as an oxidiser.

Table 4.19: Structural details of calcium iridium oxide pyrochlores synthesised using Li_2O_2 and KO_2 obtained from Rietveld refinement of powder XRD data.

Atom	Site	*x*	*y*	*z*	Occ	U_{iso} / Å^2
Li_2O_2 Pyrochlore : *a* = 10.24030(3) Å / Crystallite Size = 33.9 ± 4.9 nm						
Ca	16*d*	0.5	0.5	0.5	0.747(3)	0.0187(6)
Ir	16*c*	0	0	0	1.000(1)	0.01661(9)
O	48*f*	0.3292(3)	0.125	0.125	1.000(6)	0.0078(12)
O'	8*b*	0.375	0.375	0.375	1.033(7)	0.034(3)
KO_2 Pyrochlore: *a* = 10.23794(8) Å / Crystallite Size = 21.7 ± 2.0 nm						
Ca	16*d*	0.5	0.5	0.5	0.718(4)	0.06(2)
Ir	16*c*	0	0	0	1.000(1)	0.0173(12)
O	48*f*	0.3280(3)	0.125	0.125	1.000(11)	0.009(3)
O'	8*b*	0.375	0.375	0.375	1.00(4)	0.026(7)

XANES measurements were carried out at the Ir L_{III}-edge, Figure 4.58, on the material produced using Li_2O_2 and showed the iridium oxidation state to be +4.5, showing that the removal of sodium from the A site does not influence the oxidation state of the B site metal.

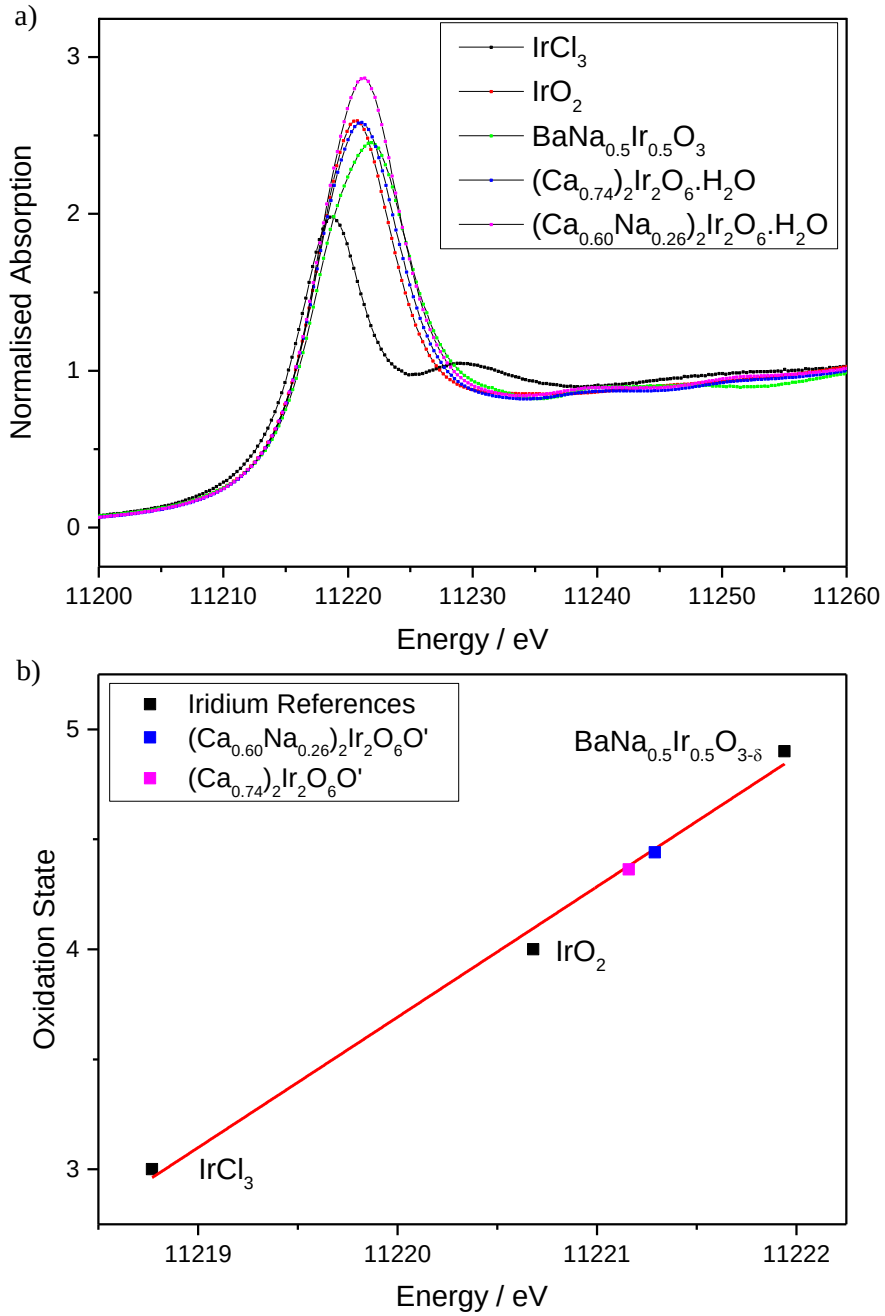

Figure 4.58 a) Ir L_{III}-edge XANES spectra of $(Ca_{0.60}Na_{0.26})_2Ir_2O_6O'$, $(Ca_{0.74})_2Ir_2O_6O'$ and reference materials for calibration. b) White line position against iridium oxidation state.

A neutron diffraction study was carried out on the material produced using Li_2O_2, Figure 4.59. It can be fitted in the same manner as the sodium containing material with only calcium on the A-site, Table 4.20.

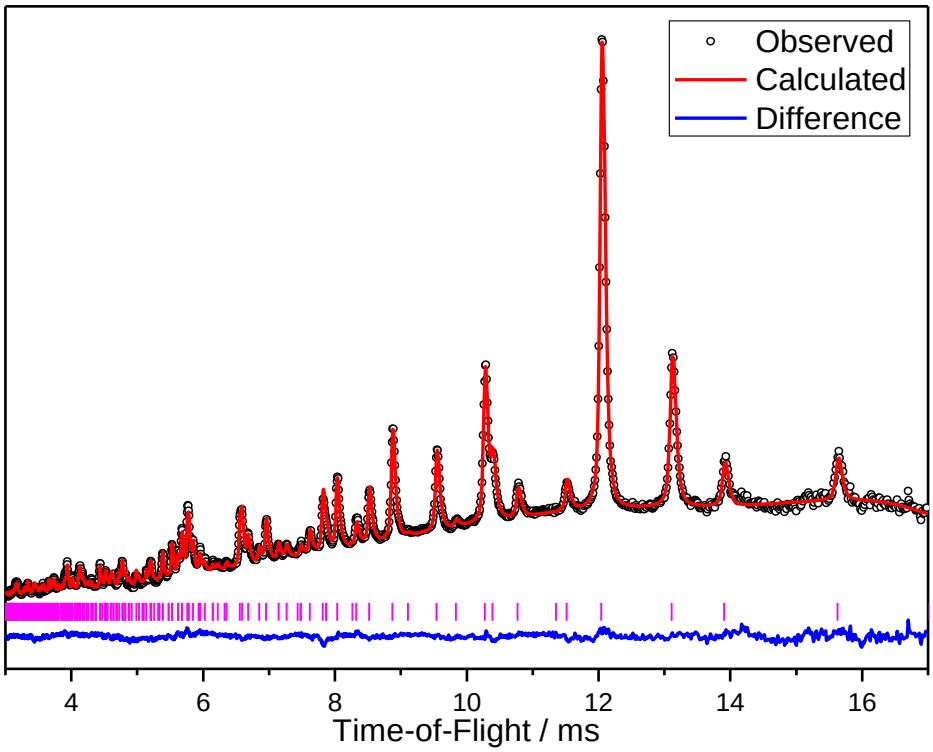

Figure 4.59: Rietveld refinements of time-of-flight neutron data from bank 5 of GEM for calcium iridium oxide produced using Li_2O_2.

Table 4.20: Structural details of pyrochlore obtained from Rietveld refinement of powder neutron diffraction data using Li_2O_2 as oxidiser.

Atom	Site	*x*	*y*	*z*	Occ	U_{iso} / Å^2
Li_2O_2 Pyrochlore: *a* = 10.24071(14) Å						
Ca	16*d*	0.5	0.5	0.5	0.741(7)	0.0136(6)
Ir	16*c*	0	0	0	1.000(2)	0.00729(11)
O	48*f*	0.3247(2)	0.125	0.125	1.000(3)	0.00804(12)
O'	8*b*	0.375	0.375	0.375	1.001(12)	0.0342(11)
H	32*e*	0.3289	0.3289	0.3289	0.502(43)	*

* U11 = 0.799(8), U22 =0.345(8) , U33 = 0.799(8), U12 = -0.269(4), U13 = -0.391(4), U23= -0.269(4)

The PDF of the calcium iridium oxide material was fitted using the model produced from the Bragg scattering, Figure 4.60, with refinement of the lattice parameter, some of the occupancies and the ADPs, Table 4.1. The model from the Bragg data fits the observed data very well.

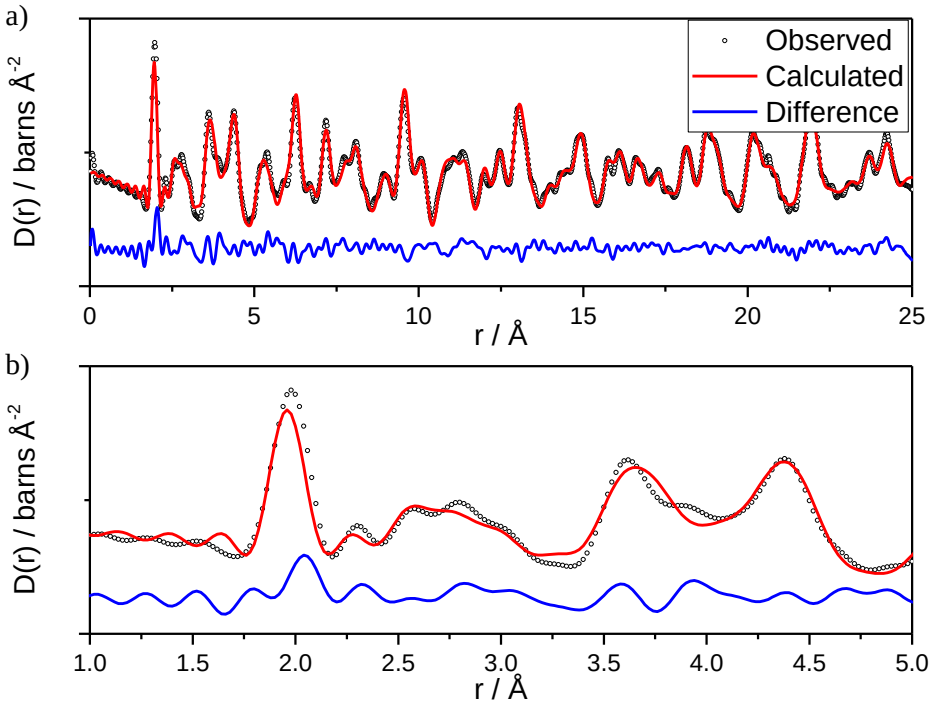

Figure 4.60: Fits of the Rietveld model against PDF data a) up to r = 25 Å and b) up to r = 5 Å of calcium iridium oxide pyrochlore

Table 4.21: Structural details of calcium iridium oxide from least squares fitting of PDF data.

Atom	Site	*x*	*y*	*z*	Occ	U_{iso} / Å^2
		Li_2O_2 Pyrochlore: *a* = 10.2173(13) Å				
Ca	16*d*	0.5	0.5	0.5	0.7201(17)	0.015(16)
Ir	16*c*	0	0	0	1.000	0.008(3)
O	48*f*	0.3247	0.125	0.125	1.000	0.010(3)
O'	8*b*	0.375	0.375	0.375	1.000	0.03(2)
H	32*e*	0.3289	0.3289	0.3289	0.500	1.3169

Like the sodium containing material, TGA-MS was employed to look for the crystal water proposed from fitting the neutron diffraction data, Figure 4.61. An initial mass loss of 1.4 % is observed, up to the end of the 4 hour hold at 120 °C, and is attributed to the loss of surface water. Taking the mass at 300 °C the temperature at which the lattice contraction has stopped in the thermodiffractometry, Figure 4.62, at which point 3.0 % of the remaining mass is lost, slightly less than the theoretical loss of 3.2 % we expect if the O' site is fully occupied by H_2O.

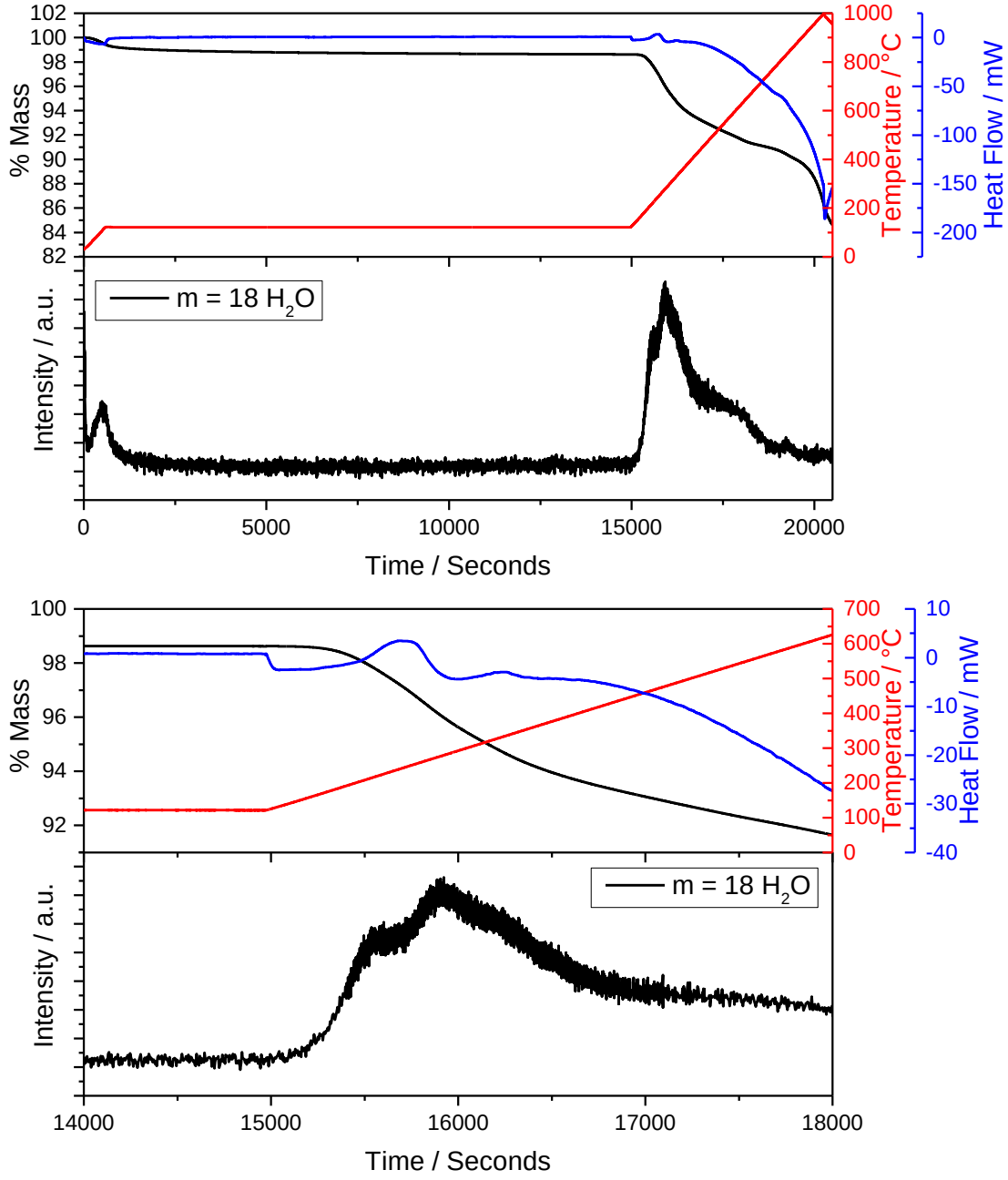

Figure 4.61: TGA-MS plots a) complete range and b) zoom of region with loss of crystal water of calcium iridium oxide.

Thermodiffractometry, Figure 4.62, reveals a lattice contraction between 200 and 300 °C, attributed to the loss of crystal water. Beyond this the pyrochlore phase remains very stable up to 800 °C at which point additional peaks start appearing in the diffraction pattern, with the only identifiable phase amongst these peaks being iridium metal, with the possibility of remnant pyrochlore phase and Ca_2IrO_4.

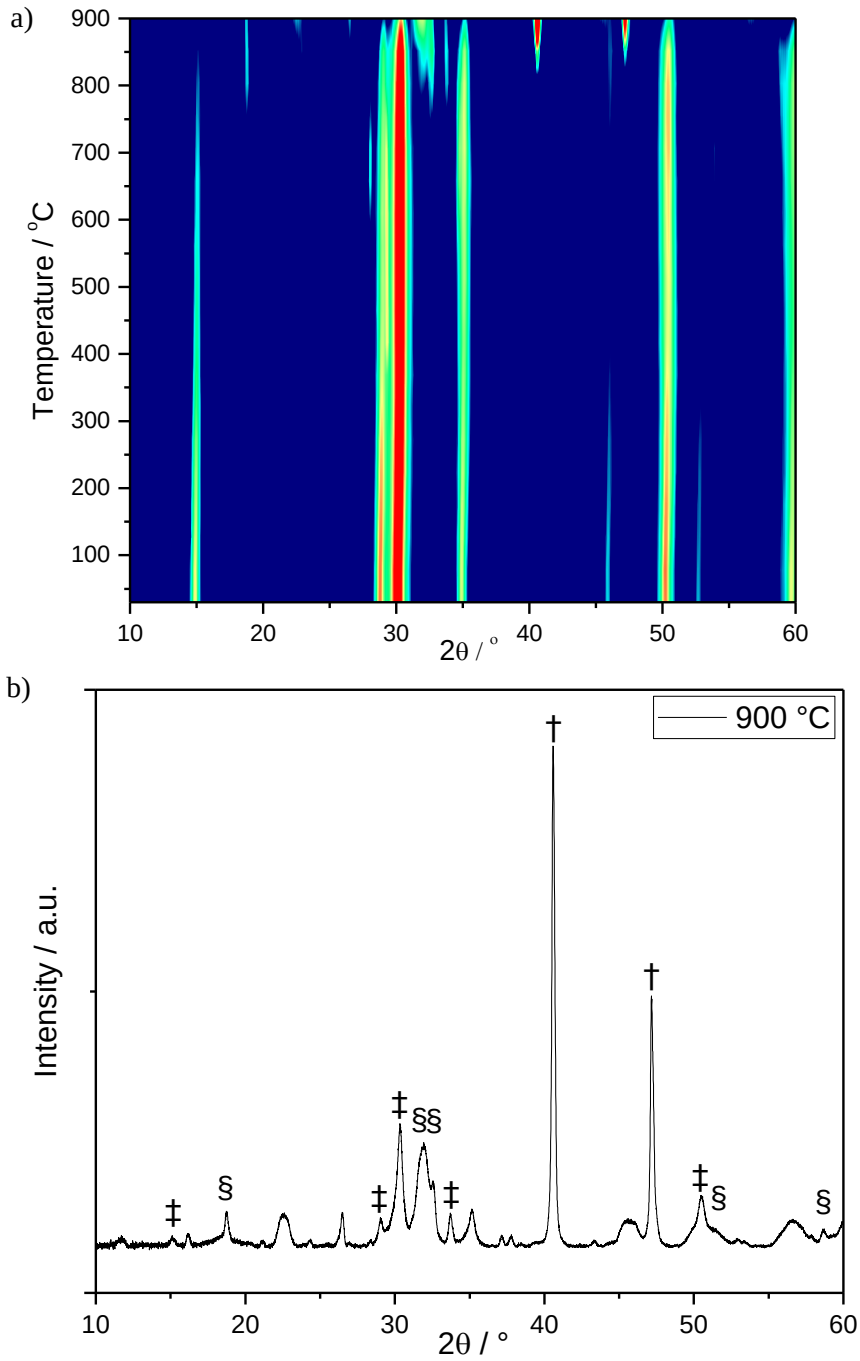

Figure 4.62: a) Thermodiffractometry (λ = 1.5418 Å) of calcium iridium oxide. b) XRD pattern at 900 °C, † denoting peaks arising from Ir metal, ‡ denoting peaks arising from possible pyrochlore phase and § denoting peaks from possible Ca_2IrO_4 phase.

4.5.2 Particle Size Exploration

A common method for adjusting the catalytic properties of materials is reducing the particle size. This has been investigated via two methods herein: (i) the reduction of NaOH concentration used in the synthesis and (ii) the reduction of reaction temperature. It was found that reducing the concentration of NaOH in the reaction to 2 M, rutile phase IrO_2

becomes the predominant phase, rather than the pyrochlore, Figure 4.63, and when the hydroxide concentration is increased to 15 M and the reaction becomes more like a hydroflux[28], a Ca_2IrO_4 phase was synthesised with the presence of a small pyrochlore impurity. The powder XRD pattern of $(Ca,Na)_{2-x}Ir_2O_6 \cdot H_2O$ synthesised in 5 M sodium hydroxide, Figure 4.64, reveals a phase pure pyrochlore has been synthesised with a very similar lattice parameter to that of the material synthesised in 10 M NaOH, Table 4.22, with a significant reduction in crystallite size . Reducing the reaction temperature proved to be just as effective for reducing the crystallite size of the synthesised materials, Figure 4.64 and Table 4.22. In addition the reduction in crystallite size a decrease in lattice parameter with decreasing reaction temperature is observed.

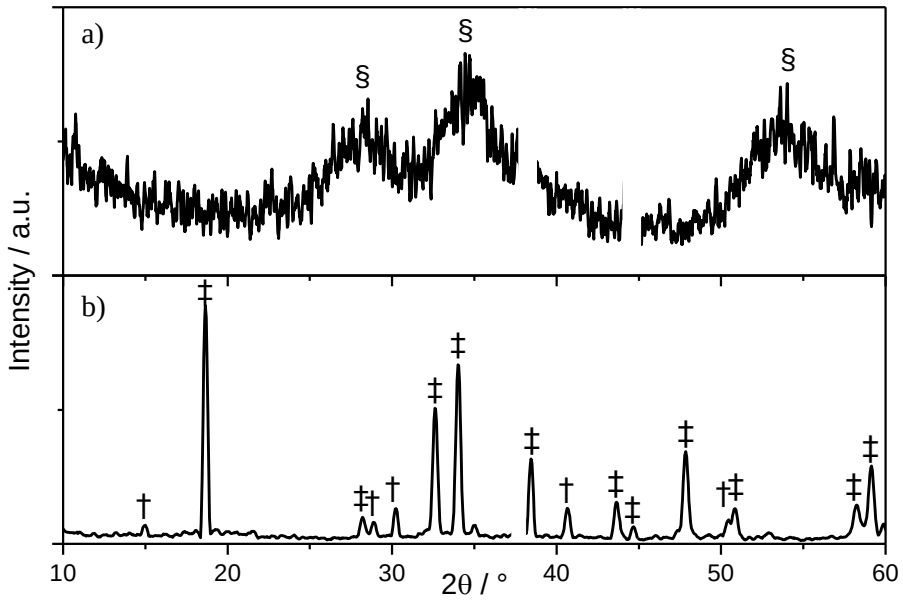

Figure 4.63: Powder XRD data (λ = 1.5418 Å) from materials produced attempting to synthesise $(Ca,Na)_{2-x}Ir_2O_6 \cdot H_2O$, a) in 2 M NaOH at 240 °C, and b) in 15 M NaOH at 240 °C. § indicating peaks arising from IrO_2, † indicating peaks arising from pyrochlore phase and ‡ indicating peaks arising from Ca_2IrO_4 phase. Peaks at form sample holder at 38 and 44 ° masked.

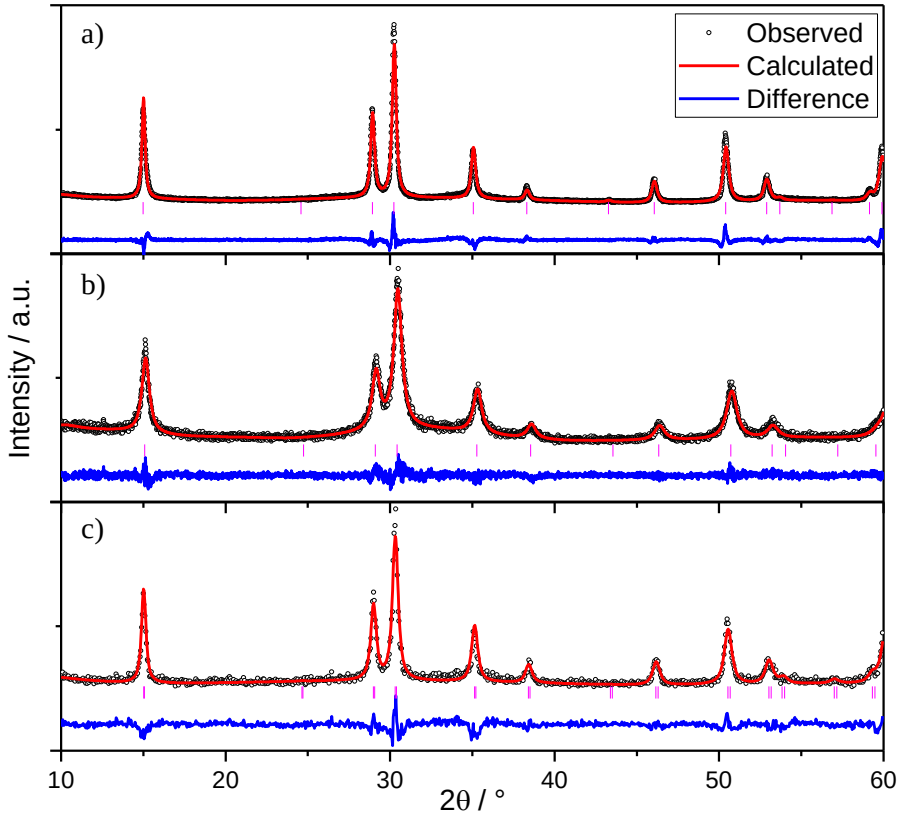

Figure 4.64: Le Bail fits to powder XRD data (λ = 1.54056 Å) from materials produced attempting to synthesise $(Ca,Na)_{2-x}Ir_2O_6 \cdot H_2O$, a) in 5 M NaOH at 240 °C, b) in 10 M NaOH at 170 °C, and c) in 10 M NaOH at 200 °C.

Table 4.22: Table detailing effect of reaction condition on lattice parameter and crystallite size of $(Ca,Na)_{2-x}Ir_2O_6 \cdot H_2O$.

Temperature	NaOH Concentration	Lattice Parameter	Crystallite Size
170 °C	10 M	10.1981(11) Å	11.2 ± 1.9 nm
200 °C	10 M	10.2142(5) Å	25.0 ± 0.7 nm
240 °C	10 M	10.23978(5) Å	36.2 ± 2.4 nm
240 °C	5 M	10.2355(2) Å	20.8 ± 4.4 nm

4.5.3 Acid Leaching

It was believed that the calcium and sodium on the A-site of these materials could be leachable under operational conditions in the MEA, resulting in damage to the ionomer or carbon support. All the powder XRD patterns of acid leached pyrochlores, Figures 4.65 and 4.66, synthesised can be indexed and fitted using the space group $Fd\bar{3}m$. In all instances the leached materials have contracted lattice parameters when compared to the as made $(Ca,Na)_{2-x}Ir_2O_6 \cdot H_2O$, Table 4.22, or $Ca_{2-x}Ir_2O_6 \cdot H_2O$, Table 4.23, as well as a decrease in crystallite size. The materials produced by leaching at 110 °C display a greater reduction in

lattice parameter and broader Bragg peaks than those leached at 80 °C, which given the increased harshness of the leaching is unsurprising as the A site metals are likely to have been extracted. The decrease in lattice parameter, Figure 4.67, is consistent with what is observed in literature: for example, when $Tl_2Ta_2O_6$ undergoes ion exchange with HCl forming $H_2Ta_2O_6 \cdot H_2O$,[8] with the protons binding to the 48*f* oxygens, rather than occupying the 16*d* site, that of the A-site metals. The leaching process affects the two materials differently, with the crystallinity of the calcium sodium iridium oxide been reduced to the point where Bragg peaks are hardly seen above the background of the powder XRD. Conversely the calcium iridium oxide retains its crystallinity to a much better degree despite the harsh reaction conditions, as evidenced by the relative broadness of the Bragg peaks. Further a high degree of asymmetry is observed in the peaks in the XRD patterns of the leached calcium sodium iridium oxide, possibly suggesting deviation from the ideal pyrochlore structure or the formation of nano domains of various compositions.

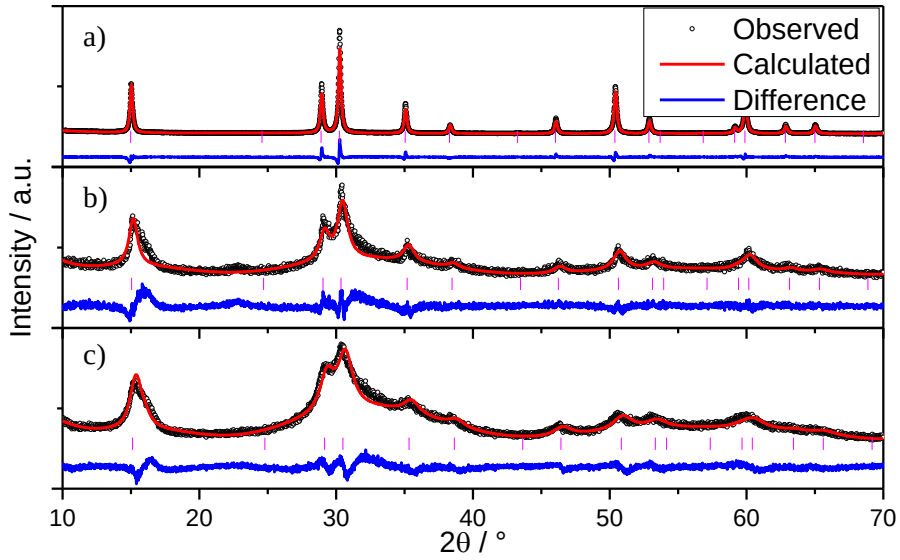

Figure 4.65: Rietveld refinements to powder XRD data (λ = 1.54056 Å) from $(Ca,Na)_{2-x}Ir_2O_6 \cdot H_2O$, a) as made b) leached at 80 °C c) leached at 110 °C.

Table 4.23: Structural details of acid leached calcium sodium iridium oxide pyrochlores obtained from Rietveld refinement of powder XRD data.

Atom	Site	*x*	*y*	*z*	Occ	U_{iso} / Å^2
(Ca,Na) Pyrochlore Leached 80 °C :						
a = 10.1921(13) Å / Crystallite Size = 6.4 ± 1.1 nm						
Ca	16*d*	0.5	0.5	0.5	0.713(15)	0.041(7)
Ir	16*c*	0	0	0	1.000(3)	0.027(1)
O	48*f*	0.3204(15)	0.125	0.125	1.00(2)	0.021(10)
O'	8*b*	0.375	0.375	0.375	1.01(6)	0.05(3)
(Ca,Na) Pyrochlore Leached 110 °C :						
a = 10.1549(15) Å / Crystallite Size = 3.9 ± 0.9 nm						
Ca	16*b*	0.5	0.5	0.5	0.724(14)	0.41(2)
Ir	16*c*	0	0	0	1.000(2)	0.039(1)
O	48*f*	0.3280(3)	0.125	0.125	0.998(17)	0.011(6)
O'	8*b*	0.375	0.375	0.375	1.01(4)	0.066(19)

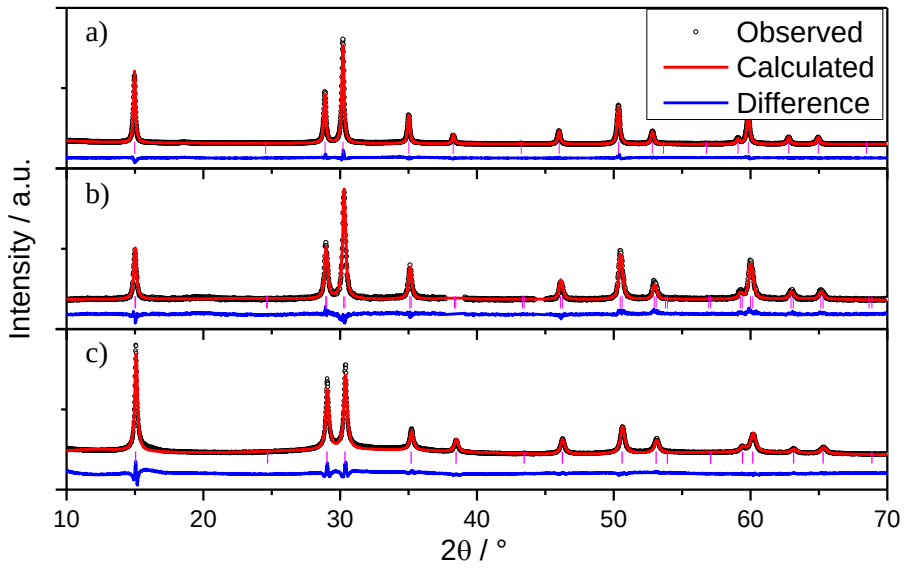

Figure 4.66: Rietveld refinements to powder XRD data (λ = 1.54056 Å) from $Ca_{2-x}Ir_2O_6 \cdot H_2O$, a) as made b) leached at 80 °C c) leached at 110 °C.

Table 4.24: Structural details of acid leached calcium iridium oxide pyrochlores obtained from Rietveld refinement of powder XRD data.

Atom	Site	*x*	*y*	*z*	Occ	U_{iso} / Å^2
Ca Pyrochlore Leached 80 °C :						
a = 10.2194(2) Å / Crystallite Size = 28.7 ± 3.4 nm						
Ca	16*d*	0.5	0.5	0.5	0.644(4)	0.042(3)
Ir	16*c*	0	0	0	1.000(3)	0.006(2)
O	48*f*	0.3267(9)	0.125	0.125	1.003(15)	0.044(10)
O'	8*b*	0.375	0.375	0.375	1.00(2)	0.061(12)
Ca Pyrochlore Leached 110 °C :						
a =10.19599(12) Å / Crystallite Size = 21.2 ± 4.7 nm						
Ca	16*d*	0.5	0.5	0.5	0.353(5)	0.058(4)
Ir	16*c*	0	0	0	1.000(1)	0.0219(2)
O	48*f*	0.3351(6)	0.125	0.125	1.000(10)	0.030(3)
O'	8*b*	0.375	0.375	0.375	1.000(12)	0.016(6)

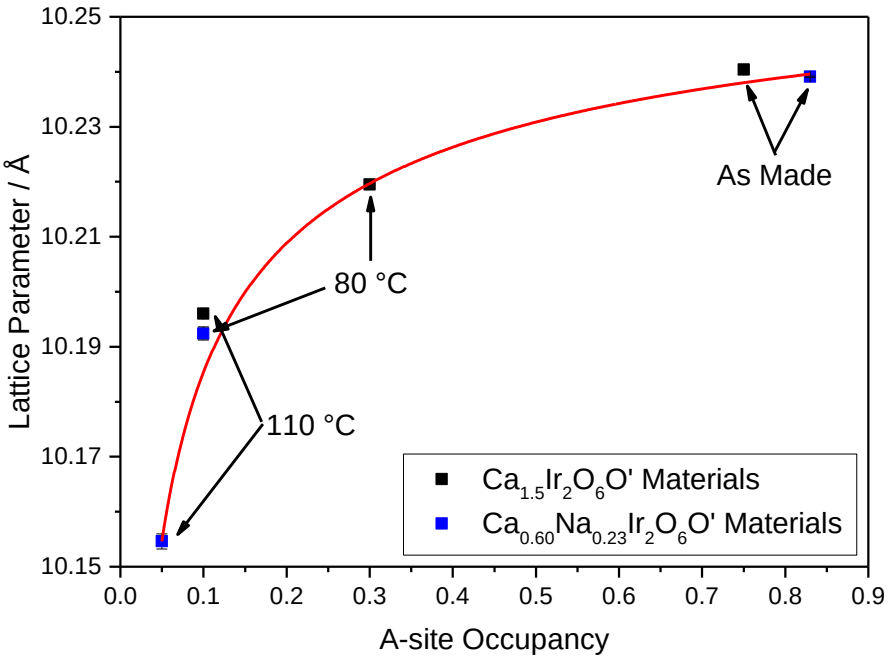

Figure 4.67: Refined Lattice Parameter of unleached and Leached materials vs. A-site occupancy from EDX. Points marked with leaching temperature.

In the X-ray diffraction of the $Ca_{2-x}Ir_2O_6{\cdot}H_2O$ leached at 110 °C, the relative intensities of the 111 and 311 Bragg peaks are greater than those in the unleached material, and the relative intensity of the 222 peak decreases. This can be accounted for by loss of electron density from the 16*d* site, Figure 4.68, which is entirely consistent with calcium being removed from the structure.

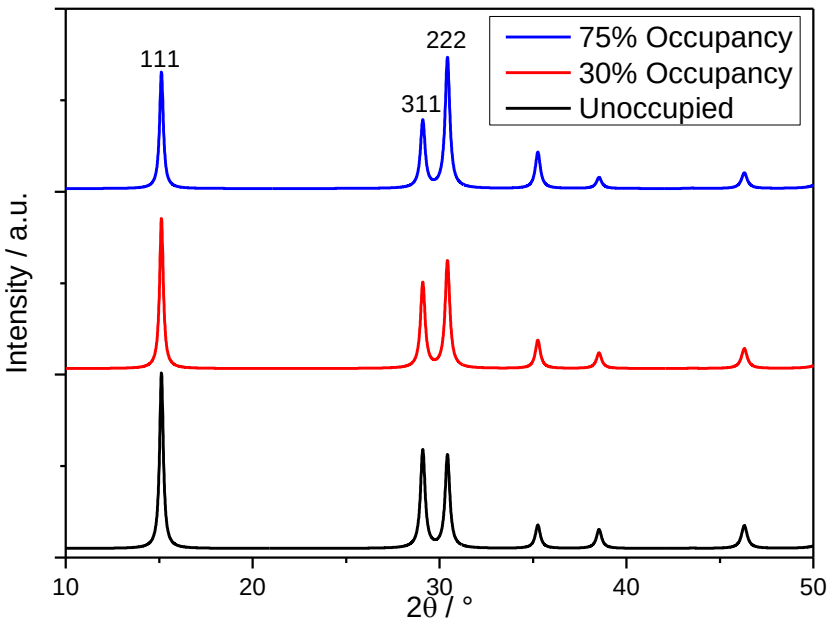

Figure 4.68: Simulated XRD patterns of a) $Ca_{1.5}Ir_2O_7$, b) $Ca_{0.6}Ir_2O_7$and c) $Ca_{0.0}Ir_2O_7$, showing effect on relative intensities of 111, 311 and 222 peaks. (λ = 1.54056 Å)

The simulations of $Ca_{1.5}Ir_2O_7$ with various 48*f* oxygen coordinates, Figure 4.69, reveal that this contributes to the relative intensity of the 111 Bragg peak in the observed diffraction patterns. However, in the fits of powder XRD data of the leached materials the x co-ordinate of the 48*f* oxygen does not change to any appreciable degree, and as any large change would distort the octahedral environment of the iridium, this is somewhat unlikely.

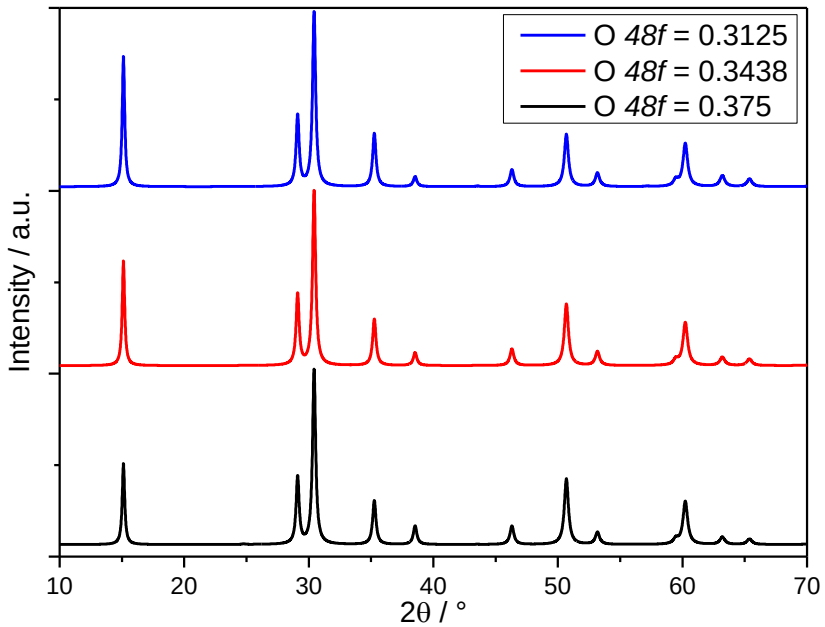

Figure 4.69: Simulated XRD patterns of $Ca_{1.5}Ir_2O_7$ with various x co-ordinates of 48*f* oxygens a) x = 0.3125, b) x = 0.3438 and c) x = 0.3750, showing effect on relative intensities of the 111 peak. (λ = 1.54056 Å)

HR-TEM images of the leached calcium sodium iridium oxide pyrochlores show the particles have maintained their size and octahedral shape despite the treatment in strong acid. In the unleached particles lattice planes are clearly observable in TEM, Figure 4.70, however once the samples underwent the leaching process, these planes are no longer resolvable, Figures 4.71 and 4.72 consistent with the decrease in crystallite size domain size observed in the XRD data.

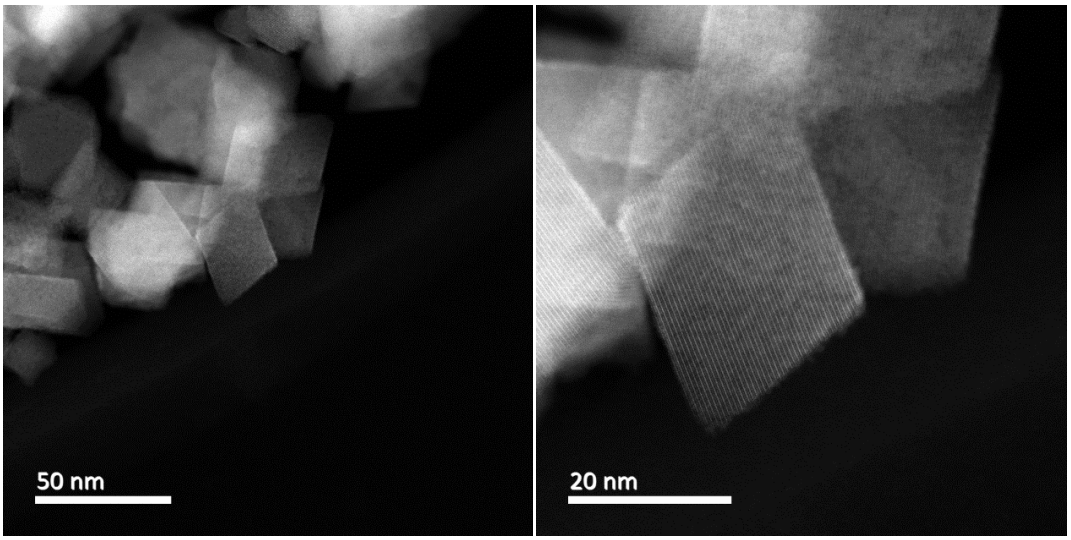

Figure 4.70: HR-TEM micrographs of as-made $(Ca_{0.60}Na_{0.23})_2Ir_2O_6 \cdot H_2O$.

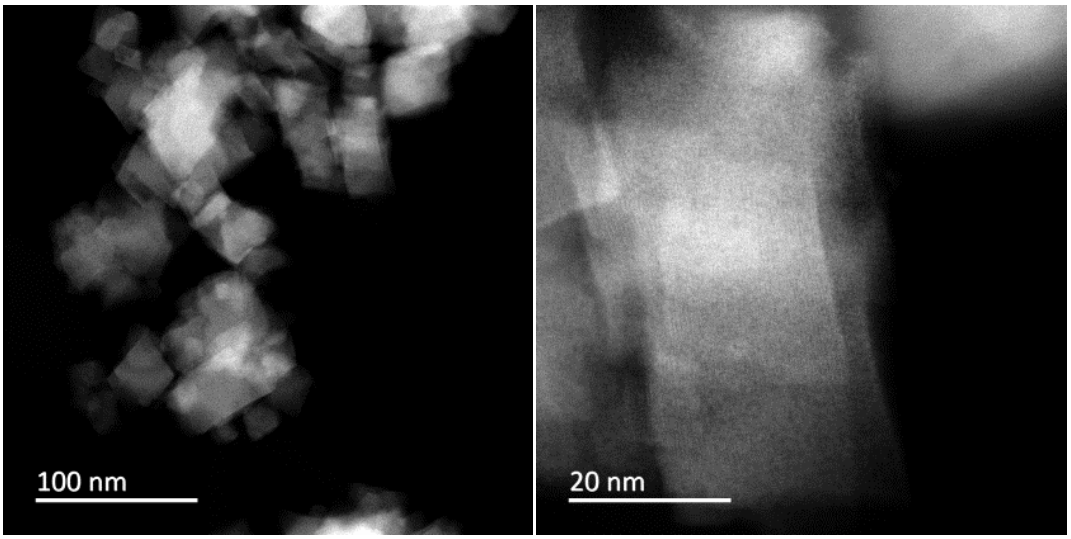

Figure 4.71: HR-TEM micrographs of $(Ca_{0.60}Na_{0.23})_2Ir_2O_6 \cdot H_2O$ leached at 80 °C.

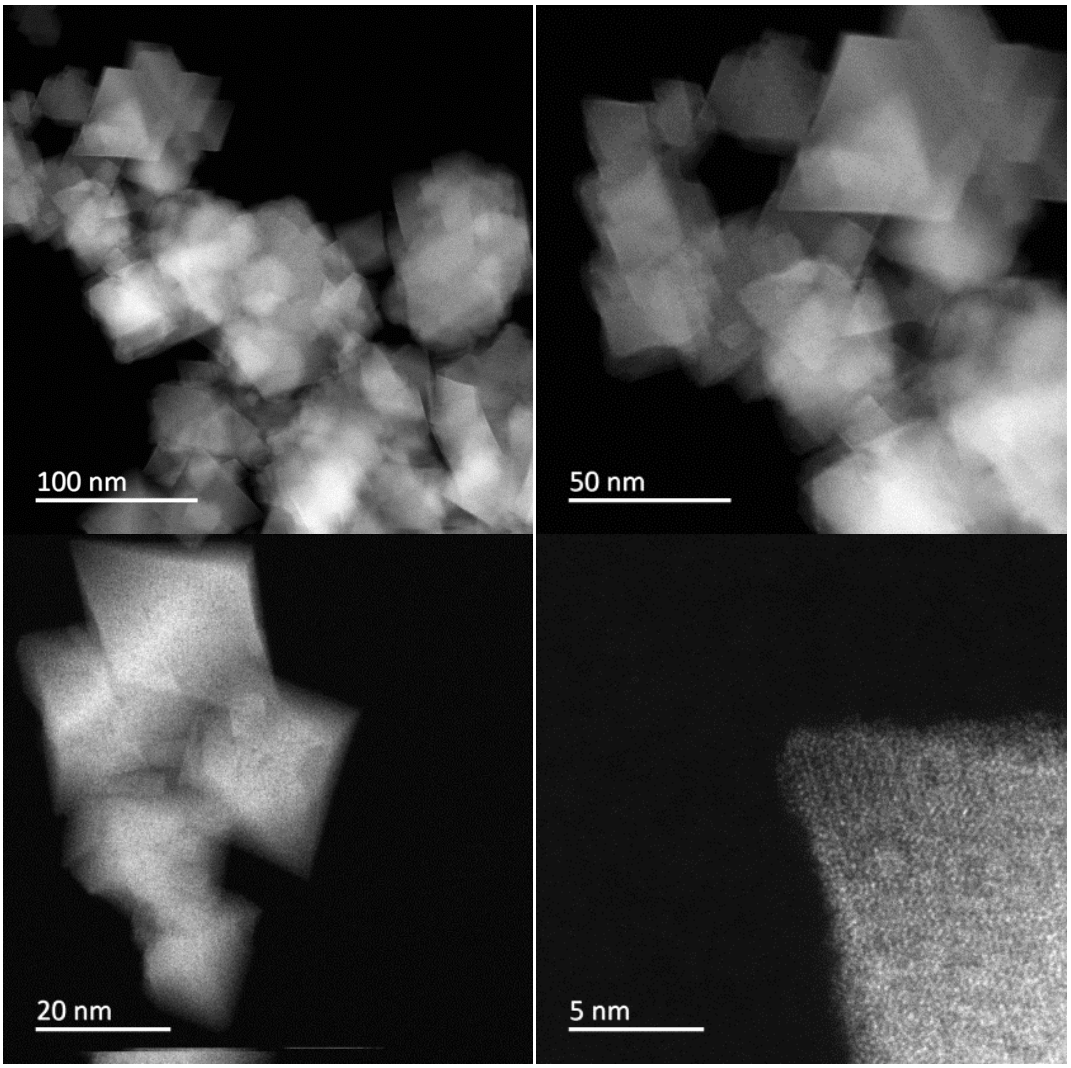

Figure 4.72: HR-TEM micrographs of $(Ca_{0.60}Na_{0.23})_2Ir_2O_6 \cdot H_2O$ leached at 110 °C.

Elemental maps, Figure 4.73, and EDXA line scans, Figure 4.74, of the as made $(Ca_{0.60}Na_{0.23})_2Ir_2O_6 \cdot H_2O$ reveal that calcium, iridium and oxygen are homogeneously distributed across to whole of the particle. One might expect a core-shell motif for the materials that underwent the leaching process, with calcium rich regions in the centres of particles, however the elemental mapping, Figure 4.75, and line scans, Figures 4.76 and 4.77, show calcium has been uniformly leached from the material. Line scans have been normalised in the manner described in Chapter 2.

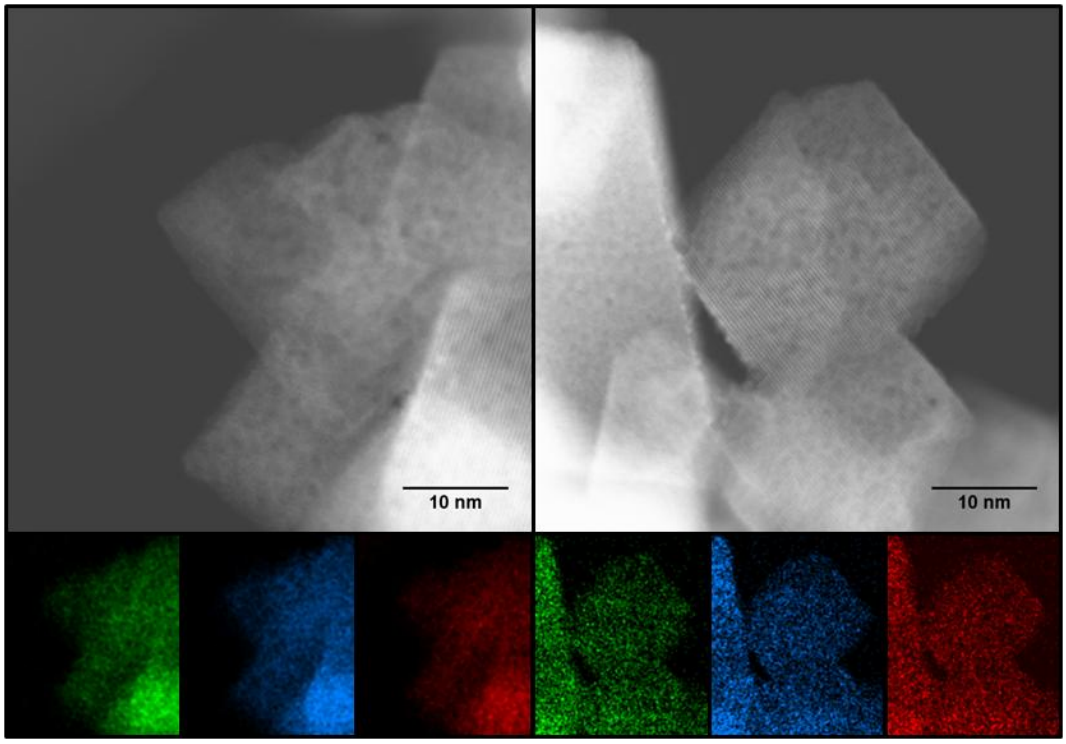

Figure 4.73: Elemental maps of as-made $(Ca_{0.60}Na_{0.23})_2Ir_2O_6 \cdot H_2O$, calcium shown in green, iridium in blue and oxygen in red.

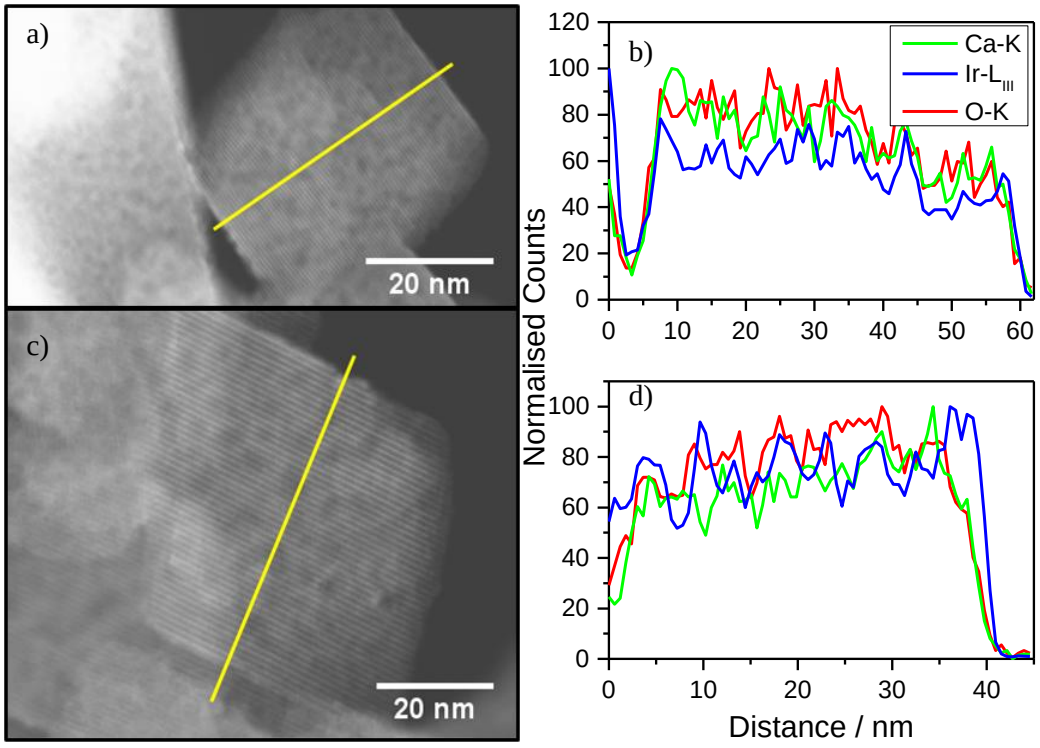

Figure 4.74: a) + c) Micrographs of $(Ca_{0.60}Na_{0.23})_2Ir_2O_6 \cdot H_2O$ with line profile region for analysis indicated, b) + d) normalised results of EDX line scans.

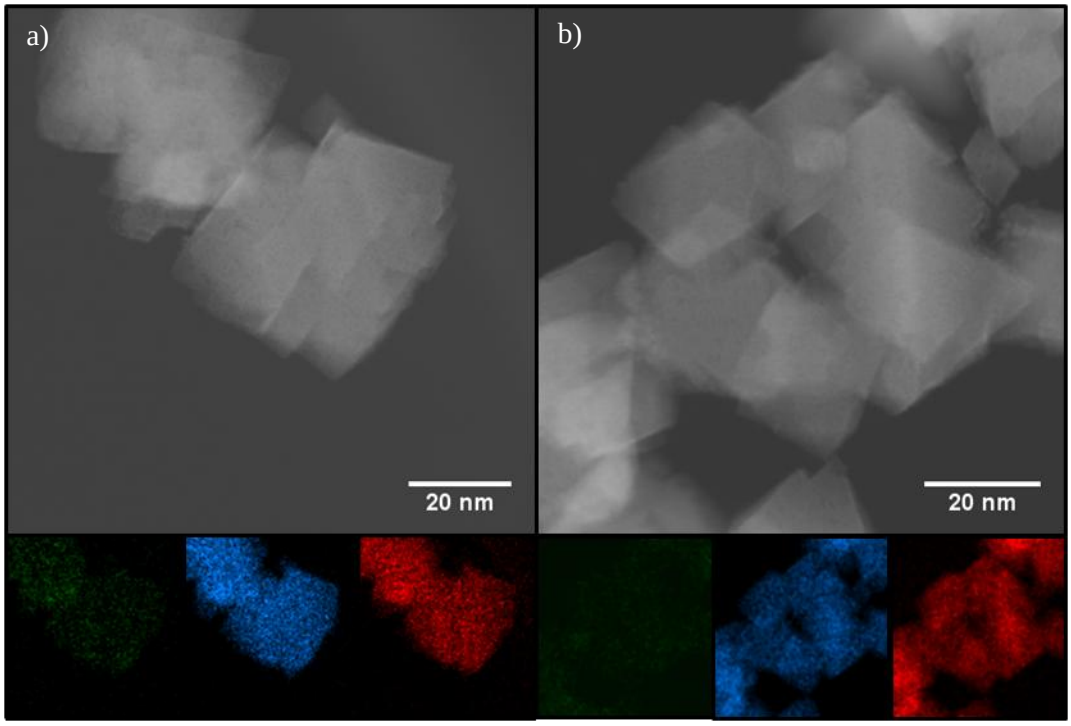

Figure 4.75: Elemental maps of $(Ca_{0.60}Na_{0.23})_2Ir_2O_6 \cdot H_2O$ leached at a) 80 °C b) 110 °C, calcium shown in green, iridium in blue and oxygen in red.

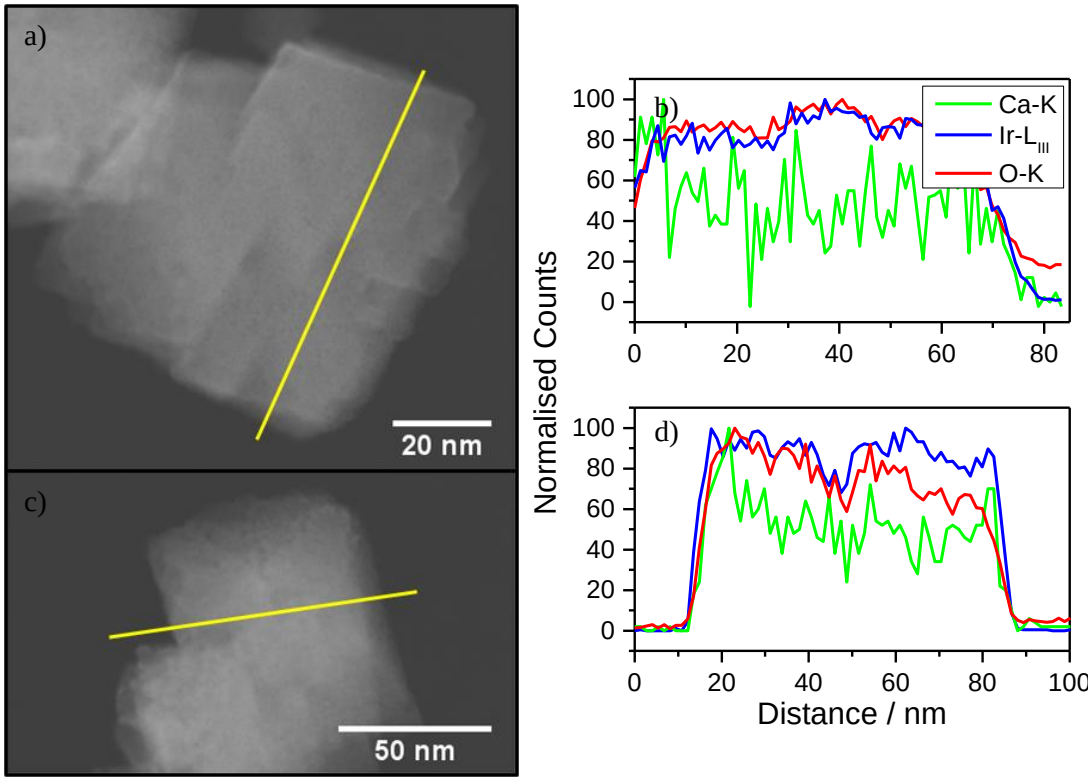

Figure 4.76: a) + c) Micrographs of $(Ca_{0.60}Na_{0.23})_2Ir_2O_6 \cdot H_2O$ leached at 80 °C with line profile region for analysis indicated, b) + d) normalised results of EDX line scans.

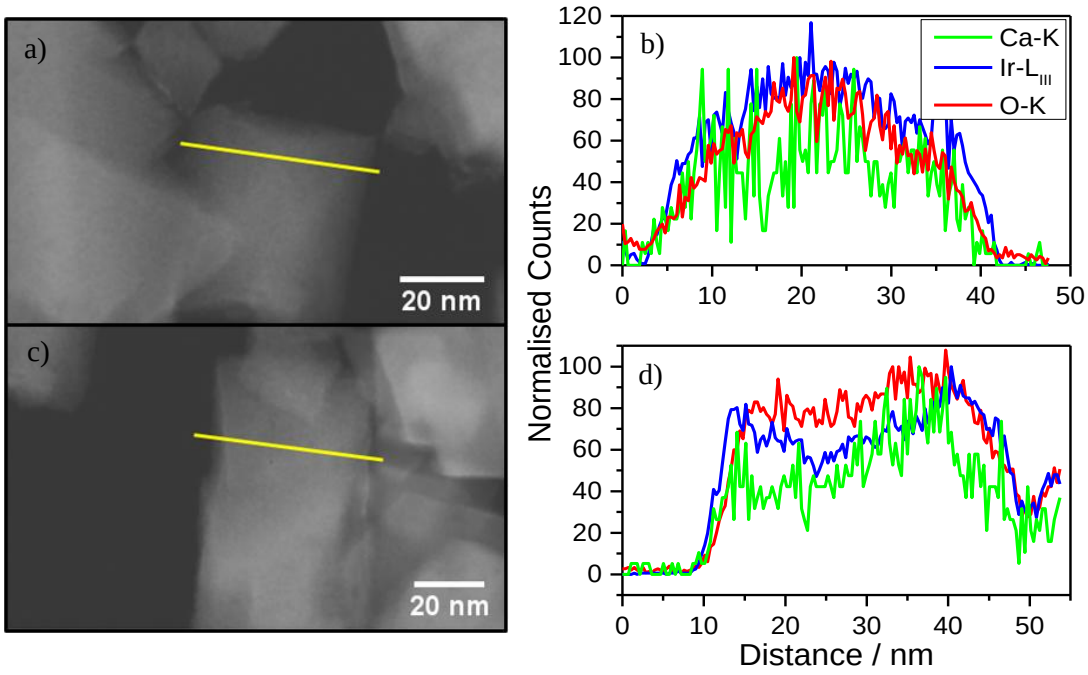

Figure 4.77: a) + c) Micrographs of $(Ca_{0.60}Na_{0.23})_2Ir_2O_6 \cdot H_2O$ leached at 110 °C with line profile region for analysis indicated, b) + d) normalised results of EDX line scans.

XANES data recorded at the Ir-L_{III} edge, Figure 4.78, of $(Ca_{0.60}Na_{0.23})_2Ir_2O_6 \cdot H_2O$ leached at 110 °C shows that the iridium remains oxidised above +4, with a measured oxidation state of +4.25. This apparent reduction is within the error of the technique as described in Section 4.4.7. So it is possible that the oxidation state of the iridium is unchanged by the leaching process.

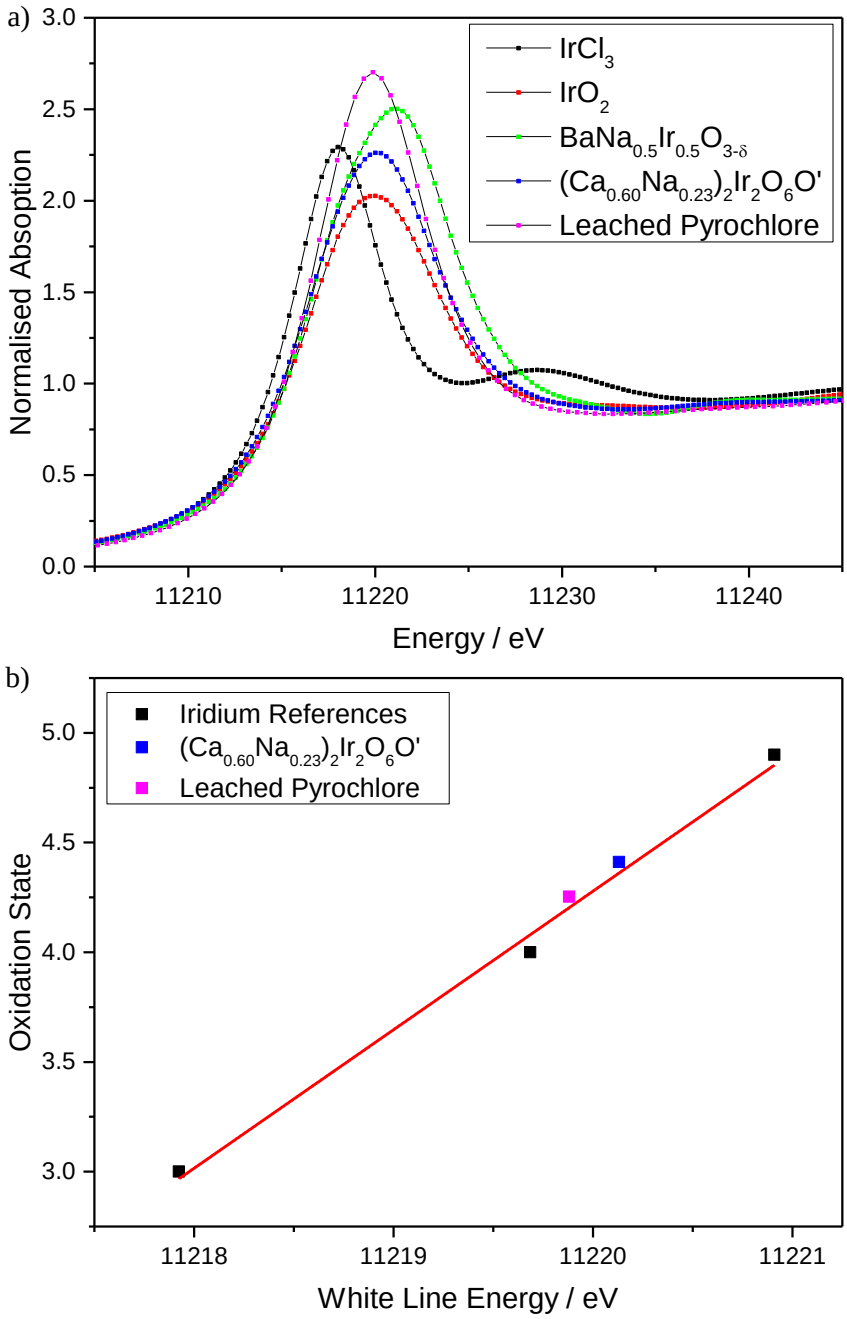

Figure 4.78: a) Ir L_{III}-edge XANES spectra of calcium sodium iridium oxide acid leached at 110 °C and reference materials for calibration. b) White line position against iridium oxidation state.

Charge balance needs to be maintained upon removal of the A-site metals, and a review of the literature would suggest this is accomplished by the coordination of protons to oxygen within the pyrochlore structure. However, there is the possibility of the cation H_3O^+ replacing calcium and sodium on the A-site. As such TGA-MS, Figure 4.79, was employed to look for not only crystal water but any H_3O^+ within the structure. In the leached calcium sodium iridium oxide an initial mass loss of 2.7 % is observed, up to the end of the 4 hour

hold at 120 °C, and can attributed to the loss of surface water. Thermodiffractometry, Figure 4.80, reveals that around 400 °C a phase change occurs, lining up perfectly with the spike in the DSC and emergence of an IrO_2 phase. Assuming the formula $H_2Ir_2O_6 \cdot H_2O$ then the theoretical loss to the formation of IrO_2 is 10.4 %. The observed loss is 9.2 %, the slight difference is likely due to residual calcium in the material forming CaO. The next major loss, the onset of which is 750 °C lines up well with IrO_2 reducing to Ir metal.

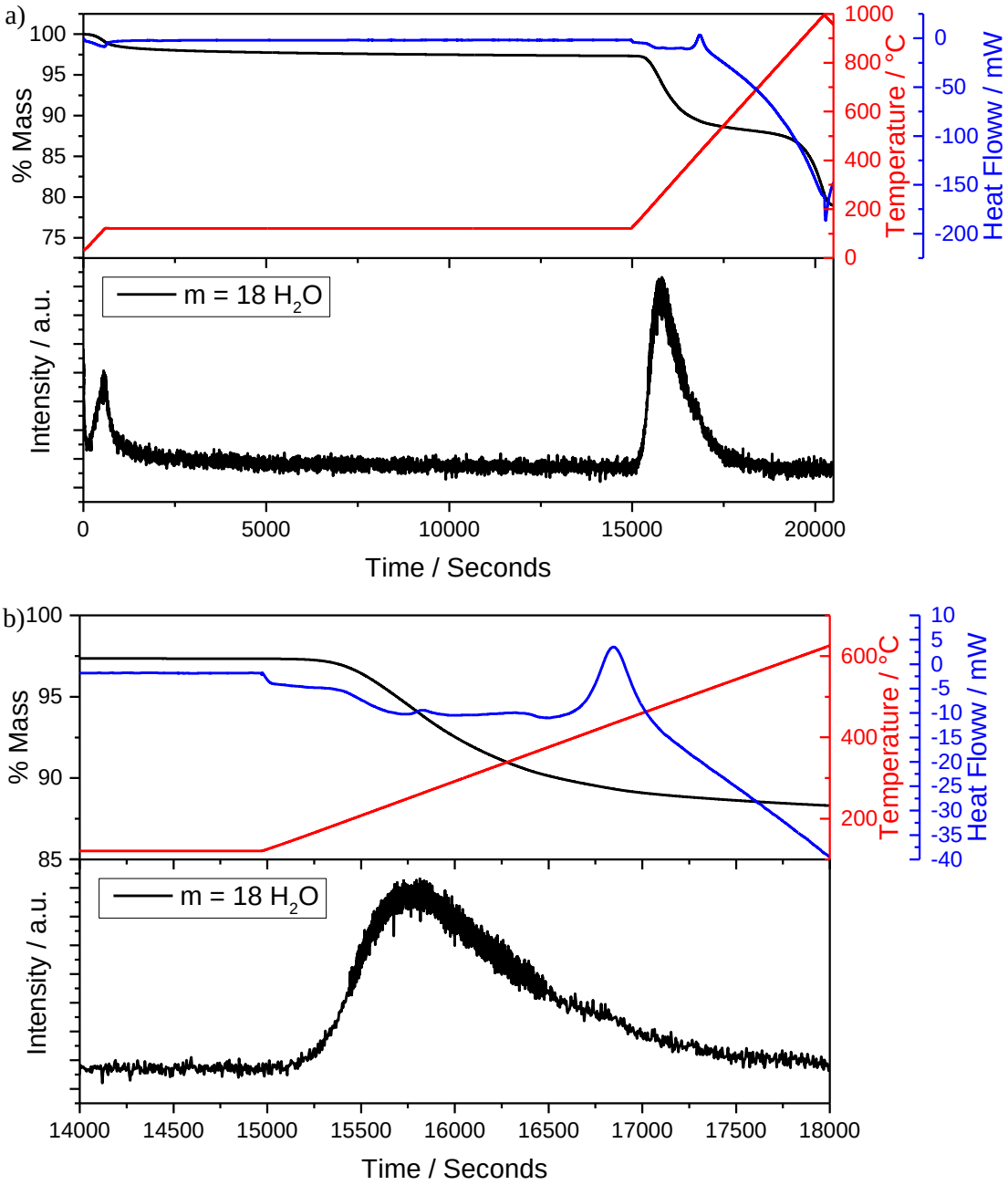

Figure 4.79: TGA-MS plots a) complete range and b) zoom of region with loss of crystal water of calcium sodium iridium oxide leached at 110 °C.

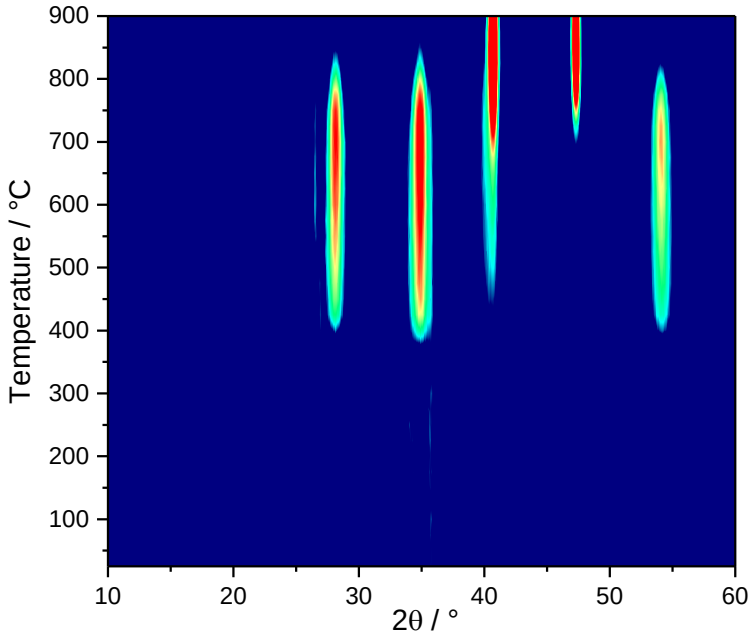

Figure 4.80: Thermodiffractometry (λ = 1.5418 Å) of acid leached calcium sodium iridium oxide.

The TGA-MS of the leached calcium iridium oxide, Figure 4.81, an initial mass loss of 2.4 % is observed, up to the end of the 4 hour hold at 120 °C, and can attributed to the loss of surface water. Thermodiffractometry, Figure 4.82, reveals a phase change to IrO_2 around 400 °C up until this point a further mass loss of 9.4 % is observed. Again assuming the formula $H_2Ir_2O_6 \cdot H_2O$ then the theoretical loss to the formation of IrO_2 is 10.4 %. The slight difference is likely due to residual calcium in the material forming CaO. The next major loss, the onset of which is 750 °C lines up well with IrO_2 reducing to Ir metal.

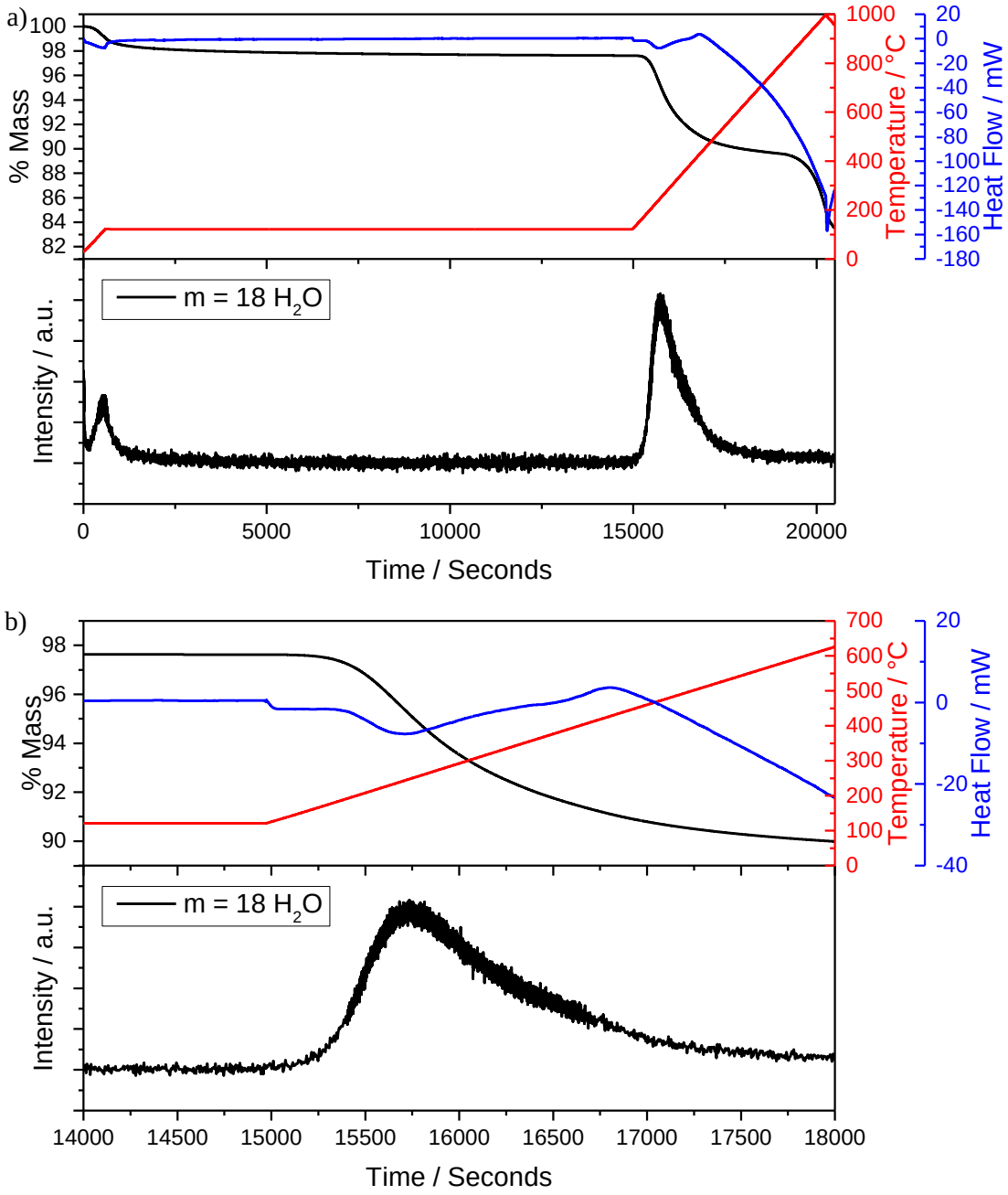

Figure 4.81: TGA-MS plots a) complete range and b) zoom of region with loss of crystal water of calcium iridium oxide leached at 110 °C.

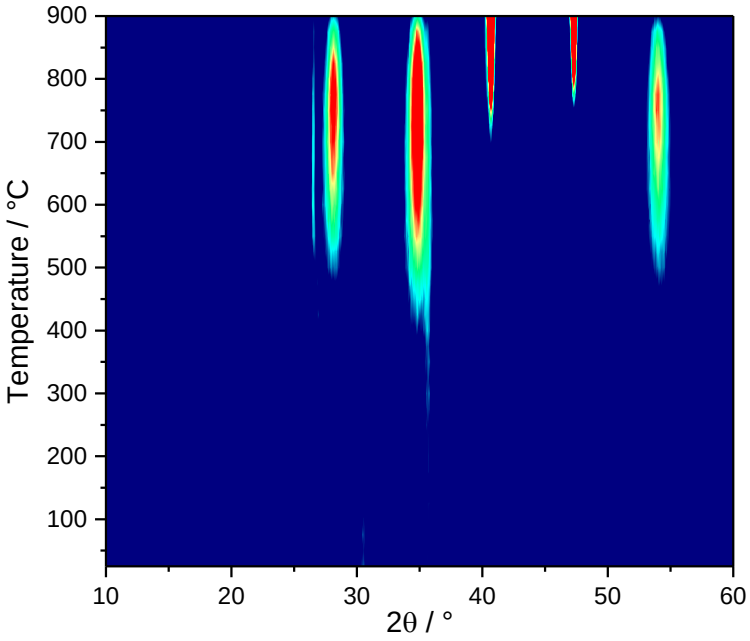

Figure 4.82: Thermodiffractometry (λ = 1.5418 Å) of acid leached calcium sodium iridium oxide.

4.5.4 Discussion

In this section it has been shown that by tuning reaction conditions or by performing post reaction acid treatment the composition and physical form of the unsubstituted pyrochlore material can be adjusted.

The synthesis of a material with only calcium on the A-site was accomplished with the formula $Ca_{1.5}Ir_2O_6{\cdot}H_2O$, and the PDF of this material matched the Rietveld crystal structure model exceedingly well, better than was found for $(Ca_{0.60}Na_{0.23})_2Ir_2O_6{\cdot}H_2O$, suggesting the inclusion of sodium onto the A-site introduces some form of extra disorder.

Two methods for regulating the crystallite size of $(Ca,Na)_{2-x}Ir_2O_6O'$ have proven effective. Tuning the concentration of NaOH solution has proven effective over a small range, as was also found for controlling crystallite size in $Bi_2Ir_2O_7$,[5] however changing the reaction temperature provides a larger range of crystallite size in the calcium sodium iridates.

Two sets of acid leached materials have been produced, and that in broad terms they all maintain the average pyrochlore structure. The biggest issue in these materials is the matter of charge balance, as if $H_2Ir_2O_6{\cdot}H_2O$ is the composition of the acid leached pyrochlore then

all the iridium would have to be +5. BVS yield iridium oxidation states between +4.8 and +5.6, which doesn't completely eliminate the possibility, however XANES data clearly shows the iridium is not oxidised that high. If the protons are not located on the 16*d* site, but are adjacent to the oxygens occupying the 48*f* site, like in $H_2Ta_2O_6 \cdot H_2O$[8], it would be possible for more than two protons to be incorporated per formula unit, yielding $H_{2+x}Ir_2O_6 \cdot H_2O$. If x = 1 then the iridium in the material would have an oxidation state of +4.5 like every other material synthesised in this body of work, and given how hard it is to oxidise iridium above +4 this seems more likely. If protons are binding to the oxygens within the structure then neutron diffraction experiments need to be performed in order to fully understand the behaviour of these light elements.

References

1 K. Sardar, E. Petrucco, C. I. Hiley, J. D. B. Sharman, P. P. Wells, A. E. Russell, R. J. Kashtiban, J. Sloan and R. I. Walton, *Angew. Chemie Int. Ed.*, 2014, **53**, 10960–10964.

2 K. Sardar, J. Fisher, D. Thompsett, M. R. Lees, G. J. Clarkson, J. Sloan, R. J. Kashtiban and R. I. Walton, *Chem. Sci.*, 2011, **2**, 1573–1578.

3 A. T. Marshall, S. Sunde, M. Tsypkin and R. Tunold, *Int. J. Hydrogen Energy*, 2007, **32**, 2320–2324.

4 M. A. Subramanian, G. Aravamudan and G. V. S. Rao, *Prog. Solid State Chem.*, 1983, **15**, 55–143.

5 K. Sardar, S. C. Ball, J. D. B. Sharman, D. Thompsett, J. M. Fisher, R. A. P. Smith, P. K. Biswas, M. R. Lees, R. J. Kashtiban, J. Sloan and R. I. Walton, *Chem. Mater.*, 2012, **24**, 4192–4200.

6 J. N. Millican, R. T. Macaluso, S. Nakatsuji, Y. Machida, Y. Maeno and J. Y. Chan, *Mater. Res. Bull.*, 2007, **42**, 928–934.

7 D.-Y. Jung, G. Demazeau, J. Etourneau and M. A. Subramanian, *Mater. Res. Bull.*, 1995, **30**, 113–123.

8 P. G. Dickens and M. T. Weller, *Solid State Commun.*, 1986, **59**, 569–573.

9 H. Y. Playford, D. R. Modeshia, E. R. Barney, A. C. Hannon, C. S. Wright, J. M. Fisher, A. Amieiro-Fonseca, D. Thompsett, L. A. O'Dell, G. J. Rees, M. E. Smith, J. V Hanna and R. I. Walton, *Chem. Mater.*, 2011, **23**, 5464–5473.

10 R. A. Beyerlein, H. S. Horowitz, J. M. Longo, M. E. Leonowicz, J. D. Jorgensen and F. J. Rotella, *J. Solid State Chem.*, 1984, **51**, 253–265.

11 Ismunandar, B. J. Kennedy, B. A. Hunter and T. Vogt, *J. Solid State Chem.*, 1997, **131**, 317–325.

12 C. I. Hiley, M. R. Lees, J. M. Fisher, D. Thompsett, S. Agrestini, R. I. Smith and R. I. Walton, *Angew. Chemie Int. Ed.*, 2014, **53**, 4423–4427.

13 R. D. Shannon, *Acta Crystallogr. Sect. A*, 1976, **32**, 751–767.

14 G. Goh, S. Haile, C. Levi and F. Lange, *J. Mater. Res.*, 2002, **17**, 3168–3176.

15 K. Li, T. Zhang, H. Wang and H. Yan, *J. Solid State Chem.*, 2006, **179**, 1029–1034.

16 L. Kong, Z. Zhang, M. de los Reyes, I. Karatchevtseva, G. R. Lumpkin, G. Triani and R. D. Aughterson, *Ceram. Int.*, 2015, **41**, 5309–5317.
17 G. D. Blundred, C. A. Bridges and M. J. Rosseinsky, *Angew. Chemie Int. Ed.*, 2004, **43**, 3562–3565.
18 T. A. Vanderah, I. Levin and M. W. Lufaso, *Eur. J. Inorg. Chem.*, 2005, **2005**, 2895–2901.
19 G. S. Babu, S. Bedanta and M. Valant, *Solid State Commun.*, 2013, **158**, 51–53.
20 B. A. Reisner and and Angelica M. Stacy, *J. Am. Chem. Soc.*, 1998, **120**, 9682–9683.
21 O. Muller and R. Roy, *J. Less Common Met.*, 1968, **16**, 129–146.
22 G. Demazeau, A. Baranov, R. Poettgen, L. Kienle, M. H. Moeller, R.-D. Hoffmann and M. Valldor, *ChemInform*, 2007, **38**, 1500–1506.
23 R. S. Nyholm, P. R. Woolliams, D. Shepard, J. Guyer and K. Cohn, in *Inorganic Syntheses*, John Wiley & Sons, Inc., 2007, pp. 56–61.
24 A. Talanov, W. A. Phelan, Z. A. Kelly, M. A. Siegler and T. M. McQueen, *Inorg. Chem.*, 2014, **53**, 4500–4507.
25 A. A. Bolzan, C. Fong, B. J. Kennedy and C. J. Howard, *Acta Crystallogr. Sect. B*, 1997, **53**, 373–380.
26 D. C. Wallace and T. M. McQueen, *Dalt. Trans.*, 2015, **44**, 20344–20351.
27 G. J. Thorogood, B. J. Kennedy, V. Luca, M. Blackford, S. K. van de Geest, K. S. Finnie, J. V Hanna and K. J. Pike, *J. Phys. Chem. Solids*, 2008, **69**, 1632–1640.
28 D. E. Bugaris, M. D. Smith and H.-C. zur Loye, *Inorg. Chem.*, 2013, **52**, 3836–3844.

Chapter 5 – Exploratory Synthesis of New Iridium and Ruthenium Oxide Materials

5.1 Introduction to and Scope of Chapter

In this chapter an exploration into the synthesis of various iridium and ruthenium oxides is reported, which was performed with the aim of producing new materials with favourable OER properties.

The first of the materials investigated is the hollandite $K_{0.25}IrO_2$. This has previously been synthesised from K_2CO_3 and IrO_2, at elevated temperatures in the solid state.[1] There is one example of the synthesis of this material that uses a hydrothermal step to synthesise a precursor material,[2] which was investigated in the current work.

Ruthenium dioxide has hydrated and dehydrated forms, both of which have been shown to be highly active catalysts for the OER under both acidic and alkaline media,[3–5] however the literature is sparse with respect to the OER properties of mixed metal ruthenium oxides adopting other structures. However the orthorhombic perovskites $CaRuO_3$ and $SrRuO_3$ as well as 4H-$BaRuO_3$, an hexagonal perovskite, have been shown to be active for the HER.[6] Recently a whole series of new ruthenium oxides have been synthesised from potassium perruthenate and group II metal peroxides.[7] It is known that choice of precursor can have a large effect on the outcome of a hydrothermal reaction, so this chapter also describes a study of the reactions of Group II peroxides and ruthenium (III) chloride.

Perovskite structured sodium tantalates and niobates have long been synthesised hydrothermally, and it was hoped that by substituting iridium and ruthenium into these materials electrochemically active catalysts could be produced. Other metals such as bismuth have previously been substituted into the material, yielding materials which are efficient catalysts for the degradation of methylene blue under visible light.[8]

In Chapter 4, it was demonstrated how to synthesise a sodium free calcium iridate, this was further investigated with the synthesis of a sodium free strontium iridate, adopting the same $KSbO_3$-type structure as seen for the sodium containing analogue.[9]

Finally the synthesis of a previously unreported barium iridate is described and attempts at trying to solve the structure are described.

5.2 $K_{0.25}IrO_2$ Hollandite

5.2.1 Synthesis of IrO_2 Precursor

Initially the synthesis of a iridium containing hollandite was attempted based on the work of Sun *et al.*[2] It became apparent a one step hydrothermal synthesis to produce $K_{0.25}IrO_2$ was not possible, and as such, steps were taken to improve the synthesis of the precursor material, Section 5.22. When the reaction proposed by Sun *et al.* was repeated, it was found to yield iridium metal rather than iridium oxide. Additionally it did not fully utilise the iridium in the reaction, as a portion of the iridium remained in solution, in the form of $Ir(OH)_3$ identified by the purple colour of the reaction solution. Metallic iridium is extremely chemically stable, as such it was decided that IrO_2 would be a better precursor, so an oxidising agent was added to the reaction to ensure the formation of IrO_2.

Sun *et al.* identified that the potassium associated with the precursor material facilitated the phase change to hollandite at elevated temperatures. Potassium volatilisation is a known issue at the elevated temperatures,[1] thus the synthesis was optimised, as to maximise the amount of potassium associated with the precursor particles. The logical way to do this is to reduce the particle size of the precursor oxide, increasing the available surface area for potassium associate with. There are many different methods in the literature for controlling particle size and shape; unfortunately many of these involve using surfactants or other additives that bind to the surface to modulate growth, which would be a problem as this would occupy surface sites, hindering potassium association. Multiple methods where found for controlling the potassium content associated with the precursor materials, Section 5.2.2.

Utilising this data, an optimised reaction for the synthesis of the precursor material was devised as is presented below.

IrO_2 precursors were synthesised utilising iridium (III) chloride pentahydrate and potassium superoxide in a ratio of 1:3 respectively, based on using 1.3 mmol of iridium chloride in 10 ml of 1 M KOH. An excess of peroxide was used to ensure the conversion of the iridium chloride to the oxide precursor. The reaction was carried out at 180 °C for three days. When cool, the black powders were collected via vacuum filtration, and not washed as it was desirable to keep as much potassium associated with the particles as possible, for reaction during the firing step, see Section 5.2.3.

5.2.2 IrO_2 Precursor Characterisation

EDXA obtained from SEM, revealed increasing the concentration of potassium superoxide in the reactions results in an increase of the observed potassium to iridium ratio, Table 5.1.

Table 5.1: EDXA of K:Ir ratios of precursor materials and how they vary with KO_2 concentration used in their synthesis.

Potassium Superoxide Concentration $moldm^{-3}$	Atomic %		Molar Ratio
	Potassium	Iridium	K:Ir
0.141	15.0	85.0	0.18:1
0.422	19.5	80.5	0.24:1
0.704	23.8	76.2	0.31:1

An additional method for further increasing the potassium to iridium ratio of the precursor material was to reduce the reaction temperature, Table 5.2.

Table 5.2: EDXA of K:Ir ratios of precursor materials and how they vary with reaction temperature.

Synthesis Temperature °C	Atomic %		Ratio
	Potassium	Iridium	K:Ir
240	23.822	76.178	0.31:1
220	28.616	71.384	0.40:1
200	30.388	69.612	0.43:1
180	33.168	66.832	0.49:1
160	38.822	61.218	0.63:1

Reactions were carried out between 240 and 120 °C; however at reaction temperatures at 160 °C and below the formation of iridium metal is observed, despite being in the presence of high concentration potassium superoxide, Figure 5.1. In addition to the formation of iridium metal at reduced reaction temperatures, the filtrate becomes increasingly purple, indicating that an increasing concentration of iridium is being left in solution.

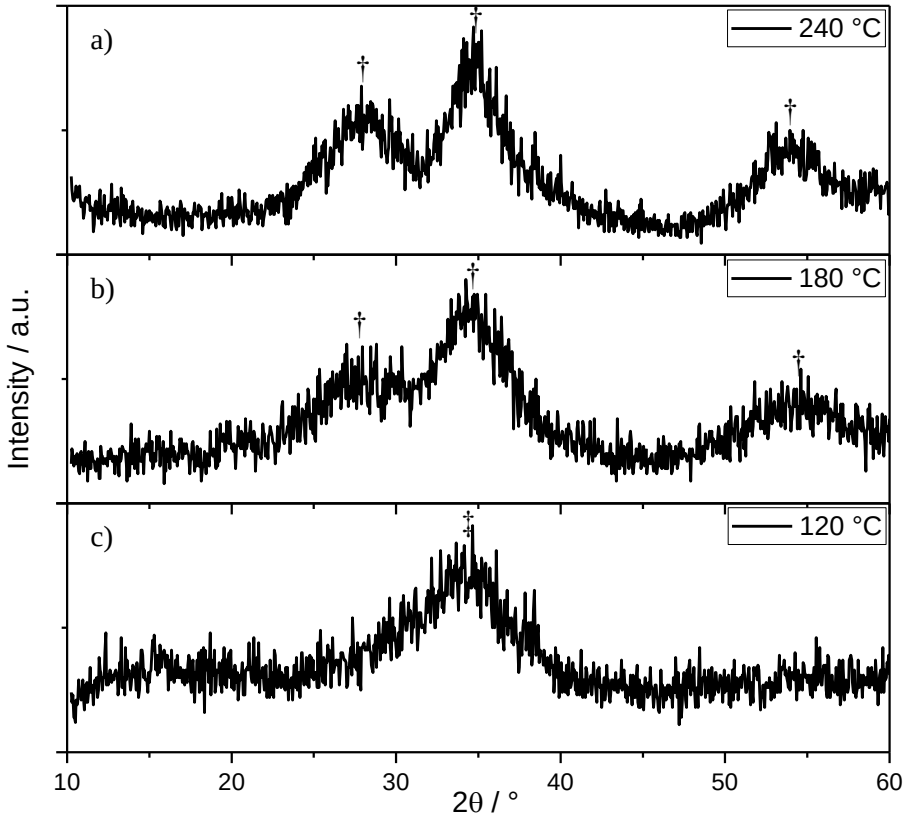

Figure 5.1: Powder XRD patterns (λ = 1.5418 Å) of precursor materials synthesised at various temperatures. a) 240 °C, b) 180 °C and c) 120 °C, using optimised potassium superoxide concentration. † denotes peaks arising from IrO_2 and ‡ peaks arising from Ir.

The powder XRD patterns of the synthesised oxide phases look virtually identical due to the nanocrystalline nature of the synthesised IrO_2, it is noted that there is no observable shift in the peak associated with the rutile type IrO_2, despite the increasing K:Ir ratio found in EDXA, Table 5.2. This suggests the potassium associated with the precursor is found on the surface rather than in the rutile lattice.

XANES spectra recorded at the Ir L_{III}-edge were employed to probe the oxidation state of the iridium in the precursor material produced at 180 °C, Figure 5.2. By comparing the white line position of the material against those of known valence it is possible to observe the effect of the interaction with surface potassium. It is revealed the iridium in the precursor material has an oxidation state of +4, however the white line energy is reduced with respect to the crystalline iridium oxide, while the variance is within the error established in Chapter 4, it is possible that the iridium oxidation state is slightly less than +4 and that potassium ions on the surface of the material are facilitating charge balance due the small crystallite size and presumably high surface area.

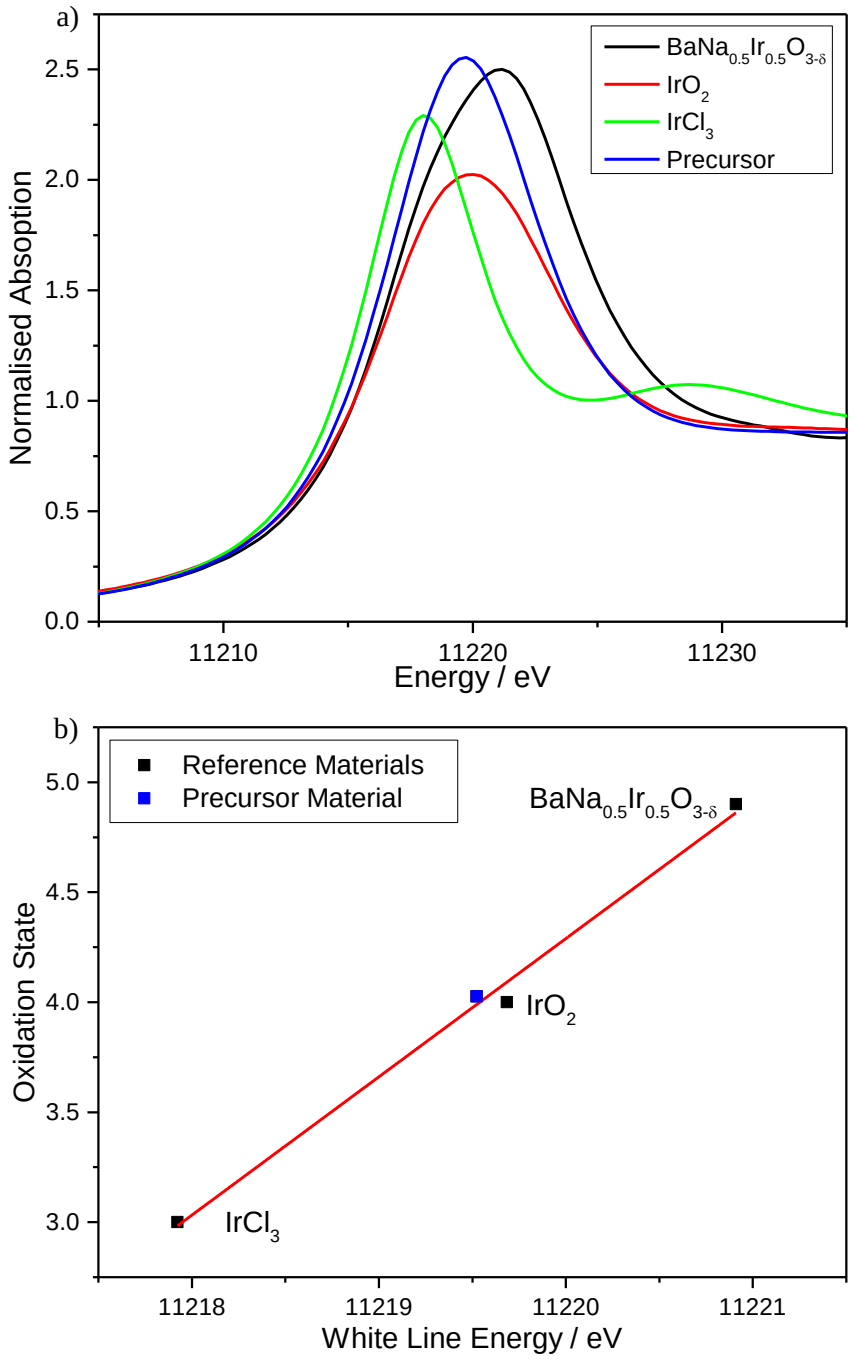

Figure 5.2: a) Ir L_{III}-edge XANES spectra of iridium oxide precursor and reference materials for calibration. b) White line Position against iridium oxidation state.

5.2.3 Characterisation of Hollandite Phase

The synthesis of $K_{0.25}IrO_2$ can be achieved between 600-1000 °C in air, utilising iridium oxide and potassium carbonate as reagents.[1] As such, preliminary reactions using the precursor were carried out at 1000 °C, however at this temperature complete reduction of the precursor to iridium metal takes place. When the same reaction was carried out at 600 °C it

yielded the hollandite $K_{0.25}IrO_2$, which can be fitted with the tetragonal space group *I* 4/*m*, Figure 5.3, with lattice parameters similar to that observed in the literature, Table 5.3.

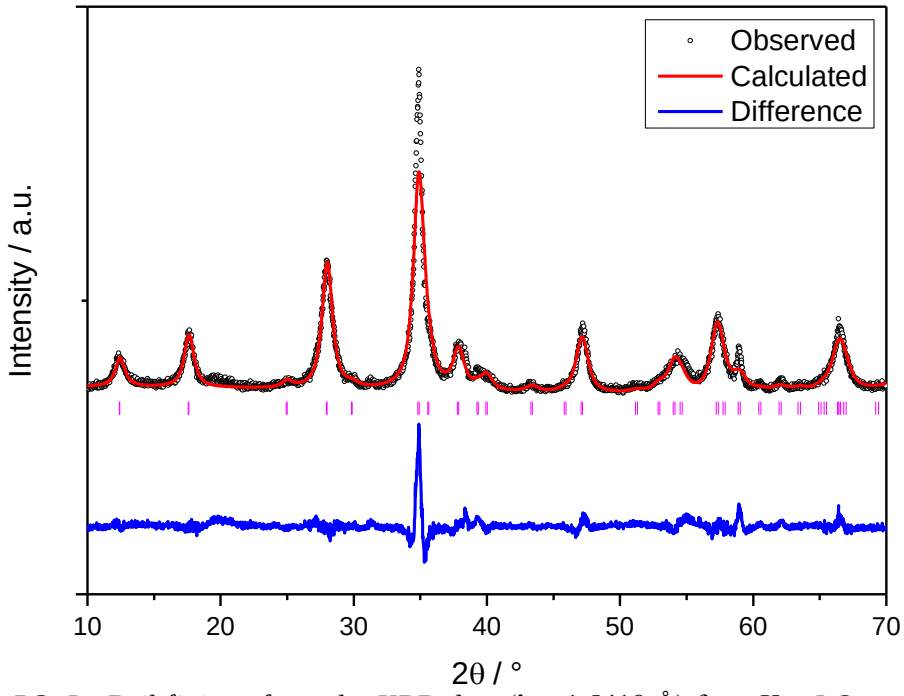

Figure 5.3: Le Bail fitting of powder XRD data (λ = 1.5418 Å) form $K_{0.25}IrO_2$, synthesised using optimised reaction conditions.

Table 5.3: Hollandite lattice parameters, adopting tetragonal space group *I* 4/*m*, for as made sample and literature values.

	Lattice Parameters	
$K_{0.25}IrO_2$	*a* / Å	*c* / Å
This Work	10.0912(10)	3.1351(4)
Literature[1]	10.0492	3.1496

Additionally it was found that if the oxidising agent was swapped from KO_2 to H_2O_2 a suitable precursor phase could still be produced, with slightly lower levels of surface potassium to those reactions performed using KO_2. This precursor phase could subsequently be used to synthesise the hollandite, Figure 5.4. In this case the synthesised hollandite is less crystalline than that synthesised using the precursor produced using KO_2 as an oxidant. Unfortunately this material appears to be impure with several sharp peaks not assignable to the hollandite phase appearing between 20 and 40 °.

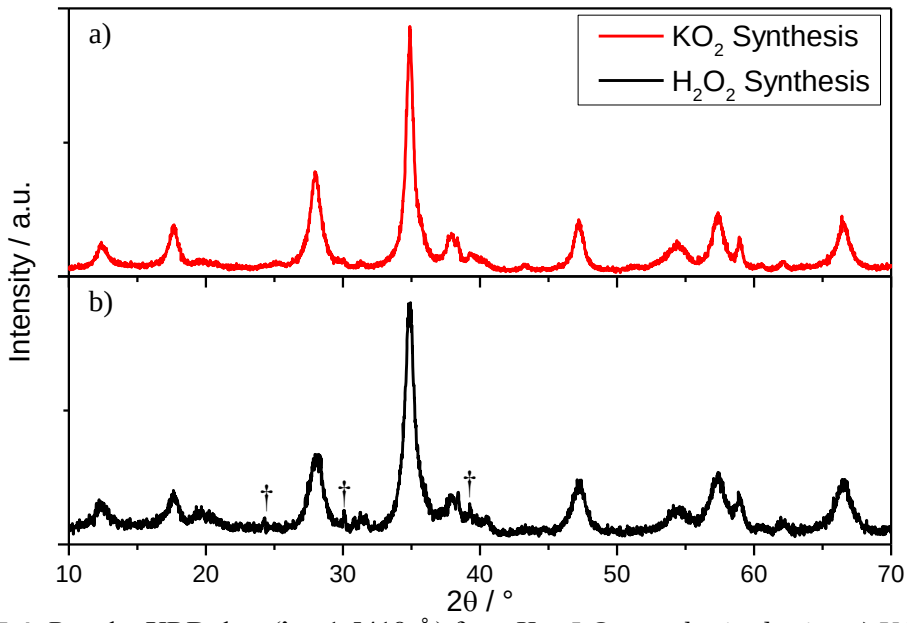

Figure 5.4: Powder XRD data (λ = 1.5418 Å) form $K_{0.25}IrO_2$, synthesised using a) KO_2 and b) H_2O_2. Peaks arising from impurity phase in H_2O_2 pattern marked with †.

The SEM of the optimised sample shows the material adopts an asbestos like morphology and associated EDXA reveals a K:Ir ratio of 1:4, which is consistent with the synthesis of $K_{0.25}IrO_2$.[1] The observed morphology is likely to produce some preferred orientation effects in the powder XRD experiments, which could explain the difference between the observed and simulated diffraction patterns, especially around the 211/121 peak at 35 ° and the 002 peak at 59 °.

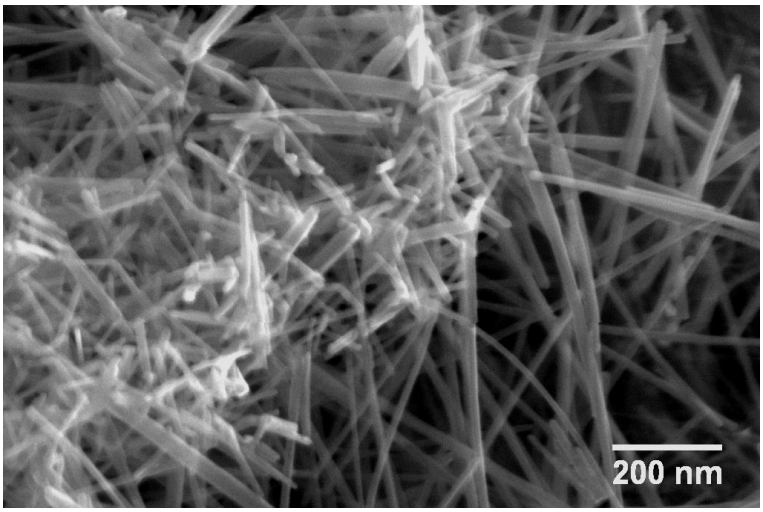

Figure 5.5: SEM image of $K_{0.25}IrO_2$, showing asbestos like morphology.

The XANES spectra recorded at the Ir L_{III}-edge, Figure 5.6, show a slight reduction of iridium after the firing process. When looking at the white line energy, a decrease was observed, from 11219.52 in the case of the precursor material to 11219.15 eV for the fired material, suggesting a reduction in iridium oxidation state from +4 to +3.75, which is consistent with the stoichiometry of the proposed hollandite, $K_{0.25}IrO_2$.

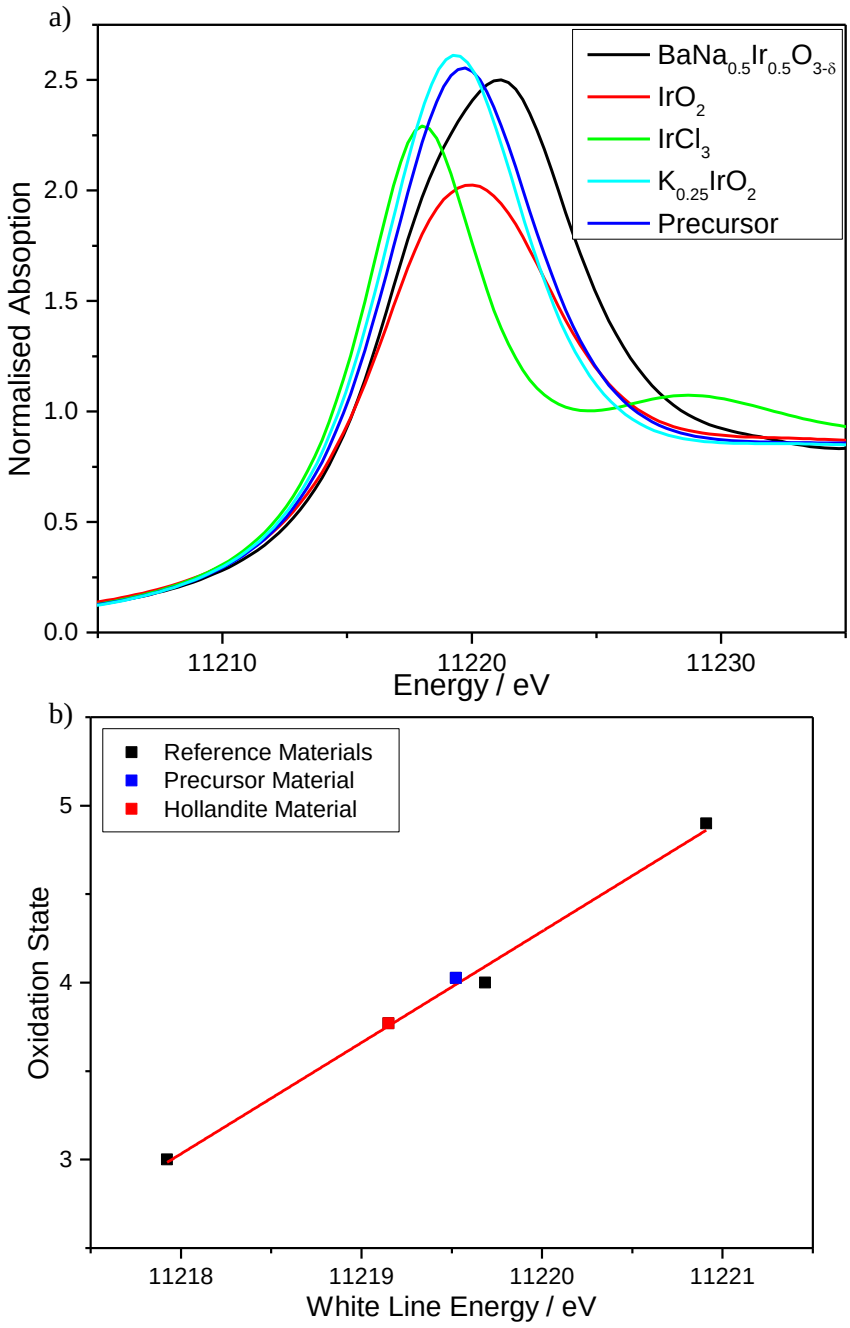

Figure 5.6: a) Ir L_{III}-edge XANES spectra of iridium oxide precursor, hollandite and reference materials for calibration. b) White line position against iridium oxidation state.

The lowest reported synthesis temperature for the potassium iridium oxide hollandite in the literature is 600 °C with reported reaction times in the hours;[1] by slowly ramping the temperature and having high dwell times the actual temperature at which the phase change occurs can be elucidated. A thermodiffractometry experiment was devised, where patterns were collected every five minutes for three hours at 10 °C intervals. Fig.5.7 clearly shows that up to 550 °C there is no phase change, although the IrO_2 does become more crystalline. When 550 °C is exceeded the hollandite phase begins to form, the additional peaks attributed to the hollandite phase grow at the same rate as those shared by IrO_2 suggesting the synthesised material is phase pure. These results demonstrate the hollandite can be produced at lower temperatures and possibly much faster than the literature would suggest.[1,2]

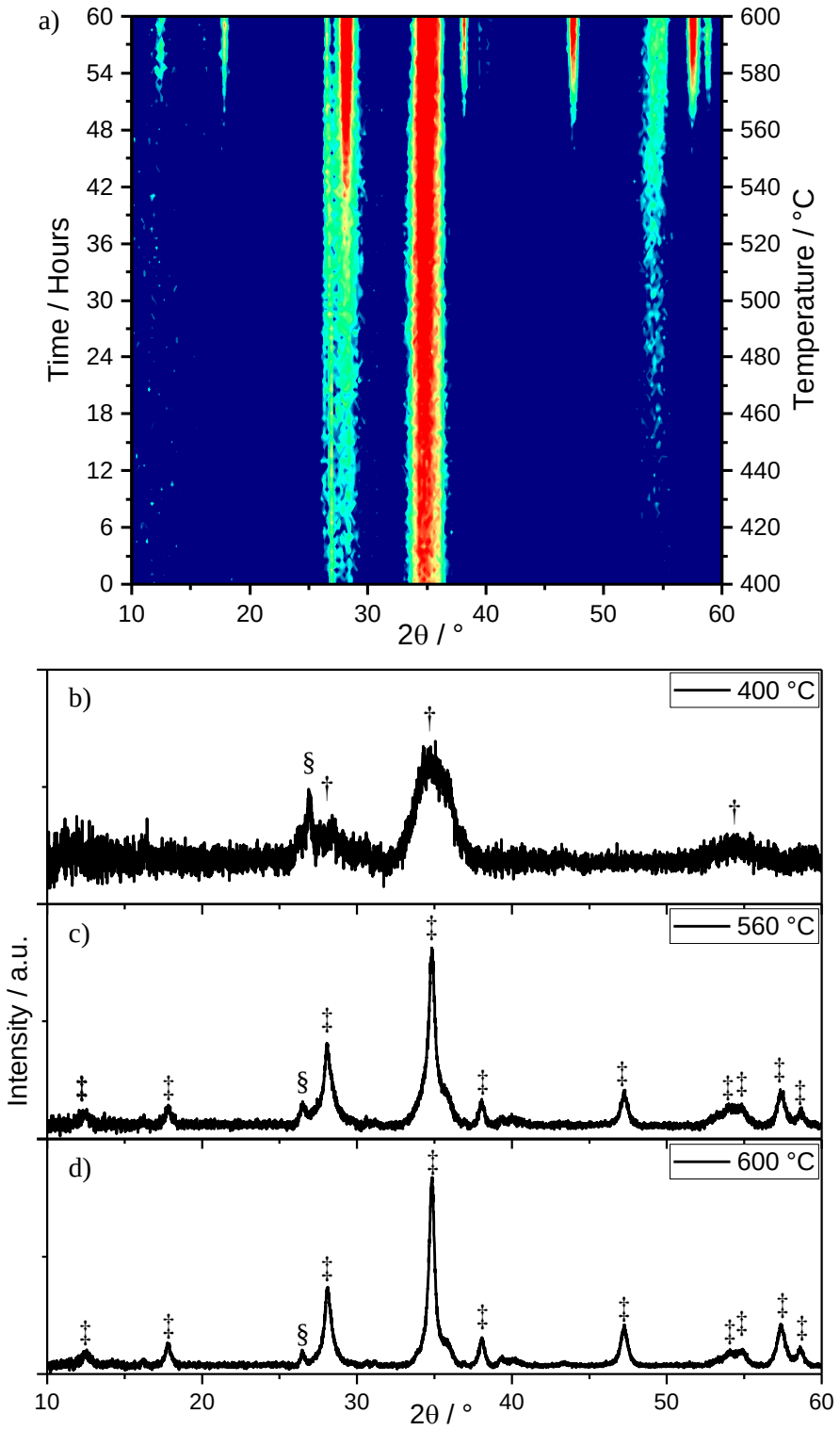

Figure 5.7: Thermodiffractometry (λ = 1.5418 Å) a) showing phase change from IrO_2 to $K_{0.25}IrO_2$. Selected powder XRD patterns at b) 400 °C, c) 560 °C and d) and 600 °C. † denotes peaks arising from IrO_2, ‡ denotes peaks arising from $K_{0.25}IrO_2$ and § denotes contaminants on sample holder.

5.3$ARuO_3$ A = Sr, Ba

5.3.1 Synthesis of $ARuO_3$ A = Sr, Ba

Ruthenium (III) chloride tetrahydrate, sodium peroxide and either strontium or barium peroxide were added to 10 ml of 4 M NaOH, in a ratio of 1:5:3 respectively. An excess of peroxide was used to facilitate the conversion of the ruthenium chloride to oxide. The reaction was carried out at 240 °C for three days. When cool the powders were then collected via vacuum filtration, and washed with 50 ml of 3 M HNO_3, followed by 20 ml of acetone.

5.3.2 Characterisation of $SrRuO_3$

The powder XRD pattern of $SrRuO_3$ can be indexed and fitted using space group $Pm\bar{3}m$ with a very similar lattice parameter to that observed in the literature, Figure 5.8.[10] It has been suggested that the cell is not cubic, and there is in fact an orthorhombic distortion.[6] This distortion can be described using the space groups *Pbnm* and *Pnma*, these space groups are equivalent with the axes swapped.

The powder pattern is fitted almost equally well using either the cubic space group $Pm\bar{3}m$ or the orthorhombic space group *Pbnm*, however the goodness of fit parameters using the cubic space group is slightly better. However zooming in on the peaks in the powder diffraction pattern, it is observed that they are all broadened with some evidence of splitting, which may suggest the lower symmetry space group. Table 5.4 shows the final fits to both possible models. Using a cubic model, the refined lattice parameters are larger than those found in the literature,[11] and using a orthorhombic model, the refined lattice parameters are all smaller than those found in the literature.[6] This could be attributed to vacancies on the A-site, however EDXA and XANES measurements, see below, support the fact the material is stoichiometric.

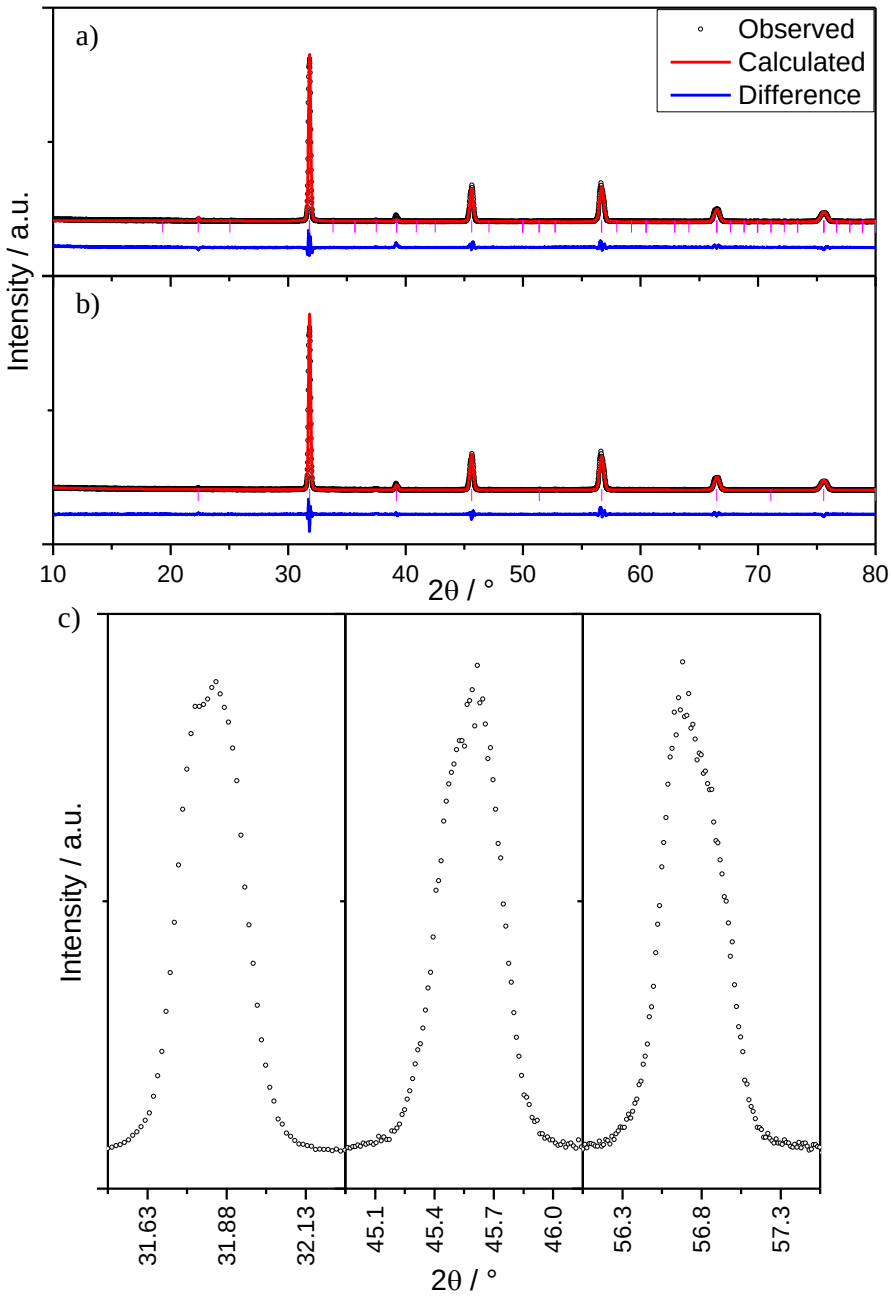

Figure 5.8: Rietveld refinements of XRD data (λ = 1.5418 Å) using space groups, a) *Pbmn*, b) $Pm\bar{3}m$ and c) Zooms on three most intense peaks in pattern, demonstrating evidence for peak splitting.

Table 5.4: Structural details of $SrRuO_3$ obtained from Rietveld refinement of powder XRD data, using cubic space group $Pm\bar{3}m$ and orthorhombic space group *Pbmn*.

Atom	Site	*x*	*y*	*Z*	Occ	U_{iso} / Å^2
Cubic $SrRuO_3$: *a* = 3.97522(3) Å / **Lit :** 3.910 Å[10]						
Sr	1*a*	0.5	0.5	0.5	1.000(2)	0.0083(4)
Ru	1*b*	0	0	0	1.000(2)	0.0232(4)
O	3*c*	0	0.5	0.5	1.000(9)	0.039(2)
Orthorhombic $SrRuO_3$: *a* = 5.61915(16) b = 5.61064(16) c = 7.9677(2) Å / **Lit :** *a* = 5.5861 b = 5.5502 c = 7.8650 Å[11]						
Sr	4*c*	0.0007(12)	0.0008(13)	0.25	1.001(2)	0.029(4)
Ru	4*b*	0.5	0	0	0.999(2)	0.037(5)
O	4*c*	0.684(3)	0.290(3)	0.25	0.999(17)	0.35(5)
O	8*d*	0.022(4)	0.499(7)	0.25	1.00(2)	0.11(5)

SEM reveals the particles are comprised mostly of cubes with bevelled edges with flakey material on the surface. There is no crystalline impurity phase in the XRD data, and EDXA on both types of particle reveal a Sr:Ru ratio of 0.94:1, which collaborates the occupancies extracted from the fitting of the powder XRD data. It seems likely that the flakey material is poorly formed $SrRuO_3$, this same two type morphology is observed in the hydrothermal synthesis of $SrMnO_3$.[12] It is possible that modifying the reaction conditions could eliminate the flakey material from the final product.

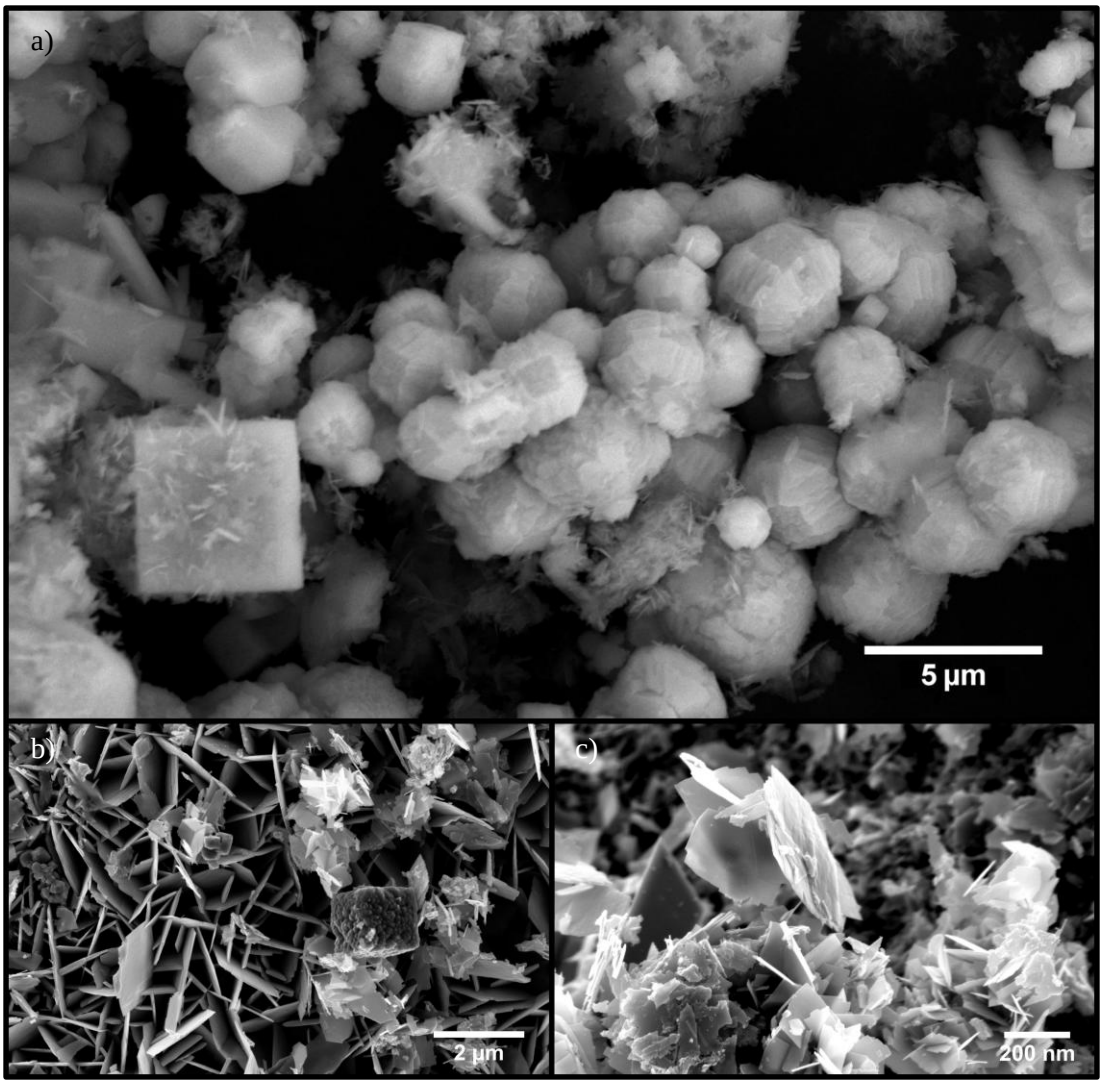

Figure 5.9: SEM images of $SrRuO_3$, a) showing agglomerates of cubes with bevelled edges, b) + c) zoom on surface showing flake like particles making up the surface.

The XANES spectra recorded at the Ru K-edge, Figure 5.10, show a slight oxidation of the ruthenium above +4 in $SrRuO_3$ to +4.1. While this small oxidation is feasible, especially given the peroxides used as reagents, rutile RuO_2 has both corner and edge sharing octahedra whereas $SrRuO_3$ only has corner sharing octahedra. This difference in local bonding environment could account for the small discrepancy.

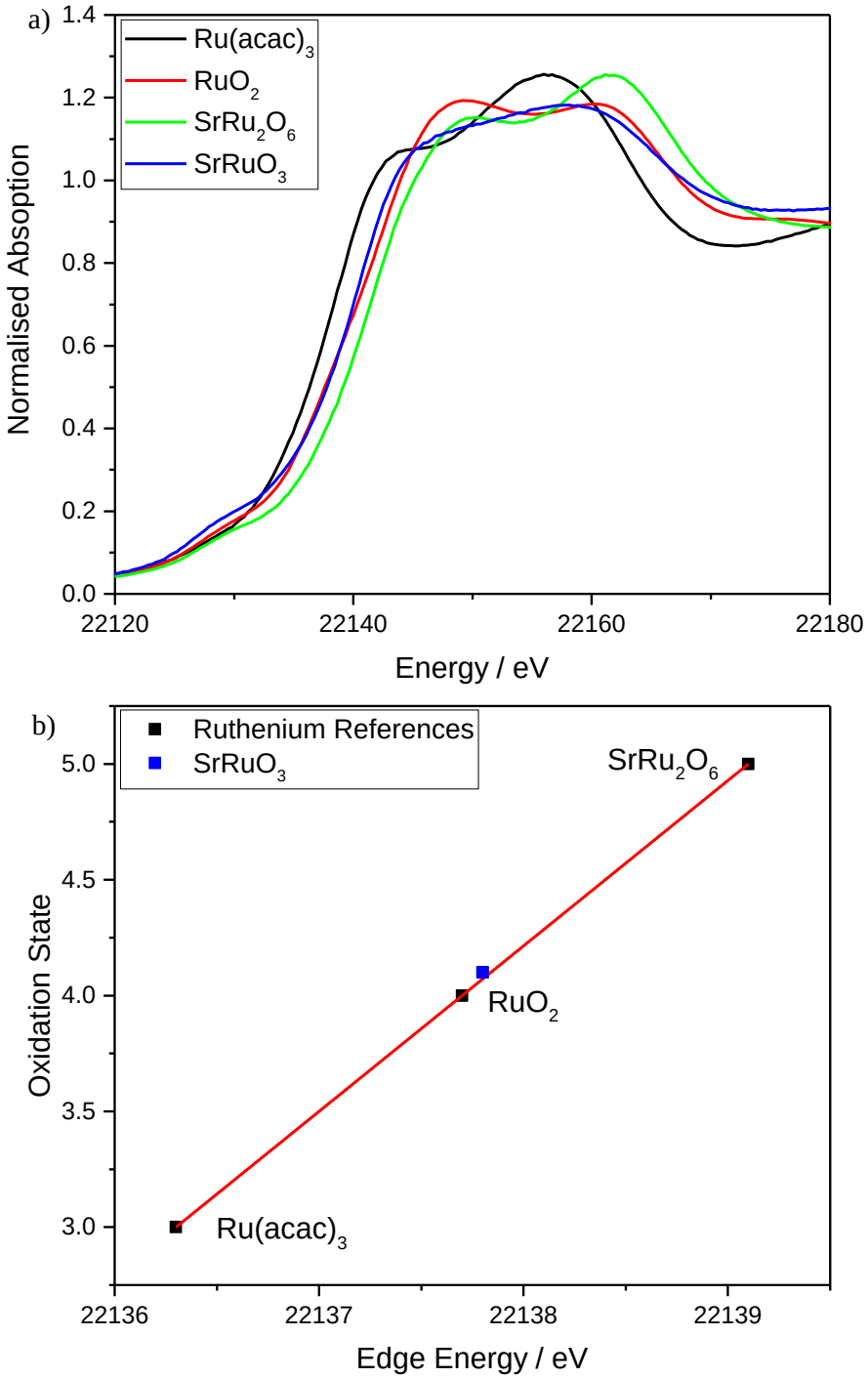

Figure 5.10: a) Ru K-edge XANES spectra of strontium ruthenium oxide and reference materials for calibration. b) Edge position against ruthenium oxidation state.

5.3.3 Characterisation of 4H-$BaRuO_3$

The powder XRD pattern of $BaRuO_3$, Figure 5.11, can be indexed and fitted using the hexagonal space group $P6_3/mmc$ with a very similar lattice parameter to that observed in the literature, Table 5.5,[13] however there is a clear mismatch between the observed and calculated patterns, most noticeably in the 110 peak at 31 °.

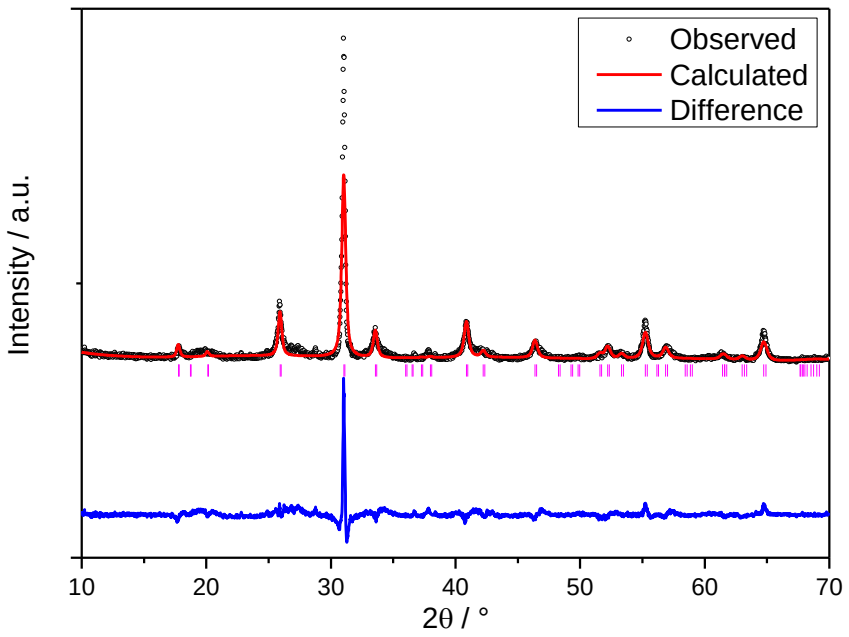

Figure 5.11: Rietveld refinement of powder XRD data (λ = 1.5418 Å) of 4H-$BaRuO_3$ using hexagonal space group $P6_3/mmc$.

Table 5.5: Structural details of 4H-$BaRuO_3$ obtained from Rietveld refinement of powder XRD data.

Atom	Site	*x*	*y*	*z*	Occ	U_{iso}/ Å^2
4H-$BaRuO_3$: *a* = 5.5761(3) Å c = 9.468(2) Å **Lit :** *a* = 5.729 Å c = 9.500 Å[13]						
Ba	*2a*	0	0	0	1.000(8)	0.007(2)
Ba	2*c*	0.3333	0.6667	0.25	1.000(11)	0.021(3)
Ru	4*f*	0.6667	0.3333	0.1248(9)	1.000(8)	0.027(2)
O	6*g*	0.5	0.5	0.5	1.00(5)	0.004(13)
O	6*h*	0.331(6)	0.165(3)	0.25	1.00(6)	0.018(14)

SEM reveals the material is made up of micron sized hexagonal plates, Figure 5.12. The plate like morphology likely gives rise to anisotropic peak broadening and preferred orientation effects, which may explain the poor fit to the powder data. EDXA reveals a Ba:Ru ratio of 1:1 supporting the occupancies extracted from fitting the X-ray data.

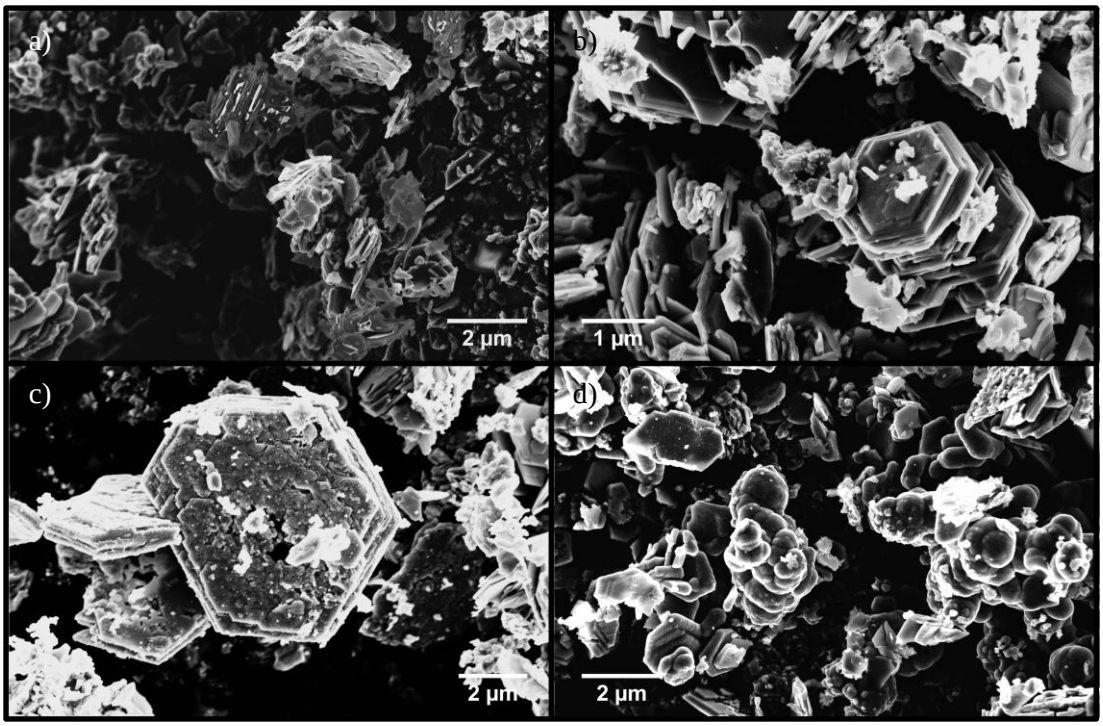

Figure 5.12: SEM images of $BaRuO_3$, showing hexagonal plate type particles.

The XANES spectra recorded at the Ru K-edge, Figure 5.13, show a slight oxidation of the ruthenium above +4 in $BaRuO_3$ to +4.1, like for $SrRuO_3$ this is probably due to different local environments as the synthesised $BaRuO_3$ is comprised of both face sharing and corner sharing octahedra.

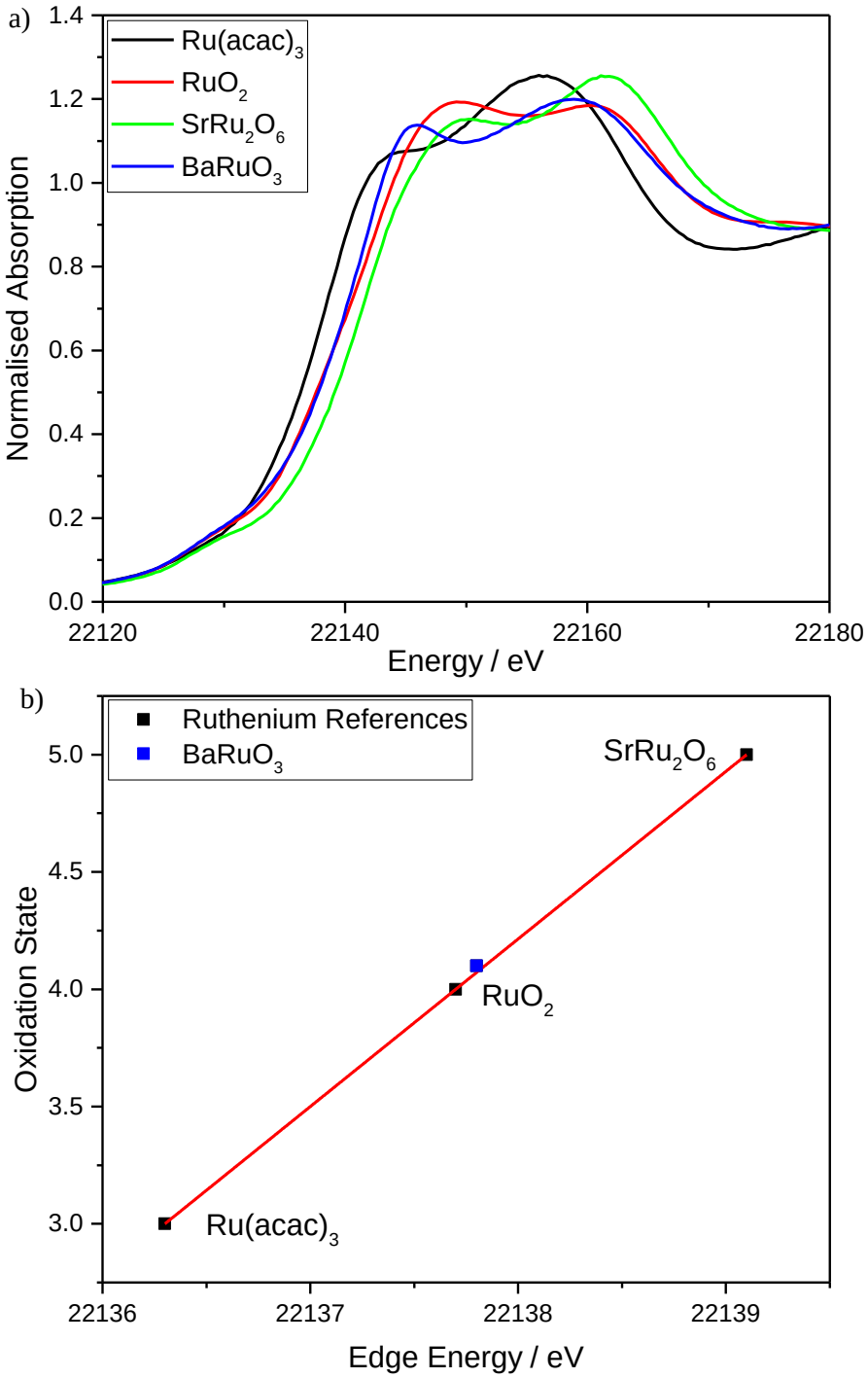

Figure 5.13: a) Ru K-edge XANES spectra of strontium ruthenium oxide and reference materials for calibration. b) Edge position against ruthenium oxidation state.

5.4 Iridium and Ruthenium Substituted Sodium Tantalates and Niobates

5.4.1 Synthesis of Substituted Sodium Tantalates and Niobates

During exploratory reactions, where the intended levels of tantalum and niobium substitution by iridium and ruthenium where 5 and 10 %, it was observed that filtrates had strong purple and orange colours for the iridium and ruthenium substitution reactions respectively. It was found that by adding hydrogen peroxide to the reaction the relative amount of iridium in the final material could be increased, however hydrogen peroxide reacted with potassium perruthenate on contact yielding a black solid, presumably RuO_2. As such the ruthenium substitutions reactions were discontinued and the work focused on the substitution of sodium tantalate by iridium.

The substituted tantalates and niobates were synthesised following the reaction of either tantalum (V) or niobium (V) oxide in 10 ml of 10 M NaOH, with a portion of the oxide replaced by either iridium (III) chloride or potassium perruthenate, based on using 1.1 mmol of Ta_2O_5. In the iridium substitution reactions the sodium hydroxide solution was made using H_2O_2 instead of water in order to better oxidise the iridium. Reactions were performed at 240 °C for three days. Once cool the powders were collected via vacuum filtration, and washed with 20 ml of 3 M HNO_3, followed by 20 ml of acetone.

5.4.2 Characterisation of Substituted Sodium Tantalates and Niobates

The powder XRD patterns of the unsubstituted materials can be fitted using with the orthorhombic space groups, *Pbnm* for $NaTaO_3$ and *Pbcm* for $NaNbO_3$, Figure 5.14, with little deviation from the lattice parameters found in literature, Table 5.6.

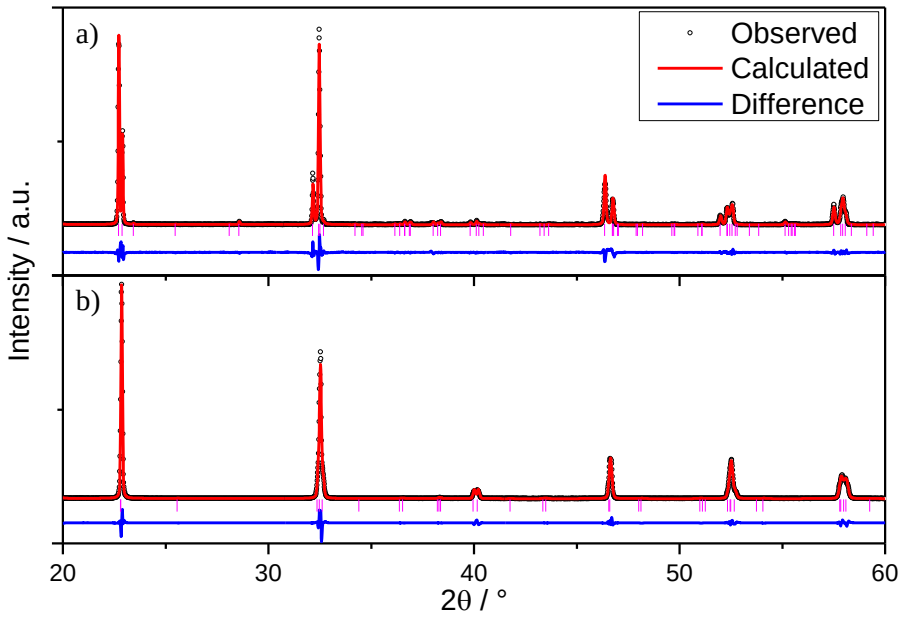

Figure 5.14: Le Bail fitting of XRD data (λ = 1.5418 Å) of a) $NaNbO_3$ b) $NaTaO_3$.

The powder XRD patterns of the iridium substituted sodium tantalate materials can be fitted using with the space group *Pbnm*, Figure 5.15. There is little deviation from the lattice parameters of the unsubstituted material, however there appears to be a small contraction across the series, Table 5.6 and Figure 5.18. This is consistent with octahedral Ta(V) 0.640 Å being larger than octahedral Ir(IV) 0.625 Å.[14]

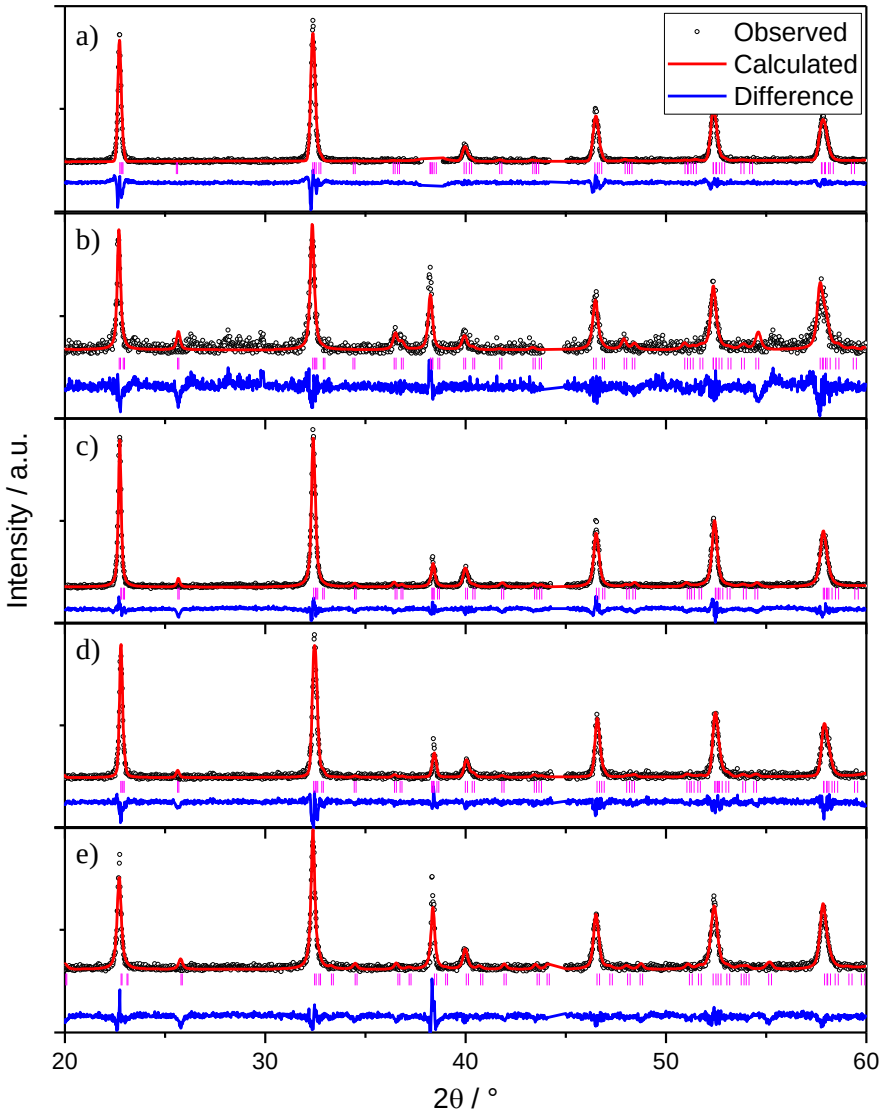

Figure 5.15: Le Bail fitting of XRD data (λ = 1.5418 Å) of $Na(Ta_{1-x}Ir_x)O_3$ with intended substitutions of a) x = 0.1, b) x = 0.2 , c) x = 0.3 , d) x = 0.4 , e) x = 0.5.

The powder XRD patterns of the ruthenium substituted sodium tantalate materials can be fitted using with the space group *Pbnm*, Figure 5.16. There is little deviation from the lattice parameters of the unsubstituted material, Table 5.6. Octahedral Ta(V) 0.640 Å is larger than octahedral Ru(IV) 0.620 Å,[14] so the lattice parameter is expected to decrease, however, given the relatively low levels of substitution this is unsurprising.

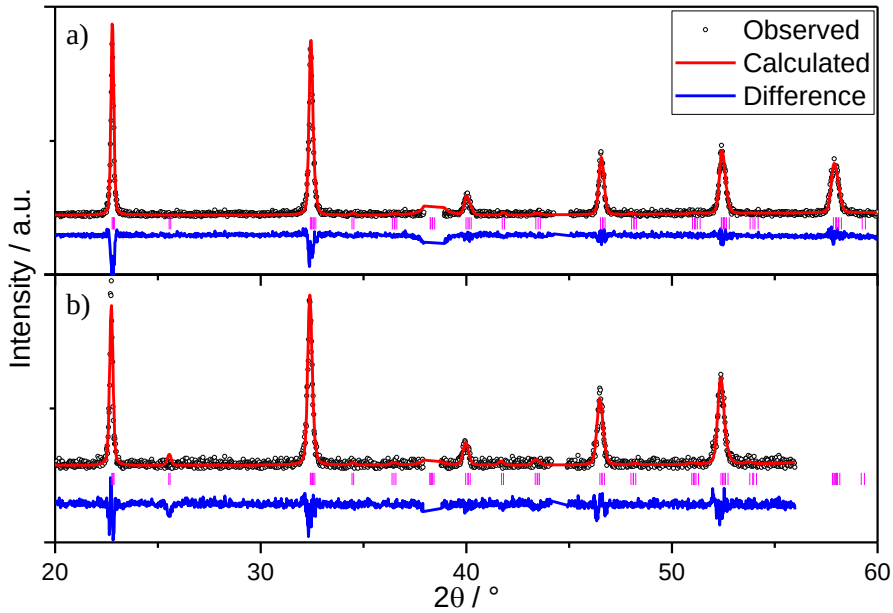

Figure 5.16: Le Bail fitting of XRD data (λ = 1.5418 Å) of $Na(Ta_{1-x}Ru_x)O_3$ with intended substitutions of a) x = 0.05, b) x = 0.1.

The powder XRD patterns of the iridium substituted sodium niobate materials can be fitted using with the space group *Pbcm*, Figure 5.17. There is little deviation from the lattice parameters of the unsubstituted material, Table 5.6. Octahedral Nb(V) 0.640 Å is larger than octahedral Ir(IV) 0.625 Å,[14] so the lattice parameter is expected to decrease, however, given the relatively low levels of substitution this is unsurprising.

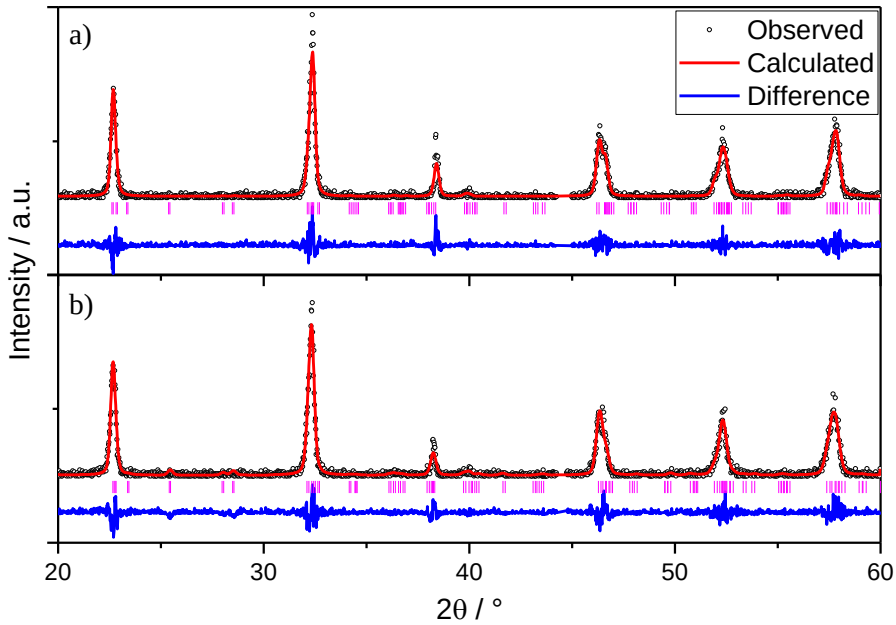

Figure 5.17: Le Bail fitting of XRD data (λ = 1.5418 Å) of $Na(Nb_{1-x}Ir_x)O_3$ with intended substitutions of a) x = 0.05, b) x = 0.1.

Table 5.6: Lattice parameters of substituted sodium tantalates and niobates from fits of powder XRD data.

	Lattice Parameter		
Material	*a* / Å	*b* / Å	*c* / Å
$NaTaO_3$-Lit[15]	5.4811	5.5235	7.7948
$NaTaO_3$	5.48964(17)	5.52886(15)	7.79872(11)
$NaTaO_3$-10% Ir	5.4745(9)	5.5271(2)	7.8123(3)
$NaTaO_3$-20% Ir	5.4404(12)	5.5283(5)	7.8228(9)
$NaTaO_3$-30% Ir	5.4467(12)	5.5183(3)	7.7996(7)
$NaTaO_3$-40% Ir	5.4532(11)	5.5203(3)	7.7959(4)
$NaTaO_3$-50% Ir	5.3753(5)	5.114(4)	7.7950(5)
$NaTaO_3$-5% Ru	5.4896(8)	5.5201(3)	7.8006(4)
$NaTaO_3$-10% Ru	5.4972(19)	5.5202(4)	7.8066(7)
$NaNbO_3$-Lit[16]	5.504	5.570	15.517
$NaNbO_3$	5.50781(14)	5.56619(13)	15.5435(2)
$NaNbO_3$-5% Ir	5.5374(8)	5.5699(7)	15.5735(19)
$NaNbO_3$-10% Ir	5.5173(8)	5.5702(7)	15.610(3)

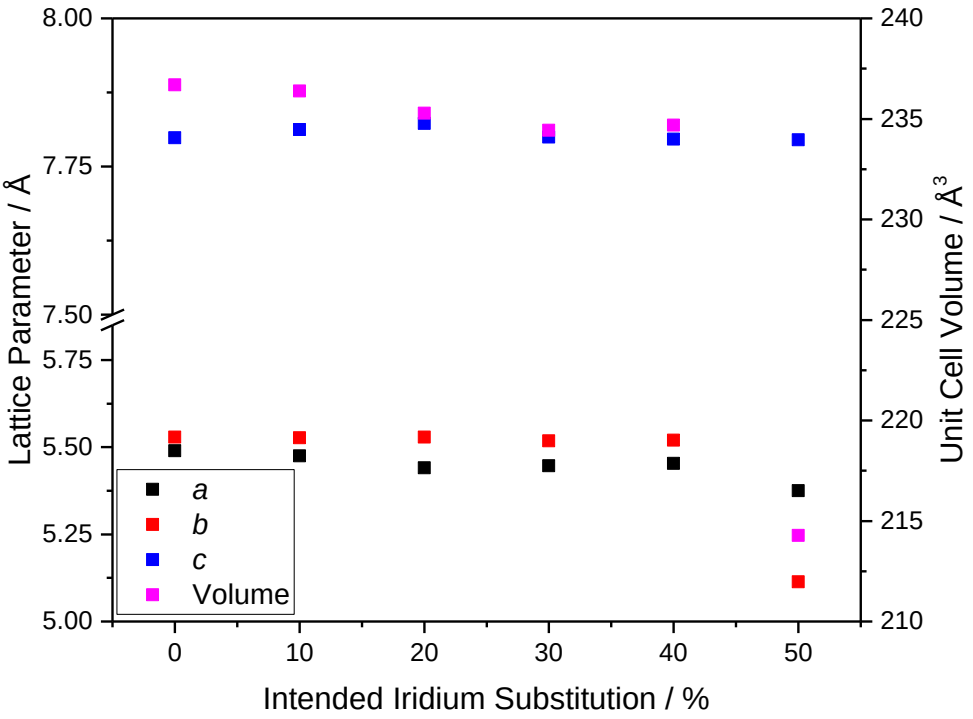

Figure 5.18: Lattice parameters and unit cell volumes plotted against intended iridium substitution for $Na(Ta_{1-x}Ir_x)O_3$.

The refined lattice parameters extracted from fitting the powder XRD do not change much, with the exception of the $Na(Ta_{1-x}Ir_x)O_3$ series, and as such do not make a convincing argument for the inclusion of precious metal in the material. However there is a clear colour change upon substitution by the precious metals, Figure 5.19, with iridium substitution resulting in a uniform green colouration and a uniform pink/red colouration in the case of ruthenium substitution.

Figure 5.19: Photographs of a) $NaTaO_3$ b) $NaNbO_3$, $Na(Ta_{1-x}Ir_x)O_3$ where c) x = 0.1, d) x = 0.2, e) x = 0.3, f) x = 0.4, g) x = 0.5, $Na(Ta_{1-x}Ru_x)O_3$ where h) x = 0.05, i) and x = 0.1, $Na(Nb_{1-x}Ir_x)O_3$ where j) x = 0.05 and k) x = 0.1.

.

The iridium substituted sodium tantalates form nanocubes with edges in the range of hundreds of nanometres, Figure 5.20, much like that of hydrothermally synthesised sodium tantalate seen in literature.[17]

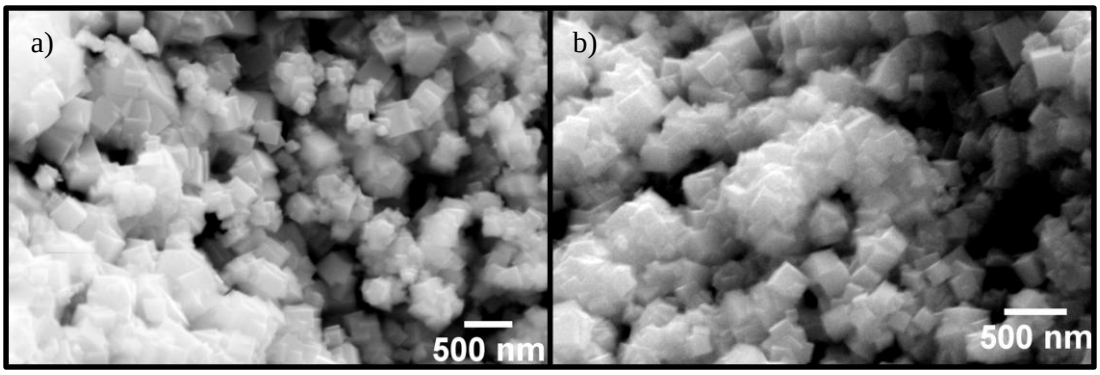

Figure 5.20: SEM images of $Na(Ta_{1-x}Ir_x)O_3$, a) x = 0.2 and b) x = 0.5, showing nanocube type particles.

The strong colour of the filtrate suggests not all the precious metal in the reaction was incorporated into the final material. EDXA reveals that only between 20 and 50 % of the precious metal used in the reaction was incorporated into the final material, Table 5.7.

Table 5.7: EDXA results from substitution reactions.

	EDXA Results		
Intended Material	Tantalum / %	Iridium / %	Assumed Formula
$NaTa_{0.90}Ir_{0.10}O_3$	97.6	2.4	$NaTa_{0.98}Ir_{0.02}O_3$
$NaTa_{0.80}Ir_{0.20}O_3$	95.3	4.7	$NaTa_{0.95}Ir_{0.05}O_3$
$NaTa_{0.70}Ir_{0.30}O_3$	91.6	8.4	$NaTa_{0.92}Ir_{0.08}O_3$
$NaTa_{0.60}Ir_{0.40}O_3$	87.8	12.2	$NaTa_{0.88}Ir_{0.12}O_3$
$NaTa_{0.50}Ir_{0.50}O_3$	85.1	14.9	$NaTa_{0.85}Ir_{0.15}O_3$
Intended Material	Tantalum / %	Ruthenium / %	Assumed Formula
$NaTa_{0.95}Ru_{0.05}O_3$	97.4	2.6	$NaTa_{0.98}Ru_{0.02}O_3$
$NaTa_{0.90}Ru_{0.10}O_3$	95.9	4.1	$NaTa_{0.96}Ru_{0.04}O_3$
Intended Material	Niobium / %	Iridium / %	Assumed Formula
$NaNb_{0.95}Ir_{0.05}O_3$	96.9	3.1	$NaNb_{0.97}Ir_{0.03}O_3$
$NaNb_{0.90}Ir_{0.10}O_3$	95.7	4.3	$NaNb_{0.96}Ir_{0.04}O_3$

XANES spectra recorded at the Ir L_{III}-edge, Figure 5.21, shows that the iridium in the iridium substituted materials has an oxidation state of approximately +4. The Ta L_{II}-edge is around 75 eV lower in energy than the Ir L_{III}-edge, as such the tantalum EXAFS contributes to the signal around the Ir L_{III}-edge which could introduce some error in the measurement.

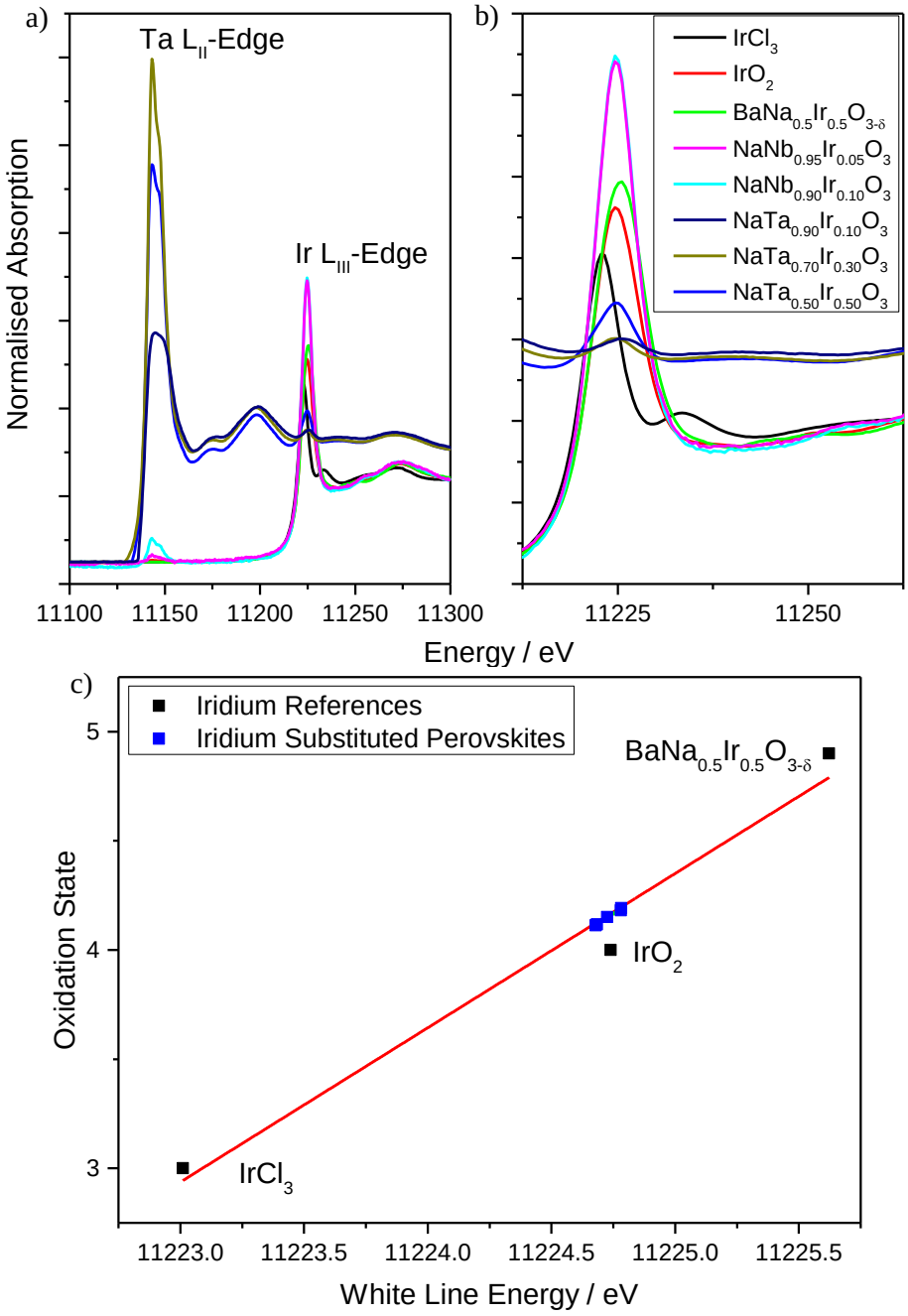

Figure 5.21: Ir L_{III}-edge XANES spectra of iridium substituted sodium tantalates/niobates and reference materials a) showing Ta L_{II}-edge and Ir L_{III}-edge, b) only Ir L_{III}-edge region. c) White line position against iridium oxidation state.

5.5 Strontium Iridate

5.5.1 Synthesis of Strontium Iridate

A $KSbO_3$-type strontium iridate was synthesised by the reaction of; iridium (III) chloride, strontium peroxide and potassium superoxide in 10 ml of 10 M KOH. The reaction was carried out at 240 °C for three days. Once cool the powders were then collected via vacuum

filtration, and washed with 50 ml of 3 M HNO_3, followed by 20 ml of acetone. The materials were then dried at 70 °C for twenty four hours to remove any excess water.

5.5.2 Characterisation of Strontium Iridate

The powder XRD pattern of $KSbO_3$ type strontium iridate can be fitted using with the cubic space group $Pn\bar{3}$, Figure 5.22. The lattice parameter of this material is greater than that of the sodium containing analogue, this can be attributed to eight coordinate strontium having a larger ionic radius, 1.26 Å, than eight coordinate sodium 1.18 Å . The fitting of the data, Table 5.8, reveals the formula to be $Sr_{2.85}Ir_3O_{11}$, which is consistent with what is extracted from EDXA, a Sr : Ir ratio of 0.92 : 1.

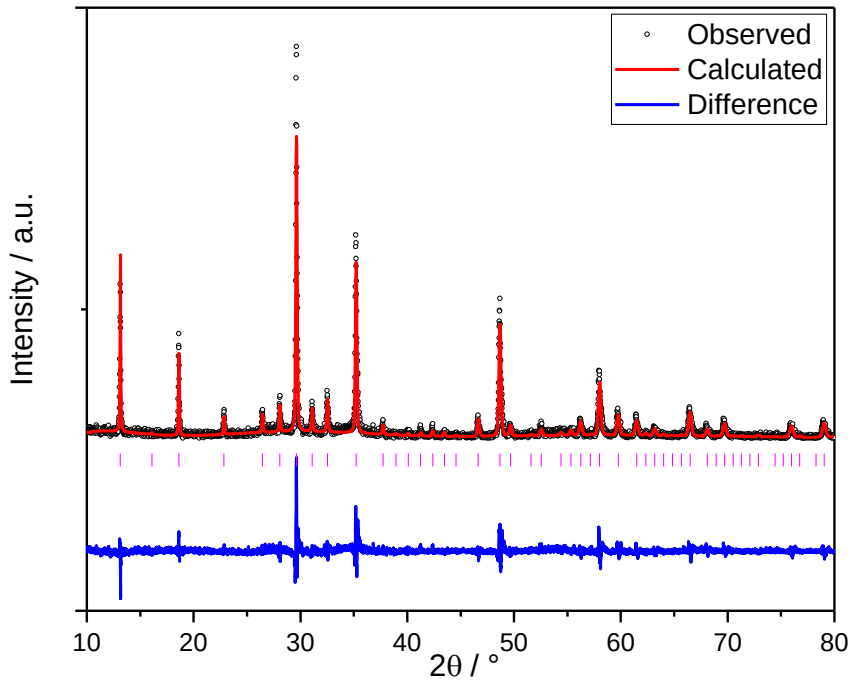

Figure 5.22: Rietveld refinements of XRD data (λ = 1.54056 Å) of $KSbO_3$ type strontium iridate.

Table 5.8: Structural details of $KSbO_3$ type strontium iridate obtained from Rietveld refinement of powder XRD data.

Atom	Site	*x*	*y*	*Z*	Occ	U*iso* / Å^2
$KSbO_3$ Type Strontium Iridate : *a* = 9.53211(17) Å **$Sr_{2.2}Na_{0.8}Ir_3O_{10.1}$**[9] **:** *a* = 9.4569 Å						
Sr	4*b*	0	0	0	1.000(18)	0.0010(3)
Sr	8*e*	0.3919(5)	0.3919(5)	0.3919(5)	0.926(12)	0.035(5)
Ir	12*g*	0.5927(3)	0.75	0.25	1.000(4)	0.0141(7)
O	12*f*	0.607(4)	0.25	0.25	1.00(6)	0.026(16)
O	24*h*	0.247(4)	0.573(3)	0.541(4)	1.00(4)	0.028(17)
O	8*e*	0.149(3)	0.149(3)	0.149(3)	1.00(5)	0.009(9)

XANES spectra recorded at the Ir L_{III}-edge, Figure 5.23, shows that the iridium in the strontium iridate materials has an oxidation state of approximately +4.3. Lower than the +5 recorded for the sodium containing analogue. The lower iridium valence results in a charge deficit, which could possibly be corrected by the inclusion of crystal water in place of oxide like in $KBiO_3 \cdot xH_2O$,[18] further work would include a combination of TGA and neutron diffraction techniques would be required to fully elucidate both the amount and location of the crystal water.

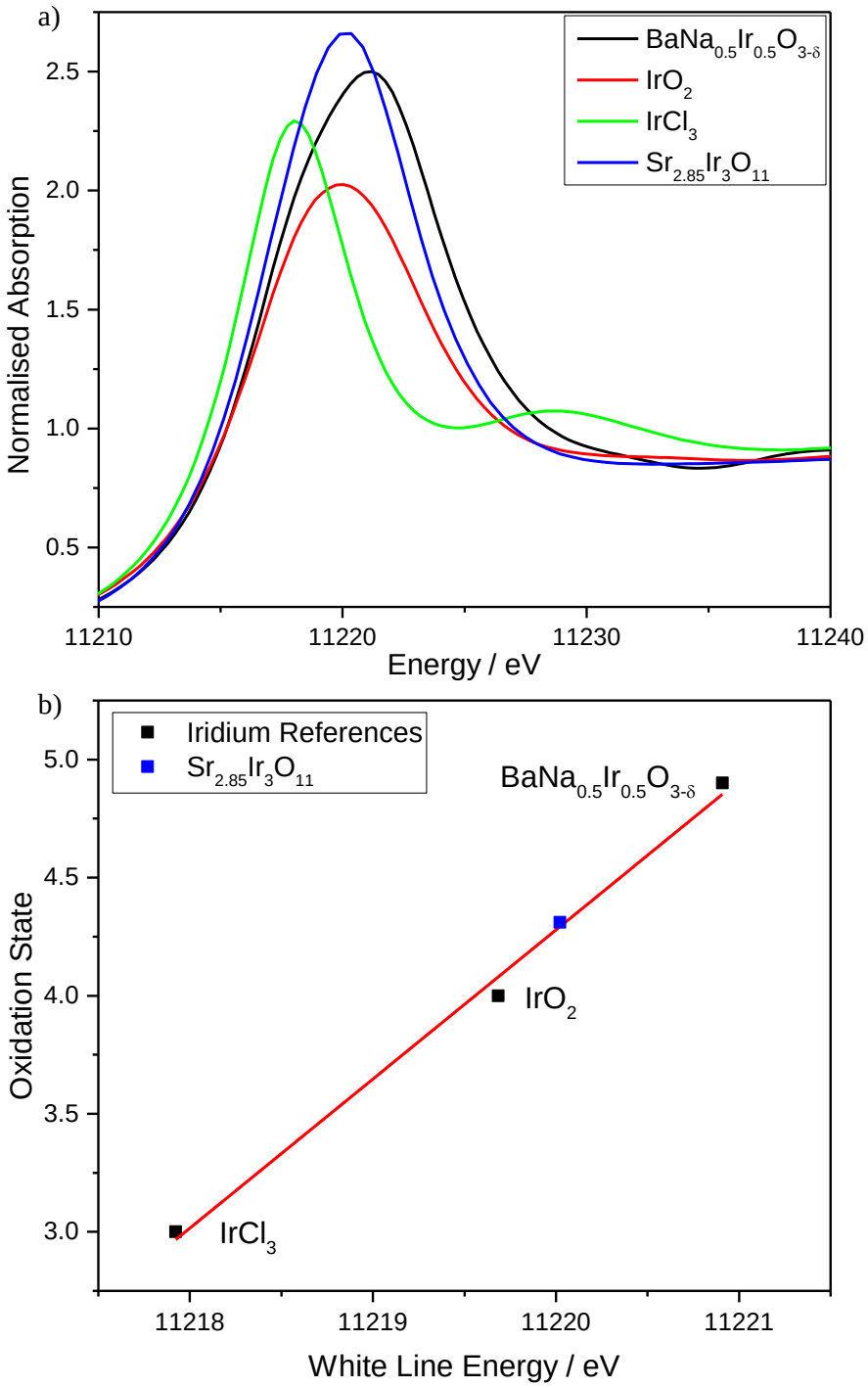

Figure 5.23: a) Ir L_{III}-edge XANES spectra of strontium iridate and reference materials, and b) white line position against iridium oxidation state.

5.6 Barium Iridate

5.6.1 Synthesis of Barium Iridate

This body of work originated from the solvothermal processing of an intermediate in the precious metal refining process. This "intermediate" has a Ba:Ir ratio of approximately 4:1 and largely consists of barium oxide and barium peroxide, Figure 5.23, the hydrothermal reaction of this material in 10 ml of either water, 10 M NaOH or 10 M KOH, yielded a new barium iridate. This was exciting as Sardar *et al.*, were unable to synthesise a barium iridium oxide hydrothermally.[9] Further work revealed the same product could be synthesised using iridium (III) chloride, barium peroxide and sodium peroxide in 10 ml of 10 M NaOH. In addition it was found replacing sodium peroxide and NaOH with potassium superoxide and KOH made no observable difference in the final materials.

The reaction was carried out at 240 °C for three days. Once cool the powders were then collected via vacuum filtration, and washed with 50 ml of 3 M HNO_3, followed by 20 ml of acetone.

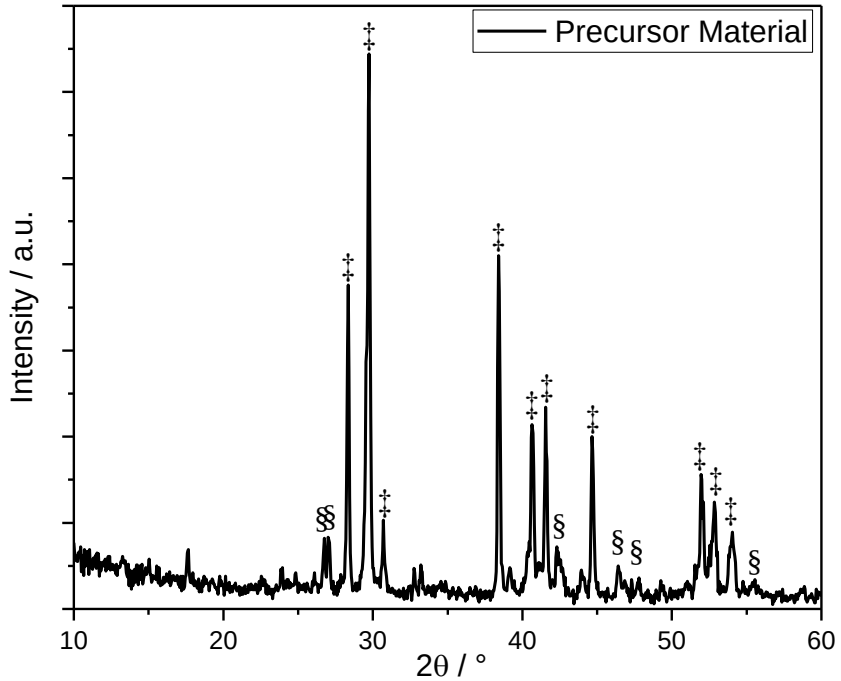

Figure 5.23: XRD patterns (λ = 1.5418 Å) from a) refining intermediate, § denotes peaks arising from barium peroxide and ‡ from barium oxide.

The powder XRD data of the material produced could not be matched to any known iridate or ruthenate (using the JCPDS database), nor could it be matched to any oxide material; indeed a free search of the JCPDS database also found no match to the powder XRD pattern. The poor crystallinity of the synthesised material made any further analysis difficult, hence these reaction conditions were carefully modified in an attempt to increase the crystallinity. The reaction parameters that were changed were solvent concentration, the base used, the oxidant used, reagent concentration, reaction temperature, duration of heating and cooling rates. In addition to these reactions, various seeding and annealing reactions were attempted.

In Chapter 3 it was shown how ruthenium can be substituted by iridium under very similar reaction conditions to those used here, and in some situations enhanced the crystallinity of the synthesised oxide, and this was also the case for the solid solution $(Ce_{0.67}Na_{0.33})_2(Ir_{1-x}Ru_x)O_7$.[19] Hence some substitution reactions were attempted, where a portion of the iridium chloride used in the synthesis was replaced either by ruthenium chloride or potassium perruthenate.

5.6.2 Characterisation of Barium Iridate

The hydrothermal processing of the refining intermediate in KOH or NaOH yielded materials with virtually identical XRD patterns, however those reactions performed in water, yielded a material that was less crystalline, Figure 5.24. In addition to the unknown phase, peaks associated with iridium metal are also observed, despite the use of either peroxide or superoxide. It was suspected that a portion of the iridium in the intermediate was in metallic form, however barium oxide peaks overlap with those of iridium metal in the diffraction pattern making this hard to qualify. Hence attempts were made to synthesise the new material in a more controlled manner.

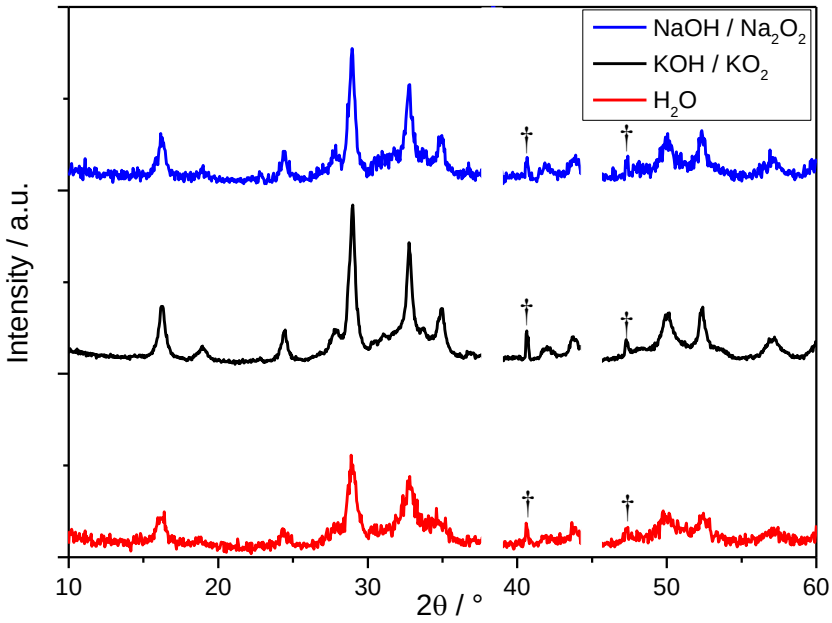

Figure 5.24: XRD patterns (λ = 1.5418 Å) from hydrothermally treated refining intermediate. Peaks at 38 and 44.5 ° are masked as they are due to aluminium sample holder. † denotes peaks arising from Ir metal.

The reaction of barium peroxide, sodium peroxide and iridium chloride in 10 M sodium hydroxide yields the same barium iridate material, without the metallic iridium impurity, Figure 5.25. Changing from using NaOH and Na_2O_2 as the mineraliser and oxidiser combination, to KOH and KO_2 yielded a material with an almost identical diffraction pattern as the material synthesised by the original method. However, using KO_2/KOH rather than Na_2O_2/NaOH as an oxidant mineraliser combination resulted in a less crystalline material.

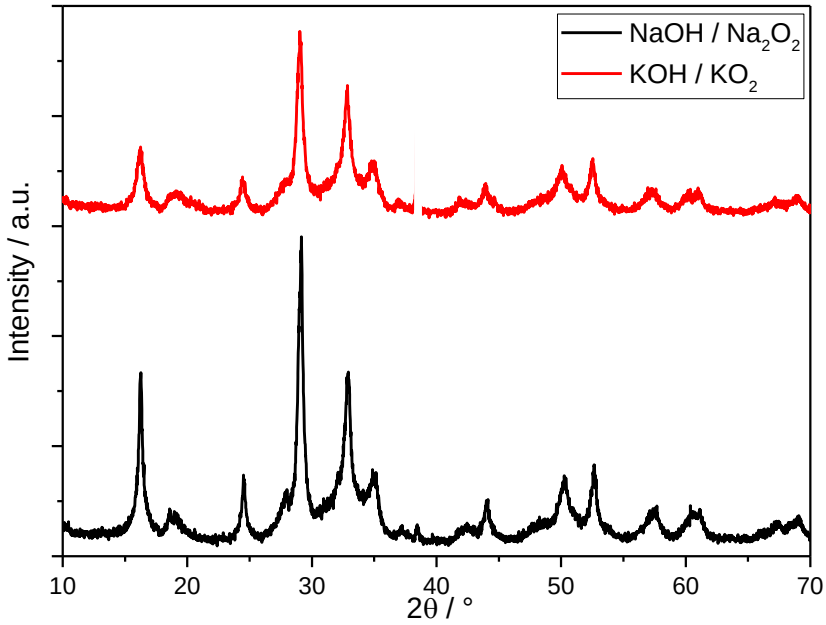

Figure 5.25: Powder XRD patterns (λ = 1.5418 Å) of barium iridium oxide synthesised from iridium chloride using specified mineraliser / oxidiser mixtures.

The JCPDS database contains many barium iridates, however none of these presented themselves as a suitable candidate for the newly synthesised barium iridate, Figure 5.26.

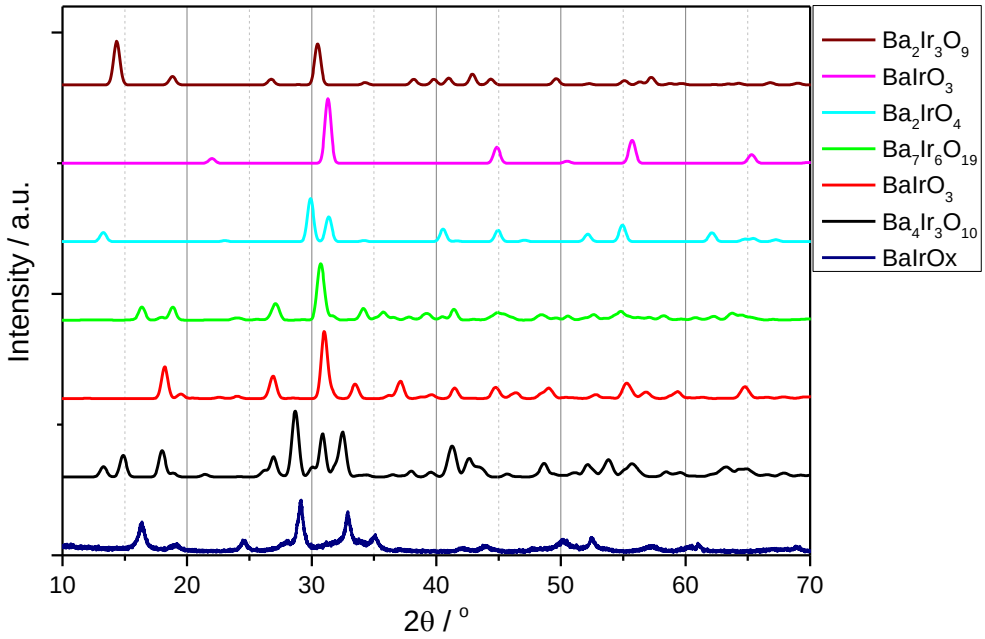

Figure 5.26: XRD patterns of known barium iridium oxides as a comparison against the synthesised material "BaIrOx".

The next step involved relaxing the constraints on the database search, taking into account similarities in ionic radii and chemical properties, the lanthanides, strontium, calcium and ruthenium were added as possible constituents. This produced an extensive list of possible

phases, those with the "most similar" powder patterns to that of the new barium iridate can be seen in Figure 5.27. Initial inspection it looks like the pattern of $Sr_4Ru_2O_9$ and the synthesised barium iridate are very similar however at $2\theta > 35$ ° the patterns are very different.

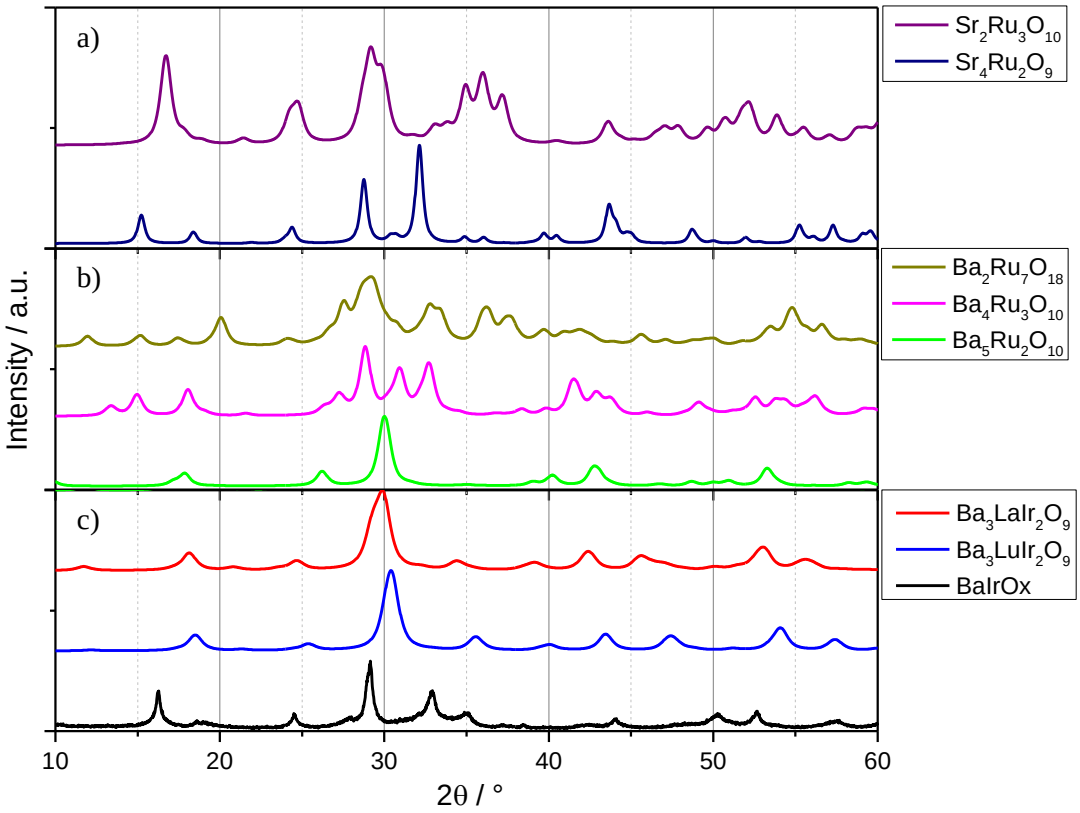

Figure 5.27: XRD patterns of a) strontium ruthenates b) barium ruthenates and c) barium lanthanide iridium oxides for comparison against the new barium iridate.

EDXA from the SEM and TEM as well as ICP results reveal a Ba : Ir ratio of 1 : 2, with no trace of sodium or potassium, Table 5.9. The exception being the ICP result for the barium iridate produced using KO_2/KOH, for which the Ba : Ir ratio is much lower than the ratio collected from EDXA. This may indicate that the barium content in this material may be flexible, however it is equally possible that a poorly crystalline IrO_2 phase is being masked in the XRD and this is where the inflated iridium signal arises. Images reveal two types of particle in the material, some larger highly angular particles with a trigonal morphology, and smaller rod like particles, Figure 5.28.

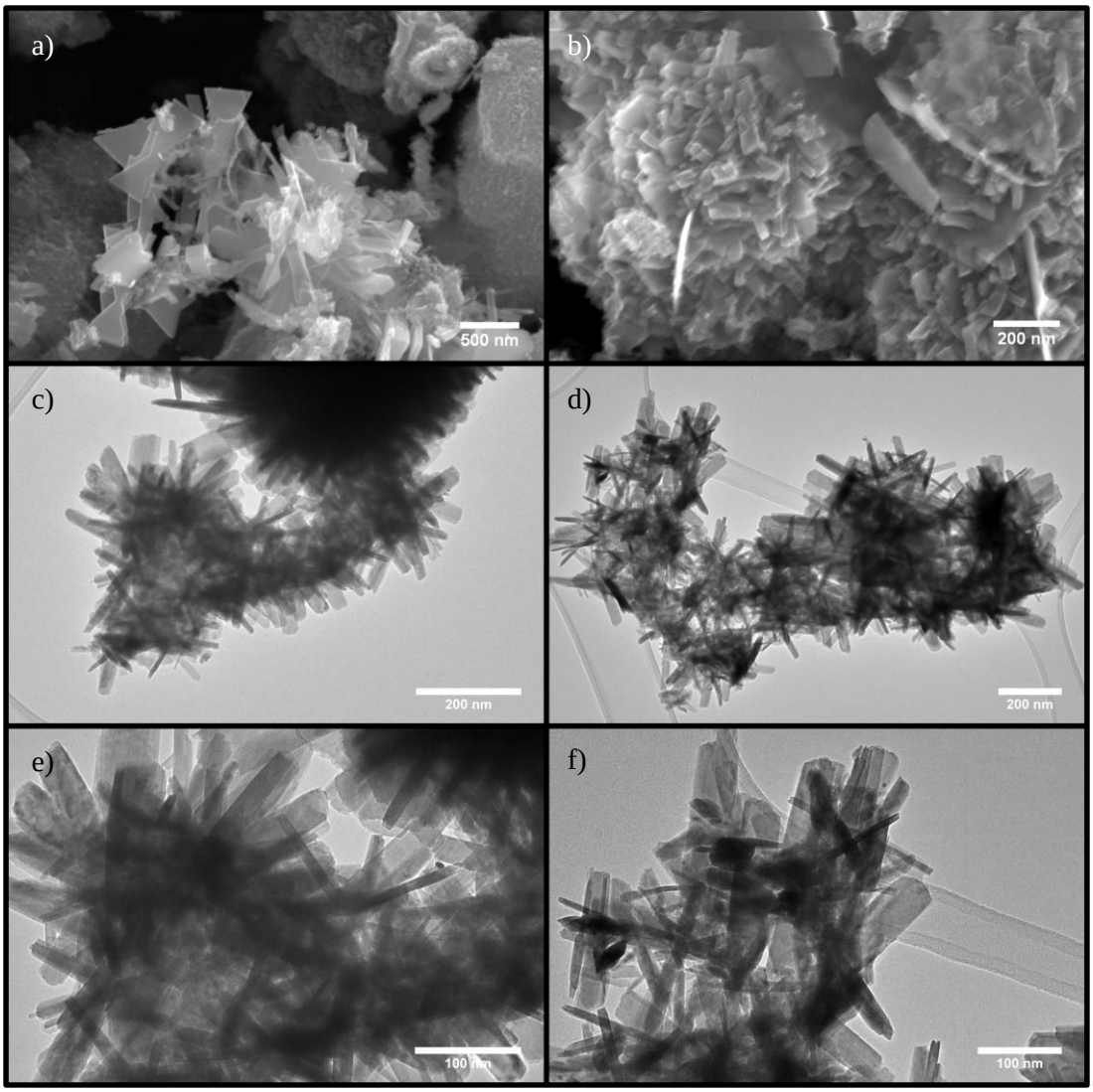

Figure 5.28: a) and b) SEM images of barium iridium oxides showing both trigonal and rod particle morphologies c), d), e) and f) TEM images showing particles with rod like morphology.

Table 5.9: Barium iridium ratios of samples produced using $NaOH/Na_2O_2$ and KOH/KO_2 obtained from EDXA and ICP-OES.

EDXA			
Sample	Ba / Atomic %	Ir / Atomic %	Ba : Ir
Sodium method	34.5	65.5	0.52 : 1
Potassium method	31.5	68.5	0.46 : 1
ICP-OES			
Sample	Ba / Atomic %	Ir / Atomic %	Ba : Ir
Sodium method	32.71	67.29	0.49 : 1
Potassium method	20.71	79.29	0.26 : 1

XANES measurements were carried out at the Ir L_{III}-edge to determine the oxidation state of the iridium within the new barium iridium oxide, Figure 5.29. The white line position was used to determine the oxidation state, which was revealed to be +4.

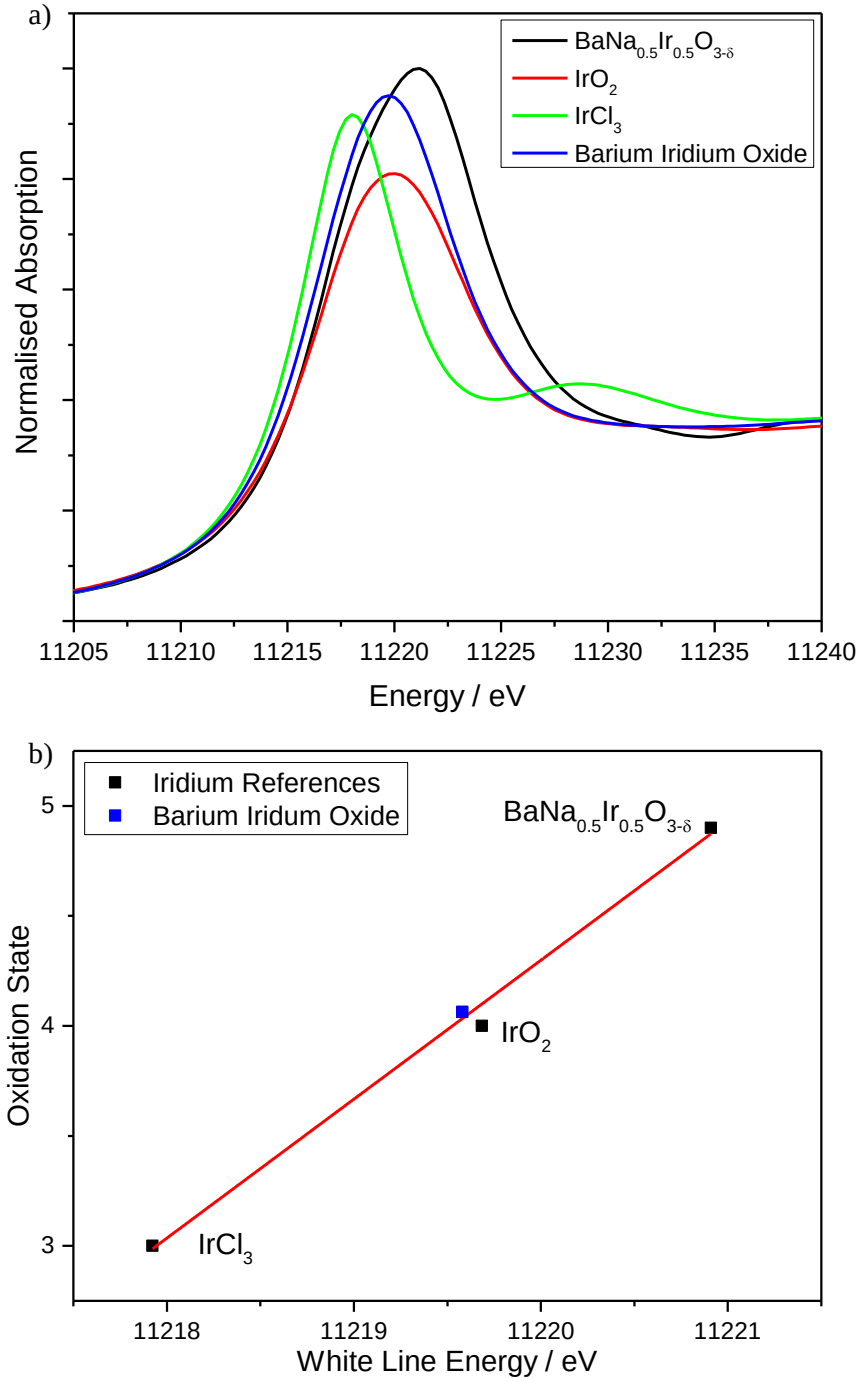

Figure 5.29: a) Ir L_{III}-edge XANES spectra of barium iridate and reference materials. b) White line position against oxidation state.

Thermodiffractometry of the new barium iridium oxide reveals several phase changes as the temperature is increased, Figure 5.30. First a constant loss of intensity from all its peaks in the thermodiffractometry is observed, up until 400 °C, at which point the phase collapses, and it is observed a portion of the iridium in the material is reduced to metallic iridium. Then between 450-550 °C an unidentifiable transient phase is seen before the formation of $BaIrO_3$

at 550 °C, which subsequently collapses at 800 °C leaving metallic iridium and barium oxide. All the mass losses observed in the TGA occur at the same temperature of the phase changes observed in the thermodiffractometry. Given the constant mass loss up until around 300 °C and the loss of intensity from the peaks resulting from the new barium iridate it seems possible that either crystal water or hydroxide could be present. Such a conclusion can be drawn since hydrothermally synthesised barium ruthenates, $Ba_4Ru_3O_{10.2}(OH)_{1.8}$[20] and $Ba_2Ru_3O_9OH$,[7] which contain hydroxyl groups have been reported.

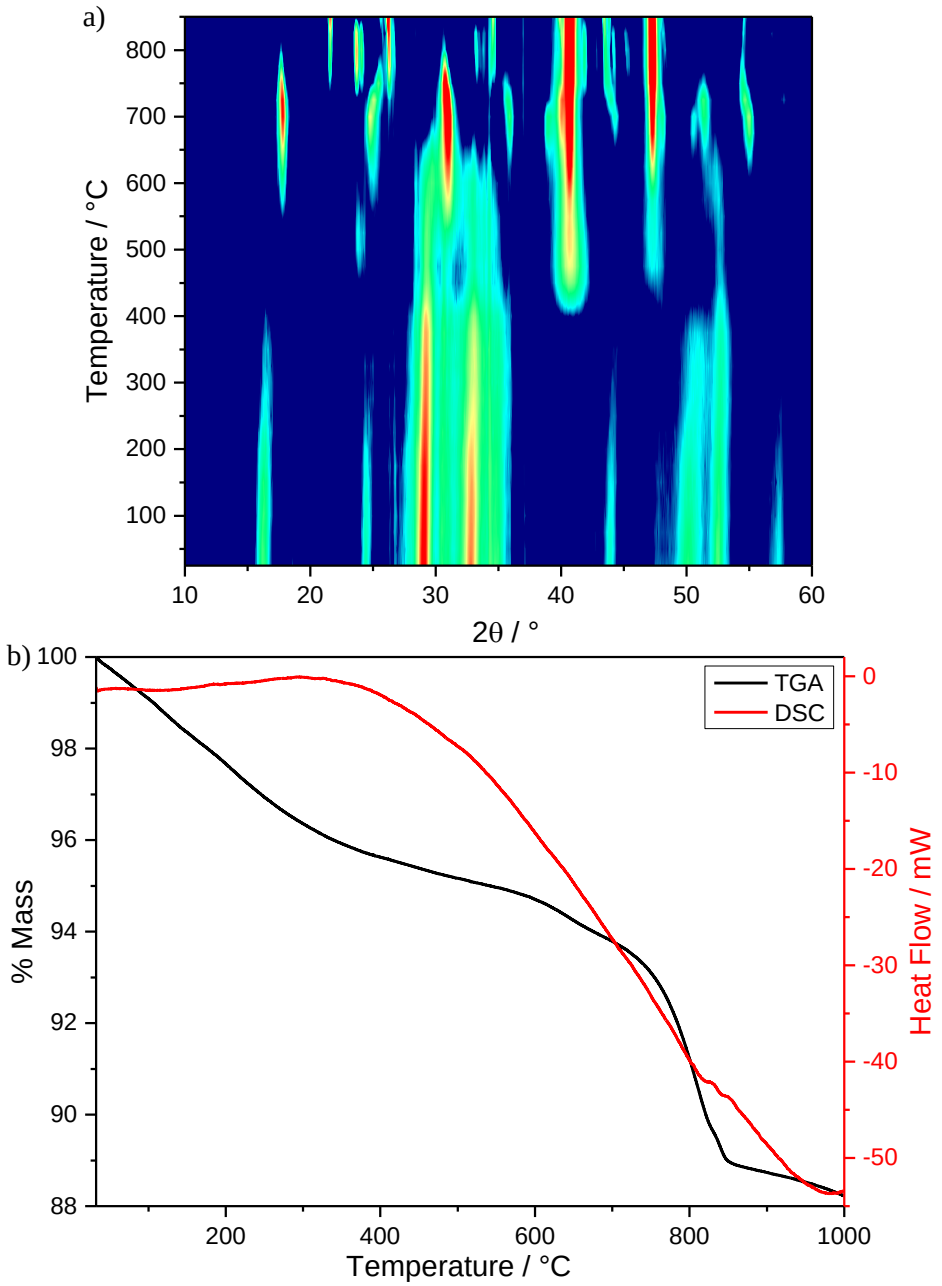

Figure 5.30: a) Thermodiffractometry (λ = 1.5418 Å) and b) TGA and DSC of barium iridate.

5.2.2 Attempts at Improving the Crystallinity of the New Barium Iridate

In an attempt to synthesise a more crystalline version of the material, to facilitate possible structural solution, the reaction conditions were carefully tuned, the XRD diffraction patterns of these materials where then compared with that of the original synthesis.

It was found that altering the molarity of the NaOH used in the reaction affected the crystallinity of the material produced, Figure 5.31. The crystallinity can be enhanced by reducing the molarity of the NaOH used in the synthesis to 5 M. Conversely when the

reaction was carried out in 15 M NaOH the crystallinity of the final material was diminished, additionally the recovered filtrate was purple rather than clear suggesting the presence of a soluble iridium species.

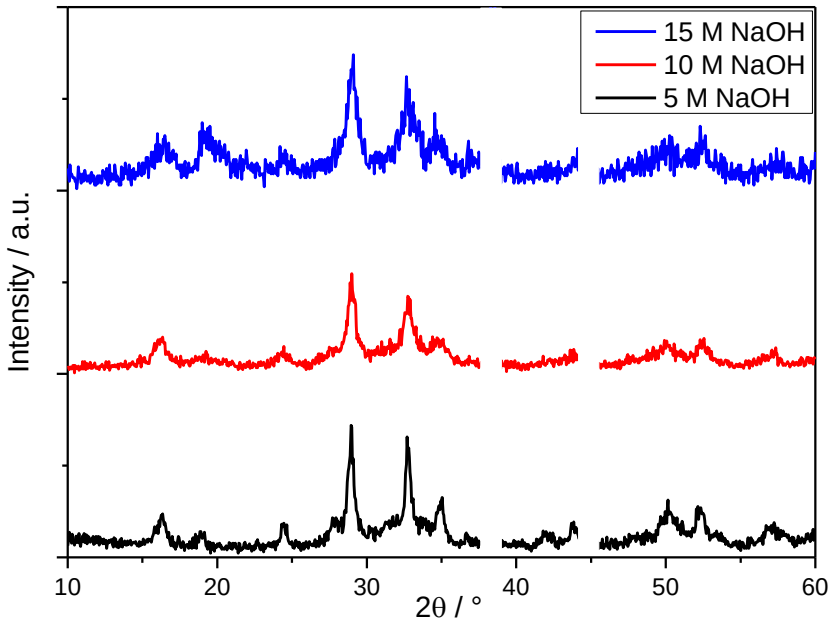

Figure 5.31: Powder XRD patterns (λ = 1.5418 Å) of barium iridium oxide synthesised in various NaOH concentrations. Peaks arising from aluminium sample holder at 38 and 44.5 ° have been masked.

The effects of changing the reaction temperature on the powder XRD pattern scan can be seen in Figure 5.32. By increasing the reaction temperature beyond 240 °C to 260 °C a decrease in crystallinity was observed. This was surprising, because in Chapter 4 it was demonstrated that reducing the reaction temperature also reduced the crystallinity of the calcium iridium oxide pyrochlore. Lowering the reaction temperature to 160 °C drastically lowers crystallinity of the synthesised materials. Reducing the heating rate to reaction temperature only slightly improves the crystallinity. Oscillating the temperature between 200 and 240 °C, every 6 hours, over the course of the reaction was also attempted to promote dissolution and recrystallisation of the material, however no increase in the crystallinity of the product formed was seen.

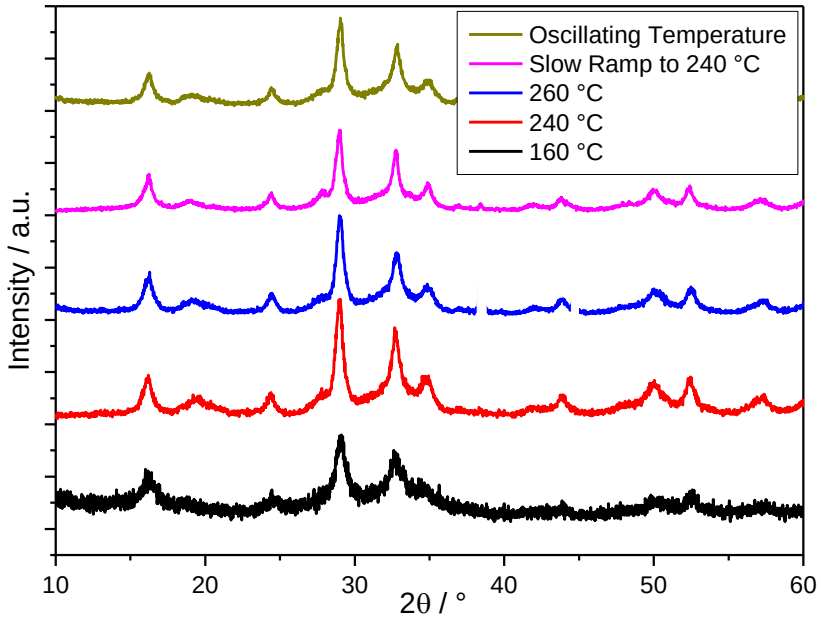

Figure 5.32: Powder XRD patterns (λ = 1.5418 Å) of barium iridium oxide synthesised at various temperatures and under specified heating protocols.

The effect of the concentration of the reagents both relative and absolute on the crystallinity of the final product were then tested, Figure 5.33. The effect of absolute reagent concentration on the crystallinity of the final product was tested using a vessel with a 40 ml internal volume rather than 20 ml, thus allowing the reaction to be performed in 20 ml of solvent rather than the standard 10 ml, but doing this made no observable difference to the crystallinity of the final product. However, it was found reducing the amount of barium peroxide used in the reaction, lowering the relative molar ratio of Ba : Ir. to 1 : 2, the ratio seen in the final product, produces a slightly more crystalline material than when an excess is used. Seeding the reaction with previously synthesised barium iridate was attempted with the idea of offering pre-existing nucleation sites for the reaction, but this gave no improvement in the crystallinity of the product.

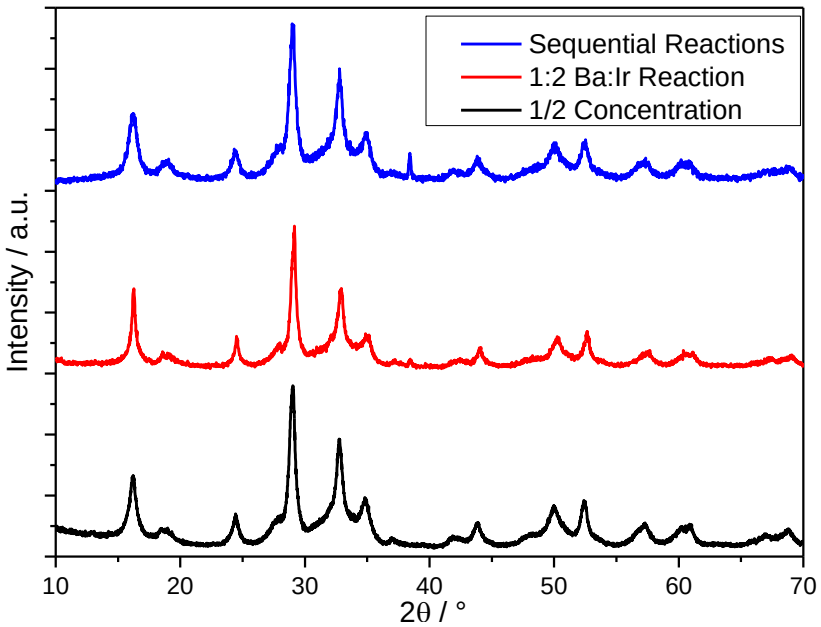

Figure 5.33: Powder XRD patterns (λ = 1.54056 Å) of barium iridium oxide synthesised under specified reagent concentration conditions.

Thermodiffractometry showed that the new barium iridate would be difficult if not impossible to anneal in air. Hence hydrothermal annealing was attempted using an Inconel reactor available at Warwick, at 315 °C in H_2O where a pressure of approximately 140 bar was generated for a period of four hours, the results of these reactions can be seen in Figure 5.34. The first reaction involved heating a previously prepared sample of the new barium iridate in 10 ml of water to the desired temperature. This resulted in a partially decomposed barium iridate, which had lost crystallinity along with an unidentifiable impurity phase. The second reaction was the same as the first but additional barium peroxide was added in an attempt to prevent the decomposition. This yielded yet another new material, as the collected material was green not black. The powder diffraction pattern of this material appears to have one set of sharp peaks and another set of broader peaks suggesting that it is not phase pure.

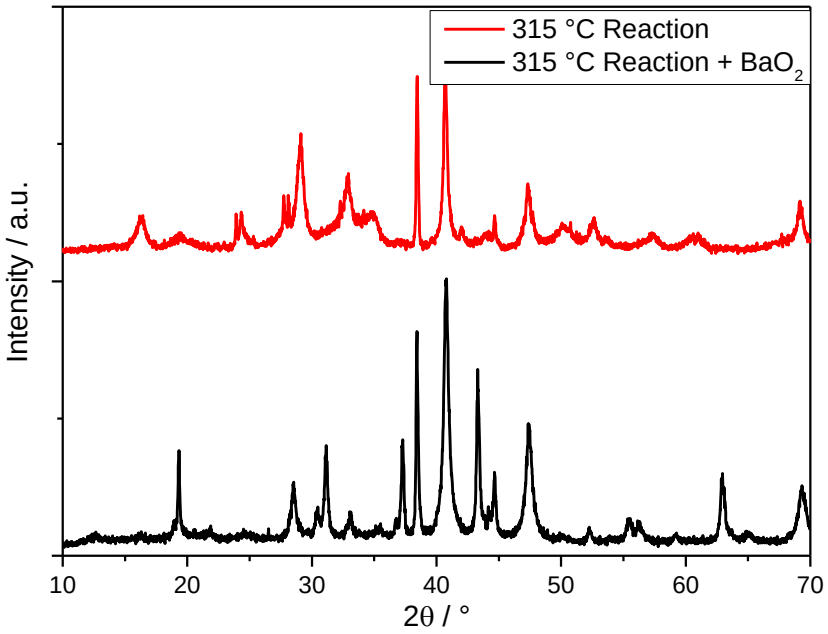

Figure 5.34: Powder XRD patterns (λ = 1.5418 Å) of barium iridium oxide treated hydrothermally at 315 °C.

The powder diffraction patterns of the ruthenium substitution reactions can be seen in Figure 5.35. In those reactions where iridium chloride was substituted with ruthenium chloride, the 4H-$BaRuO_3$ phase became observable in the XRD patterns. However when $KRuO_4$ was used as a ruthenium source, a secondary phase was observed in the XRD pattern with a similar pattern to that of $Ba_2Ru_3O_9OH$.

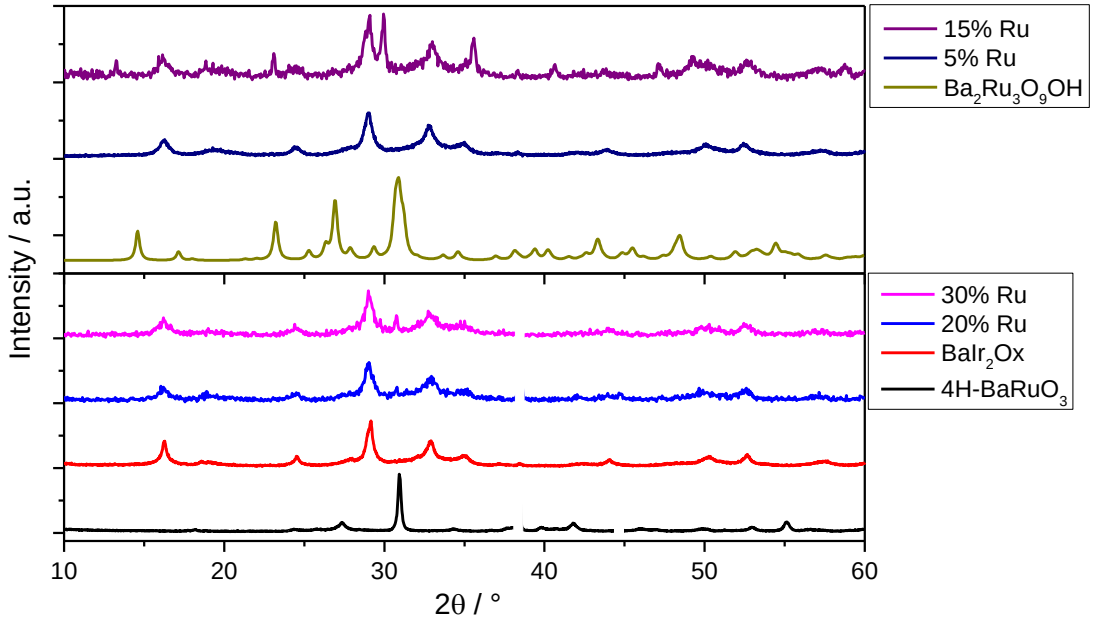

Figure 5.35: Powder XRD patterns (λ = 1.5418 Å) of barium iridium oxide from ruthenium substitution reactions.

An optimised synthesis was devised, based on the aforementioned experiments, incorporating all the factors that lead to a more crystalline product with the exception of the slow ramp to reaction temperature. In addition to these optimisations, the temperature was reduced from 240 °C to 230 °C as our collaborators at Johnson Matthey had found this also yielded a more crystalline material.

This reaction produced a material yielding an XRD with sharper peaks however the increase in crystallinity was not great enough to make any headway in indexing the diffraction pattern, despite resolving some additional peaks not observed in the powder pattern of the original less crystalline material, Figure 5.36.

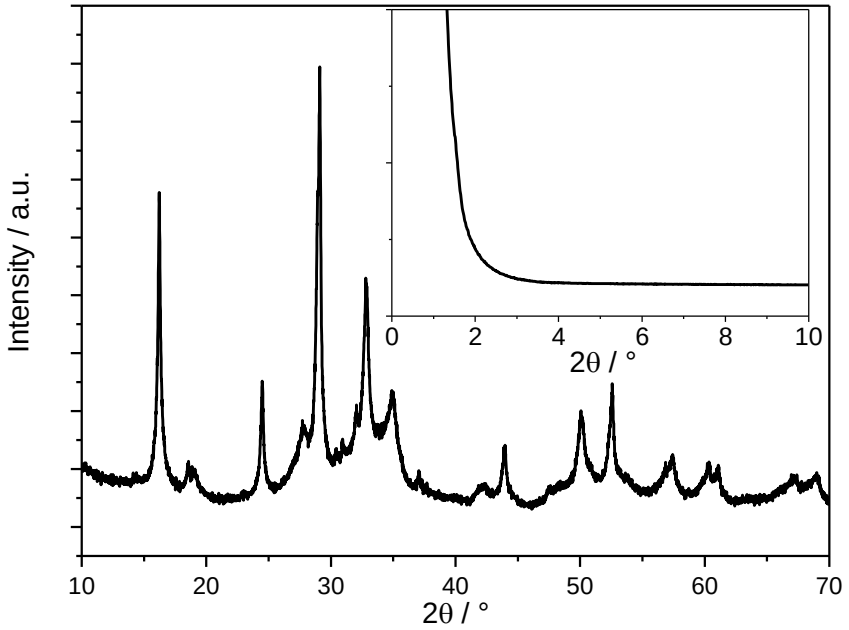

Figure 5.36: Powder XRD pattern (λ = 1.54056 Å) of barium iridium oxide produced from the optimised synthesis. Inset contains low angle data showing that there are no low angle peaks.

Currently, without better crystallographic data a structural solution for this barium iridate remains elusive. Low angle data were collected to ensure that no additional large *d*-spacing peaks were present, Figure 5.36 inset. The pattern has been run though multiple auto indexing programs, including FOX[21], CMPR[22] and Topas,[23] and no suitable cell has been obtained. The lattice fringes observed in the HR-TEM, Figure 5.37, reveal a possible lattice

spacing of 5.4 Å, which corresponds to the peak observed at 16 ° in the powder pattern, however this alone does not yield a unit cell.

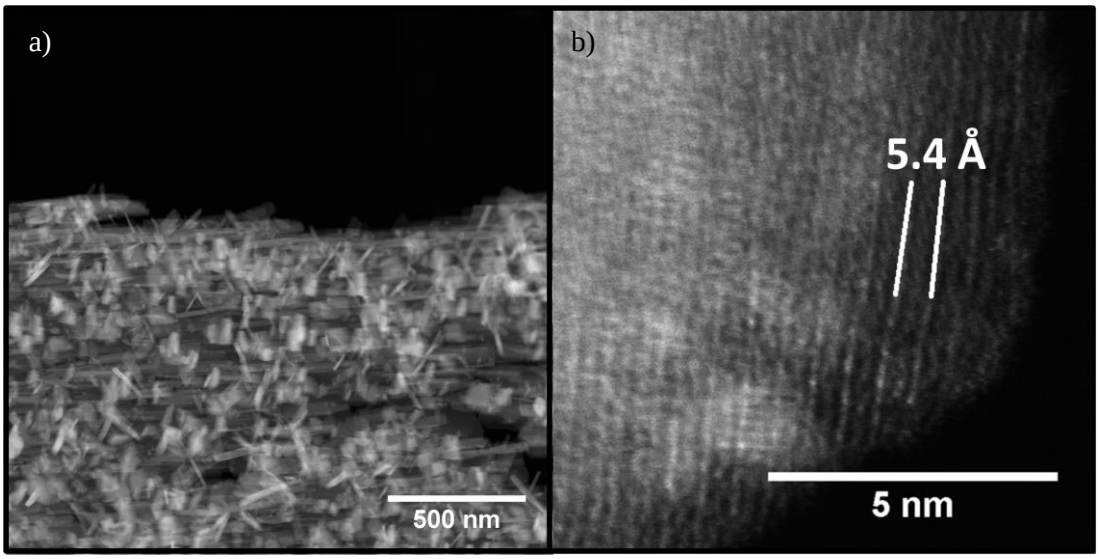

Figure 5.37: TEM micrographs of barium iridium oxide from optimised synthesis, a) showing presence of interwoven particles forming large flake and b) high magnification image showing lattice fringes.

There are several things now known about this new material:

- The Ba : Ir ratio is 1 : 2.
- The iridium has an oxidation state of 4+.

Taking these two facts into account one could assume an empirical formula to be $BaIr_2O_5$. However if there is OH or H_2O present in the structure, as suspected due to the loss of crystallinity in thermodiffractometry and constant mass loss in TGA up till 300 °C, then the formula could be corrected to $BaIr_2O_{5-x}(OH)_{2x}\cdot nH_2O$.

References:

1 A. Talanov, W. A. Phelan, Z. A. Kelly, M. A. Siegler and T. M. McQueen, *Inorg. Chem.*, 2014, **53**, 4500–4507.

2 W. Sun, Y. Song, X.-Q. Gong, L. Cao and J. Yang, *ACS Appl. Mater. Interfaces*, 2016, **8**, 820–826.

3 A. Michas, J. M. Kelly, R. Durand, M. Pineri and J. M. D. Coey, *J. Memb. Sci.*, 1986, **29**, 239–257.

4 T. Audichon, T. W. Napporn, C. Canaff, C. Morais, C. Comminges and K. B. Kokoh, *J. Phys. Chem. C*, 2016, **120**, 2562–2573.

5 N. Danilovic, R. Subbaraman, K.-C. Chang, S. H. Chang, Y. J. Kang, J. Snyder, A. P. Paulikas, D. Strmcnik, Y.-T. Kim, D. Myers, V. R. Stamenkovic and N. M. Markovic, *J. Phys. Chem. Lett.*, 2014, **5**, 2474–2478.

6 N. F. Atta, A. Galal and S. M. Ali, *Int. J. Electrochem. Sci.*, 2012, **7**, 725–746.

7 C. I. Hiley, M. R. Lees, J. M. Fisher, D. Thompsett, S. Agrestini, R. I. Smith and R. I. Walton, *Angew. Chemie Int. Ed.*, 2014, **53**, 4423–4427.

8 P. D. Kanhere, J. Zheng and Z. Chen, *J. Phys. Chem. C*, 2011, **115**, 11846–11853.
9 K. Sardar, J. Fisher, D. Thompsett, M. R. Lees, G. J. Clarkson, J. Sloan, R. J. Kashtiban and R. I. Walton, *Chem. Sci.*, 2011, **2**, 1573–1578.
10 W. Bensch, H. W. Schmalle and A. Reller, *Solid State Ionics*, 1990, **43**, 171–177.
11 B. J. Kennedy and B. A. Hunter, *Phys. Rev. B*, 1998, **58**, 653–658.
12 J. Spooren and R. I. Walton, *J. Solid State Chem.*, 2005, **178**, 1683–1691.
13 S.-T. Hong and A. W. Sleight, *J. Solid State Chem.*, 1997, **128**, 251–255.
14 R. D. Shannon, *Acta Crystallogr. Sect. A*, 1976, **32**, 751–767.
15 R. H. Mitchell and R. P. Liferovich, *J. Solid State Chem.*, 2004, **177**, 4420–4427.
16 K. E. Johnston, C. C. Tang, J. E. Parker, K. S. Knight, P. Lightfoot and S. E. Ashbrook, *J. Am. Chem. Soc.*, 2010, **132**, 8732–8746.
17 X. Li and J. Zang, *J. Phys. Chem. C*, 2009, **113**, 19411–19418.
18 J. Tréhoux, F. Abraham and D. Thomas, *Mater. Res. Bull.*, 1982, **17**, 1235–1243.
19 K. Sardar, E. Petrucco, C. I. Hiley, J. D. B. Sharman, P. P. Wells, A. E. Russell, R. J. Kashtiban, J. Sloan and R. I. Walton, *Angew. Chemie Int. Ed.*, 2014, **53**, 10960–10964.
20 C. I. Hiley, M. R. Lees, D. L. Hammond, R. J. Kashtiban, J. Sloan, R. I. Smith and R. I. Walton, *Chem. Commun.*, 2016, **52**, 6375–6378.
21 V. Favre-Nicolin and R. Cerný, *J. Appl. Cryst.*, 2002, **35**, 734–743.
22 B. H. Toby, *J. Appl. Cryst.*, 2005, **38**, 1040–1041.
23 A. A. Coelho, *J. Appl. Cryst.*, 2000, **33**, 899–908.

Chapter 6 – Electrocatalysis Using New Precious Metal Oxides

6.1 Introduction to and Scope of Chapter

In this chapter electrocatalytic data for materials whose synthesis was described in earlier chapters are presented. Catalytic performance is assessed with three measures of activity: the onset voltage of the oxygen evolution reaction, the mass activity, which is a measure of how active the material is per gram of platinum group metal (PGM), and specific activity, which describes how active the materials are based on their surface area. In addition the total dissipated charge and the selectivity towards the oxygen evolution reaction over the carbon oxidation reaction are measured.

Using XANES data collected on B18 at Diamond Light Source, the response of the electroactive metals oxidation states to applied potential is measured, both prior to and after the onset of oxygen evolution. This was done with the aim of understanding the mechanism by which the oxygen evolution reaction takes place.

6.2 Experimental

6.2.1 Powder Conductivity

These measurements were carried out to determine whether a sample was suitably conducting to be a viable catalyst for OER. Measurements were carried out in a custom piece of equipment at Johnson Matthey Technology Centre, Sonning Common, UK. Approximately 1 mm of sample is loaded into a 13 mm diameter tube, which is then compressed between two brass plates under 2 bar then 3 bar of nitrogen. Potential is then applied across the plates and the resulting current recorded.

6.2.2 Gold Rotating Disc Electrode

To fabricate an electrode, first an ink was produced from the powdered electrocatalyst. A typical ink preparation involved adding 60 mg of catalyst to 1.1 ml of propan-2-ol, 4.4 ml of deionised water and 503 µL of 5.52 %wt aqueous Nafion™ solution. The mixture was then

homogenised by a sonic probe operating at 6 W for active duration of ten minutes. The probe operates in pulsed mode: each cycle was comprised of 30 s on and 30 s off. Typically five minutes of exposure was enough to ensure homogenisation. 15 µL of the ink was then deposited on to the gold rotating disc electrode (RDE) (Pine Instrument, 0.196 cm^2). The electrode was then dried, by loading the electrode into the upside down motor then spinning the electrode at 700 rpm until all the solvent had evaporated. Electrodes prepared in this fashion typically have a solids loading of approximately 820 μgcm^{-2}.

6.2.3 Wet Cell Testing

The oxygen evolution reaction starts at approximately 1.4 V *vs* reversible hydrogen electrode (RHE), under acidic conditions, thus once a material is determined to be conducting the next step is to check that it evolves oxygen within the desired potential range.[1] To test this the gold RDE (working electrode) loaded with catalyst is loaded into a three electrode electrochemical cell filled with 1.0 M H_2SO_4 with a standard RHE (reference electrode) and Pt wire (counter electrode). The measurements were carried out at 25 °C, with the working electrode rotating at 900 rpm to minimise the formation of bubbles on the electrode surface, continuous purging of the electrolyte solution is carried out by bubbling nitrogen through the solution. Typical voltammograms were recorded between 0.02 and 1.5 V with a sweep rate of 100 mVs^{-1}, while additional scans were often carried out between 1.0 and 1.6 V at a sweep rate of 1 mVs^{-1}. A characteristic spike is current is observed as the potential is increased past 1.4 V due to the onset of the oxygen evolution reaction.

6.2.4 Electrode Fabrication

To fabricate a membrane electrode assembly, 100 mg of oxide catalyst was added to 0.5 g of Hispec18600, a commercial platinum-on-carbon catalyst. Aqueous Nafion™ solution (11.92 %wt solids, 1 ml) was added and was mixed in a planetary mixer for 15 seconds. Additional Nafion™ solution was added to give an ink containing 110 %wt Nafion™ with respect to oxide catalyst. The ink was then shear-mixed in a planetary mixer using 5 mm diameter yttrium stabilised zirconia ceramic beads for 3 minutes at 3000 rpm. The ink was

then stirred manually with a spatula to break up any sediment and was then mixed for a further 5 minutes in the planetary mixer.

The ink was screen printed onto a PTFE sheet to give a layer with an overall PGM loading of between 0.05 and 0.15 $mgcm^{-2}$, verified using X-ray fluorescence (XRF) measurements. The layer was transferred from the PTFE sheet onto Nafion™ N117 membrane at 150 ^{o}C with pressure. A Pt/C layer was transferred to the opposite side of the Nafion™ N117 membrane simultaneously in order to produce the catalyst coated membrane.

6.2.5 Membrane Electrode Assembly Testing

The electrode was placed between two flow field plates backed with microporous layer coated carbon paper, Toray TGP-H-060, cut to the desired size. The catalyst coated membrane was then tested at 80 °C with 10 psig of humidified H_2/N_2 reactant gas. The electrochemical surface areas of the platinum in both layers were measured via CO stripping voltammetry. Cyclic voltammograms were collected, scanning the potential from 0.02 to 1.6 V *vs* RHE at 5 mVs^{-1}. The membrane electrode assembly was then cycled 500 times between 0.05 and 1.0 V *vs* RHE at 100 mVs^{-1}, to simulate ageing. The cyclic voltammograms collected between 0.02 and 1.6 V *vs* RHE at 10 mVs^{-1} were then repeated. The stability of the layers was tested by galvanostatically controlling the layer, evolving oxygen in several steps, each generating a greater current until holding at 200 $mAcm^{-2}$. Oxygen evolution was maintained until reaching a voltage cutoff of 3 V *vs* RHE. Throughout this process the levels of hydrogen, oxygen, carbon and carbon dioxide were monitored using a mass spectrometer.

From this test, five metrics for the catalytic performance of the materials were extracted.

1. **Mass Activity**

   The mass activity is a measure of how active the synthesised materials are based on the mass of platinum group metal they contain, and is recorded in A/gPGM. The mass activity is derived from the cyclic voltammograms obtained pre and post

cycling, using the current produced at 1.5 V *vs* reversible hydrogen electrode. This is recorded at beginning of life (BOL) and after cycling at the end of life (EOL).

2. **Specific Activity**

   Specific activity is calculated using the mass activity and the surface areas obtained from BET, and is a measure of how active the material is based on the total surface area, being recorded in A/m^2.

3. **Oxygen Evolution Reaction Onset Potential**

   The oxygen evolution onset potential was taken as the onset of a visible O_2 signal which is typically 1 mA above the background current.

4. **Total Dissipated Charge**

   The total dissipated charge is another measure of activity but also measures durability of the catalyst layer, as the amount of charge produced is dependent on both the activity of the catalyst and the duration of the experiment. This is measured in C/µgPGM.

5. **O_2:CO_2 Selectivity**

   O_2:CO_2 selectivity measures the selectivity of the catalyst towards the oxygen evolution reaction over the carbon oxidation reaction. This is achieved by analysing the composition of the exhaust gas using a mass spectrometer.

The total dissipated charge and O_2:CO_2 selectivity are obtained from the final experiment where the layers are tested to failure. The layer is held galvanostatically for defined time steps. There are fourteen steps, the first of which draws 0.085A from the layer and the last drawing 1.0 A once the final step has finished. If the layer still has not reached the voltage cut off, a further hold drawing 1.2 A was carried out until the 3 V cut off is reached, signalling the failure of the layer.

The materials prepared in the earlier results chapters are compared against two benchmark materials, ruthenium iridium oxide and iridium tantalum oxide. These were OER catalysts that Johnson Matthey sold commercially at the start of the project.

Figure 6.1 shows two sets of cyclic voltammograms as examples of typical data sets: a) data for calcium iridium oxide are shown where the onset potential of the oxygen evolution reaction is lowered and the material subsequently becomes more active as a result of cycling, b) data are shown for calcium sodium ruthenium oxide where the material deactivates and the onset voltage for oxygen evolution increases as a result of cycling.

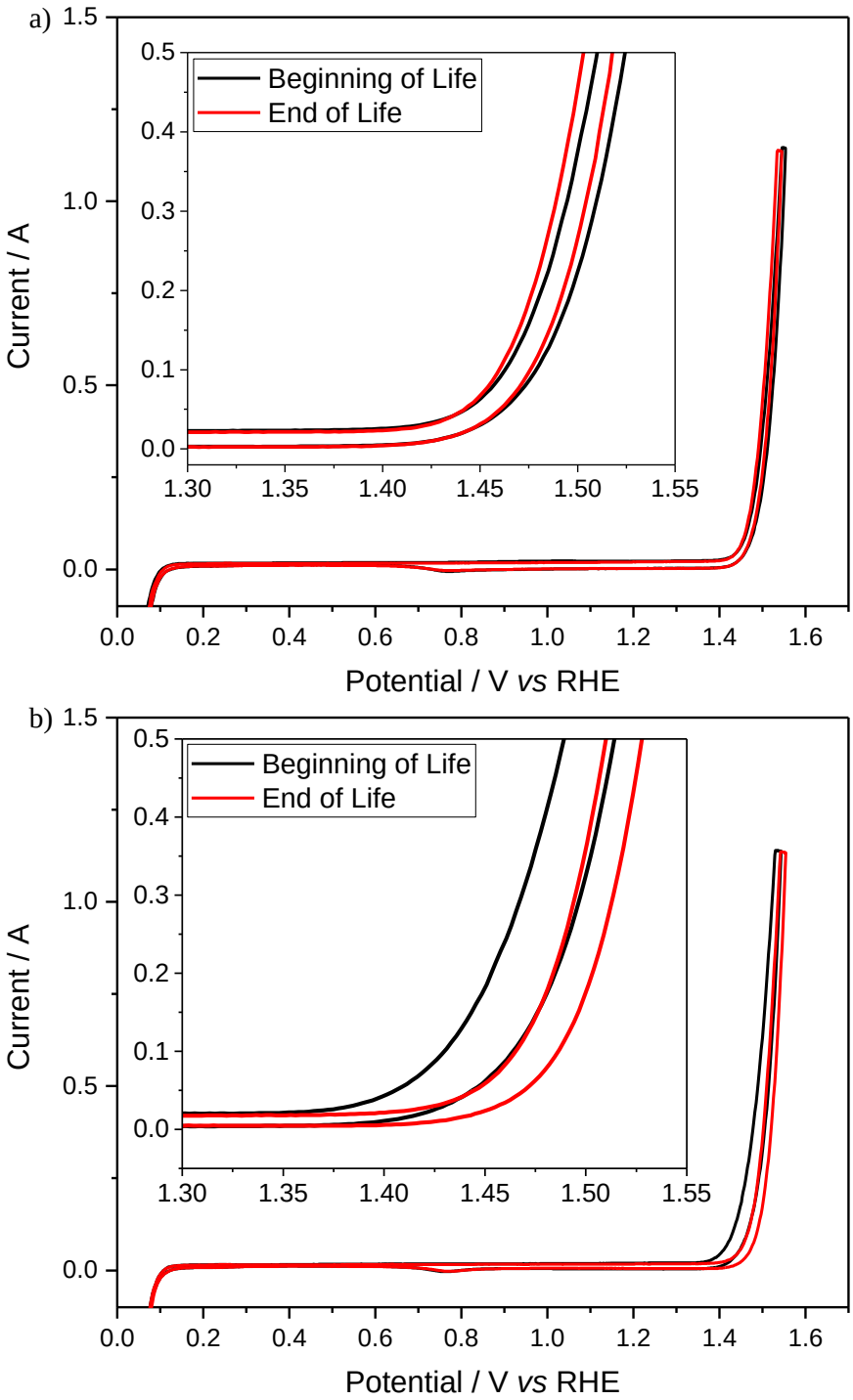

Figure 6.1: a) Cyclic voltammograms from calcium iridium oxide layer, showing a reduction in oxygen evolution onset voltage post cycling. b) Cyclic voltammograms from calcium sodium ruthenium oxide layer, showing an increase in oxygen evolution onset voltage post cycling.

Figure 6.2 shows data from end of life experiments of a stable and an unstable material. In Figure 6.2a it is shown that calcium iridium oxide produces oxygen at an ever increasing rate with increased current drawn up until approximately 7500 seconds, at which point there is a sharp increase in applied potential. At this point the oxygen evolution reaction is no longer

the favoured reaction, and the carbon oxidation reaction dominates, leading to a greater proportion of CO_2 detected in the exhaust gases. In Figure 6.2b it is shown that calcium sodium ruthenium oxide does not endure the first part of the test, as the failure of the layer occurs around the 1500 seconds corresponding to the 7^{th} step on the galvanostatically controlled staircase, at which point only 0.47 A is been drawn from the layer. This is considerably less than the 1.2 A which would have been drawn during the final hold. Beyond this point an ever increasing amount of both CO_2 and carbon in the exhaust gases and a decrease in the amount of oxygen is observed. The sum of any other carbon species produced during operation, such as carbon monoxide, are recorded under the carbon label.

The catalyst loading of the layer also affects the duration of these experiments, with those with greater loading lasting longer. To ensure consistency between experiments, layers with Pt loading closest to 100 $mgcm^{-2}$ via XRF were selected for testing.

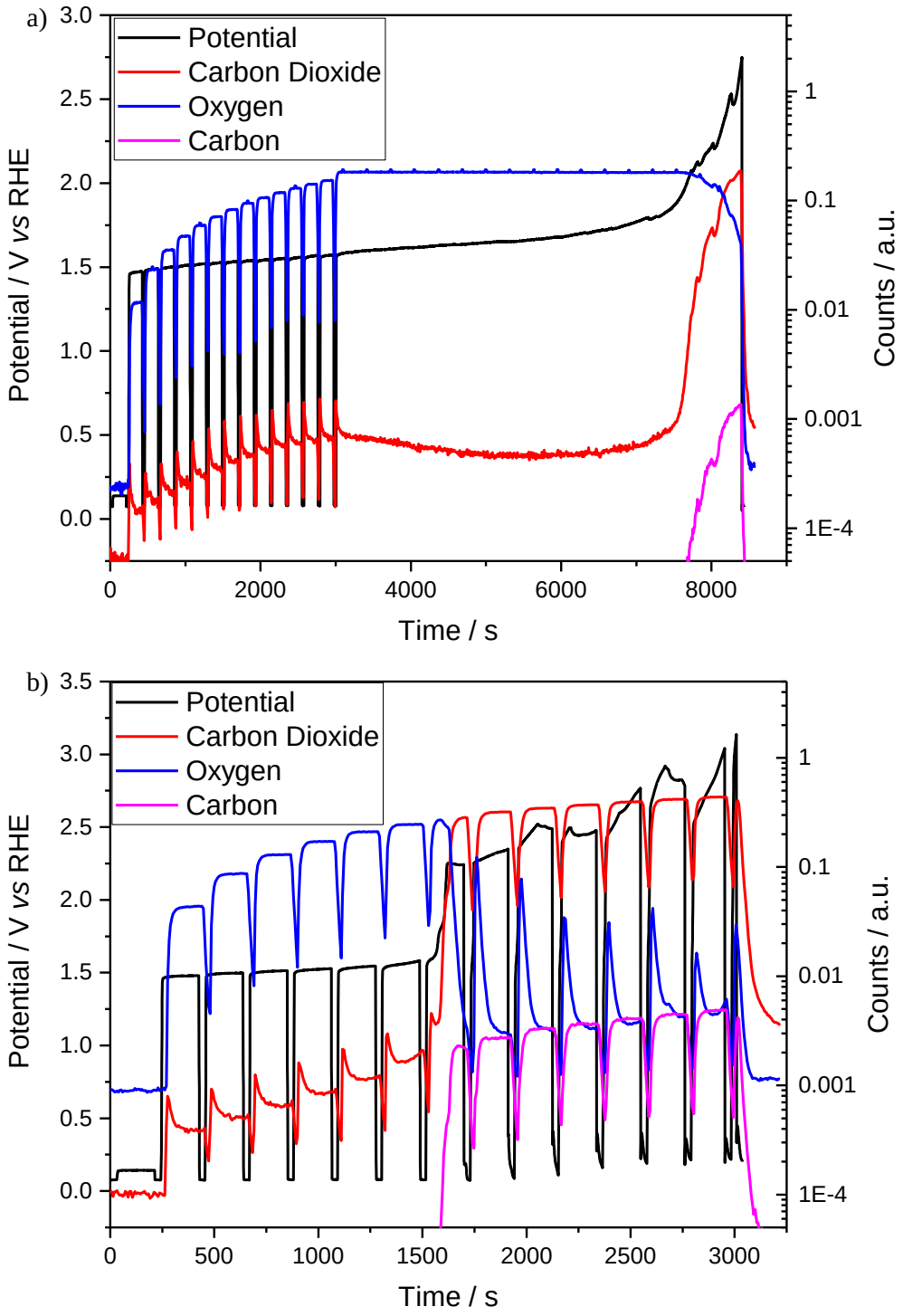

Figure 6.2: End of life experiments showing the difference between a) calcium iridium oxide, a stable material, and b) calcium sodium ruthenium oxide, an unstable material.

6.2.6 *In situ* XANES and EXAFS

Catalyst powders were mixed into inks using Nafion™ (11.92 %wt solids) as a binder. These were then painted onto microporous layer coated carbon paper, Toray TGP-H-060, to fabricate electrodes. Electrodes were produced with loadings of approximately 0.5 mgcm^{-2} of

the absorbing metal (Ir, Rh or Ru) under investigation. Those materials containing more than one electroactive element required electrodes of various loadings produced, one for each edge under investigation.

Figure 6.3 shows the experimental set up for the *in situ* XAS measurements. A custom cell was used, borrowed from Professor Andrea Russell from the University of Southampton. To carry out the experiment, 20 ml of 0.5 M H_2SO_4 was pumped around the cell using a non-pulsating pump, to avoid vibrations of the Kapton window, which would affect the quality of the collected data. A platinum counter electrode and a Hg/Hg_2SO_4 (MMS) reference electrode were used. MMS electrodes have a potential of +0.68 V in 0.5 M H_2SO_4 *vs* RHE.

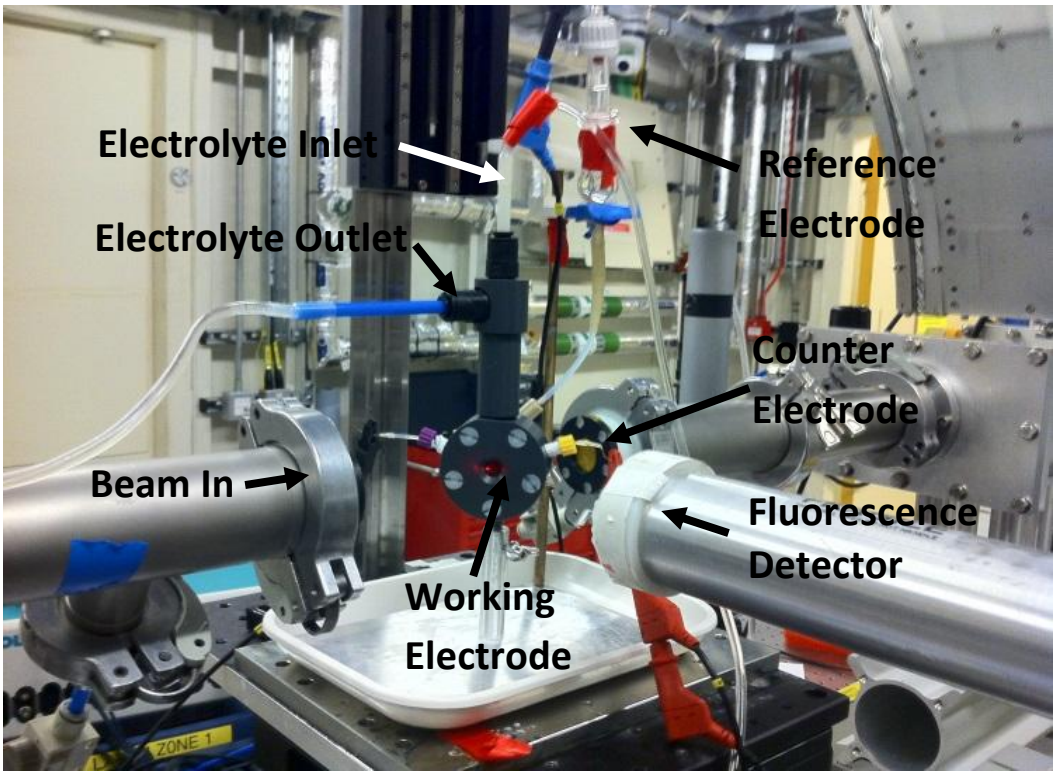

Figure 6.3: Photograph of cell used to carry out *in situ* XAS experiments.

Measurements were carried out in fluorescence mode on B18 using a germanium 9-element detector. Data were collected at the Ir L_{III}-edge, Ru K-edge, Rh K-edge and Sb K-edge, and were continuously monitored to ensure bubble formation due to oxygen evolution did not influence the data. If bubbles were produced in the beam path the stage was repositioned to rectify the problem. Most data were collected at the open circuit voltage (OCV), 0.3, 0.7, 0.9,

1.1, 0.3, -0.2 and 1.1 V *vs* MMS in sequence, Figure 6.4. Two additional experiments were run. In the first, more voltage steps were carried out on the initial ramp from OCV to 1.1 V for one calcium sodium iridium oxide sample. In the second, during the Sb K-edge experiments the applied potential was set to -0.6 V vs MMS to see if the antimony could be reduced. Ten XAFS scans were collected per voltage to ensure reliable data were collected.

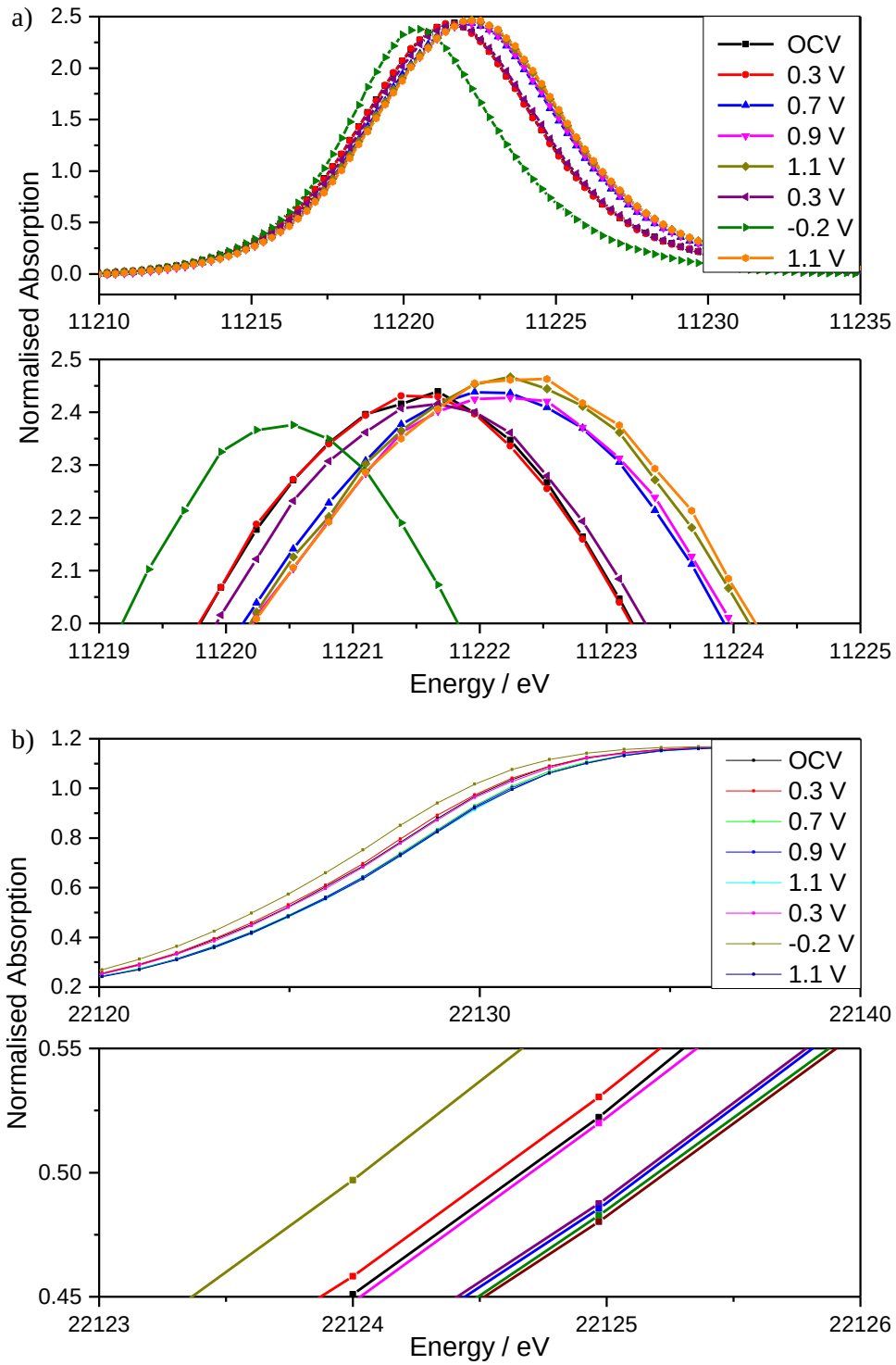

Figure 6.4: Example XANES spectra demonstrating a) white line shift of iridium L_{III}-edge and b) edge shift of ruthenium K-edge with applied potential.

Good spectra at each voltage were then merged and normalised. For iridium the white line energy was extracted and for the other elements the edge position when normalised absorption was equal to 0.5 was used. The point at which no potential was applied, OCV,

was then used as the point for zero change, the shift in oxidation state was calibrated using the dry reference materials, used in earlier chapters.

For calcium sodium iridium oxide full EXAFS data were collected in addition to the XANES data, Figure 6.5, the analysis of which was performed by Professor Richard Walton, using a single shell fit to obtain structural parameters describing the metal-oxygen shell.

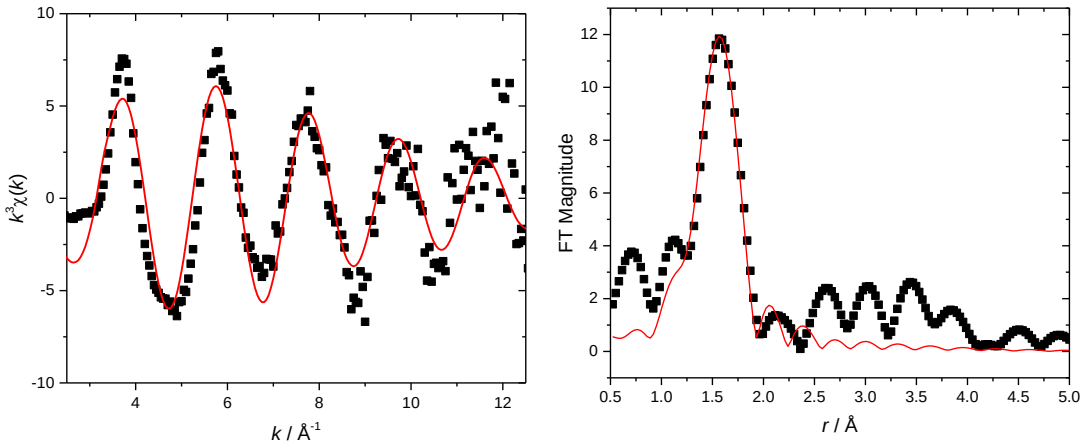

Figure 6.5: a) Ir L_{III}-edge EXAFS spectra and b) Fourier transform of calcium sodium iridium oxide at open circuit.

6.3 Substituted Rutile OER Catalysis

The first set of materials tested were the ruthenium rutiles substituted with magnesium or one of the first row transition metals. Table 6.1 shows various properties of the substituted rutile materials. The powder conductivity values for these materials are all within the same order of magnitude. While there is some variation in the surface areas of these materials, it is not very large and given they are all synthesised in the same manner this is somewhat expected. The OER onset voltages for all the substituted ruthenium oxides are considerably lower than that of the rutile $Ru_{0.9}Ir_{0.1}O_2$, which evolves oxygen at 1.439 V at beginning of life.[2] The new substituted rutiles then display an increase in the onset voltage post cycling with the exception of the cobalt substituted material.

Table 6.1: Conductivities, surface areas and oxygen evolution onset voltages at the beginning and end of life for substituted rutile materials.

Material	Powder Conductivity / Scm^{-1}	BET Surface Area / m^2g^{-1}	OER Onset Voltage / V	
			Beginning of Life	End of Life
$Zn_{0.15}Ru_{0.85}O_2$	0.08	27.1	1.399	1.416
$Mg_{0.15}Ru_{0.85}O_2$	0.02	42.5	1.395	1.413
$Ni_{0.15}Ru_{0.85}O_2$	0.05	33.9	1.385	1.399
$Co_{0.15}Ru_{0.85}O_2$	0.06	37.6	1.400	1.397
$Cu_{0.15}Ru_{0.85}O_2$	0.03	45.8	1.383	1.412

Figure 6.6 shows activity and durability/selectivity data for the substituted ruthenium oxide materials, with benchmark materials ruthenium iridium oxide and iridium tantalum oxide.

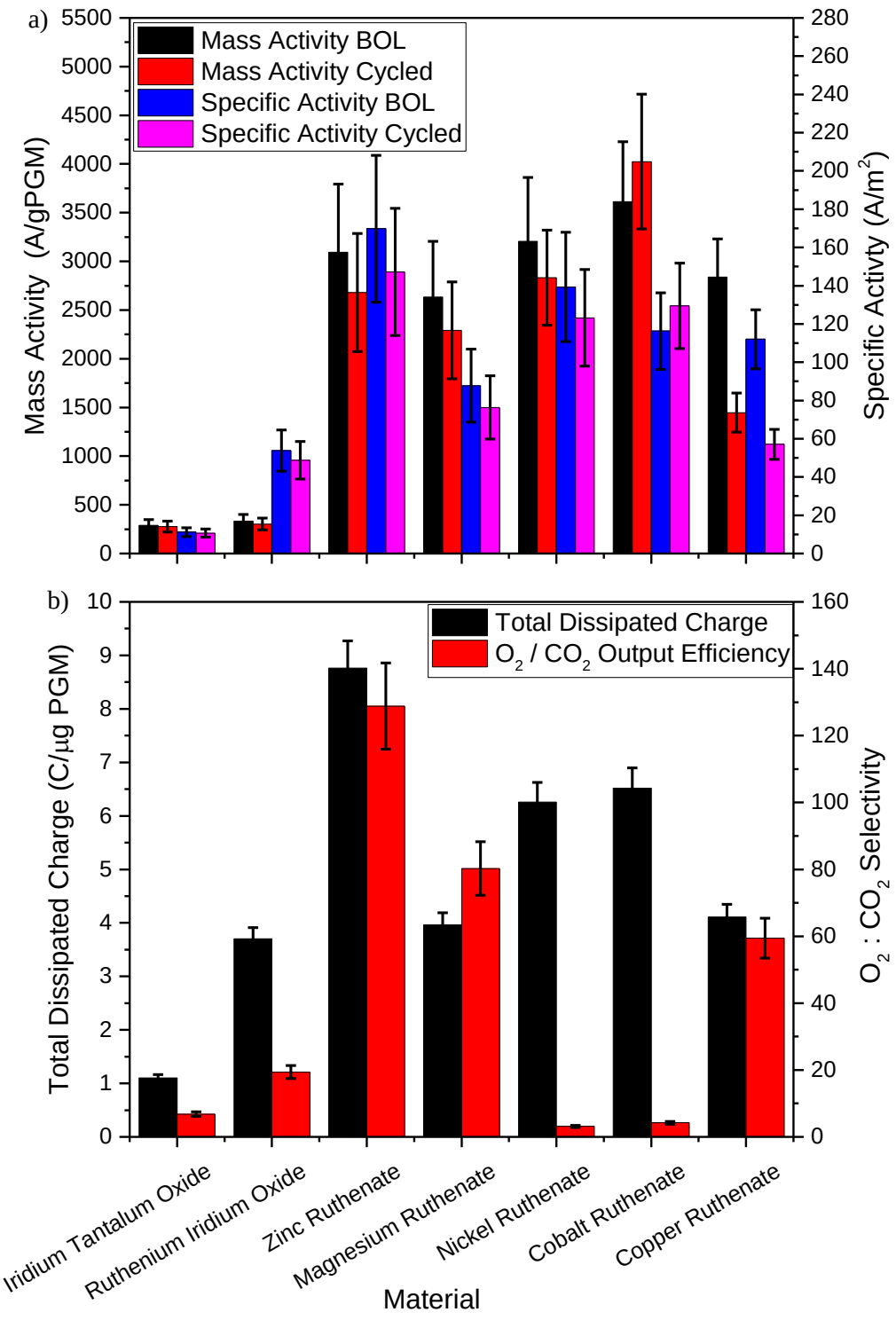

Figure 6.6: a) Activity metrics, and b) durability and selectivity metrics for substituted rutiles.

Upon first inspection all the synthesised materials are considerably more active than the benchmark materials. All five substituted rutile materials have a very similar beginning of life mass activities. Of these materials, cobalt ruthenate appears to be slightly more active than the other four. This may be due to cobalt being electroactive, as shown in the series of

barium strontium iron cobalt oxide materials, some of the most active materials for the oxygen evolution reaction under alkaline conditions.[3] Utilising DFT calculations it has been postulated that substituting ruthenium by either nickel or cobalt in ruthenium oxide can yield materials more active than RuO_2, as the overpotential should reduce.[4] Post cycling, all materials suffer a loss in activity except the cobalt substituted one, suggesting a highly active, cobalt rich, surface layer is forming as a result of cycling. Those materials where ruthenium has been substituted with zinc, magnesium, nickel and copper display a loss of activity post cycling. The magnitude of this loss is between 12.5 - 15 % in all cases except for the copper substituted material which displays a loss of 50 %. Ruthenium in RuO_2 is known to dissolve through the Ru^{4+} / Ru^{6+} redox couple,[5] this dissolution is probably what causes the loss of activity in most cases. It is also possible that the dissolved metals bind with the acid sites of Nafion™, increasing ionic transport resistance, which could exaggerate any losses in activity. The huge drop in activity observed in the copper material is maybe due to phase separation within the material, due to switching between Cu^{+} and Cu^{2+} that may be possible during the cycling.

The magnesium and copper substituted rutiles both dissipate a similar amount of charge to the iridium ruthenium oxide, while the zinc, nickel and cobalt substituted materials all dissipate considerably more. The zinc substituted material dissipates the most charge, twice that of the iridium ruthenium oxide, this is likely due to the zinc conferring more stability to the synthesised materials than any of the other substituents. The nickel and cobalt substituted materials likely dissipate more charge than the magnesium and copper materials as they are slightly more active.

The O_2:CO_2 selectivities are vastly different depending on the substituent: the zinc substituted material is the most selective towards the oxygen evolution reaction followed by magnesium then copper. Despite being more active, the nickel and cobalt substituted materials have poor O_2:CO_2 selectivities, meaning the rate of carbon oxidation is higher and

they destroy the carbon within the layer. This could be due to cobalt and nickel leaching out of the catalyst and binding to acid sites in Nafion™.

In conclusion, all the new substituted rutiles outperform the benchmark materials. The zinc substituted ruthenium oxide material is the best of the substituted rutile materials as it is the most balanced in terms of performance. The zinc substituted material has one of the highest activities of the substituted rutiles, with only the cobalt substituted material having a significantly higher activity. However, zinc substituted material dissipates more charge and is much more selective towards the oxygen evolution reaction than the cobalt substituted rutile.

6.4 Pyrochlore OER Catalysis

6.4.1 $(Ca,Na)_{2-x}Ir_2O_6O'$

Table 6.2 shows various properties of the calcium sodium iridium oxide pyrochlore. The powder conductivity of this material is recorded an order of magnitude greater than the substituted rutile materials previously studied; whether this is due to chemical differences or powder packing differences is unclear. The surface area and OER onset voltages of the calcium sodium iridium oxide are roughly the same as those of the substituted rutile material, however, unlike the rutile materials there is no detectable change in potential for the onset of oxygen evolution post cycling.

Table 6.2: Conductivity, surface area and oxygen evolution onset voltage at the beginning and end of life for calcium sodium iridium oxide pyrochlore.

Material	Powder Conductivity / Scm^{-1}	BET Surface Area / m^2g^{-1}	OER Onset Voltage / V	
			Beginning of Life	End of Life
$(Ca,Na)_{2-x}Ir_2O_6O'$	0.32	20.0	1.422	1.420

Figure 6.7 shows the activity and stability/selectivity data for calcium sodium iridium oxide pyrochlore, zinc substituted rutile with benchmark materials ruthenium iridium oxide and

iridium tantalum oxide. This is the "standard" calcium sodium iridium oxide prepared at 240 °C in 10 M NaOH, as described in Chapter 4.

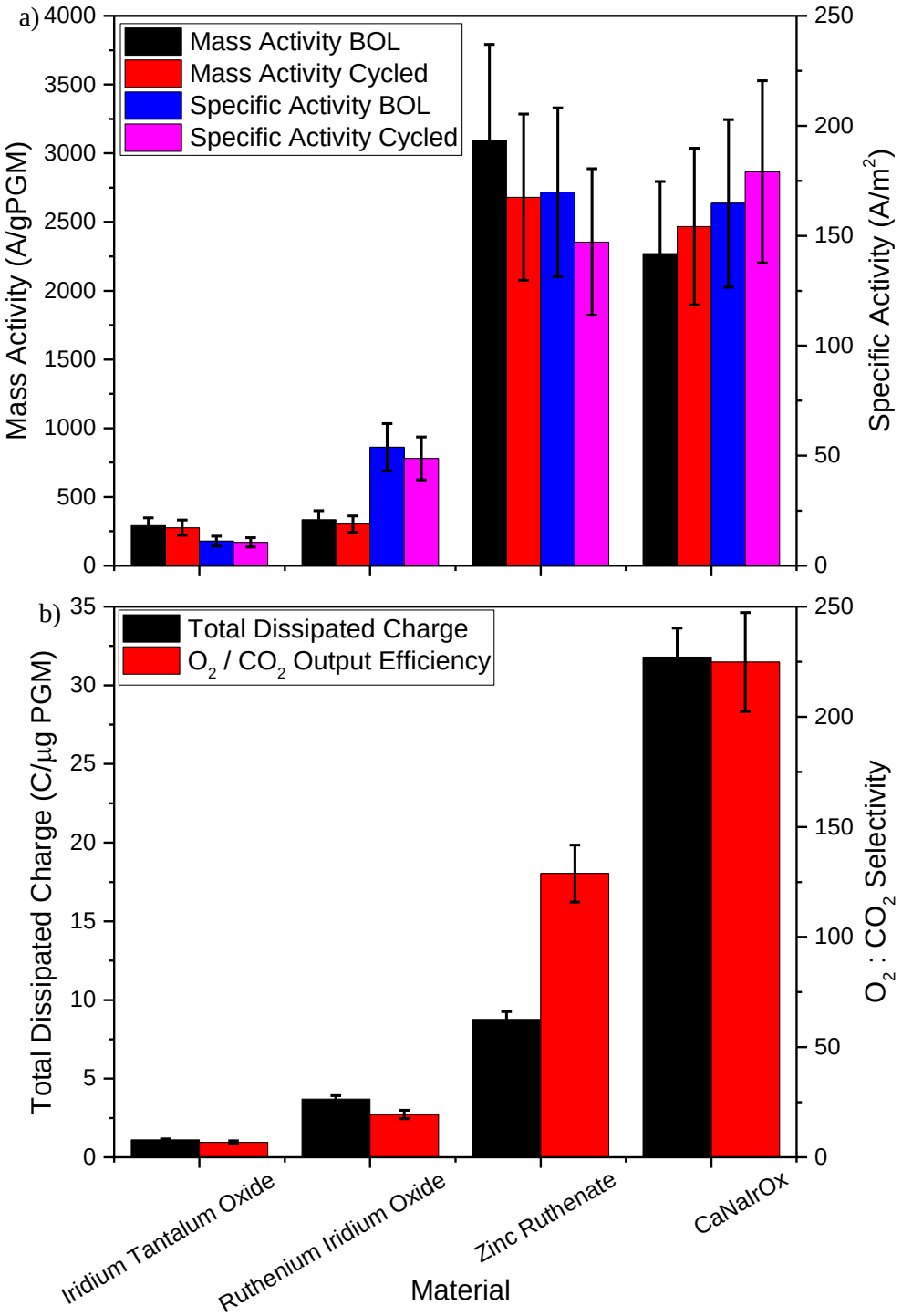

Figure 6.7: a) Activity metrics, and b) selectivity metrics benchmark materials and calcium sodium iridium oxide pyrochlore.

The calcium sodium iridium oxide material is considerably more active than the benchmark materials and is almost as active as the substituted rutile materials, despite the electroactive

element being iridium rather than ruthenium. Having an iridium based material achieving the same levels of activity as ruthenium based materials is outstanding as in ruthenium iridium systems it has always been believed the ruthenium that is mainly active and the iridium serves to stabilise the material. Materials with only iridium as an electroactive element, like the iridium tantalum oxide, tend to fall short of their ruthenium containing counterparts. Diaz-Morales *et al.* recently presented a set of iridium containing double perovskites, that are claimed to be more active than IrO_2,[6] however there is no comparison to RuO_2 presented. In addition to being vastly more active than the benchmark materials, the calcium sodium iridium oxide pyrochlore also gains activity post cycling, unlike the benchmark materials.

Furthermore, an order of magnitude more charge is dissipated from the pyrochlore material than the benchmarks, and the O_2:CO_2 selectivity is also an order of magnitude greater, meaning that this material is considerably more stable and more selective towards the oxygen evolution reaction than the benchmark materials.

6.4.2 $(Ca,Na)_{2-x}(Ir_{1-y}M_y)_2O_6O'$ (M = Sb, Zr, Ru, Rh and Mn)

The next set of materials looked at were the B site substituted pyrochlore materials, $(Ca,Na)_{2-x}(Ir_{1-y}M_y)O_6O'$ where M = Sb or Zr and y = 0.25 or 0.5, with the aim of establishing whether the substituent could improve the catalytic properties of the pyrochlore, or at the least maintain the performance of the unsubstituted material while diluting the iridium.

Table 6.3 shows various properties of antimony and zirconium substituted calcium sodium iridium oxide pyrochlore materials. In most cases the powder conductivity of the materials decreases with increasing substitution levels, this is consistent with Sb^{5+} and Zr^{4+} providing fewer electrons to the conduction band of the material than $Ir^{4.5+}$. As the substitution level of both antimony and zirconium increases there is an increase in surface area of the synthesised material consistent with decrease in crystallite size observed in Chapter 4. The oxygen evolution onset voltages of the antimony and zirconium substituted materials are slightly

higher than the unsubstituted material at the beginning of life and while there is some variation in the onset voltage post cycling the change is negligible.

Table 6.3: Conductivities, surface areas and oxygen evolution onset voltages at the beginning and end of life for zirconium and antimony substituted calcium sodium iridium oxide pyrochlore materials.

Material	Powder Conductivity / Scm^{-1}	BET	OER Onset Voltage / V	
		Surface Area / m^2g^{-1}	Beginning of Life	End of Life
25 % Sb Substituted	0.13	50.0	1.426	1.425
50 % Sb Substituted	0.02	81.6	1.441	1.431
25 % Zr Substituted	0.43	52.1	1.434	1.433
50 % Zr Substituted	0. 17	89.3	1.437	1.433

Figure 6.8 shows the activity and stability/selectivity data for antimony and zirconium substituted calcium sodium iridium oxide materials plotted with the unsubstituted material for comparison.

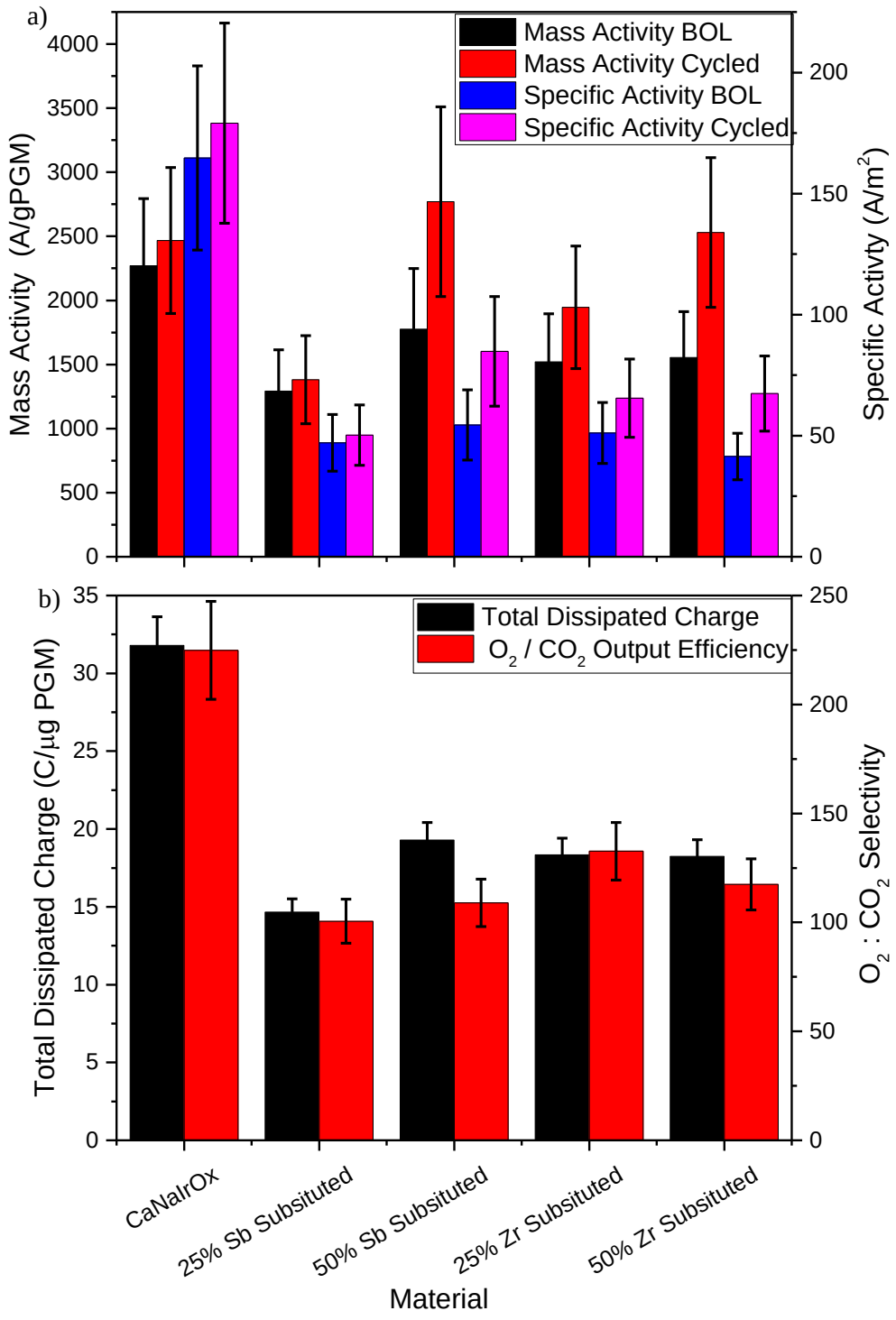

Figure 6.8: a) Activity metrics, and b) selectivity metrics for antimony and zirconium substituted pyrochlores.

Regardless of the substitution level there is a loss of mass activity and specific activity when substituting iridium by either antimony or zirconium, non-electroactive elements towards OER. This could possibly be due to electroactive surface sites being occupied by the redox inactive substituents. The loss could also be related to the drop in conductivity observed with

increasing substituent level. Like the unsubstituted material, the antimony and zirconium substituted materials all show an increase in activity post cycling.

While there is a small loss of activity when iridium is substituted for antimony or zirconium, all substituted material dissipate approximately only half the charge of the unsubstituted material. In addition, the selectivity of the oxygen evolution reaction over the carbon oxidation reaction suffers. As in all cases the O_2:CO_2 selectivity is approximately halved.

Table 6.4 shows various properties of the ruthenium substituted calcium sodium iridium oxide pyrochlore materials. The powder conductivity of the materials is rather similar across the series, which is unsurprising as $Ru^{4.5+}/Ru^{5+}$ contribute electrons to the conduction band of the materials. The oxygen evolution onset voltages of the ruthenium substituted materials at the beginning of life decrease across the solid solution, consistent with what is observed in the solid solution $(Ce_{0.66}Na_{0.34})_2(Ir_{1-x}Ru_x)_2O_7$.[2] Post cycling a large increase is seen in the oxygen evolution reaction onset potential for all materials, compared to the values at beginning of life.

Table 6.4: Conductivities, surface areas and oxygen evolution onset voltages at the beginning and end of life for ruthenium substituted calcium sodium iridium oxide pyrochlore materials.

Material	Powder Conductivity / Scm^{-1}	BET	OER Onset Voltage / V	
		Surface Area / m^2g^{-1}	Beginning of Life	End of Life
25 % Ru Substituted	0.35	46.7	1.380	1.414
50 % Ru Substituted	0.44	46.3	1.361	1.391
75 % Ru Substituted	0.29	44.9	1.326	1.395
100 % Ru Substituted	0.15	36.6	1.304	1.397

Figure 6.9 shows the activity and stability/selectivity data for ruthenium substituted calcium sodium iridium oxide materials in addition to the unsubstituted material for comparison.

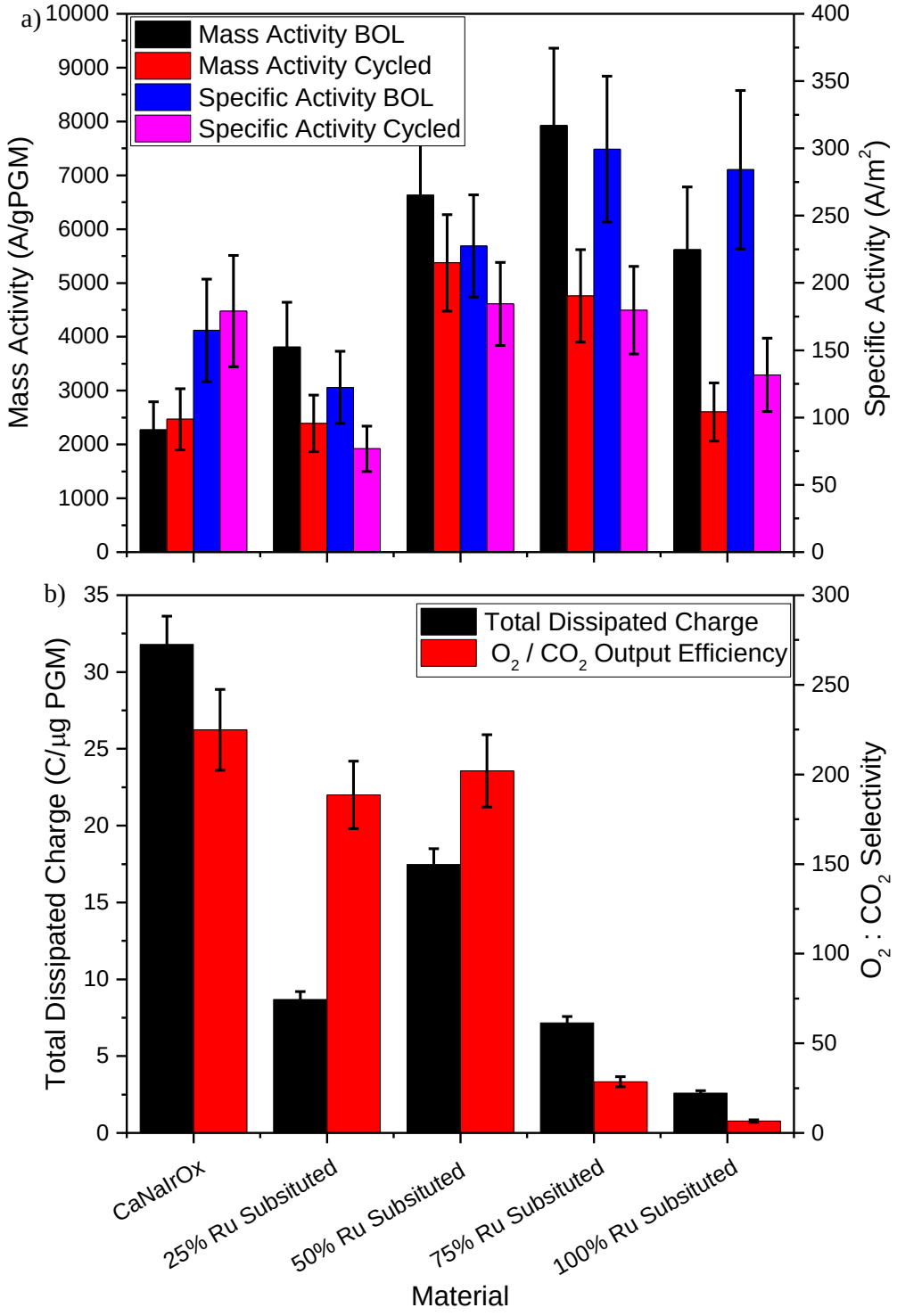

Figure 6.9: a) Activity metrics, and b) selectivity metrics for ruthenium substituted pyrochlores.

Unsurprisingly substituting iridium with ruthenium in the pyrochlore material yields materials considerably more active than the pure iridium material, which is consistent with what is seen the literature for $Ir_{1-x}Ru_xO_2$ oxygen evolution reaction catalysts.[7,8] The 75 % substituted material has a beginning of life mass activity almost four times greater than that

of the pure iridium material and a linear increase in beginning of life mass activity is observed between these points in the solid solution, Figure 6.10. There is then a significant reduction in mass activity for the pure ruthenium sample.

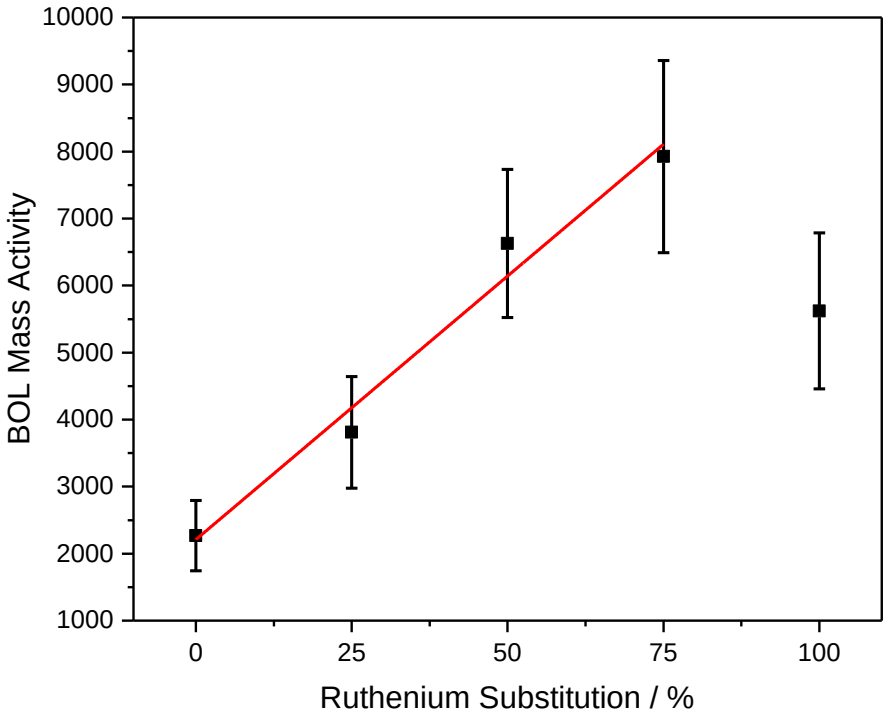

Figure 6.10: Beginning of life mass activities of ruthenium substituted calcium sodium iridium oxide materials.

Unlike the pure iridium material and the antimony and zirconium substituted materials the ruthenium substituted materials all lose activity after cycling, as is observed in the substituted ruthenium rutile materials. This is likely through the dissolution of ruthenium through the Ru^{4+} / Ru^{6+} redox couple as seen for RuO_2,[5] and phase separation of the material.

Despite being more active, the ruthenium substituted materials all dissipate considerably less charge than their pure iridium counterpart. The charge dissipated was highest for the 50 % substituted material. However this material only generates half the charge of the unsubstituted material, demonstrating the relative instability of ruthenium compared to iridium in this type of oxide catalyst.

The selectivity towards the OER over the COR is also worse than that of the pure iridium material for the ruthenium substituted materials. In the 25 and 50 % ruthenium substituted

materials the O_2:CO_2 selectivity is approximately half that of the unsubstituted material, but when the substitution level exceeds 50 % the O_2:CO_2 selectivity is an order of magnitude lower.

Table 6.5 shows various properties of the rhodium and manganese substituted calcium sodium iridium oxide pyrochlore materials. The powder conductivity of the materials show no trend across substitution level or substituted element, however all values are within an order of magnitude of the unsubstituted material. It is likely that both rhodium and manganese contribute electrons to the conduction band of the material but the substitution levels are relatively low so it is not surprising there is little variation. The beginning of life oxygen evolution onset voltages of both the rhodium and manganese substituted materials are similar to that of the unsubstituted material, while post cycling there is minimal change in onset voltage for all rhodium and manganese substituted materials.

Table 6.5: Conductivities, surface areas and oxygen evolution onset voltages at the beginning and end of life for rhodium and manganese substituted calcium sodium iridium oxide pyrochlore materials.

Material	Powder Conductivity / Scm^{-1}	BET	OER Onset Voltage / V	
		Surface Area / m^2g^{-1}	Beginning of Life	End of Life
15 % Rh Substituted	0.61	55.0	1.421	1.419
30 % Rh Substituted	0.15	61.2	1.417	1.415
15 % Mn Substituted	1.25	102.0	1.426	1.424
30 % Mn Substituted	0.44	95.6	1.426	1.418

Figure 6.11 shows the activity and stability/selectivity data for both the rhodium and manganese substituted calcium sodium iridium oxide materials in addition to the unsubstituted material for comparison.

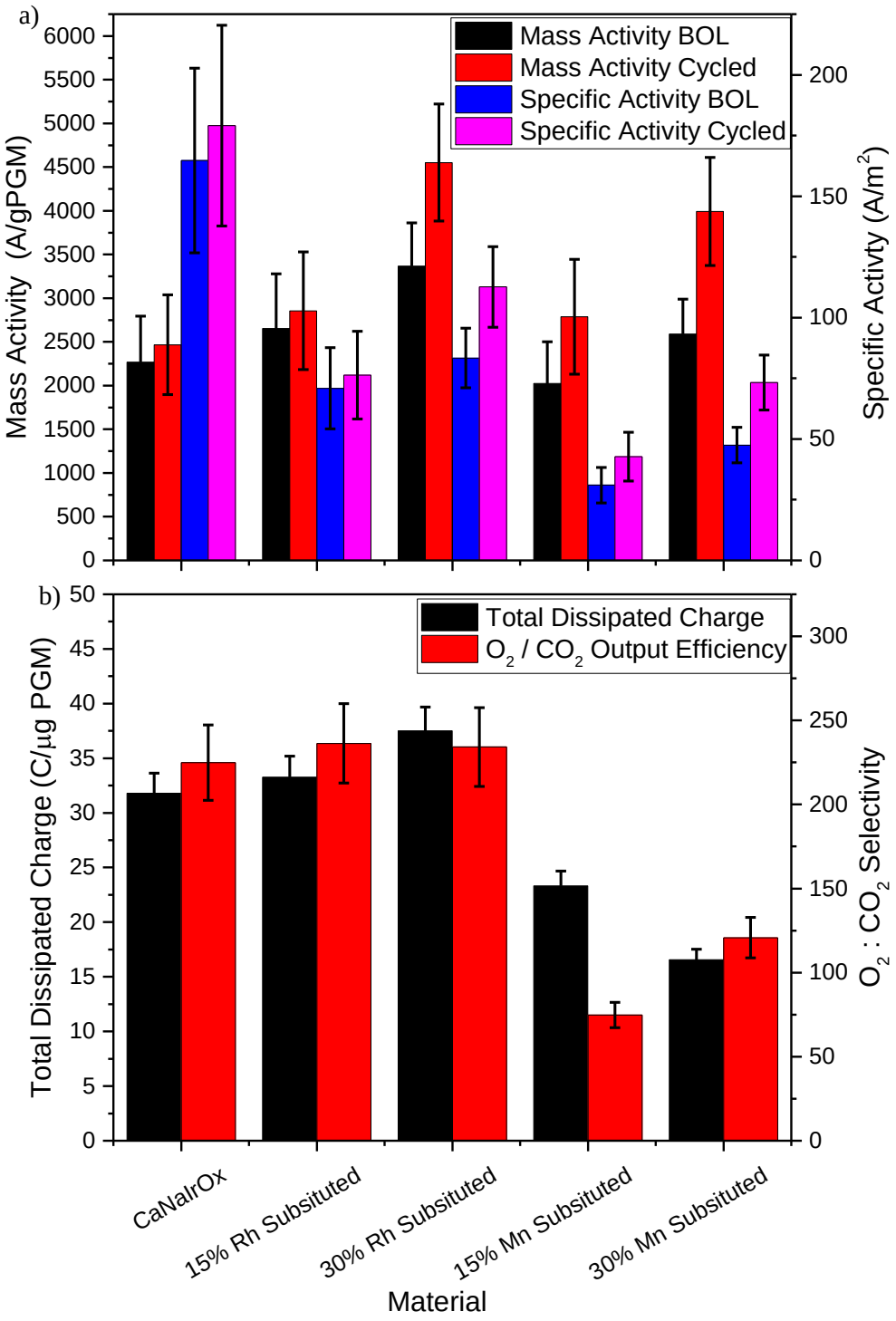

Figure 6.11: a) Activity metrics, and b) selectivity metrics for rhodium and manganese substituted pyrochlores.

When rhodium is substituted into the pyrochlore materials there is an increase in the beginning of life mass activity, whereas the beginning of life mass activity of the manganese substituted materials remains unchanged with respect to the unsubstituted material.

Post cycling all these materials show increase in the mass activity, with the 30 % substituted materials showing larger activity gains than the 15 % substituted materials.

Rhodium substitution produces materials with slightly increased values for the total dissipated charge. In addition to this the O_2:CO_2 selectivities are equal to those of the pure iridium material. Unfortunately, the manganese substituted materials both suffer from a reduced total dissipated charge and O_2:CO_2 selectivity.

6.4.3 Summary of Electrocatalysis from B-Site Substituted Iridate Pyrochlores

From the above discussion, the following can be deduced:

- Given the increase magnitude of the post cycling gains and losses of all the B-site substituted materials compared to the unsubstituted material, it seems likely that segregation of the B-site metals occurs during cycling as has been reported in $(Ni_{1-x}Fe_x)OOH$, an active OER catalyst in alkaline environments.[9] Other factors such as the materials' band structure,[10] M - O binding energy,[11] oxygen vacancies in the pyrochlore structure[12] and the level of hydroxylation/hydration[9] are all variables that may affect the activity of OER catalysts. By substituting iridium with other metals it is likely all of these will be affected to some degree, so it is difficult to say definitively what causes the changes in activity observed.
- The losses in total dissipated charge and O_2:CO_2 selectivity could be due to leaching of metals from these materials into the highly acidic Nafion. Mono and divalent metal ions have been shown bind to the Nafion resulting in cross linking between polymer chains and a brittle membrane, but also causes kinetic losses at the cathode and anode, ohmic loss, water flux and losses in proton conductivity across the membrane.[13] It is possible that this is not limited to mono and divalent cations and could extend to any of the metals found in these materials. Additionally the carbon support is also vulnerable to carbon oxidation through chemical degradation.[14]

Regarding specific substituents:

- Antimony and zirconium are not common substituents in oxygen evolution catalysts however it is possible that like many other metal oxides they solubilise at the potentials required for oxygen evolution.[15–17]
- Ruthenium substitution results in materials that deactivate post cycling. This is likely due to segregation of iridium and ruthenium, with ruthenium migrating to the surface and then dissolving, via the Ru^{4+}/Ru^{6+} redox couple,[5] through oxidation of ruthenium from the +4 state to the more soluble +6 through the binding of oxide/hydroxide surface species. Further the drop in activity between the 75 % ruthenium material and the pure ruthenium material would suggest the presence of a cooperative effect between the surface iridium and ruthenium sites, similar to that described in literature for $Ru_{1-x}Ir_xO_2$,[18,19] $(Ce_{0.67}Na_{0.33})_2(Ir_{1-x}Ru_x)O_7$[2] and $(Ni_{1-x}Fe_x)OOH$.[9]
- Rhodium substitution has little effect on the catalytic properties, and given rhodium is chemically similar to iridium this is unsurprising.
- The gains in mass activity post cycling displayed by the manganese substituted samples, are likely due to the same sort of phase separation postulated for the ruthenium substituted samples where manganese is replacing iridium on the surface sites. Manganese oxide is known to be an active oxygen evolution catalyst under acidic conditions, however it has been shown to dissolve under load.[16]

Thus the substitution of iridium in the pyrochlore does not lead to production of improved materials for use as oxygen evolution reaction catalysts.

6.4.4 A-Site Variations of $(Ca,Na)_{2-x}Ir_2O_6O'$

Every attempt to substitute iridium for another metal on the B site of the pyrochlore, with the exception of rhodium, lead to reduced durability of the catalyst material and reduced selectivity for the oxygen evolution reaction over the carbon oxidation reaction, under acidic conditions. Hence, the A-site substitution of calcium sodium iridium oxide was investigated:

see Chapter 4 where it is proved that Ca^{2+} and/or Na^{+} can be removed from the pyrochlore material. Table 6.6 shows various properties of the acid leached and as made calcium sodium and calcium iridium oxide pyrochlore materials. The powder conductivity of the materials remains relatively constant regardless of degree of leaching, which is unsurprising given the B-site sub lattice is largely unaffected by A-site substitution, See Chapter 4. The oxygen evolution onset voltages of calcium iridium oxide are virtually the same as those for calcium sodium iridium oxide, in addition leaching A-site metals from these materials seems to have little effect on the onset voltage.

Table 6.6: Conductivities, surface areas and oxygen evolution onset voltages at the beginning and end of life for calcium iridium oxide and calcium sodium iridium oxide pyrochlore materials under various degrees of acid leaching.

Material / Leaching Temperature	Powder Conductivity / Scm^{-1}	BET Surface Area / m^2g^{-1}	OER Onset Voltage / V	
			Beginning of Life	End of Life
$(Ca,Na)_{2-x}Ir_2O_6O'$ / 80 °C	0.40	39.7	1.433	1.429
$(Ca,Na)_{2-x}Ir_2O_6O'$ / 110 °C	0.42	22.6	1.407	1.409
$Ca_{2-x}Ir_2O_6O'$	0.40	27.3	1.421	1.422
$Ca_{2-x}Ir_2O_6O'$ / 80 °C	0.58	30.6	1.422	1.422
$Ca_{2-x}Ir_2O_6O'$ / 110 °C	0.25	28.9	1.407	1.412

Figure 6.12 shows the activity and stability/selectivity data for the calcium sodium and calcium iridium oxide materials and their acid leached derivatives. The variance in mass activities is not very large with the changing A-site composition of the of the iridium pyrochlore. The only exception to this is the calcium sodium iridium oxide leached at 80 °C, which is slightly less active than the rest of the materials. Of these materials the calcium iridium oxide leached at 110 °C is the most active. The process of acid leaching removes metals from the A-site of the material and the loss of charge must be balanced. It is likely this is achieved with protons binding to the oxygen atoms on the 48*f* site of the pyrochlore lattice, see Chapter 4, it is possible that this could cause the variance in performance observed between materials. Much like the calcium sodium iridium oxide the calcium iridium oxide has an increased activity post cycling, as do those materials leached at 80 °C. During the leaching process both materials leached at 110 °C yielded purple solutions,

indicative of a soluble iridium species being leached. It is possible the materials leached at 110 °C have suffered some chemical damage prior to been incorporated into a layer, and are subsequently more susceptible to further degradation under operating conditions.

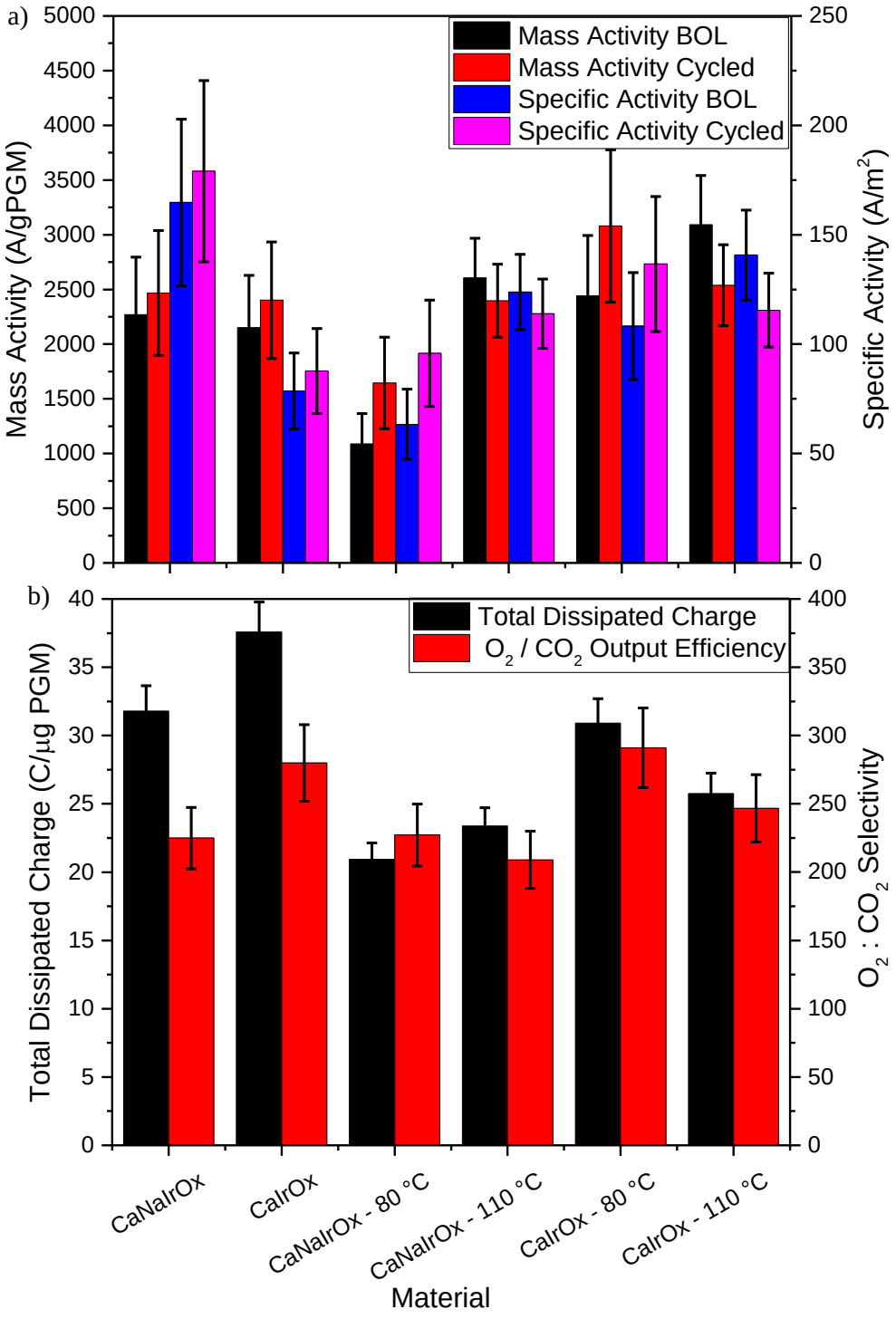

Figure 6.12: a) Activity metrics, and b) selectivity metrics for acid leached calcium sodium and calcium iridium oxide pyrochlores and their unleached counterparts.

While the total dissipated charge does not change much for this set of materials, certain conclusions can be drawn. The calcium iridium oxide dissipates more charge than calcium sodium iridium oxide. It may be proposed that this difference is due to the sodium being more leachable than the calcium in these materials, due to the difference in valence. The reduced total dissipated charge observed in the acid leached materials compared to the as made materials is likely due to damage to the electroactive lattice during the process of leaching. The O_2:CO_2 selectivity follows much the same trend as the total dissipated charge with the calcium iridium oxide outperforming the calcium sodium iridium oxide however the leached samples have similar O_2:CO_2 selectivities to their parent materials.

In addition to removing metal from the A-site of calcium sodium iridium oxide, the effect of surface area on the catalytic performance was tested. Table 6.7 shows various properties of two additional calcium sodium iridium oxide pyrochlore materials with increased surface areas. The two materials tested were those produced utilising reduced temperature reactions, see Chapter 4, with the small and medium particle size materials having crystallite sizes, from Scherrer analysis, of 11.2 and 25.0 nm respectively, compared to the 36.2 nm of the standard "large" particle size material. The powder conductivity of the materials remains within an order of magnitude regardless of the particle size. It might be expected that the powder conductivity would drop as the particle size is reduced due to the increased number of grain boundaries, however the powder conductivity of the small particle size material is higher than that of the larger particle size materials, which does not agree with grain boundary argument. The oxygen evolution onset voltages of all the calcium sodium iridium oxides are virtually the same as those for the original, large particle size calcium sodium iridium oxide.

Table 6.7: Conductivities, surface areas and oxygen evolution onset voltages at the beginning and end of life for calcium sodium iridium oxide pyrochlore materials with various particle sizes.

Material / Particle Size	Powder Conductivity / Scm^{-1}	BET	OER Onset Voltage / V	
		Surface Area / m^2g^{-1}	Beginning of Life	End of Life
$(Ca,Na)_{2-x}Ir_2O_6O'$ - Medium	0.29	40.3	1.414	1.424
$(Ca,Na)_{2-x}Ir_2O_6O'$ - Small	0.72	62.7	1.414	1.412

Beginning of life mass activities of the calcium sodium iridium oxide with various particle size do not vary much, Figure 6.13, however the material with the smallest particle size does have the greatest activity of the three samples. Post cycling however a slight increase in mass activity with decreasing particle size. However given the magnitude of the surface area changes across the series the relatively small change in activity is noteworthy.

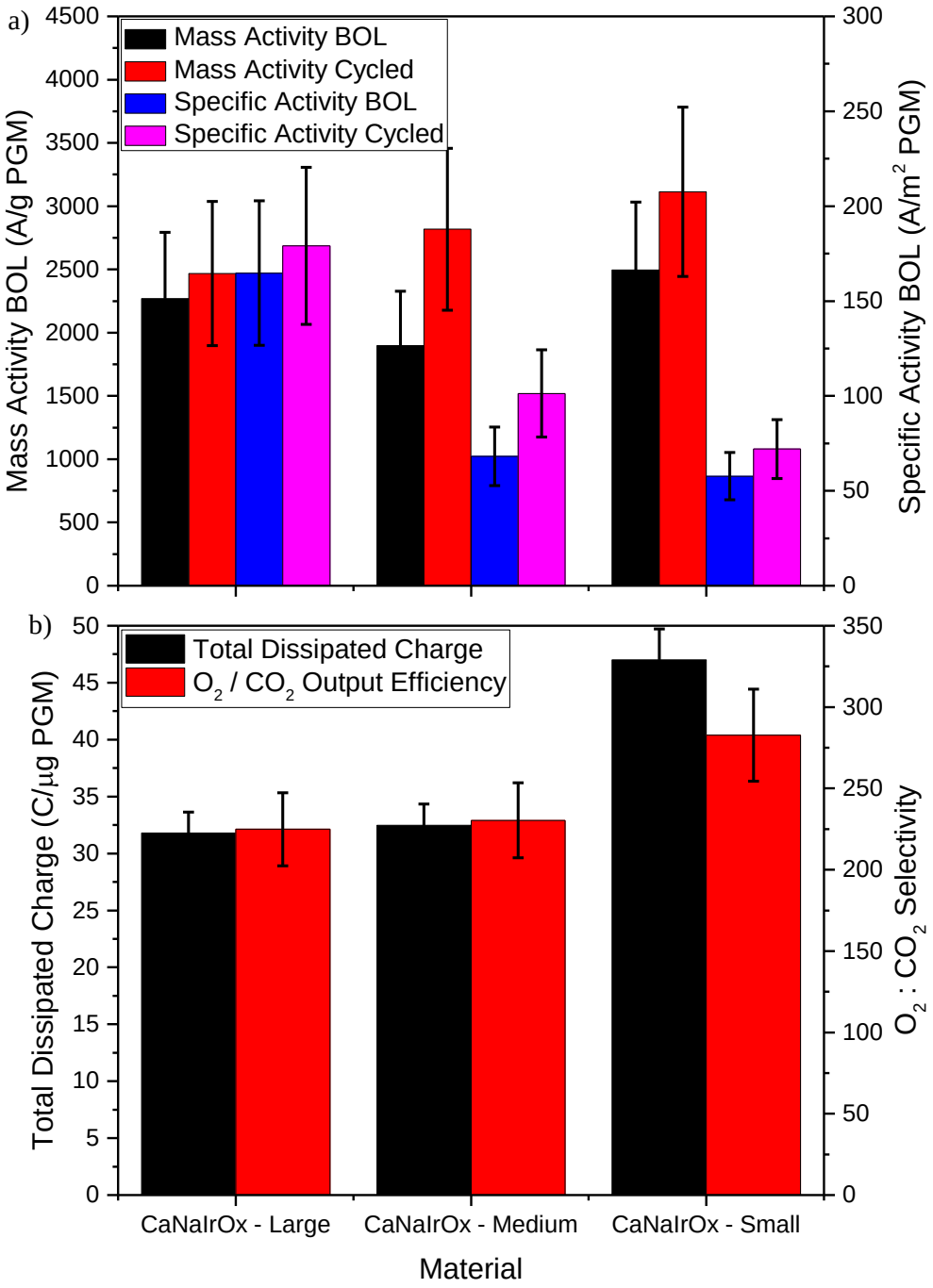

Figure 6.13: a) Activity metrics, and b) selectivity metrics for variable particle size pyrochlores.

The total dissipated charge and the O_2:CO_2 selectivity are virtually identical for the large and medium particle size materials, however there is a slight increase in both metrics for the small particle size material. This could be due to a more evenly distributed catalyst in the layer leading to fewer/smaller dead zones in the layer when the layer starts degrading.

6.4.5 Summary of Electrocatalysis from A-Site Substituted Iridate Pyrochlores

From the above discussion, the following can be deduced:

- The A-site composition has little effect on the catalytic performance of calcium sodium and calcium iridium oxides.
- The lack of any notable change in activity when the size of particles is reduced and associated surface area is increased suggests that the bulk, underlying crystal structure may be the dominant effect in OER catalytic activity.

6.5 Other Iridium Oxides for OER Catalysis

Various other oxide materials were synthesised in addition to the rutile and pyrochlore materials, see Chapter 5, and Table 6.8 shows various properties of these materials. Data for three barium iridium oxide materials are presented; $BaIr_2O_x$ - JM is the material produced from refining intermediate in NaOH, $BaIr_2O_x$ is the material produced from the "standard" synthesises at 240 °C in NaOH and $BaIr_2O_x$-Small is the material produced in the 160 °C reaction in NaOH. The powder conductivity of these materials vary a great deal but that is to be expected as many different structure types and compositions are represented. The oxygen evolution onset voltages of the potassium iridium oxide hollandite are higher than the rest of the oxides, while the strontium and barium iridium oxides have slightly lower onset voltages, which are comparable to that of calcium sodium iridium oxide.

Table 6.8: Conductivities, surface areas and oxygen evolution onset voltages at the beginning and end of life for other mixed metal iridium oxide materials with various particle sizes.

Material	Powder Conductivity / Scm^{-1}	BET Surface Area / m^2g^{-1}	OER Onset Voltage / V	
			Beginning of Life	End of Life
$Sr_{2.85}Ir_3O_{11}$	1.32	40.3	1.444	1.442
$BaIr_2O_x$ - JM	0.72	24.4	1.440	1.439
$BaIr_2O_x$	0.11	30.1	1.436	1.440
$BaIr_2O_x$ - Small	0.91	51.9	1.409	1.412
$K_{0.25}IrO_2$	0.03	6.1	1.465	1.453

Figure 6.14 shows the mass activities of the "other" oxides. With the exception of the potassium iridium oxide hollandite material all these materials are as active as calcium sodium iridium oxide. This is despite literature claiming that the hollandite displays excellent OER activity compared to IrO_2 based upon having a lower Tafel slope, as well as a lower overpotential at a current density of 20 $mAcm^{-2}$.[20] Of the various barium iridium oxides the small particle size version is the most active, however the difference in the mass activities is slight, much like what is observed in the pyrochlore study.

The total dissipated charge and the O_2:CO_2 selectivity of the hollandite are much lower than that of any other of the materials studied here, the rest of the materials are as stable and selective as the calcium sodium iridium oxide towards the oxygen evolution reaction. The small particle size barium iridium oxide dissipates slightly less charge than the rest of the materials this could be due to an increased rate of barium solubilisation given the increased surface area.

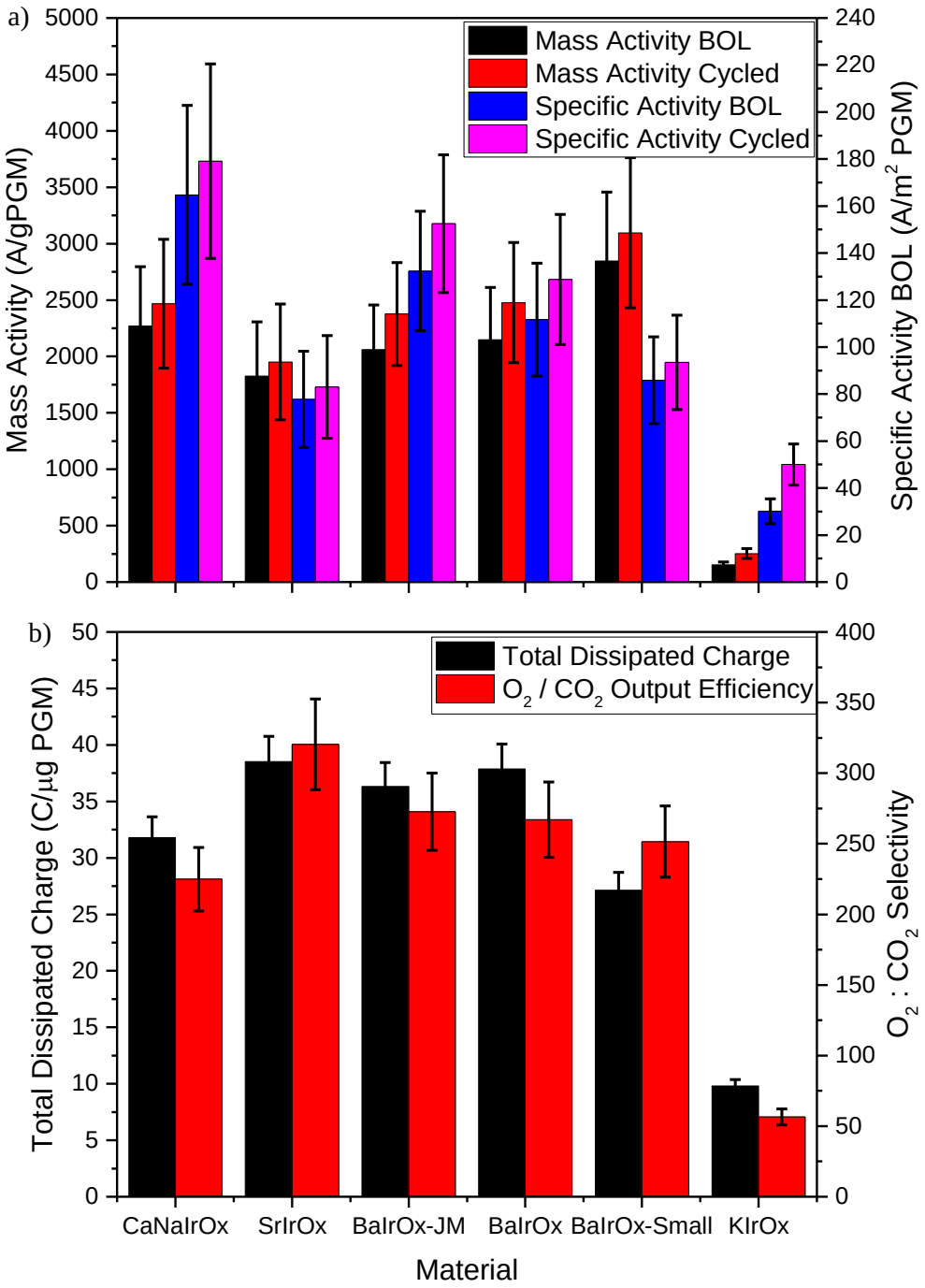

Figure 6.14: a) Activity metrics, and b) selectivity metrics for various other materials.

From the above discussion, the following can be deduced:

- While the hollandite material performs considerably worse than the rest of the materials studied in this section, it slightly outperforms the benchmark $Ru_{0.9}Ir_{0.1}O_2$.
- Like the calcium sodium iridium oxide pyrochlore, it is possible that not only the surface but the bulk material is involved in the oxygen evolution reaction in the

barium iridium oxide materials, demonstrated by the lack of any significant change in activity when the surface area is reduced.

6.6 *In situ* XAS

Of the substituted rutiles only the zinc and magnesium materials were studied *in situ.* Figure 6.15 shows how the oxidation state of the ruthenium found within the substituted rutiles changes with applied potential. The first observation is that there is a steady increase in oxidation state between 0.98 and 1.78 V *vs* RHE. This is significant as the onset of the oxygen evolution reaction occurs at just above 1.38 V *vs* RHE, so the ruthenium is oxidised before the onset of OER. It also appears the ruthenium in the zinc substituted material can be oxidised further than the magnesium substituted analogue,. The final observation to make is that the oxidation state switching doesn't appear to be completely reversible: as when both materials are returned to 0.98 V *vs* RHE after been held at 1.78 V the zinc and magnesium substituted materials have an oxidation state 0.25 and 0.1 higher than the first time they were held at 0.98 V. Further, upon applying 1.78 V for the second time both the zinc and magnesium substituted materials neither see the same oxidation state gain achieved the first time 1.78 V was applied. This could possibly be explained by phase separation of the substituted materials yielding a portion of RuO_2.

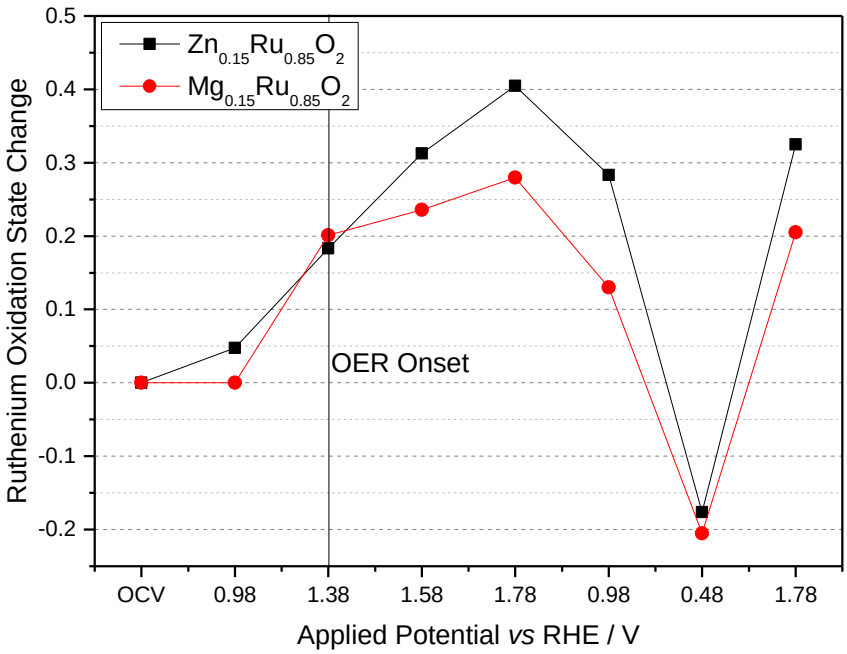

Figure 6.15: Plot showing shifts in oxidation state of ruthenium derived from analysis of *in situ* XANES spectra measured during electrochemistry of $(M_{0.15}Ru_{0.85})O_2$ materials.

Like the ruthenium in the substituted rutiles, it is observed that the iridium within the calcium sodium iridium oxide undergoes oxidation with increasing applied potential, Figure 6.16. However, unlike the substituted rutiles the iridium in these materials is oxidised and reduced much more reversibly with the relative degree of oxidation at both 0.98 and 1.78 V being virtually the same both times those potentials were applied. This implies that the calcium sodium iridium oxide is a more robust material than the substituted rutiles, which might be expected for an iridium oxide compared to a ruthenium oxide.

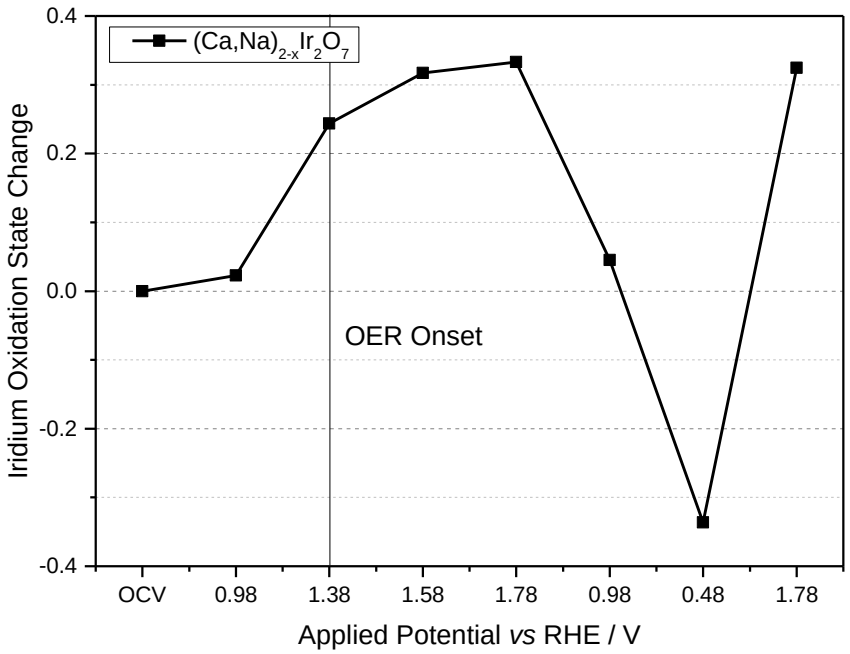

Figure 6.16: Plot showing shifts in oxidation state of iridium derived from analysis of *in situ* XANES spectra measured during electrochemistry of $(Ca,Na)_{2-x}Ir_2O_7$.

The calcium sodium iridium oxide was further studied, as in the literature two redox couples are commonly observed for iridium oxide layers, involving Ir^{3+}/Ir^{4+} and Ir^{4+}/Ir^{5+}, which happen at specific potentials.[21] The cyclic voltammetry of this pyrochlore shows similar features, Figure 6.17, where the Ir^{3+}/Ir^{4+} and Ir^{4+}/Ir^{5+} redox couples can be seen at 0.75 and 1.3 V *vs.* RHE.

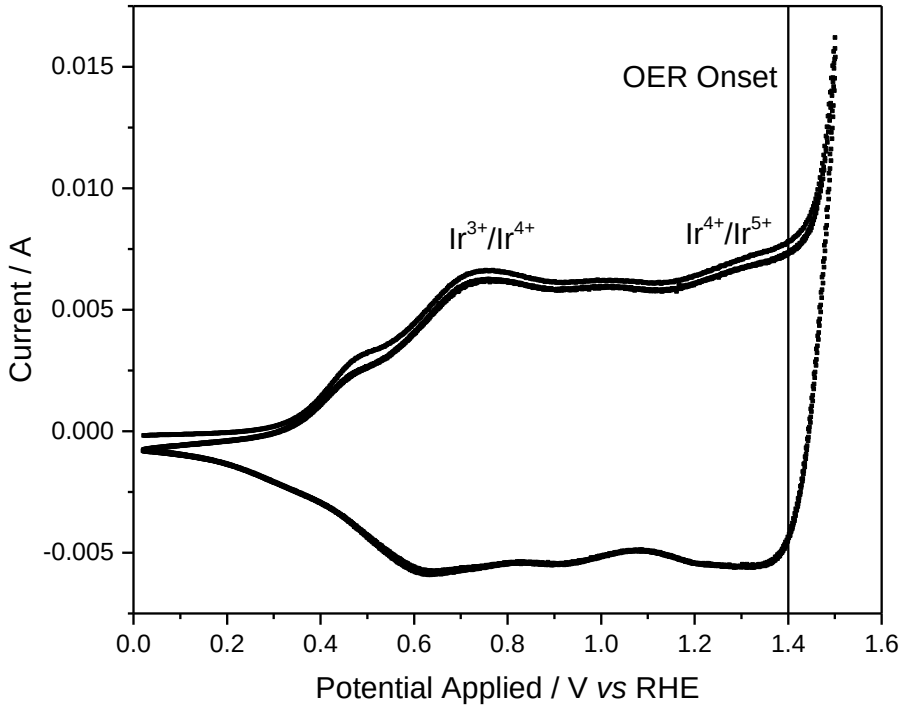

Figure 6.17: Cyclic Voltammetry of $(Ca,Na)_{2-x}Ir_2O_7$ with redox couples marked.

Thus one might expect that the oxidation state should not change with increasing applied potential until the applied potential corresponding to one of these redox couples is applied, at which point an abrupt change in oxidation should be observed. However, in Figure 6.18, a very linear increase in iridium oxidation state with applied potential is observed, even through the onset of OER at 1.38 V *vs* RHE. Further, Figure 6.18 shows repeated *in situ* results from calcium sodium iridium oxide measured during two different beamtimes at Diamond Light Source to check reproducibility of the results.

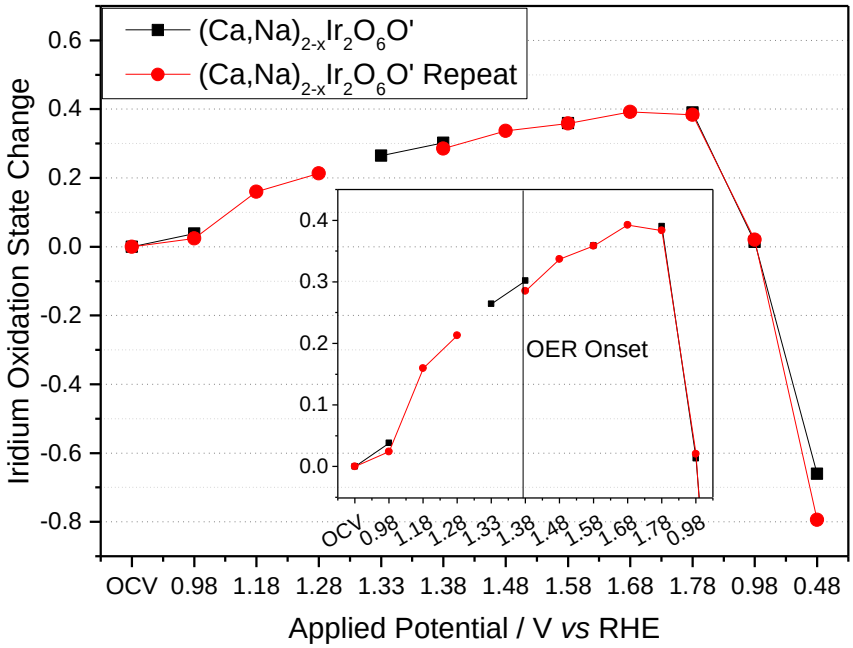

Figure 6.18: Plot showing shifts in oxidation state of iridium derived from analysis of *in situ* XANES spectra measured during electrochemistry of $(Ca,Na)_{2-x}Ir_2O_7$, from two different beam times and one with greater range of applied potentials on initial ramp. The inset highlights the steady increase in iridium oxidation state with increasing applied potential.

With the repeated set of data in Figure 6.18 the energy range over which XAFS data were collected was extended, allowing EXAFS analysis to be carried out. From the first shell fits to this data a mirror image of Figure 6.18 can be produced, where the Ir-O bond length shortens with applied potential, Figure 6.19. Performing EXAFS analysis the Debye-Waller factor can be extracted, which is a combined measure of thermal motion and static disorder (the distribution of bond distances). Assuming a negligible amount of heating from the OER, which is minimised by circulating the electrolyte, it can be assumed that any variation in the Debye-Waller factor can be attributed to variation of metal oxygen bond lengths within the material. This is informative as Hillman *et al.* suggested two models for OER in electrochemically deposited IrO_2, the bond model and the band model.[22] The bond model stipulates that only the surface reacts to applied potential, with conductivity resulting from electrons hoping between sites, as such there would two types of metal oxygen bond those on the surface and those unaffected in the bulk, which would result in an increasing Debye-Waller factor with increasing applied potential. If the band model holds true then all the metal oxygen bonds in the particle react in the same way to applied potential resulting in a

Debye-Waller that does not change with increasing potential. Here virtually no variation in the Debye-Waller factor is observed with increasing applied potential, suggesting that this pyrochlore follows the band model as all the iridium is responding in the same manner. If the material followed the bond model only the Ir-O bonds on the surface would be shortening, while those of the bulk would remain the same. While a decrease in the average bond distance would still be observed, the variance in bond length would increase and this would be seen in an increased Debye-Waller factor.

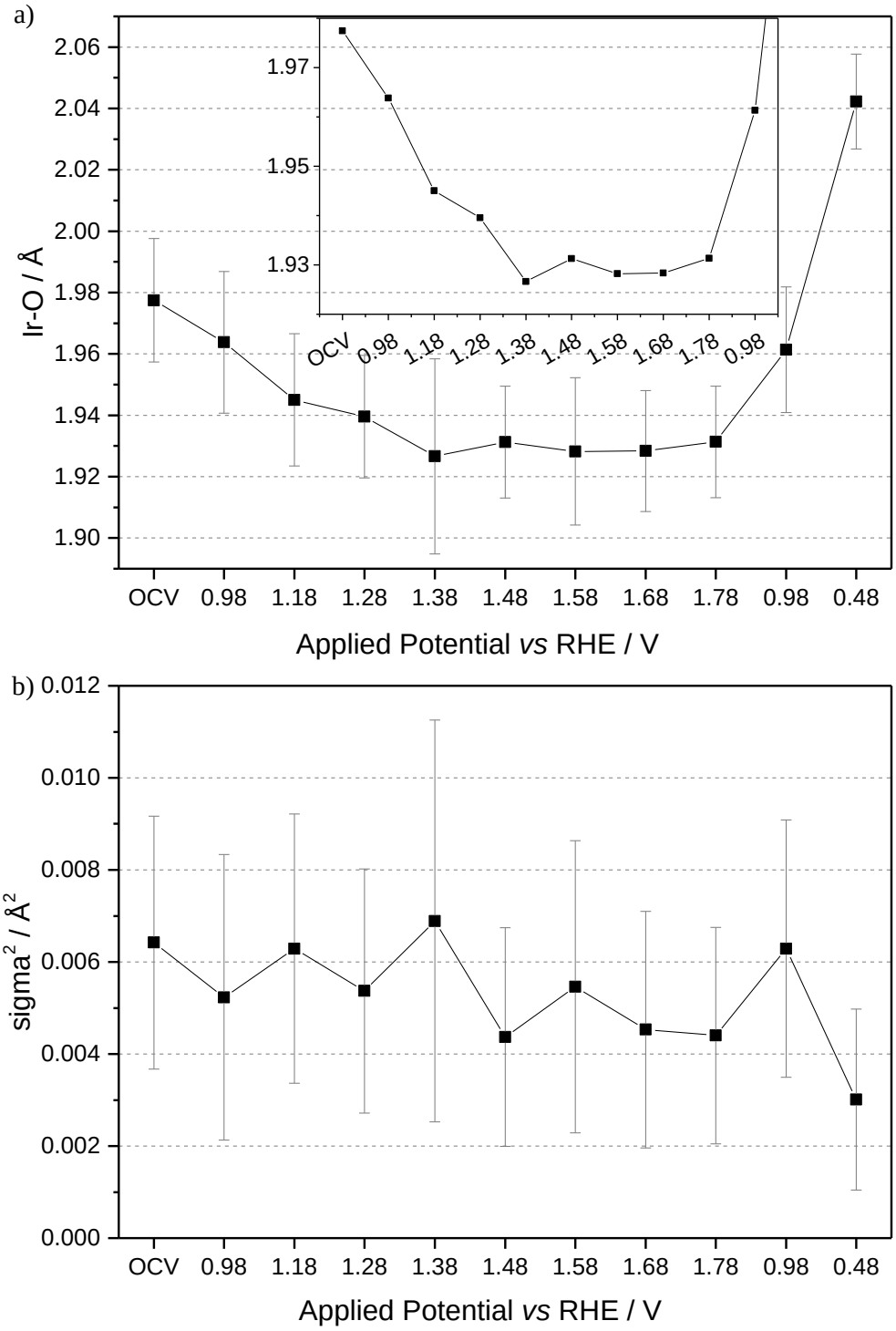

Figure 6.19: a) Plot showing shifts in iridium oxygen bond length derived from analysis of *in situ* EXAFS spectra measured during electrochemistry of $(Ca,Na)_{2-x}Ir_2O_7$. b) Debye-Waller factor σ^2 with applied potential.

When antimony is substituted into the pyrochlore the remaining iridium responds in the same fashion as the unsubstituted material, Figure 6.20. The substituent level does not change the magnitude or the reversibility of the change in oxidation state with respect to applied potential.

XANES spectra were also collected at the Sb K-edge for the antimony substituted materials, Figure 6.20. All antimony in the substituted materials was found to be in the +5 state in the dry powders, hence it is possible for the antimony to reduce to the +3 state, which is also stable, when 0.48 V as applied. It was found that regardless of the applied potential the oxidation state of the antimony in the 50 % substituted material does not change, even when 0.08 V was applied, in an attempt to force the reduction of antimony.

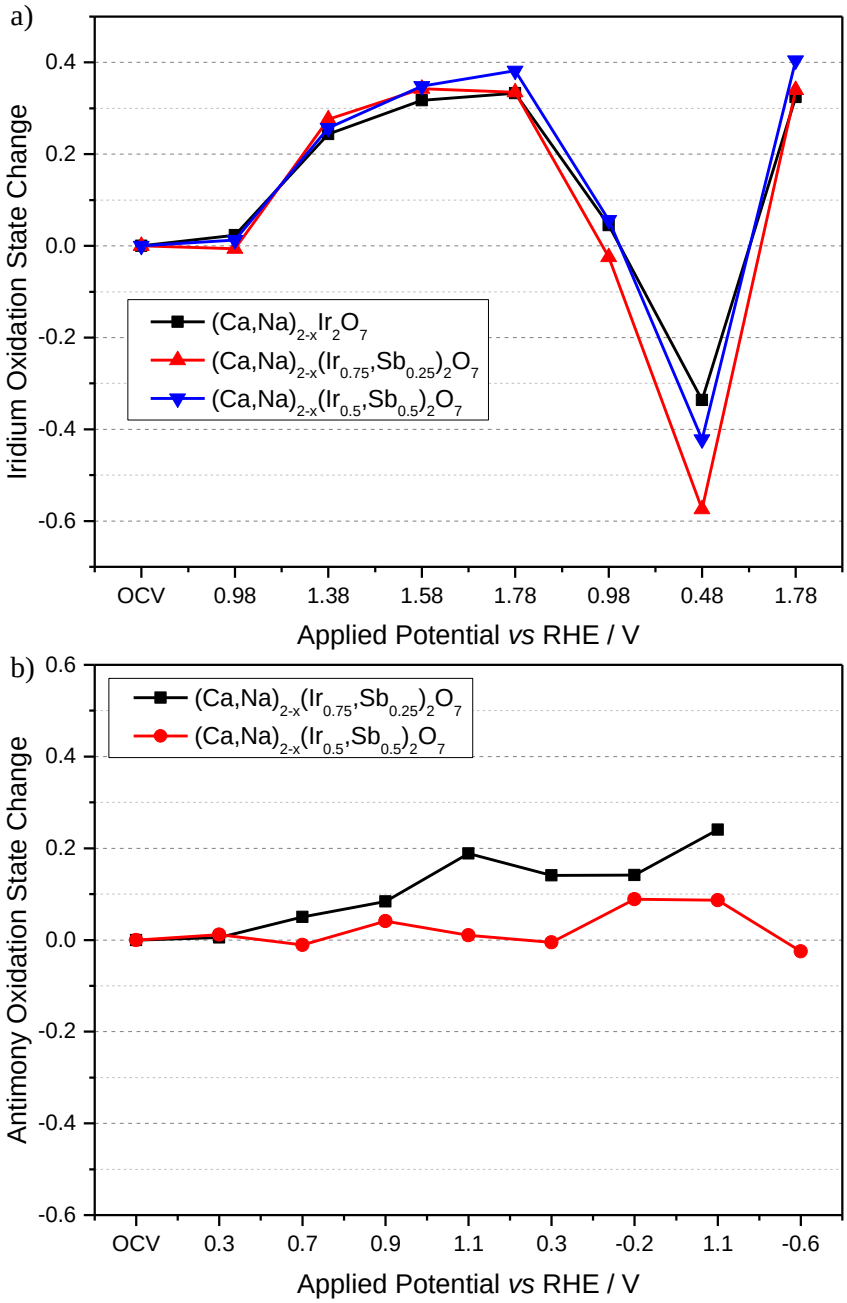

Figure 6.20: Plot showing shifts in oxidation state of a) iridium and b) antimony derived from analysis of *in situ* XANES spectra measured during electrochemistry of antimony substituted pyrochlore materials, with the unsubstituted material as a comparison.

Like the antimony substituted pyrochlore materials, when zirconium is substituted into the pyrochlore materials the remaining iridium responds in the same fashion as the unsubstituted material, Figure 6.21. The substituent level does not change the magnitude or the reversibility of the change in oxidation state with respect to applied potential.

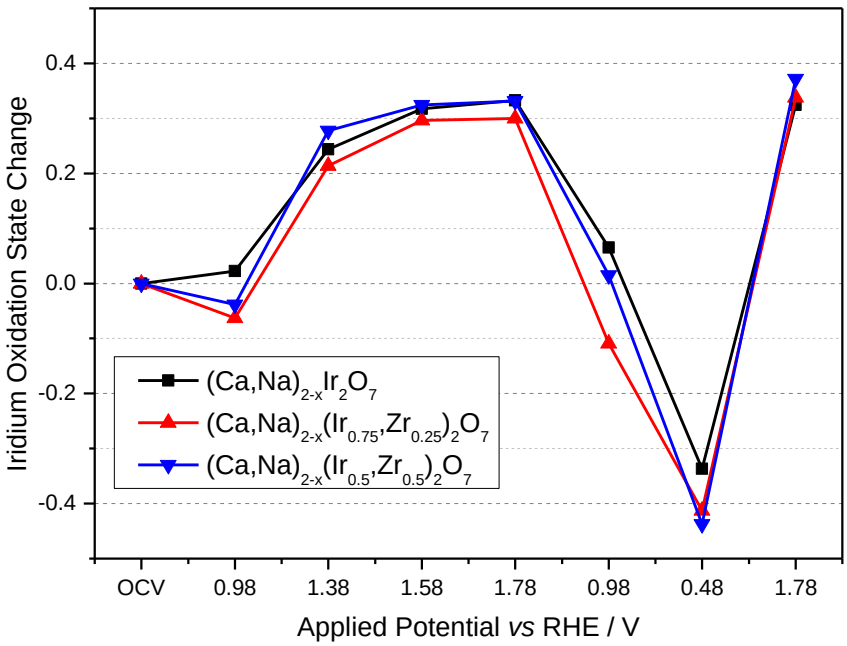

Figure 6.21: Plot showing shifts in oxidation state of iridium derived from analysis of *in situ* XANES spectra measured during electrochemistry of zirconium substituted pyrochlore materials, with the unsubstituted material as a comparison.

Substituting iridium with ruthenium appears to make the iridium instantly more responsive to the applied potential, Figure 6.22. There is then a drop in responsiveness as more iridium is substituted with ruthenium, however the responsiveness never drops as low as the pure iridium material. Previously the solid solution $(Ce_{0.67}Na_{0.33})_2(Ir_{1-x}Ru_x)_2O_7$ was studied in the same manner.[2] For that set of materials, a drop in the responsiveness of iridium oxidation state was also observed with increasing ruthenium fraction, however there was no initial increase and the by the time x = 0.5 there was virtually no response in the iridium oxidation state with applied potential. Across the solid solution, as the iridium responsiveness decreases the ruthenium compensates, becoming more responsive the higher its concentration in the material. Across the solid solution $(Ca,Na)_{2-x}(Ir_{1-y}Ru_y)_2O_7$ there is no obvious shift in the responsiveness of the ruthenium oxidation state.

Further, the iridium in these materials displays reversibility, behaving in the same manner as every other iridium containing pyrochlore in the study up to this point. The ruthenium also displays a high degree of reversibility when found in material also containing iridium, however in $(Ca,Na)_{2-x}Ru_2O_7$ behaviour similar to that of the substituted rutiles is observed. This gives further credence to the assertion that iridium stabilises ruthenium in OER catalysts.

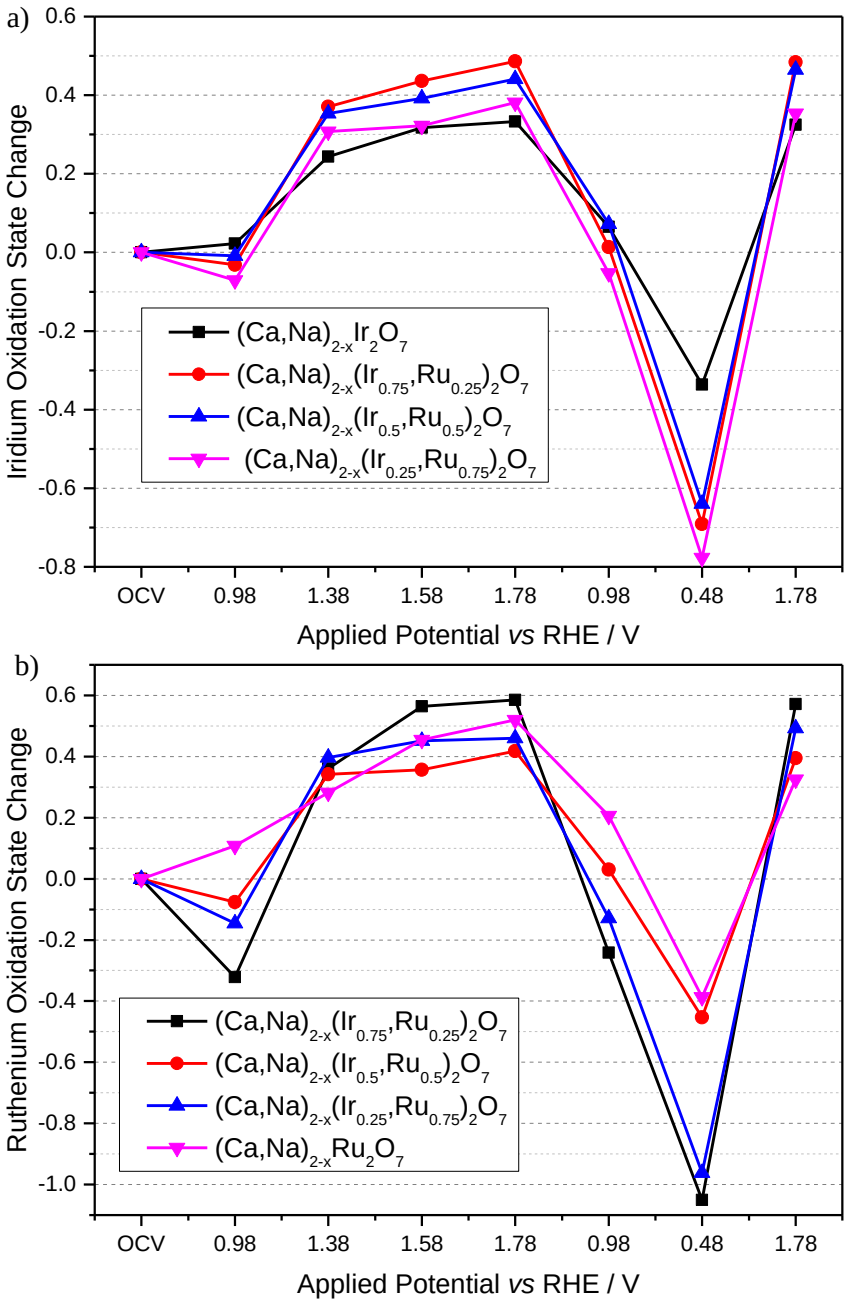

Figure 6.22: Plot showing shifts in oxidation state of a) iridium and b) ruthenium derived from analysis of *in situ* XANES spectra measured during electrochemistry of ruthenium substituted pyrochlore materials, with the unsubstituted material as a comparison.

Importantly, no evidence of the evolution of a pre-edge feature in the ruthenium XANES is observed, which would be indicative of the tetrahedral anions $[RuO_4]^{2-}$ and $[RuO_4]^{-}$, Figure 6.23.

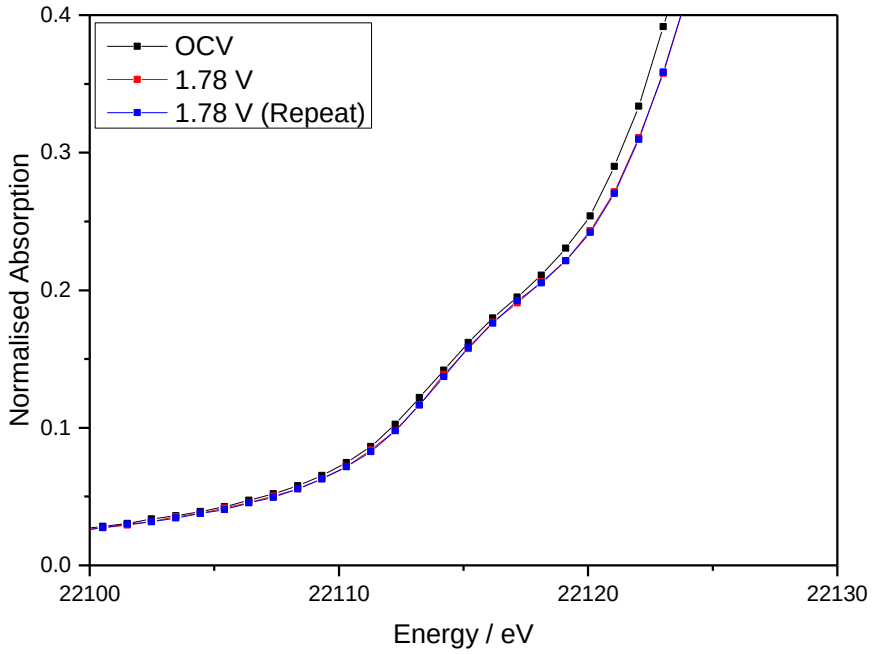

Figure 6.23: Show edge region of ruthenium K-edge XANES spectra from $(Ca,Na)_{2-x}(Ir_{0.5}Ru_{0.5})O_7$ during operation *in situ*.

Substituting iridium with rhodium leads to an increase in responsiveness of the iridium to the applied potential, however the rhodium is barely affected varying by only ±0.1 of an oxidation state in response to applied potential, Figure 6.24. This is opposite to what is observed when ruthenium is taking over from iridium in the $(Ce_{0.67}Na_{0.33})_2(Ir_{1-x}Ru_x)_2O_7$ materials, this offers strong evidence of a cooperative effect between the metals present.

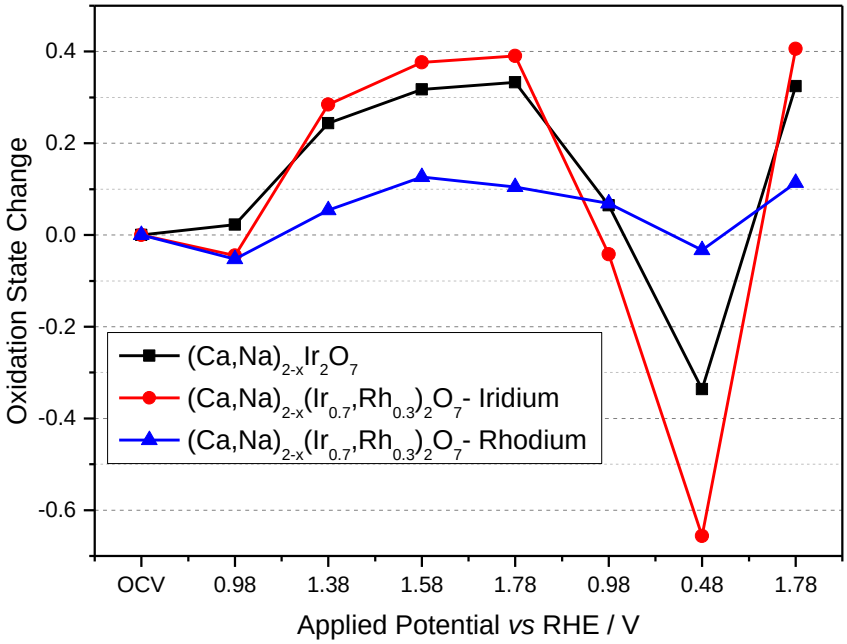

Figure 6.24: Plot showing shifts in oxidation state of iridium and rhodium derived from analysis of *in situ* XANES spectra measured during electrochemistry of ruthenium substituted pyrochlore materials, with the unsubstituted material as a comparison.

Figure 6.25, compares the oxidation state shifts of calcium sodium and calcium iridium oxides. The difference between calcium iridium oxide and calcium sodium iridium oxide is negligible, with calcium iridium oxide being slightly more responsive, correlating with the calcium iridium oxide being more active. The aged sample was the same sample used for the calcium sodium iridium oxide measurement, however after coming out of the beam it was cycled 500 times between 0.68 and 1.33 V *vs* RHE to replicate the cycling done in the MEA testing. After this the sample was put back in the beam and retested. Post cycling an increase in iridium responsiveness is observed, consistent with the increase in activity seen post cycling in the MEA, otherwise the response is largely unchanged. Upon forcefully removing the A site metal, by acid leaching at 110 °C, similar behaviour to the as made and aged samples is observed. There is still a linear increase in the iridium oxidation state with applied potential, and the maximum gain in oxidation state is the same as the unleached material. However, hysteresis is observed, as after reducing the applied potential form 1.78 to 0.98 V, the iridium remains partially oxidised approximately 0.15 of a oxidation state unit higher than the first time 0.98 V was applied. Additionally after increasing the potential from 0.48

to 0.98 V the iridium remains partially reduced approximately -0.15 of an oxidation state unit lower, with respect to the first time 0.3 V was applied.

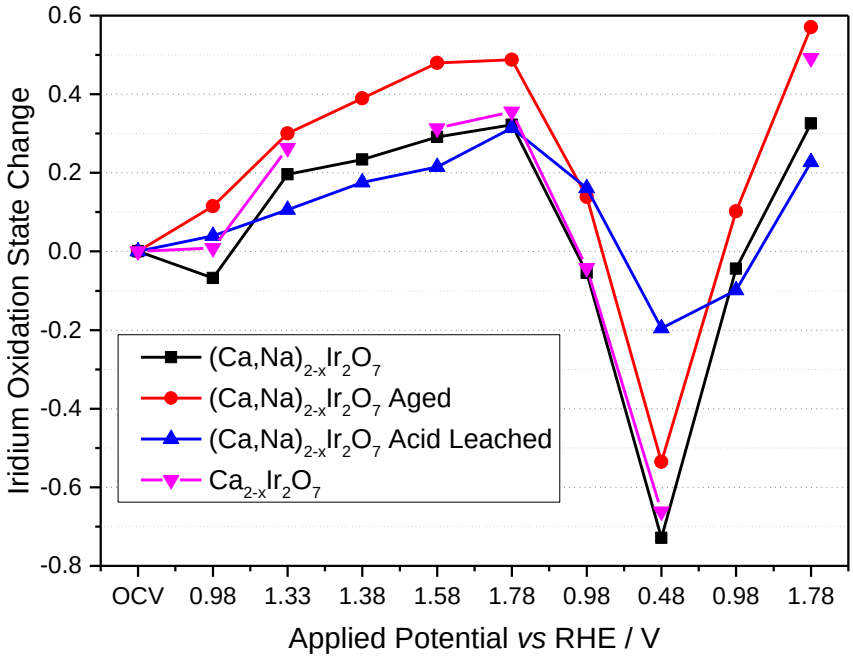

Figure 6.25: Plot showing shifts in oxidation state of iridium derived from analysis of *in situ* XANES spectra measured during electrochemistry of pyrochlore materials with various A site compositions.

Figure 6.26 shows the effect of particle size on the iridium response to applied potential. Both the large and medium particle sizes of calcium sodium iridium oxide behave in much the same way, while the small particle size is more responsive with applied potential. This agrees well with what is seen in MEA testing, with the small particle size sample being the most active.

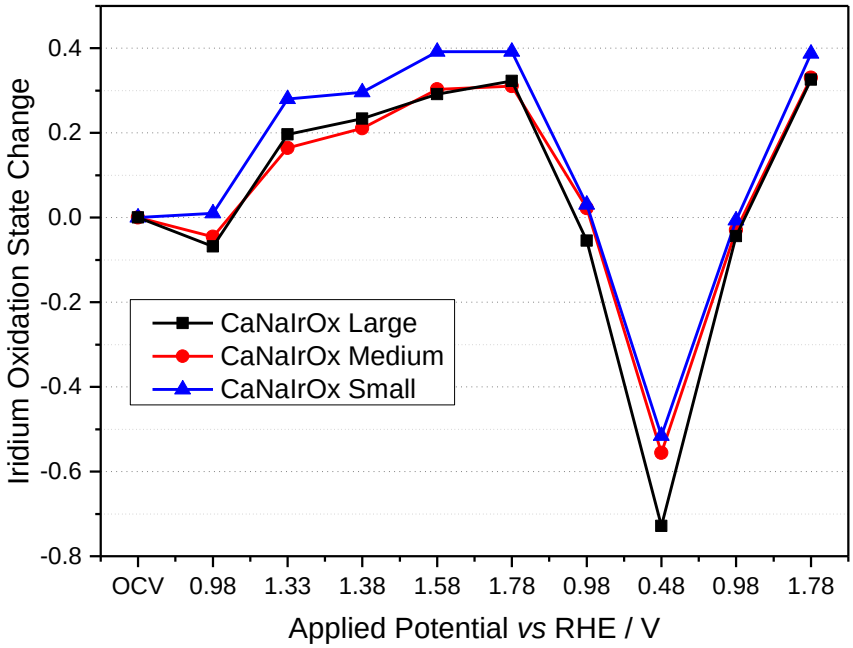

Figure 6.26: Plot showing shifts in oxidation state of iridium derived from analysis of *in situ* XANES spectra measured during electrochemistry of pyrochlore materials with various particle sizes.

Figure 6.27 shows the barium iridium oxide behaves in much the same fashion as calcium iridium oxide pyrochlore with a large gain in iridium oxidation state up till 1.78 V *vs* RHE. This is unsurprising given that barium iridium oxide is just as active as the pyrochlore material.

The iridium hollandite on the other hand is much less active than either the barium iridium oxide and calcium iridium oxides. This is mirrored in the iridium oxidation state shift with respect to applied potential.

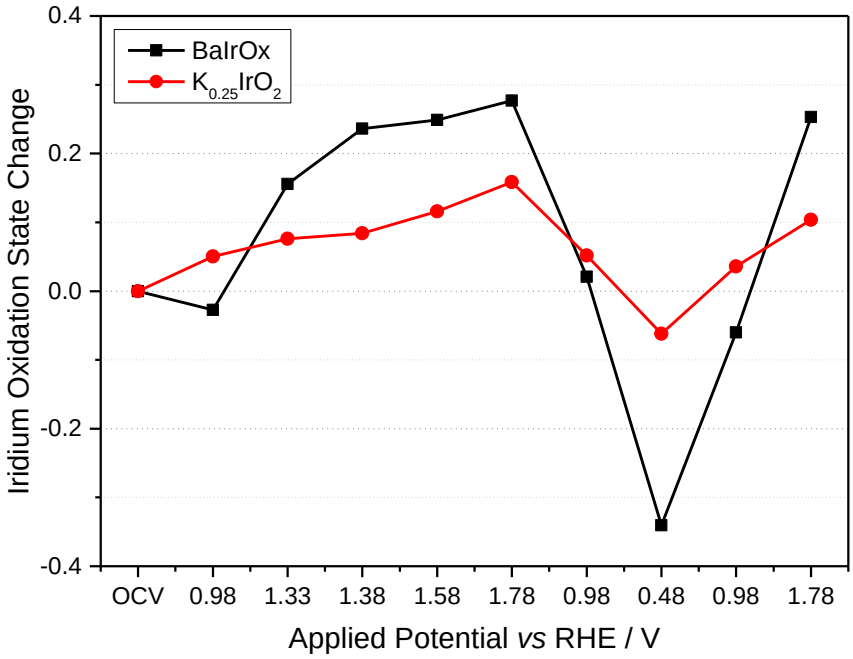

Figure 6.27: Plot showing shifts in oxidation state of iridium derived from analysis of *in situ* XANES spectra measured during electrochemistry of barium iridium oxide and the iridium hollandite.

6.7 Conclusions

With the exception of the potassium iridium oxide hollandite material, everything tested massively outperforms the benchmark materials in all aspects of catalytic performance. Figure 6.28 shows the beginning of life mass activities against the cycled mass activities of all tested materials, with those points above the line showing a gain in activity post cycling and those below it showing a decrease in activity post cycling. While in some cases there is significant deviation from this line, generally by ruthenium containing materials, there is a strong correlation between beginning of life mass activity and cycled mass activity .

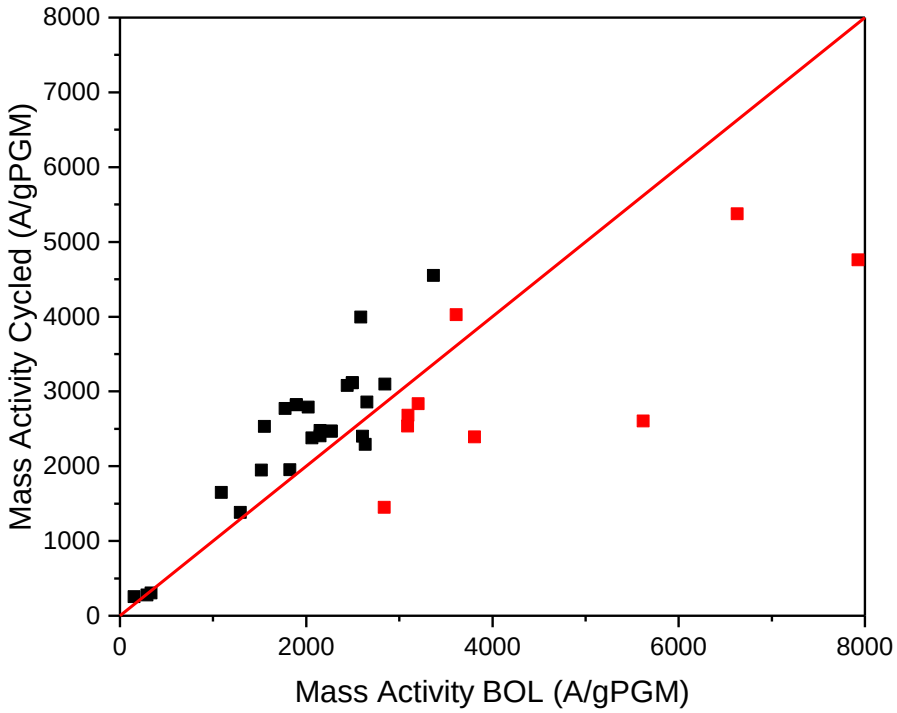

Figure 6.28: Plot showing the effect of cycling on the mass activates of all the tested materials. Ruthenium containing materials marked in red. Line indicating the point of no change in mass activity post cycling.

Figure 6.29 shows the total dissipated charge plotted against the O_2:CO_2 selectivity. A very strong correlation is observed between these parameters, which is understandable as any carbon dioxide given off must come from the carbon support and damage/corrosion of this could result in premature failure of the layer, reducing the total dissipated charge.

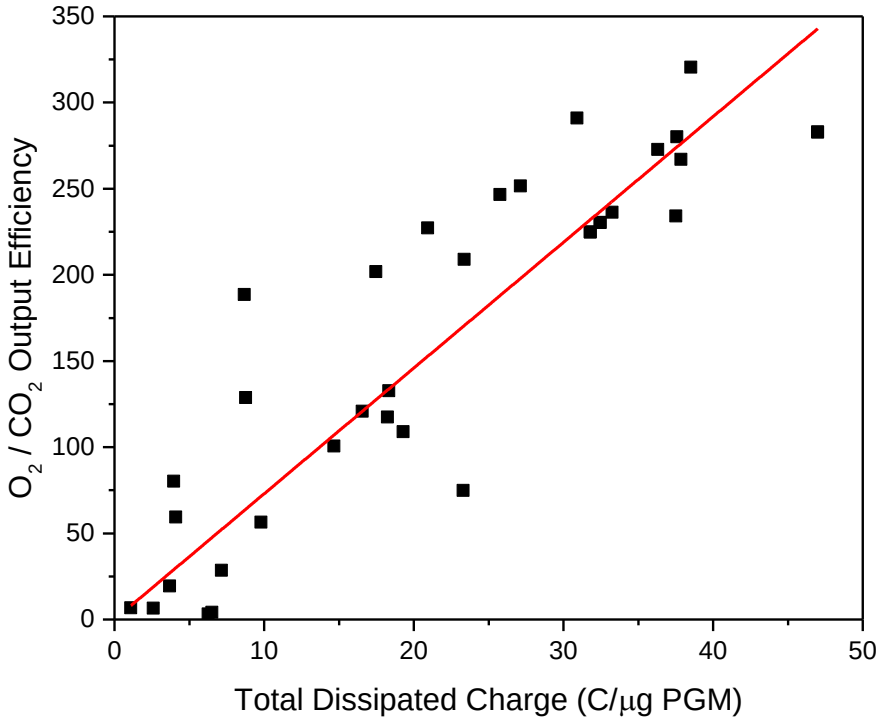

Figure 6.29: Plot correlating O_2:CO_2 selectivity with the total dissipated charge of all the tested materials.

Figure 6.30 shows a plot of the responsiveness of the oxidation state of the tested materials, obtained from *in situ* XAS and their BOL mass activities. The trend suggests the more active the material is the more the metal oxidation state responds to the applied potential. The exception to this is the ruthenium substituted pyrochlore materials, where the responsiveness of the ruthenium and iridium appear to decrease with increasing mass activity. This could be further evidence for the cooperative effect alluded to earlier in this chapter.

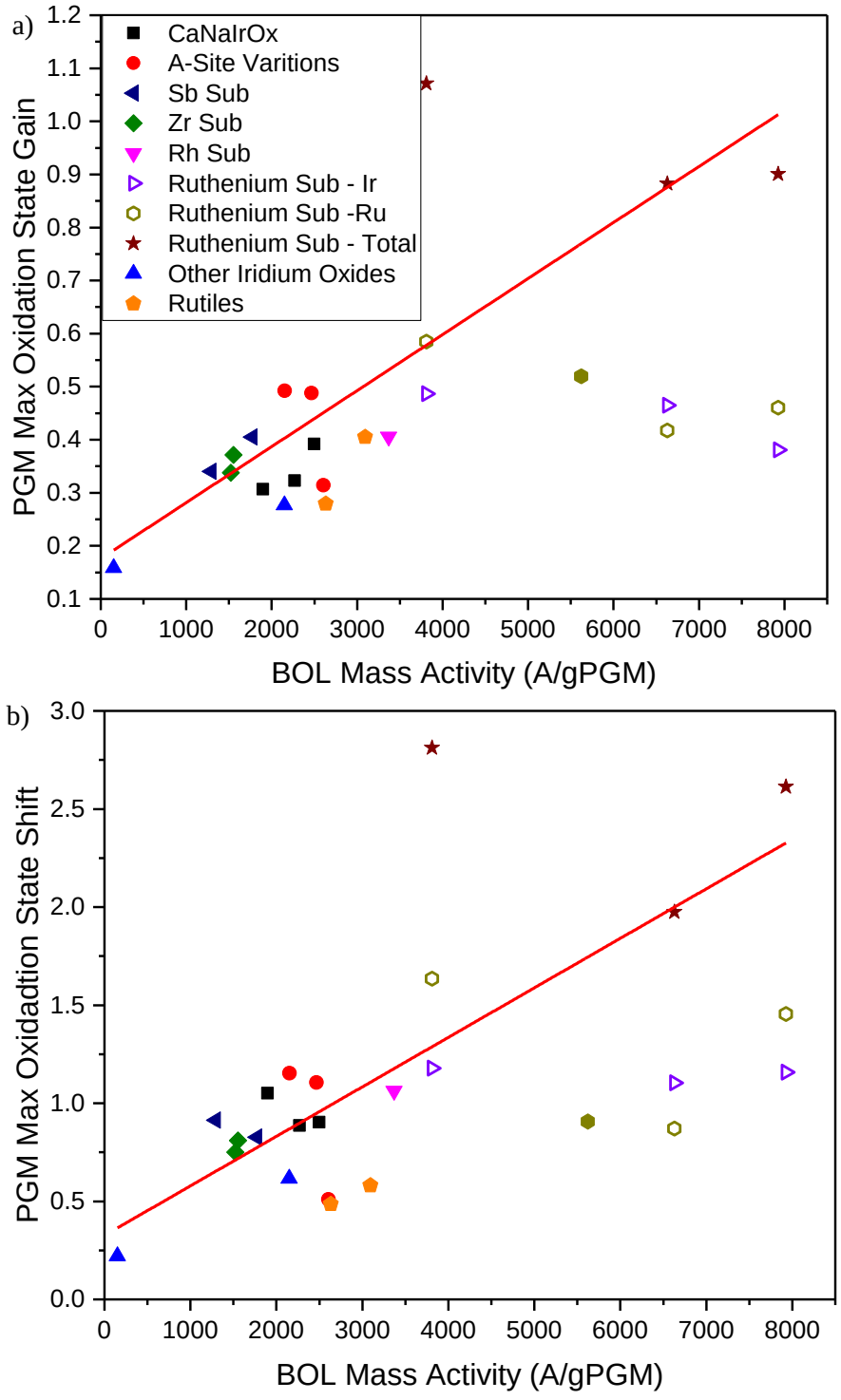

Figure 6.30: Plot correlating beginning of life mass activity with a) the maximum gain in PGM oxidation state obtained from *in situ* XAS and b) the flexibility in the PGM oxidation state obtained from *in situ* XAS.

The catalytic performance of a material towards the oxygen evolution reaction has previously been linked to several factors. Including the band structure,[10] M - O binding energy,[11] oxygen vacancies in the pyrochlore structure[23] and the level of hydroxylation/hydration of the material.[9] It can be suggested that the oxidation state

flexibility of metals found in metal oxide catalysts could relate to both oxide vacancies and the level of hydroxylation/hydration of a material. In this work, it is observed that the hollandite material, which has neither oxide vacancies nor hydroxyl/water within the crystal structure, displays little flexibility in metal oxidation state in response to applied potential, much like rutile $Ru_{1-x}Ir_xO_2$.[2] The pyrochlores and other materials studied all have at least one crystal site where the occupancy of oxygen is flexible and in Chapter 4 it was proven this site was occupied with crystal water. It is also assumed the strontium and barium iridate materials have crystal hydroxide or water within the structure, see Chapter 5. Thus the observed changes in metal oxidation state with applied potential could be due to the binding oxide ions to vacant sites or the deprotonation of hydroxyl or water already within the crystal structure. The active double perovskites recently reported,[6] have some potential for oxide vacancies and crystal hydroxyl/water compared to rutile materials so could, contribute to the fact they are more active than IrO_2. However the pyrochlore materials presented here are likely to have a much greater proportion of these defects. From these observations it appears the crystallographic density of materials could play a role in the activity, with the tightly packed rutile materials being less active than the less closely packed perovskites and hollandite type materials. These in turn are less active than the pyrochlore and $KSbO_3$-type structures which are the least dense crystallographically and have the most flexibility when it comes to crystallographic vacancies and level of hydration.

In reality it is difficult to compare the materials synthesised in this study with the double perovskites in the literature earlier, since their testing is designed and data is presented according to an “active surface area” that is calculated by an unconvincing method. The active surface area, also referred to as electrochemical surface area (ECSA) and is estimated from the double layer capacitance, as described by McCrory *et al.*, where it is stated, "In general, we believe the ECSA estimates to be accurate within about an order of magnitude, but caution that the values should be considered only as an approximate guide for comparing surface roughness."[24] Moreover, galvanostatic oxygen evolution on Au RDEs, as used in the

aforementioned work may lose activity via erosion of the catalyst. Additionally the repeatability/reliability of the coating method may affect the measured activity. In comparison the catalyst coated membranes produced for MEA testing are not susceptible to this erosion.

It has been shown that for calcium sodium iridium oxide activity is apparently independent of surface area, and that the band structure of the material responds to applied potential not just the surface atoms. This suggests more than just the surface is involved in the oxygen evolution reaction. It is not clear how applicable the mechanisms described in literature are to these new materials,[25,26] given that in all cases they only describe surface species, however, of the mechanisms presented in literature the electrochemical oxide path seems to be the most likely route to oxygen evolution given it displays the least variation in surface oxide species, which would agree with the lack of variation in the Debye-Waller factor with increasing applied potential. However the models presented in the literature are dominated by the modelling of thermodynamically controlled reactions, and it may be the case that the oxygen evolution reaction is kinetically controlled, in which case none of the models presented would adequately describe the behaviour of the catalyst. Further these models are somewhat simplified and may not be able to account for band type behaviour, as a band model would require the modelling of an entire particle rather than just the surface layer, as such determination of the mechanism by which the oxygen evolution reaction takes place for these materials lies outside the scope of this work and opens the possibility of further investigation.

References

1 Y. Lee, J. Suntivich, K. J. May, E. E. Perry and Y. Shao-Horn, *J. Phys. Chem. Lett.*, 2012, **3**, 399–404.

2 K. Sardar, E. Petrucco, C. I. Hiley, J. D. B. Sharman, P. P. Wells, A. E. Russell, R. J. Kashtiban, J. Sloan and R. I. Walton, *Angew. Chemie Int. Ed.*, 2014, **53**, 10960–10964.

3 J. Suntivich, K. J. May, H. A. Gasteiger, J. B. Goodenough and Y. Shao-Horn, *Science.*, 2011, **334**, 1383–1385.

4 N. B. Halck, V. Petrykin, P. Krtil and J. Rossmeisl, *Phys. Chem. Chem. Phys.*, 2014, **16**, 13682–13688.

5 J. M. Zen, A. S. Kumar and J. C. Chen, *J. Mol. Catal. A Chem.*, 2001, **165**, 177–188.

6 O. Diaz-Morales, S. Raaijman, R. Kortlever, P. J. Kooyman, T. Wezendonk, J. Gascon, W. T. Fu and M. T. M. Koper, *Nat. Commun*, 2016, **7**, 12363.
7 T. Audichon, T. W. Napporn, C. Canaff, C. Morais, C. Comminges and K. B. Kokoh, *J. Phys. Chem. C*, 2016, **120**, 2562–2573.
8 M. E. G. Lyons and S. Floquet, *Phys. Chem. Chem. Phys.*, 2011, **13**, 5314–5335.
9 M. S. Burke, L. J. Enman, A. S. Batchellor, S. Zou and S. W. Boettcher, *Chem. Mater.*, 2015, **27**, 7549–7558.
10 N. A. Vante, B. Schubert, H. Tributsch and A. Perrin, *J. Catal.*, 1988, **112**, 384–391.
11 S. Trasatti, *Electrochim. Acta.*, 1984, **29**, 1503–1512.
12 G. Gökağaç and B. J. Kennedy, *J. Electroanal. Chem.*, 1994, **368**, 235–239.
13 Y. Luan and Y. Zhang, in *PEM Fuel Cell Failure Mode Analysis*, Hoboken, NJ: CRC Press, 2011, pp. 73–108.
14 S. Maass, F. Finsterwalder, G. Frank, R. Hartmann and C. Merten, *J. Power Sources*, 2008, **176**, 444–451.
15 S. Zou, M. S. Burke, M. G. Kast, J. Fan, N. Danilovic and S. W. Boettcher, *Chem. Mater.*, 2015, **27**, 8011–8020.
16 M. Huynh, D. K. Bediako and D. G. Nocera, *J. Am. Chem. Soc.*, 2014, **136**, 6002–6010.
17 R. Frydendal, E. A. Paoli, B. P. Knudsen, B. Wickman, P. Malacrida, I. E. L. Stephens and I. Chorkendorff, *ChemElectroChem*, 2014, **1**, 2075–2081.
18 F. I. Mattos-Costa, P. de Lima-Neto, S. A. S. Machado and L. A. Avaca, *Electrochim. Acta.*, 1998, **44**, 1515–1523.
19 R. Kötz and S. Stucki, *Electrochim. Acta*, 1986, **31**, 1311–1316.
20 W. Sun, Y. Song, X.-Q. Gong, L. Cao and J. Yang, *ACS Appl. Mater. Interfaces*, 2016, **8**, 820–826.
21 P. Steegstra, M. Busch, I. Panas and E. Ahlberg, *J. Phys. Chem. C*, 2013, **117**, 20975–20981.
22 A. R. Hillman, M. A. Skopek and S. J. Gurman, *Phys. Chem. Chem. Phys.*, 2011, **13**, 5252–5263.
23 G. Goekagac and B. J. Kennedy, *ChemInform*, 1994, **25**, no--no.
24 C. C. L. McCrory, S. Jung, J. C. Peters and T. F. Jaramillo, *J. Am. Chem. Soc.*, 2013, **45**, 16977–16987.
25 J. O. Bockris, *J. Chem. Phys.*, 1956, **24**, 817.
26 E. Fabbri, A. Habereder, K. Waltar, R. Kotz and T. J. Schmidt, *Catal. Sci. Technol.*, 2014, **4**, 3800–3821.

Chapter 7 – Conclusions and Further Work

The four preceding results chapters have dealt with the synthesis and characterisation of a variety of new mixed metal oxides, and subsequent electrocatalytic testing of the materials. The work demonstrates the power of soft chemical methods in producing metal oxide phases that would be very hard if not impossible to synthesise in the solid state,[1] many of which, display favourable catalytic properties for oxygen evolution from water.

7.1 Substituted Ruthenium Oxides

A method for substituting ruthenium with elements of lower valence in rutile structured ruthenium oxide was discovered to produce materials $M_{0.15}Ru_{0.85}O_2$, where M = Zn, Mg, Ni, Co or Cu. XANES reveals that the ruthenium is oxidised above +4 in order to maintain charge balance in these materials. The nickel, cobalt and copper "peroxide" precursor materials used in the synthesis of some of these materials are poorly characterised, making optimisation of the reaction difficult, as such other materials could be investigated as potential regents. Preliminary work on the synthesis of the zinc substituted ruthenium oxide revealed that using zinc nitrate as a zinc source resulted in virtually amorphous materials, as such metal oxides could be investigated as possible reagents, following the successful reaction of silver oxide with potassium perruthenate yielding β-Ag_3RuO_4, by Prasad *et al.*.[2]

Raman spectroscopy, X-ray and neutron diffraction all show that when ruthenium is substituted the average rutile structure, described by space group $P4_2/mnm$, is maintained. Analysis of the Bragg scattering and PDF of the copper substituted material revealed the possibility of a Jahn-Teller distortion in the Cu-O octahedra. This possibility should be explored using Reverse Monte Carlo modelling, a method which fits atom positions in a large box to be consisted with experimental data . This would allow the simultaneous analysis of the Bragg, PDF and EXAFS data, yielding a more complete description of the copper substituted material.

7.2 Iridium Oxide Pyrochlores

First a more reliable method for the synthesis of $(Ca,Na)_{2-x}Ir_2O_6 \cdot H_2O$ than that of Sardar *et al.* was discovered.[3] It was found that the metals on both the A and B site could be substituted. Diffraction techniques reveal all these materials adopt the pyrochlore structure, with cubic space group $Fd\bar{3}m$, and PDF analysis of a selection of these materials shows this to be true even at the local scale, with the exception of the 50 % zirconium substituted material. Neutron diffraction revealed that some of the zirconium in this material could be found on the A-site of the pyrochlore and the low *r* region of the PDF showed clear peak splitting. This is likely due to the mismatch in ionic radii between zirconium and the rest of the metals, on both the A and B-site of the pyrochlore. Better fits to the data could be achieved in a couple of ways, either the zirconium could be shifted off the ideal A-site position or the oxygens could be shifted from their ideal positions, but a combination of these is also a possible explanation. All the proposed scenarios need to be tested using the software PDFgui, however RMC modelling may need to be employed to build a more complete model.

The average iridium oxidation state in all synthesised materials is +4.5, even though the substituent metals all have different oxidation states to that of iridium. This raises questions about how the materials are charge balanced. Several options were presented, the most likely solutions being variations in A-site occupancy and substitution of H_2O on the O' site with OH^- or O^{2-}. To further explore this ^{1}H and ^{17}O NMR studies would have to be undertaken, however even if this is carried out distinguishing between water and hydroxide could prove challenge, due to the mixture of these species on the O' site. The paramagnetic effects arising from unpaired electrons of iridium and some of the other metals in this set of materials could also complicate the NMR. While less likely, but it could be possible for a small portion of the larger of the B-site metals to migrate to the A-site like in the zirconium substituted material.

A method for stripping the A-site metals from the calcium and calcium sodium iridium oxide pyrochlore has been devised by acid leaching. While it is clear that to charge balance the material protons must replace the A-site metals, the question remains as to where they are located within the structure. Literature suggests the protons can be bound to the oxygen atoms within the pyrochlore lattice,[4] but to prove this a combination of neutron diffraction and spectroscopic techniques would be required.

7.3 Other Ruthenium and Iridium Oxides

Various other classes of oxide material were synthesised over the course of this project. Inspired by the work of Hiley *et al.*,[5,6] $SrRuO_3$ and 4H-$BaRuO_3$ have been synthesised hydrothermally, both which have previously only been produced through solid-state methods. The structure of these materials had previously been solved,[7,8] however due to what appear to be preferred orientation effects in the new samples, there are inconsistencies in the diffraction data, thus diffraction experiments need to be carried out where these effects can be limited. However, it may be possible that due to the soft chemical approach used in their synthesis, the new materials may adopt a slightly different structure their counterparts synthesised in the solid state. For example, oxide defects may be present.

It has been shown that iridium and ruthenium can be substituted into the perovskites $NaNbO_3$ and $NaTaO_3$. Owing to the very low levels of substitution achieved, it is unsurprising that these substituted materials maintain the crystal symmetry of their parent materials. It became apparent that substituting enough precious metal into these materials to make them electrically conductive may be impossible, a prerequisite for an OER catalyst. Given these materials are coloured, green and pink respectively for the iridium and ruthenium substituted materials, it is clear they have band gaps corresponding to light in the visible region of the spectrum. Thus while they are unsuitable for use as OER catalysts, it is possible they could find use as photocatalysts.

A strontium iridate adopting a $KSbO_3$ type structure has been synthesised. The strontium iridate is very similar to the hydrothermally produced $(Sr_{2.2}Na_{0.8})Ir_3O_{10.1}$,[3] however to address the issue of charge balance, there must be either crystal H_2O or OH^- contained in the structure. Thus TGA-MS and spectroscopic techniques should be employed in the search for these species. Ideally a neutron diffraction experiment would be undertaken, to locate which oxygen in the structure is substituted, however given iridium's high nuclear absorption, accurately doing this would prove challenging.

Finally a new barium iridate has been produced and unlike the rest of the materials presented in this body of work, the determination of a unit cell and space group that fit the XRD data has not been achieved. Using HR-TEM a lattice plane has been identified with a *d*-spacing of approximately 5.4 Å, this corresponds to the first observable peak in the XRD pattern, as such it is likely that at least one of the unit cell parameters corresponds to this distance or at the very least a multiple of it. Although the material is polycrystalline during the HR-TEM experiment a large intergrown crystal yielded an electron diffraction pattern with distinct spots, unlike the rings normally observed and if this could be indexed and a unit cell extracted it would aid the characterisation of this material. It may be possible to obtain information regarding the crystal symmetry from Raman spectroscopy, and identify possible crystal symmetries. Ideally a neutron diffraction experiment would then be undertaken, as this would yield another set of information. When the unit cell has been solved, these data would prove instrumental in locating the position and occupancy of the lighter atoms within the unit cell.

7.4 Catalytic Studies

Of the materials studied, the ones with the best balance between activity and selectivity for the OER reaction in aqueous acid were found to be the calcium, strontium and barium iridates as well as the acid leached calcium iridate pyrochlores. All of which outperform $Ru_{0.9}Ir_{0.1}O_2$ the benchmark in all chosen measures of performance. They also have less PGM per gram of material and have the advantage of being synthesised as fine powders that are

easily processed and made into catalyst coated membranes. In real devices, metal ions that leach from the catalysts, and subsequently bind to the Nafion are a major problem. Thus further experiments need to be undertaken in which the metal content in the electrolyte is monitored. In addition, analysis of the used catalyst layers should be undertaken and EDXA from TEM or ICP-OES are probably the most appropriate tools for this, looking for changes in the ratios of A and B-site metals. This is because the catalyst layers contain a large mass fraction of platinum on carbon catalysts, which has the potential to dominate many other analytical techniques, such as PXRD.

It has been demonstrated that substituting iridium with another metal in the calcium sodium iridium oxide pyrochlore material detrimentally affects selectivity of the material towards the OER for most cases investigated. Substituting iridium for ruthenium or manganese can increase the activity of the material but the losses in selectivity do not compensate for this.

The cobalt and nickel substituted ruthenium oxide rutile materials show no significant lowering of OER onset potential compared with $Ru_{0.9}Ir_{0.1}O_2$, despite what has been postulated using DFT calculations.[9] This suggests that the OER does not proceed via the two site model proposed in the literature for this type of material. All the substituted ruthenium oxide materials showed no advantages over the iridium oxide pyrochlores for OER, as such their further catalytic testing is not necessary.

Analysis of the *in situ* XAS data reveals that the iridium and ruthenium contained with all the materials reacts in the same manner when potential is applied under realistic OER conditions. Analysis of the EXAFS data from the calcium sodium iridium oxide reveals that while the Ir-O bond distances do shorten with increasing potential there is no increase in the variance of bond length. This suggests that the whole particle responds to applied potential not just the surface layer and this is in contrast with previous EXAFS studies of IrO_2 materials by Hillman *et al.*[10] Data were collected over a reduced energy range for the substituted materials, however it should still be possible to obtain a first shell fit to the

EXAFS data. This could possibly shed some light on the suspected cooperative effect between ruthenium and iridium in this type of OER catalyst.

Prior to commercialisation, the long term stability of the best catalysts needs to be tested, as while beyond the scope of this work is a necessary step towards implementation of viable PEMFC. The scale up of hydrothermal reactions has proven unreliable in the past.[11] Collaborators at Johnson Matthey Technology Centre have successfully scaled up the synthesis of the calcium sodium iridium oxide material using the peroxide method in large autoclaves. However, scaling up synthesis of the other materials is yet to be undertaken. Given the similarities between the technologies, it is likely these materials would also be excellent OER catalysts in water electrolysers and should be tested as such.

References

1 K. Byrappa and M. Yoshimura, *Handbook of Hydrothermal Technology: A Technology for Crystal Growth and Materials Processing*, Noyes Publications, New Jersey, USA, 2001.

2 B. E. Prasad, P. Kazin, A. C. Komarek, C. Felser and M. Jansen, *Angew. Chemie Int. Ed.*, 2016, **55**, 4467–4471.

3 K. Sardar, J. Fisher, D. Thompsett, M. R. Lees, G. J. Clarkson, J. Sloan, R. J. Kashtiban and R. I. Walton, *Chem. Sci.*, 2011, **2**, 1573–1578.

4 P. G. Dickens and M. T. Weller, *Solid State Commun.*, 1986, **59**, 569–573.

5 C. I. Hiley, M. R. Lees, D. L. Hammond, R. J. Kashtiban, J. Sloan, R. I. Smith and R. I. Walton, *Chem. Commun.*, 2016, **52**, 6375–6378.

6 C. I. Hiley, M. R. Lees, J. M. Fisher, D. Thompsett, S. Agrestini, R. I. Smith and R. I. Walton, *Angew. Chemie Int. Ed.*, 2014, **53**, 4423–4427.

7 W. Bensch, H. W. Schmalle and A. Reller, *Solid State Ionics*, 1990, **43**, 171–177.

8 S.-T. Hong and A. W. Sleight, *J. Solid State Chem.*, 1997, **128**, 251–255.

9 N. B. Halck, V. Petrykin, P. Krtil and J. Rossmeisl, *Phys. Chem. Chem. Phys.*, 2014, **16**, 13682–13688.

10 A. R. Hillman, M. A. Skopek and S. J. Gurman, *Phys. Chem. Chem. Phys.*, 2011, **13**, 5252–5263.

11 S. S. Joshi and V. V Ranade, *Industrial Catalytic Processes for Fine and Specialty Chemicals*, Elsevier Science, Amsterdam, Netherlands, 2016.